



ROMA TRE UNIVERSITY

DEPARTMENT OF MATHEMATICS AND PHYSICS

DOCTORAL SCHOOL IN MATHEMATICS AND PHYSICS  
XXX CYCLE

PH.D. THESIS IN PHYSICS

---

**Time series analysis:  
A new methodological approach  
for a worldwide comparison of  $^7\text{Be}$   
and meteorological parameters**

---

*Author*

STEFANO BIANCHI

*Tutor*

Prof. WOLFANGO PLASTINO

*Coordinator*

Prof. GIUSEPPE DEGRASSI

Rome, 2017

---

# Contents

---

<b>Introduction</b>	<b>1</b>
<b>1 CTBT and International Monitoring System</b>	<b>3</b>
1.1 Comprehensive Nuclear-Test-Ban Treaty . . . . .	3
1.1.1 Atmospheric tests . . . . .	3
1.1.2 High atmosphere tests . . . . .	5
1.1.3 Underwater tests . . . . .	5
1.1.4 Underground tests . . . . .	5
1.2 International Monitoring System . . . . .	5
1.2.1 Seismic monitoring . . . . .	7
1.2.2 Hydroacoustic monitoring . . . . .	8
1.2.3 Infrasound monitoring . . . . .	9
1.2.4 Radionuclide monitoring . . . . .	10
1.3 Environmental chemistry of Beryllium 7 . . . . .	13
1.4 Applications of Beryllium 7 . . . . .	14
<b>2 Models and methods</b>	<b>18</b>
2.1 Logical scheme . . . . .	18
2.2 Block A . . . . .	20
2.2.1 Detrend . . . . .	20
2.2.2 GLS . . . . .	23
2.3 Block B . . . . .	27
2.3.1 Filter . . . . .	27
2.3.2 Residuals . . . . .	28
2.4 Block C . . . . .	28
2.4.1 Distribution fit . . . . .	28
2.4.2 GOF test . . . . .	32
2.4.3 Normalisation & Outliers . . . . .	33

2.4.4	DFA . . . . .	34
2.4.5	Local Hurst . . . . .	37
2.5	Detrended Cross-Correlation Analysis . . . . .	40
<b>3</b>	<b><sup>7</sup>Be worldwide time series analysis</b>	<b>41</b>
3.1	Missing data . . . . .	41
3.2	Data pre-processing . . . . .	42
3.3	Analysis of <sup>7</sup> Be time series . . . . .	45
3.3.1	Chatham Island, New Zealand (RN46) . . . . .	46
3.3.2	Kaitaia, New Zealand (RN47) . . . . .	49
3.3.3	Rarotonga, Cook Islands (RN23) . . . . .	52
3.3.4	Melbourne, VIC, Australia (RN04) . . . . .	55
3.3.5	Perth, WA, Australia (RN10) . . . . .	58
3.3.6	Buenos Aires, Argentina (RN01) . . . . .	61
3.3.7	Townsville, QLD, Australia (RN06) . . . . .	64
3.3.8	Stockholm, Sweden (RN63) . . . . .	67
3.3.9	Darwin, NT, Australia (RN09) . . . . .	70
3.3.10	Charlottesville, VA, USA (RN75) . . . . .	73
3.3.11	Ulaanbaatar, Mongolia (RN45) . . . . .	76
3.3.12	Yellowknife, N.W.T., Canada (RN16) . . . . .	79
3.3.13	Rio de Janeiro, Brazil (RN11) . . . . .	82
3.3.14	Cocos Islands, Australia (RN08) . . . . .	85
3.3.15	Ashland, KS, USA (RN74) . . . . .	88
3.3.16	Schauinsland/Freiburg, Germany (RN33) . . . . .	91
3.3.17	Tristan da Cunha, United Kingdom (RN68) . . . . .	94
3.3.18	Melbourne, FL, USA (RN72) . . . . .	97
3.3.19	Nadi, Fiji (RN26) . . . . .	100
3.3.20	Oahu, Hawaii, USA (RN79) . . . . .	103
3.3.21	Panama City, Panama (RN50) . . . . .	106
3.3.22	Tanay, Philippines (RN52) . . . . .	109
3.3.23	St. John's, N.L., Canada (RN17) . . . . .	112
3.3.24	Nouakchott, Mauritania (RN43) . . . . .	115
3.3.25	Okinawa, Japan (RN37) . . . . .	118
3.3.26	Sand Point, Alaska, USA (RN71) . . . . .	121
3.3.27	Salchaket, Alaska, USA (RN76) . . . . .	124
3.3.28	Dar Es Salaam, Tanzania (RN64) . . . . .	127
3.3.29	Petropavlovsk, Russian Federation (RN60) . . . . .	130
3.3.30	Dubna, Russian Federation (RN61) . . . . .	133
<b>4</b>	<b>Results and applications</b>	<b>136</b>
4.1	Comparison of <sup>7</sup> Be stations . . . . .	136
	<b>Conclusions</b>	<b>144</b>

A ${}^7\text{Be} - {}^{22}\text{Na}$	145
B ${}^7\text{Be} - {}^{133}\text{Xe}$	147
C $\text{CO}_2$	150
D Uranium	155
Bibliography	159

---

## List of Figures

---

1.1	Worldwide nuclear testing (1945 - 2016) . . . . .	4
1.2	International monitoring system . . . . .	6
1.3	P waves for an earthquake and an explosion . . . . .	7
1.4	Scheme for the hydroacoustic monitoring at IMS stations . . . . .	8
1.5	Natural and man-made sources of infrasound waves . . . . .	9
2.1	Flow chart for the method . . . . .	19
2.2	Detrending for synthetic time series . . . . .	21
2.3	Example of the sifting procedure . . . . .	22
2.4	Generalised Lomb-Scargle spectrum for a synthetic time series . . . . .	27
2.5	Residuals for the synthetic time series . . . . .	29
2.6	Histogram of residuals for the synthetic time series . . . . .	32
2.7	Normalised residuals for the synthetic time series . . . . .	33
2.8	Example of DFA procedure . . . . .	34
2.9	Detrended Fluctuations Analysis (DFA) for the residuals of three synthetic time series . . . . .	36
2.10	Local Hurst exponent $H_t$ derivation . . . . .	38
2.11	Local Hurst exponent $H_t$ for the residuals of three synthetic time series . . . . .	39
3.1	Total percentage of $^7\text{Be}$ missing data in every station . . . . .	42
3.2	Total percentage of meteorological parameters' missing data in every station . . . . .	44
3.3	Examples of poor quality time series of meteorological parameters . . . . .	45
3.4	RN46: Time series with trend . . . . .	46
3.5	RN46: Normalised residuals . . . . .	46
3.6	RN46: GLS spectrum . . . . .	46
3.7	RN46: Histogram of residuals . . . . .	46
3.8	RN46: DFA . . . . .	46

3.9	RN46: $H_t$ (time window of two weeks)	46
3.10	RN46: Dynamic analysis	47
3.11	RN46: DCCA coefficient	48
3.12	RN47: Time series with trend	49
3.13	RN47: Normalised residuals	49
3.14	RN47: GLS spectrum	49
3.15	RN47: Histogram of residuals	49
3.16	RN47: DFA	49
3.17	RN47: $H_t$ (time window of two weeks)	49
3.18	RN47: Dynamic analysis	50
3.19	RN47: DCCA coefficient	51
3.20	RN23: Time series with trend	52
3.21	RN23: Normalised residuals	52
3.22	RN23: GLS spectrum	52
3.23	RN23: Histogram of residuals	52
3.24	RN23: DFA	52
3.25	RN23: $H_t$ (time window of two weeks)	52
3.26	RN23: Dynamic analysis	53
3.27	RN23: DCCA coefficient	54
3.28	RN04: Time series with trend	55
3.29	RN04: Normalised residuals	55
3.30	RN04: GLS spectrum	55
3.31	RN04: Histogram of residuals	55
3.32	RN04: DFA	55
3.33	RN04: $H_t$ (time window of two weeks)	55
3.34	RN04: Dynamic analysis	56
3.35	RN04: DCCA coefficient	57
3.36	RN10: Time series with trend	58
3.37	RN10: Normalised residuals	58
3.38	RN10: GLS spectrum	58
3.39	RN10: Histogram of residuals	58
3.40	RN10: DFA	58
3.41	RN10: $H_t$ (time window of two weeks)	58
3.42	RN10: Dynamic analysis	59
3.43	RN10: DCCA coefficient	60
3.44	RN01: Time series with trend	61
3.45	RN01: Normalised residuals	61
3.46	RN01: GLS spectrum	61
3.47	RN01: Histogram of residuals	61
3.48	RN01: DFA	61
3.49	RN01: $H_t$ (time window of two weeks)	61
3.50	RN01: Dynamic analysis	62

3.51	RN01: DCCA coefficient . . . . .	63
3.52	RN06: Time series with trend . . . . .	64
3.53	RN06: Normalised residuals . . . . .	64
3.54	RN06: GLS spectrum . . . . .	64
3.55	RN06: Histogram of residuals . . . . .	64
3.56	RN06: DFA . . . . .	64
3.57	RN06: $H_t$ (time window of two weeks) . . . . .	64
3.58	RN06: Dynamic analysis . . . . .	65
3.59	RN06: DCCA coefficient . . . . .	66
3.60	RN63: Time series with trend . . . . .	67
3.61	RN63: Normalised residuals . . . . .	67
3.62	RN63: GLS spectrum . . . . .	67
3.63	RN63: Histogram of residuals . . . . .	67
3.64	RN63: DFA . . . . .	67
3.65	RN63: $H_t$ (time window of two weeks) . . . . .	67
3.66	RN63: Dynamic analysis . . . . .	68
3.67	RN63: DCCA coefficient . . . . .	69
3.68	RN09: Time series with trend . . . . .	70
3.69	RN09: Normalised residuals . . . . .	70
3.70	RN09: GLS spectrum . . . . .	70
3.71	RN09: Histogram of residuals . . . . .	70
3.72	RN09: DFA . . . . .	70
3.73	RN09: $H_t$ (time window of two weeks) . . . . .	70
3.74	RN09: Dynamic analysis . . . . .	71
3.75	RN09: DCCA coefficient . . . . .	72
3.76	RN75: Time series with trend . . . . .	73
3.77	RN75: Normalised residuals . . . . .	73
3.78	RN75: GLS spectrum . . . . .	73
3.79	RN75: Histogram of residuals . . . . .	73
3.80	RN75: DFA . . . . .	73
3.81	RN75: $H_t$ (time window of two weeks) . . . . .	73
3.82	RN75: Dynamic analysis . . . . .	74
3.83	RN45: Time series with trend . . . . .	76
3.84	RN45: Normalised residuals . . . . .	76
3.85	RN45: GLS spectrum . . . . .	76
3.86	RN45: Histogram of residuals . . . . .	76
3.87	RN45: DFA . . . . .	76
3.88	RN45: $H_t$ (time window of two weeks) . . . . .	76
3.89	RN45: Dynamic analysis . . . . .	77
3.90	RN45: DCCA coefficient . . . . .	78
3.91	RN16: Time series with trend . . . . .	79
3.92	RN16: Normalised residuals . . . . .	79

3.93	RN16: GLS spectrum . . . . .	79
3.94	RN16: Histogram of residuals . . . . .	79
3.95	RN16: DFA . . . . .	79
3.96	RN16: $H_t$ (time window of two weeks) . . . . .	79
3.97	RN16: Dynamic analysis . . . . .	80
3.98	RN16: DCCA coefficient . . . . .	81
3.99	RN11: Time series with trend . . . . .	82
3.100	RN11: Normalised residuals . . . . .	82
3.101	RN11: GLS spectrum . . . . .	82
3.102	RN11: Histogram of residuals . . . . .	82
3.103	RN11: DFA . . . . .	82
3.104	RN11: $H_t$ (time window of two weeks) . . . . .	82
3.105	RN11: Dynamic analysis . . . . .	83
3.106	RN11: DCCA coefficient . . . . .	84
3.107	RN08: Time series with trend . . . . .	85
3.108	RN08: Normalised residuals . . . . .	85
3.109	RN08: GLS spectrum . . . . .	85
3.110	RN08: Histogram of residuals . . . . .	85
3.111	RN08: DFA . . . . .	85
3.112	RN08: $H_t$ (time window of two weeks) . . . . .	85
3.113	RN08: Dynamic analysis . . . . .	86
3.114	RN08: DCCA coefficient . . . . .	87
3.115	RN74: Time series with trend . . . . .	88
3.116	RN74: Normalised residuals . . . . .	88
3.117	RN74: GLS spectrum . . . . .	88
3.118	RN74: Histogram of residuals . . . . .	88
3.119	RN74: DFA . . . . .	88
3.120	RN74: $H_t$ (time window of two weeks) . . . . .	88
3.121	RN74: Dynamic analysis . . . . .	89
3.122	RN74: DCCA coefficient . . . . .	90
3.123	RN33: Time series with trend . . . . .	91
3.124	RN33: Normalised residuals . . . . .	91
3.125	RN33: GLS spectrum . . . . .	91
3.126	RN33: Histogram of residuals . . . . .	91
3.127	RN33: DFA . . . . .	91
3.128	RN33: $H_t$ (time window of two weeks) . . . . .	91
3.129	RN33: Dynamic analysis . . . . .	92
3.130	RN33: DCCA coefficient . . . . .	93
3.131	RN68: Time series with trend . . . . .	94
3.132	RN68: Normalised residuals . . . . .	94
3.133	RN68: GLS spectrum . . . . .	94
3.134	RN68: Histogram of residuals . . . . .	94

3.135 RN68: DFA . . . . .	94
3.136 RN68: $H_t$ (time window of two weeks) . . . . .	94
3.137 RN68: Dynamic analysis . . . . .	95
3.138 RN68: DCCA coefficient . . . . .	96
3.139 RN72: Time series with trend . . . . .	97
3.140 RN72: Normalised residuals . . . . .	97
3.141 RN72: GLS spectrum . . . . .	97
3.142 RN72: Histogram of residuals . . . . .	97
3.143 RN72: DFA . . . . .	97
3.144 RN72: $H_t$ (time window of two weeks) . . . . .	97
3.145 RN72: Dynamic analysis . . . . .	98
3.146 RN72: DCCA coefficient . . . . .	99
3.147 RN26: Time series with trend . . . . .	100
3.148 RN26: Normalised residuals . . . . .	100
3.149 RN26: GLS spectrum . . . . .	100
3.150 RN26: Histogram of residuals . . . . .	100
3.151 RN26: DFA . . . . .	100
3.152 RN26: $H_t$ (time window of two weeks) . . . . .	100
3.153 RN26: Dynamic analysis . . . . .	101
3.154 RN26: DCCA coefficient . . . . .	102
3.155 RN79: Time series with trend . . . . .	103
3.156 RN79: Normalised residuals . . . . .	103
3.157 RN79: GLS spectrum . . . . .	103
3.158 RN79: Histogram of residuals . . . . .	103
3.159 RN79: DFA . . . . .	103
3.160 RN79: $H_t$ (time window of two weeks) . . . . .	103
3.161 RN79: Dynamic analysis . . . . .	104
3.162 RN79: DCCA coefficient . . . . .	105
3.163 RN50: Time series with trend . . . . .	106
3.164 RN50: Normalised residuals . . . . .	106
3.165 RN50: GLS spectrum . . . . .	106
3.166 RN50: Histogram of residuals . . . . .	106
3.167 RN50: DFA . . . . .	106
3.168 RN50: $H_t$ (time window of two weeks) . . . . .	106
3.169 RN50: Dynamic analysis . . . . .	107
3.170 RN50: DCCA coefficient . . . . .	108
3.171 RN52: Time series with trend . . . . .	109
3.172 RN52: Normalised residuals . . . . .	109
3.173 RN52: GLS spectrum . . . . .	109
3.174 RN52: Histogram of residuals . . . . .	109
3.175 RN52: DFA . . . . .	109
3.176 RN52: $H_t$ (time window of two weeks) . . . . .	109

3.177 RN52: Dynamic analysis . . . . .	110
3.178 RN17: Time series with trend . . . . .	112
3.179 RN17: Normalised residuals . . . . .	112
3.180 RN17: GLS spectrum . . . . .	112
3.181 RN17: Histogram of residuals . . . . .	112
3.182 RN17: DFA . . . . .	112
3.183 RN17: $H_t$ (time window of two weeks) . . . . .	112
3.184 RN17: Dynamic analysis . . . . .	113
3.185 RN17: DCCA coefficient . . . . .	114
3.186 RN43: Time series with trend . . . . .	115
3.187 RN43: Normalised residuals . . . . .	115
3.188 RN43: GLS spectrum . . . . .	115
3.189 RN43: Histogram of residuals . . . . .	115
3.190 RN43: DFA . . . . .	115
3.191 RN43: $H_t$ (time window of two weeks) . . . . .	115
3.192 RN43: Dynamic analysis . . . . .	116
3.193 RN43: DCCA coefficient . . . . .	117
3.194 RN37: Time series with trend . . . . .	118
3.195 RN37: Normalised residuals . . . . .	118
3.196 RN37: GLS spectrum . . . . .	118
3.197 RN37: Histogram of residuals . . . . .	118
3.198 RN37: DFA . . . . .	118
3.199 RN37: $H_t$ (time window of two weeks) . . . . .	118
3.200 RN37: Dynamic analysis . . . . .	119
3.201 RN37: DCCA coefficient . . . . .	120
3.202 RN71: Time series with trend . . . . .	121
3.203 RN71: Normalised residuals . . . . .	121
3.204 RN71: GLS spectrum . . . . .	121
3.205 RN71: Histogram of residuals . . . . .	121
3.206 RN71: DFA . . . . .	121
3.207 RN71: $H_t$ (time window of two weeks) . . . . .	121
3.208 RN71: Dynamic analysis . . . . .	122
3.209 RN71: DCCA coefficient . . . . .	123
3.210 RN76: Time series with trend . . . . .	124
3.211 RN76: Normalised residuals . . . . .	124
3.212 RN76: GLS spectrum . . . . .	124
3.213 RN76: Histogram of residuals . . . . .	124
3.214 RN76: DFA . . . . .	124
3.215 RN76: $H_t$ (time window of two weeks) . . . . .	124
3.216 RN76: Dynamic analysis . . . . .	125
3.217 RN76: DCCA coefficient . . . . .	126
3.218 RN64: Time series with trend . . . . .	127

3.219 RN64: Normalised residuals . . . . .	127
3.220 RN64: GLS spectrum . . . . .	127
3.221 RN64: Histogram of residuals . . . . .	127
3.222 RN64: DFA . . . . .	127
3.223 RN64: $H_t$ (time window of two weeks) . . . . .	127
3.224 RN64: Dynamic analysis . . . . .	128
3.225 RN64: DCCA coefficient . . . . .	129
3.226 RN60: Time series with trend . . . . .	130
3.227 RN60: Normalised residuals . . . . .	130
3.228 RN60: GLS spectrum . . . . .	130
3.229 RN60: Histogram of residuals . . . . .	130
3.230 RN60: DFA . . . . .	130
3.231 RN60: $H_t$ (time window of two weeks) . . . . .	130
3.232 RN60: Dynamic analysis . . . . .	131
3.233 RN60: DCCA coefficient . . . . .	132
3.234 RN61: Time series with trend . . . . .	133
3.235 RN61: Normalised residuals . . . . .	133
3.236 RN61: GLS spectrum . . . . .	133
3.237 RN61: Histogram of residuals . . . . .	133
3.238 RN61: DFA . . . . .	133
3.239 RN61: $H_t$ (time window of two weeks) . . . . .	133
3.240 RN61: Dynamic analysis . . . . .	134
3.241 RN61: DCCA coefficient . . . . .	135
4.1 Sunspot number from 1985 to 2020 . . . . .	137
4.2 Map of percentages for $^7\text{Be}$ stations . . . . .	138
4.3 Variability of the one-year harmonic for the $^7\text{Be}$ stations . . . . .	139
4.4 Values of the Hurst exponent for the first two regimes of DFA . . . . .	140
4.5 Values of the local Hurst exponent for the four stations chosen for a detailed comparison . . . . .	141
4.6 Normalised residuals for the four stations chosen for a detailed com- parison . . . . .	142
4.7 DCCA for the four stations chosen for a detailed comparison . . . . .	143
A.1 Local Hurst exponent $H_t$ for $^7\text{Be}$ and $^{22}\text{Na}$ comparison . . . . .	145
A.2 Normalised residuals for $^7\text{Be}$ and $^{22}\text{Na}$ comparison . . . . .	146
A.3 DCCA for $^7\text{Be}$ and $^{22}\text{Na}$ comparison . . . . .	146
B.1 Local Hurst exponent $H_t$ for $^7\text{Be}$ and $^{133}\text{Xe}$ comparison . . . . .	148
B.2 Normalised residuals for $^7\text{Be}$ and $^{133}\text{Xe}$ comparison . . . . .	149
B.3 DCCA for $^7\text{Be}$ and $^{133}\text{Xe}$ comparison . . . . .	149
C.1 Time series with trend for Lampedusa and Mauna Loa . . . . .	151
C.2 GLS periodogram for Lampedusa and Mauna Loa time series . . . . .	151

C.3	Normalised residual for Lampedusa and Mauna Loa time series . . .	152
C.4	DFA for Lampedusa and Mauna Loa time series . . . . .	153
C.5	Local Hurst exponent $H_t$ for Lampedusa and Mauna Loa time series	154
D.1	Uranium time series . . . . .	156
D.2	Uranium residuals . . . . .	157
D.3	Local Hurst exponent $H_t$ for uranium residuals . . . . .	158
D.4	DCCA for uranium residuals . . . . .	158

---

## List of Tables

---

1.1	IMS technical specifications for particulate monitoring . . . . .	11
1.2	Calculation of the minimum detectable concentration (MDC) . . . . .	12
2.1	Results for frequencies found in the synthetic time series . . . . .	28
3.1	Stations' ID and their exact location . . . . .	43
3.2	RN46: Periodicities . . . . .	47
3.3	RN46: Outliers . . . . .	47
3.4	RN47: Periodicities . . . . .	50
3.5	RN47: Outliers . . . . .	50
3.6	RN23: Periodicities . . . . .	53
3.7	RN23: Outliers . . . . .	53
3.8	RN04: Periodicities . . . . .	56
3.9	RN04: Outliers . . . . .	56
3.10	RN10: Periodicities . . . . .	59
3.11	RN10: Outliers . . . . .	59
3.12	RN01: Periodicities . . . . .	62
3.13	RN01: Outliers . . . . .	62
3.14	RN06: Periodicities . . . . .	65
3.15	RN06: Outliers . . . . .	65
3.16	RN63: Periodicities . . . . .	68
3.17	RN63: Outliers . . . . .	68
3.18	RN09: Periodicities . . . . .	71
3.19	RN09: Outliers . . . . .	71
3.20	RN75: Periodicities . . . . .	74
3.21	RN75: Outliers . . . . .	74
3.22	RN45: Periodicities . . . . .	77
3.23	RN45: Outliers . . . . .	77
3.24	RN16: Periodicities . . . . .	80

3.25	RN16: Outliers . . . . .	80
3.26	RN11: Periodicities . . . . .	83
3.27	RN11: Outliers . . . . .	83
3.28	RN08: Periodicities . . . . .	86
3.29	RN08: Outliers . . . . .	86
3.30	RN74: Periodicities . . . . .	89
3.31	RN74: Outliers . . . . .	89
3.32	RN33: Periodicities . . . . .	92
3.33	RN33: Outliers . . . . .	92
3.34	RN68: Periodicities . . . . .	95
3.35	RN68: Outliers . . . . .	95
3.36	RN72: Periodicities . . . . .	98
3.37	RN72: Outliers . . . . .	98
3.38	RN26: Periodicities . . . . .	101
3.39	RN26: Outliers . . . . .	101
3.40	RN79: Periodicities . . . . .	104
3.41	RN79: Outliers . . . . .	104
3.42	RN50: Periodicities . . . . .	107
3.43	RN50: Outliers . . . . .	107
3.44	RN52: Periodicities . . . . .	110
3.45	RN52: Outliers . . . . .	110
3.46	RN17: Periodicities . . . . .	113
3.47	RN17: Outliers . . . . .	113
3.48	RN43: Periodicities . . . . .	116
3.49	RN43: Outliers . . . . .	116
3.50	RN37: Periodicities . . . . .	119
3.51	RN37: Outliers . . . . .	119
3.52	RN71: Periodicities . . . . .	122
3.53	RN71: Outliers . . . . .	122
3.54	RN76: Periodicities . . . . .	125
3.55	RN76: Outliers . . . . .	125
3.56	RN64: Periodicities . . . . .	128
3.57	RN64: Outliers . . . . .	128
3.58	RN60: Periodicities . . . . .	131
3.59	RN60: Outliers . . . . .	131
3.60	RN61: Periodicities . . . . .	134
3.61	RN61: Outliers . . . . .	134

---

## List of Acronyms

---

AD	- Anderson-Darling
ATM	- Atmospheric Transport Models
CTBT	- Comprehensive Nuclear-Test-Ban Treaty
CTBTO	- Comprehensive Nuclear-Test-Ban Treaty Organization
DCCA	- Detrended Cross-Correlation Analysis
DFA	- Detrended Fluctuation Analysis
EMD	- Empirical Mode Decomposition
FFT	- Fast Fourier Transform
FWHM	- Full Width at Half Maximum
GLS	- Generalised Lomb-Scargle
GOF	- Goodness of Fit
HPGe	- High Purity Germanium
IDC	- International Data Centre
IMF	- Intrinsic Mode Function
IMS	- International Monitoring System
KS	- Kolmogorov-Smirnov
LS	- Lomb-Scargle
MDC	- Minimum Detectable Concentration
MF DFA	- Multifractal Detrended Fluctuation Analysis
PDF	- Probability Density Function
REB	- Reviewed Event Bulletin
RN	- Radionuclide
SOFAR	- Sound Frequency and Ranging
STP	- Standard Temperature and Pressure

---

## Introduction

---

Beryllium 7 is a cosmogenic radionuclide produced by spallation reactions of cosmic rays formed primarily in the stratosphere (the atmospheric layer between about 15 km and 60 km) from cosmic-ray spallation of oxygen and nitrogen, but some is also produced in the troposphere (first layer of atmosphere, between the ground and 10-15 km).  ${}^7\text{Be}$  has a relatively short half-life ( $T_{1/2} = 53.12 \pm 0.07$  days) and is useful for tracing and quantifying environmental processes on small time scales, with direct applications in geophysics. Beryllium 7 is measured in a great variety of locations on Earth. Specifically, the data used for the analysis of  ${}^7\text{Be}$  and meteorological parameters have been provided by the International Monitoring System (IMS). The IMS is a network of stations for seismic, hydroacoustic, infrasound and radionuclide signals monitoring, established in order to verify the Comprehensive Nuclear-Test-Ban Treaty (CTBT), a treaty whose aim is the total ban of every kind of nuclear test. IMS network covers the whole globe with 66 certified stations, providing time series coming from stations that are in really distant and different places. These data are often used for atmospheric transport models and interpolated between the various stations to give information on the radionuclide's activity in every part of the world. In doing so, local properties of Beryllium 7 are lost, along with a possible comparison among the stations. The aim of this thesis is to define a procedure for time series analysis in order to characterise the local properties of the measurement sites, and hence to highlight differences and similarities among the stations. The procedure is based on time series analysis and uses different well-established methods, organised in such a way to best describe the properties of the time series. Moreover, a common problem in geophysical time series is the presence of missing data, mainly due to instrument failures or adverse meteorological conditions. Thus, some of the methods need to be modified in order to take into account the possible presence of missing data. The analysis is principally focused on the characterisation of three terms that compose the time series: The trend, i.e. a monotonic function that describes the overall growth of

the data; the periodic term, from which the frequencies associated with the characteristic periodicities of the time series can be obtained; the residuals, i.e. the stochastic process underlying the trend and periodicities. Results are expected to show differences among the stations, especially for what concerns the residuals, that should depend mostly on the local properties of the site. Similarities are instead expected for the periodic term since periodicities should depend on global processes like the Earth's rotation, or on external processes like the activity of the sun and consequently the cosmic rays. Furthermore, the procedure has been applied to other time series in order to show the validity of the method. Specifically, it has been applied to another cosmogenic radionuclide ( $^{22}\text{Na}$ ), a radionuclide of anthropogenic origin ( $^{133}\text{Xe}$ ),  $\text{CO}_2$  records, and uranium groundwater time series. This thesis is organised into four chapters:

- in Chapter 1, a historical overview of the Comprehensive Nuclear-Test-Ban Treaty's stipulation is first presented. Then, the four monitoring systems of the International Monitoring System are described, with particular attention to radionuclide signals monitoring, and especially particulate monitoring. Finally, properties of Beryllium 7 are presented, along with some applications of the cosmogenic radionuclide in atmospheric physics;
- Chapter 2 describes in details the procedure of analysis. It is also tested on synthetic time series in order to verify its reliability;
- Chapter 3 initially presents how some of the methods in the procedure have been modified in the presence of missing data. Then, results of the analysis are presented individually for each of the available IMS stations;
- in Chapter 4, results of Chapter 3 are summarised in order to highlight similarities and differences among the stations. Some applications of the methodological approach described in Chapter 2 to other time series are presented in the appendices.

---

## CTBT and International Monitoring System

---

### 1.1 Comprehensive Nuclear-Test-Ban Treaty

Between 1945 and 1996, over two thousand nuclear tests have been carried out by different countries (Figure 1.1). Nuclear explosions happened in different environments: on the ground, underground (almost until 2400 *m*), on the sea surface, and under the sea, reaching a maximum depth of 600 *m*. Moreover, bombs detonated also in the atmosphere at heights of over 500 *km*. Due to the international concern about radioactive fallout, nuclear tests started to be banned, and in 1996 the Comprehensive Nuclear-Test-Ban Treaty (CTBT) was stipulated, which banned every kind of nuclear test. To verify the treaty, the international community developed the International Monitoring System (IMS), a network of stations for seismic, hydroacoustic, infrasound and radionuclide signals monitoring. Measures of radionuclides' atmospheric concentrations, radioxenon in particular, are of fundamental importance in order to monitor a possible secret test and are interpreted by means of Atmospheric Transport Models (ATM) simulations. In this Chapter, the four measuring methods constituting the IMS will be described, after a short historical overview on nuclear tests.

#### 1.1.1 Atmospheric tests

Out of the over two thousand tests performed on Earth between 1945 and 1996, about five hundred were atmospheric tests. The international concern about radioactive fallout coming from atmospheric tests grew rapidly in the 1950s when, on March 1954, the United States tested a hydrogen bomb (named Castle Bravo) at Marshall Islands in the Pacific Ocean. Even if by mistake, civilians and US soldiers were contaminated by the radioactive fallout. To mitigate the growing worries

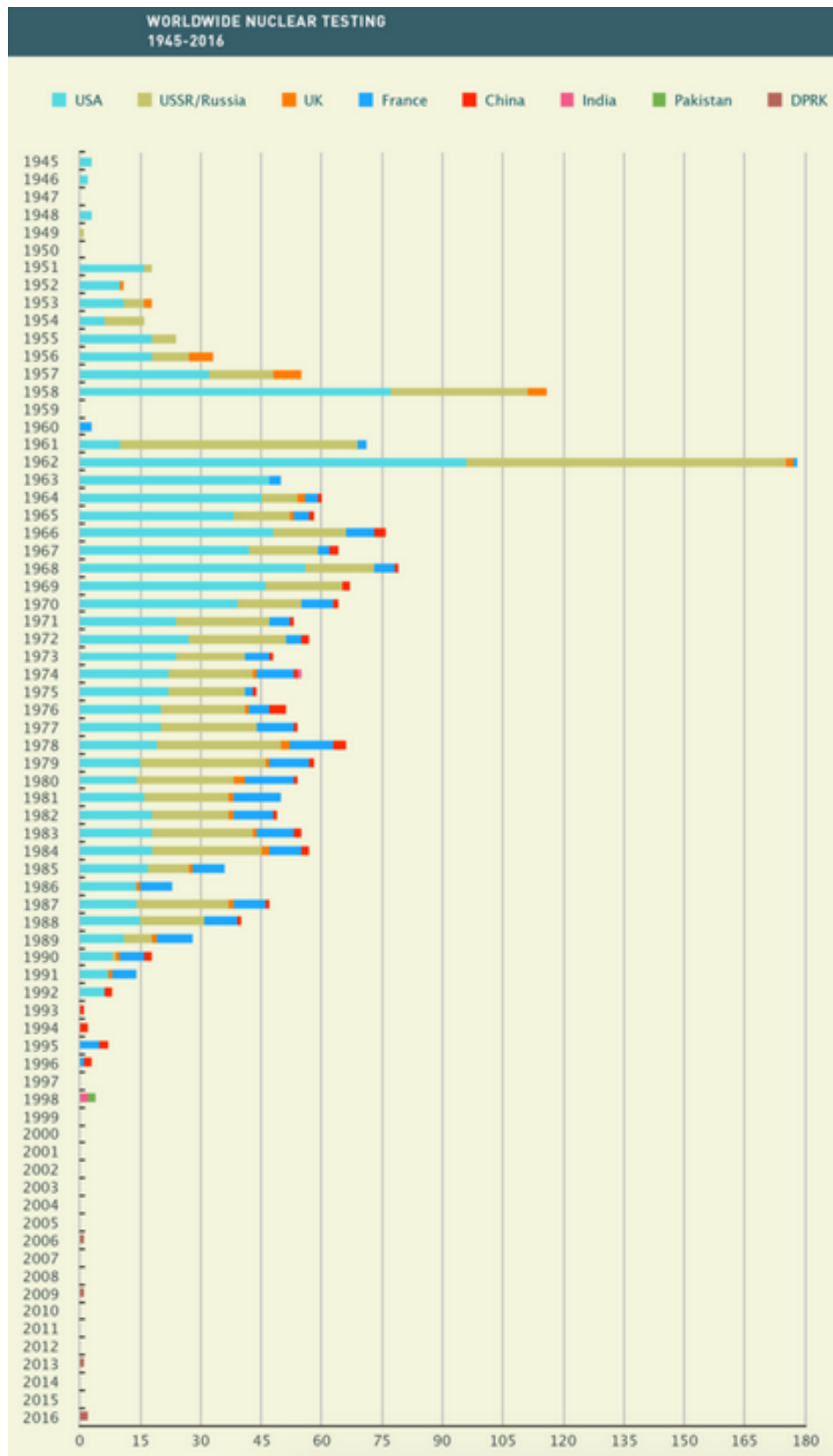


Figure 1.1: Nuclear tests performed between 1945 and 2016, different colours for different countries. Figure can be found in [1].

spread around the world, atmospheric tests were banned in 1963 by the Partial Test Ban Treaty. The IMS's infrasound stations monitor the atmosphere, searching for low-frequency sound waves, which are distinctive of a nuclear explosion.

### 1.1.2 High atmosphere tests

From 1958 to 1962, about 20 nuclear tests were carried out by the United States and the Soviet Union at heights ranging from 40 *km* to 540 *km*. Their principal aim was to test a possible use of nuclear weapons like a protection against ballistic missiles, or like a weapon against satellites. The most powerful of these tests (Starfish Prime Test, 1.4 megatons) was carried out by the United States on July 9th, 1962, when tensions due to Cold War were high. A few months earlier, in October 1961, the Soviet Union detonated the Tsar bomb, which with its 50 megatons was the most powerful nuclear device ever exploded. 1962 also was a particular year, with 178 nuclear devices detonated.

### 1.1.3 Underwater tests

The aim of these tests was to verify their effects on military ships. Underwater nuclear explosions can release a great amount of water and radioactive vapour, hence contaminate what is in the proximity of the explosion site. Underwater tests were also banned by the Partial Test Ban Treaty in 1963. The IMS is equipped with a network of hydroacoustic stations, in order to detect signals that propagate in the ocean after an underwater detonation.

### 1.1.4 Underground tests

Underground tests compose the 75% of the totality of the nuclear experiments. Bombs are detonated at different depths, and the radioactive fallout in the atmosphere depends on the level of containment of site where the test is carried out. Underground explosions can be detected through seismic activity, which allows finding the power of the nuclear device. Hence, IMS stations are equipped with a seismometer, in order to monitor Earth searching for signals assimilable to nuclear explosions. Underground tests were definitely banned by the CTBT in 1996, along with every other kind of nuclear test.

## 1.2 International Monitoring System

The data used for the analysis of  $^7\text{Be}$  and meteorological parameters (Chapters 3 and 4) have been provided by the IMS. The whole network is presented in Figure 1.2. When completed, the IMS will be composed of over three hundred stations: Seismic stations (170), hydroacoustic stations (11), infrasound stations

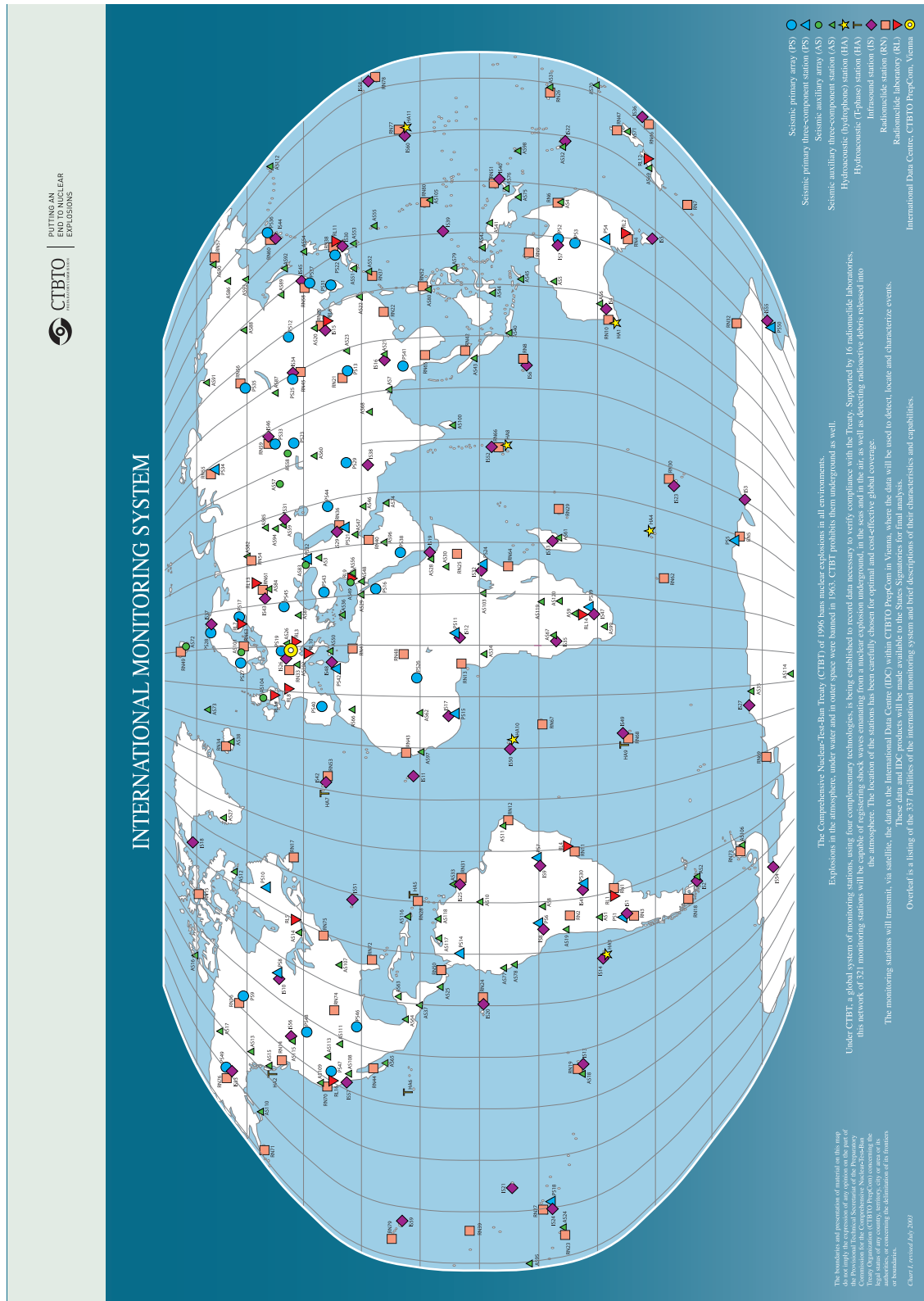


Figure 1.2: International monitoring system (IMS), different symbols for different kind of stations. Figure can be found in [1].

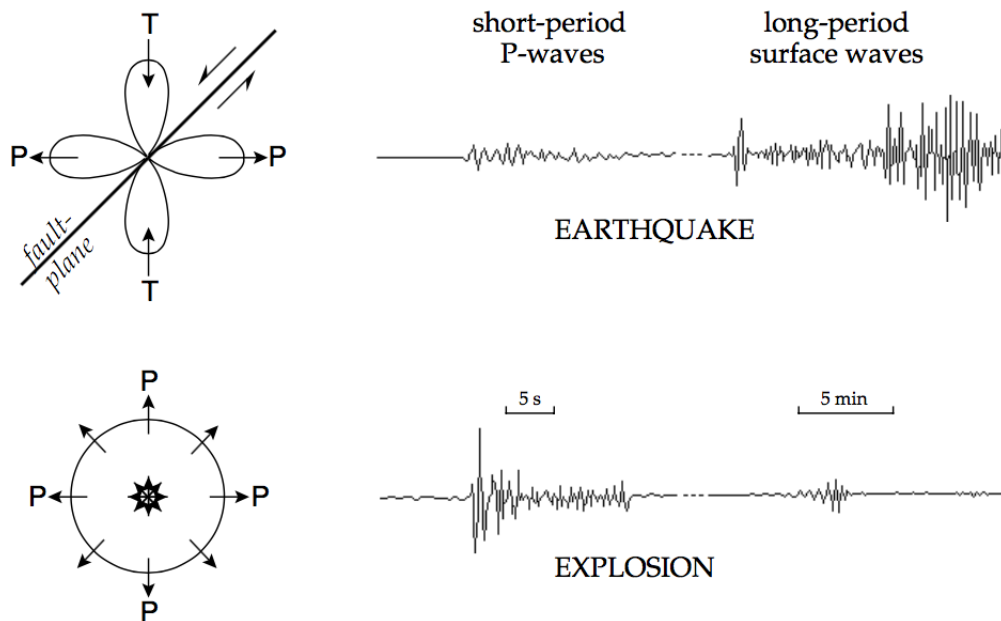


Figure 1.3: Difference between P waves of an earthquake and an explosion. Figure can be found in [2].

(60), and radionuclide monitoring stations (80). Data originating from the network are sent to the International Data Centre (IDC), Vienna, where they are processed, analysed and inserted in the Reviewed Event Bulletin (REB).

The eighty radionuclide stations (RN) are equipped with atmospheric aerosol samplers and high resolution germanium detectors, in order to detect radionuclides concentrations released during the explosion of a nuclear device. However, the signal detected strongly depends on the atmospheric dynamics, making the precise localisation of the source impossible. RN signals are then interpreted by means of atmospheric modelling software, FLEXPART in particular.

IMS stations employ three methods of measure, based on the analysis of seismic, hydroacoustic, and infrasound waves. Moreover, air samples are analysed to establish the presence of the isotopes. IMS data can be used to give real-time information about the occurrence of natural phenomena or to study scientific problems, such as oceans, climate change, and atmospheric dynamics.

### 1.2.1 Seismic monitoring

Seismology is the study of seismic waves, their propagation through the Earth, their sources and their effects. Seismic waves result not only from earthquakes but also from other natural and man-made events. IMS's seismic stations are 170, 50 primary and 120 auxiliary, and monitor seismic waves that propagate inside the Earth or on its surface. The majority of these waves is caused by earthquakes, that differentiate from explosions by energy release. An earthquake is indeed the result

of a sudden displacement of blocks of terrestrial crust. The amplitude of P waves (compressional waves that alternately compress and expand the ground in the direction of the wave's propagation), measured by seismometers, has a characteristic configuration named radiation pattern. It has four alternated lobes, corresponding to compression and expansion zones. An underground explosion instead increases the pressure outwards, all around the source. The P waves generated by an explosion are thus different, as depicted in Figure 1.3, allowing to distinguish between a nuclear explosion and an earthquake. Then, seismic data provide information on the location of a suspected underground nuclear explosion and help to identify the area for an on-site inspection. Seismic monitoring also allows reconstructing the intensity of the explosion. This is fundamental in order to distinguish between a nuclear explosion and a chemical one, that hardly can exceed one kiloton of released power [3].

### 1.2.2 Hydroacoustic monitoring

Hydroacoustics refers to the study of the propagation of sound waves in the water. Hydroacoustic monitoring involves recording signals that show pressure changes

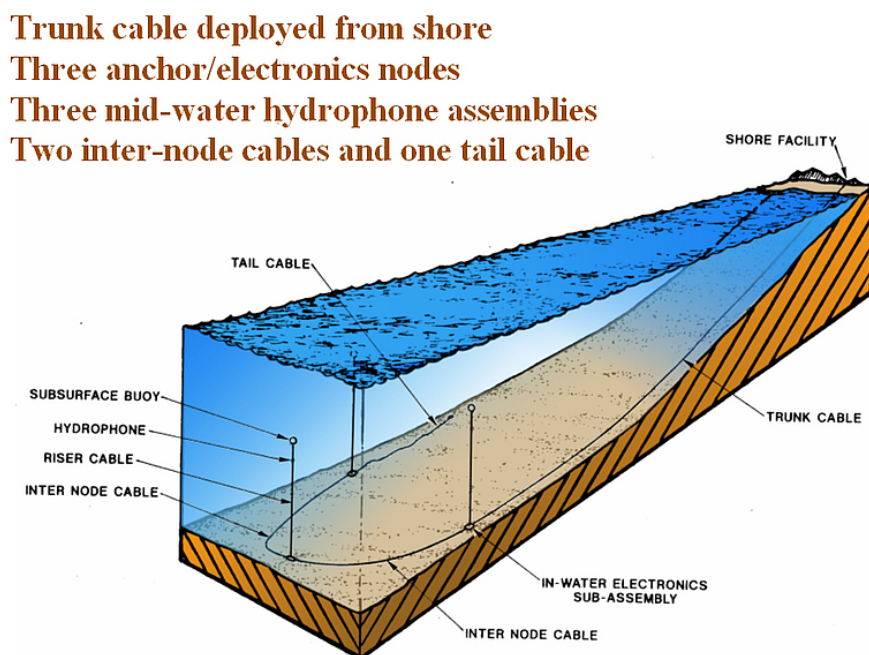


Figure 1.4: Scheme for the hydroacoustic monitoring at IMS stations. Figure can be found in [1].

in water, due to sound waves. Sound waves propagate very efficiently in water and can travel great distances, taking advantage of the so-called SOFAR channel (Sound Frequency and Ranging channel). In the SOFAR channel sound travels slower but more efficiently. The scheme for the hydroacoustic monitoring at IMS stations is shown in Figure 1.4. Hydroacoustic measures developed in the early

twentieth century with the aim of increasing safety of sea travel. The sonar (sound navigation and ranging) was introduced, especially in submarine navigation and detection. Only eleven stations are present in the whole network and aim at detecting sound waves produced by possible underwater explosions. Due to the efficient transmission of sound through water, even comparatively small signals are readily detectable at very long distances. Thus, eleven stations are sufficient to monitor the Earth's big oceans, with emphasis on the Southern Hemisphere which is largely dominated by water.

### 1.2.3 Infrasound monitoring

Acoustic waves with very low frequencies are called infrasound. In fact, these waves are below the frequency band audible to the human ear, which typically ranges from 20  $Hz$  to 20.000  $Hz$ . Infrasound is produced by a variety of natural and man-made sources (Figure 1.5): Exploding volcanoes, earthquakes, meteors, storms, and auroras; nuclear, mining and large chemical explosions, as well as aircraft and rocket launches. IMS consists of a total of sixty infrasound stations. Infrasound monitoring allows to distinguish, for instance, between a nuclear and a volcanic explosion, but not between a nuclear and a chemical explosion.

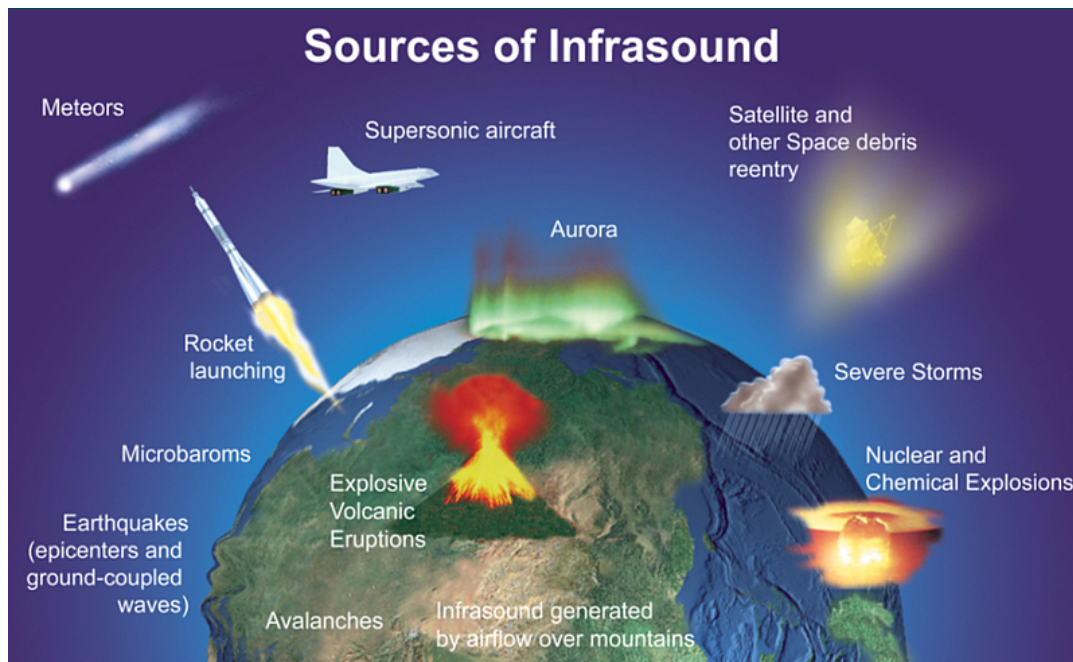


Figure 1.5: Natural and man-made sources of infrasound waves. Figure can be found in [1].

## 1.2.4 Radionuclide monitoring

The radionuclide technology is complementary to the three waveform verification technologies - seismic, infrasound and hydroacoustic - employed by the CTBTO (Comprehensive Nuclear-Test-Ban Treaty Organization) verification regime. This technology is the only one that is able to confirm whether an explosion detected and located by the others is indicative of a nuclear test. The radionuclide monitoring technology measures the abundance of radioactive particles (particulate) and noble gases, i.e. radionuclides, in the air. A radionuclide is an isotope with an unstable nucleus that loses its excess energy by emitting radiation in the form of particles or electromagnetic waves. This process is called radioactive decay. Radionuclides may occur naturally, but they can also be artificially produced.

The eighty-stations radionuclide monitoring network enables a continuous world-wide observation of aerosol samples of radionuclides. A radionuclide particulate monitoring station contains an air sampler, detection equipment, computers and a communication set-up. At the air sampler, air is forced through a filter, which retains more than 85% of all particles that reach it. Filters are replaced daily. The used filter is first cooled for a period of 24 hours and then measured for another 24 hours in the detection device at the monitoring station. The result is a gamma ray spectrum that is sent to the International Data Centre for further analysis.

Data sent by the radionuclide stations to the IDC do not only include gamma radiation spectra, but also meteorological and state-of-health information. State-of-health data provide information on the station's operational status and the quality of the raw monitoring data it transmits. Support is provided by 16 radionuclide laboratories, which conduct sample analyses if and when necessary. The laboratories analyse samples suspected of containing radionuclide materials that may have been produced by a nuclear explosion. They also conduct routine analyses of regular samples to provide quality control of a station's air sample measurements.

The eighty radionuclide stations are divided into four regions - the Americas, Europe and Eurasia, Asia and Oceania, and the Mediterranean and Africa - with each region supported by four radionuclide laboratories. Since this thesis deals with the analysis of  $^7\text{Be}$  time series, particulate is of primary interest among all radionuclides.

## Particulate monitoring

Table 1.1 lists the IMS technical specifications for particulate monitoring. Every station is equipped with a filter and an air sampler. The flow rate of the air sampler should be at least  $500 \text{ m}^3\text{h}^{-1}$ , measured at standard temperature and pressure (STP) during the sampling periods. It follows that at least a total air volume of  $10800 \text{ m}^3$  ( $500 \text{ m}^3\text{h}^{-1} \times 24 \text{ h}$  (-10 %)) at STP will pass through each filter sample. The total air volume collected is then normalised to STP. The airflow rate of  $500 \text{ m}^3\text{h}^{-1}$  specified in Table 1.1 is not defined to any special condition. However, due

Characteristics	Minimum requirements
<i>System</i>	Manual or automated
<i>Airflow</i>	500 m <sup>3</sup> h <sup>-1</sup>
<i>Collection time</i> <sup>1</sup>	24 h
<i>Decay time</i> <sup>2</sup>	≤ 24 h
<i>Measurement time</i> <sup>3</sup>	≥ 20 h
<i>Time before reporting</i>	≤ 72 h
<i>Reporting frequency</i>	Daily
<i>Filter</i>	Adequate composition for compaction, dissolution and analysis
<i>Particulate collection efficiency</i>	For filter: ≥ 80% at $\varnothing = 0.2 \mu m$ Global <sup>4</sup> : ≥ 60% at $\varnothing = 10 \mu m$
<i>Measurement mode</i>	HPGe high resolution gamma spectrometry
<i>HPGe relative efficiency</i>	≥ 40%
<i>HPGe resolution</i>	< 2.5 keV at 1332 keV
<i>Base line sensitivity</i> <sup>5,6</sup>	10 to 30 $\mu Bqm^{-3}$ for <sup>140</sup> Ba
<i>Calibration range</i>	88 to 1836 keV
<i>Data format for gamma spectra and auxiliary data</i>	RMS (Radionuclide Monitoring System) format <sup>7</sup>
<i>State of health</i>	Status data transmitted to IDC
<i>Communication</i>	Two-way
<i>Auxiliary data</i>	Meteorological data Flow rate measurement every 10 minutes
<i>Data availability</i>	≥ 95%
<i>Down time</i> <sup>8</sup>	≤ 7 consecutive days ≤ 15 days annually

<sup>1</sup> Time specifications allow for an uncertainty of 10%, except for the reporting time parameter.

<sup>2</sup> This value can be reduced, down to a minimum of 6 hours, if a suspicious event is detected by other stations or techniques.

<sup>3</sup> This value allows for authentication measurements for manual systems.

<sup>4</sup> This global value includes the 80% filter efficiency and the collection efficiency of the incoming air circuitry. It was never specified but the IMS consider the particle dimensions given here as Equivalent Aerodynamic Diameter (EAD).

<sup>5</sup> The upper limit is intended for high background areas.

<sup>6</sup> Certification procedures to be defined for baseline sensitivities (a posteriori MDCs) as well as the efficiency. Sample preparation losses should not affect base line sensitivities.

<sup>7</sup> This format should make provision from auxiliary data, authentication data and state of health data.

<sup>8</sup> Provision should be made for spare parts in particular areas where periodicity of transportation facilities is more than seven days.

Table 1.1: IMS technical specifications for particulate monitoring [4].

$L_D$	Lower limit of detection at the 95% confidence level, $L_D = 2.71 + 4.65\sqrt{\mu_B}$
$\sqrt{\mu_B}$	Standard deviation of the background at the energy of interest $\sqrt{\mu_B} = \sum^{ROI} \text{counts}_i$ (ROI is defined as $\pm 1.25$ FWHM ( $\pm 3\sigma$ ) on either side of the hypothetical peak centroid)
$T$	Acquisition live time [s]
$\epsilon_E$	Attenuation corrected efficiency (counts per gamma) at the energy of interest
$\gamma_i$	Branching ratio of gamma energy (gamma per decay) of the isotope $i$
$V_0$	Sampled air volume [ $m^3$ ] at STP
$\xi_i$	Air sampling system global collection efficiency (%) for the isotope $i$ For certification set to 1
$K_S$	Decay correction during sampling time (constant concentrations) $K_S = \lambda_i t_S / [1 - \exp(-\lambda_i t_S)]$
$K_W$	Decay correction between end of sampling and acquisition start $K_W = \exp(\lambda_i t_W)$
$K_C$	Decay correction during acquisition time $K_C = \lambda_i t_C / [1 - \exp(-\lambda_i t_C)]$
$\lambda_i$	Decay constant for the isotope $i$ [ $s^{-1}$ ]
$t_C$	Clock real time between start and end of acquisition [s]
$t_W$	Clock real time between end of sampling and begin of spectral acquisition [s]
$t_S$	Clock real time between start and end of sampling [s]

Table 1.2: Calculation of the minimum detectable concentration (MDC) [4].

to differences in temperature and air pressure at stations with different climate and altitude, equal volumes of air do not necessarily correspond to an equal quantity of air. As the volume of collected air is inversely proportional to the minimum detectable concentration (MDC), defined by the following equation (with parameters' meaning listed in Table 1.2),

$$\text{MDC}(Bq m^{-3}) = \frac{L_D}{T \cdot V_0 \cdot \epsilon_E \cdot \gamma_i \cdot \xi_i} \cdot K_S \cdot K_W \cdot K_C \quad (1.1)$$

it is necessary to normalise the volume of air. The flow rate specification should be therefore referenced to a standard condition independent of these factors. For the IMS's purposes, STP (273.15 K and 101325 Pa) is used for all calculations.

The measurement system is based on high resolution gamma spectrometry using a high purity germanium detector (HPGe) with a minimum relative efficiency

of at least 40%, and a peak resolution better than 2.5 *keV* at full width at half maximum (FWHM) at the gamma ray energy of 1332 *keV* under operational conditions.

The local weather conditions can affect significantly the atmospheric concentrations of both naturally occurring and artificial radionuclides. Therefore, it is important that the information concerning the local meteorology would be provided from the station, in order to facilitate the interpretation of the radionuclide data provided to the IDC. The essential meteorological parameters for this purpose are temperature ( $^{\circ}\text{C}$ ), precipitation (*mm*), relative humidity (%), barometric pressure (*Pa*), wind speed ( $\text{ms}^{-1}$ ) and wind direction (degrees from the north,  $0^{\circ}$ - $360^{\circ}$ , clockwise).

### 1.3 Environmental chemistry of Beryllium 7

In this section, an overview of the characteristics of Beryllium 7 is presented, following Kaste et al. [5]. In addition to the stable isotope  $^9\text{Be}$ , Beryllium is also formed as two cosmogenic isotopes of interest to earth scientists. Cosmogenic Beryllium is formed primarily in the stratosphere (the atmospheric layer between about 15 *km* and 60 *km*) from cosmic-ray spallation of oxygen and nitrogen, but some is also produced in the troposphere (first layer of atmosphere, between the ground and 10-15 *km*). After its formation in the atmosphere, cosmogenic Beryllium adsorbs electrostatically to aerosols that may be washed out by precipitation and delivered to ecosystems. The amount of cosmogenic Beryllium that reaches the surface of the earth is a function of production rate (cosmic-ray intensity), stratosphere-troposphere mixing, circulation and advection within the troposphere, and efficiency of removal from the troposphere (wet and dry deposition) [6]. The focus of this section is the short-lived radionuclide  $^7\text{Be}$  ( $T_{1/2} = 53.12 \pm 0.07$  days [7]). Due to its short half-life, relative ease of measurement, and well-defined source term,  $^7\text{Be}$  serves as a useful tool for tracing and quantifying environmental processes on the  $< 1$  year timescale, and has applications in meteorology, soil science, sedimentology, geomorphology, hydrology, geochemistry, and nuclear physics.

$^7\text{Be}$  decays to stable  $^7\text{Li}$  by electron capture. 89.5% of the atoms decay directly to the ground state of  $^7\text{Li}$ , while 10.5% decay first to the excited state of  $^7\text{Li}$ , which decays to ground state  $^7\text{Li}$  via gamma-ray emission at 477.6 *keV*.  $^7\text{Be}$  activities are normally determined in environmental samples using gamma spectrometers that detect the 477.6 *keV* gamma, using high-purity germanium detectors with high resolution ( $< 2$  *keV*) and high counting efficiencies.

Production of  $^7\text{Be}$  depends on the cosmic-ray flux, which varies with latitude, altitude, and solar activity. Production rates are different between troposphere and stratosphere: Going from the equator to the poles, production increases by a factor of approximately one to three in the troposphere, and by a factor of four to five in the stratosphere. Cosmogenic Beryllium is known to vary with the 11-year

solar cycle, with a minimum of concentration corresponding to a maximum of the solar activity, and vice versa [8]. There is, therefore, an inverse relationship.

The residence time of  $^7\text{Be}$  is also different in the two lower layers of the atmosphere. As a matter of fact, aerosols stay approximately 14 months in the stratosphere, a time that exceeds the half-life of Beryllium 7. In the troposphere instead, the residence time of  $^7\text{Be}$  is much shorter, primarily due to wash-out. Thus, there is a high concentration gradient between stratosphere and troposphere. Moreover, the activity of  $^7\text{Be}$  in the stratosphere remains fairly constant, while concentrations in the troposphere exhibit seasonal fluctuations. Stratosphere-troposphere exchange [9] can increase the concentrations of Beryllium 7 in the troposphere, by means of air masses' mixing. This can be due to the warming of the earth's surface during the spring and summer that increases convection, which transports  $^7\text{Be}$  from the upper troposphere to near-surface air, and to intense thunderstorms that increase the probability of scavenging by precipitation. Interestingly, where there is a clear seasonal variation in precipitation, rainfall and  $^7\text{Be}$  show an inverse relationship, confirming the importance of wash-out in Beryllium 7 detection.

Finally, nuclear detonations do not contribute to  $^7\text{Be}$  production. The next Section will explain better the properties and the uses of Beryllium 7.

## 1.4 Applications of Beryllium 7

Beryllium 7 has been applied to study different problems, and its characteristics, related to atmospheric parameters or other radionuclides, are presented in this Section.

One of the most important results for Beryllium 7 is directly linked to its source, i.e. cosmic rays and especially the sun. Monthly  $^7\text{Be}$  specific activities in surface air have been found to be inversely correlated with solar activity. Gerasopoulos et al. [10] calculated the cross-correlation coefficients between  $^7\text{Be}$  with the sunspot number and the heliocentric potential. The result was a strong anti-correlation between Beryllium 7 and the sunspot number (-0.86), with  $^7\text{Be}$  lagging 5 months behind, while another strong anti-correlation at lag zero was found with the heliocentric potential (-0.80). An explanation of this time delay has to take into account the relation between the two indices used (sunspot number, heliocentric potential) and the solar activity. The sunspot number is an index that quantifies the solar activity. Changes in the solar wind density released by the sun have to travel some distance before reaching the earth and therefore affecting the cosmic rays intensity at the earth. On the other hand, the effect of the solar wind on the galactic cosmic rays spectrum can be described by the heliocentric potential, whose magnitude at the earth's orbit is equal to the energy loss per unit charge of the primary particles interacting with the solar wind. The heliocentric potential is, therefore, a direct measure of the intensity of the cosmic rays flux. Moreover, one has to assume that the solar wind density variation which proceeds out from the sun, modulating

the incoming cosmic rays, and the sunspot number have a common cause, or that sunspots in some way cause this variation. The solar wind must go some distance into the interplanetary medium to be able to intercept and modulate the incoming cosmic rays on their way to a depth in the heliosphere corresponding to the earth's orbit. Thus, the time delay of 5 months is the time needed for the changing solar wind to establish the equivalent heliocentric potential, which is in turn directly (without delay) reflected in the production of  $^7\text{Be}$ . Other studies [11, 12] found a similar value of anti-correlation between Beryllium 7 and the sunspot number.

A positive correlation has instead been found between Beryllium 7 concentrations in surface air and the tropopause height [13, 14]. Therefore, increased  $^7\text{Be}$  values are associated with high tropopause level. The tropopause marks the boundary between troposphere and stratosphere, the first two layers of the atmosphere. A fundamental characteristic of the tropopause is the change in its static stability (temperature lapse rate) across the interface. The height of the tropopause is variable in space and time, because of the latitudinal and seasonal dependence of solar irradiation as well as the changes due to weather patterns. In the tropics, the tropopause is relatively thick ( $\sim 16 \text{ km}$ ), reflecting a transition between radiative-convective balance in the troposphere and radiative balance in the stratosphere. The tropopause in the extratropics is thinner (8-12  $\text{km}$ ), with an equilibrium structure determined by baroclinic wave dynamics. The extratropical tropopause is characterised by large dynamic variability, often with complex spatial structure. The positive correlation between tropopause height and  $^7\text{Be}$  activity concentrations reflects both downward transport from the upper troposphere during anticyclonic conditions and less wet scavenging during these conditions. Although stratosphere-to-troposphere exchange events are usually associated with upper-level troughs or cut-off lows, the stratospheric air typically descends stations within upper-level ridges (and surface anticyclones) following the troughs.

Air masses originating in the upper troposphere or in the lower stratosphere contain less  $^7\text{Be}$  than air masses at the surface. Thus, Beryllium 7 can be used as an atmospheric tracer and is useful for the study of air masses exchange between stratosphere and troposphere.  $^7\text{Be}$  is a very useful tracer in atmospheric transport studies because it:

- has a short half-life;
- is produced at a relatively constant rate;
- rapidly attaches to aerosols after formation;
- has a large concentration gradient between the stratosphere and troposphere.

Since it attaches to aerosols, and hence its tropospheric lifetime is primarily controlled by the wet scavenging of the carrier aerosol, the ratio of  $^7\text{Be}$  and  $^{10}\text{Be}$  is used as a stratospheric tracer.  $^{10}\text{Be}$  has a much longer half-life,  $1.51 \times 10^6$  years. Thus the  $^{10}\text{Be}/^7\text{Be}$  ratio in the atmosphere can be used as a clock to determine

air mass age, and also to indicate the intrusion of stratospheric air into the troposphere [15, 16, 17, 18], stratospheric air masses characteristically having a relatively high  $^{10}\text{Be}/^7\text{Be}$  ratio. Beryllium 7 and Beryllium 10 production ratio is virtually constant throughout the atmosphere at a value of approximately 0.6 [19], but because of the much longer decay time of  $^{10}\text{Be}$ , their concentration ratio is always larger than that. In the stratosphere, where wet and dry depositions are ineffective,  $^{10}\text{Be}/^7\text{Be}$  ratios are much higher than in the troposphere and are controlled by the residence time (months to years) of the air in the stratosphere [20]. One weakness of using the  $^{10}\text{Be}/^7\text{Be}$  ratio as a stratospheric tracer to determine the stratospheric flux into the troposphere is that an important fraction of the production of both  $^{10}\text{Be}$  and  $^7\text{Be}$  occurs in the upper troposphere and hence surface concentrations of these radionuclides can be also influenced by downward mixing within the troposphere [6].

Another example of a radionuclide studied together with  $^7\text{Be}$  is  $^{210}\text{Pb}$ . The contrasting source terms of  $^7\text{Be}$  and  $^{210}\text{Pb}$  make the  $^7\text{Be}/^{210}\text{Pb}$  ratio a useful tool for investigating air mass sources and vertical transport within the troposphere [17, 21, 22, 23, 24, 25].  $^{210}\text{Pb}$  ( $T_{1/2} = 22.2$  years) is derived from the decay of  $^{222}\text{Rn}$  gas ( $T_{1/2} = 3.8$  days). Radon is an inert noble gas which is released from the ground to the atmosphere predominantly from continental surfaces. The source location and source term of  $^{210}\text{Pb}$  are therefore very different from that of  $^7\text{Be}$ . Therefore,  $^{210}\text{Pb}$  concentrations in the air should decrease with altitude and distance from land.  $^7\text{Be}$  instead, being of cosmogenic origin, should have uniform concentrations in the air over land and sea, always increasing with altitude. In contrast with  $^7\text{Be}$ , the  $^{210}\text{Pb}$  concentration in the air decreases with elevation from the ground due to its production close to the earth surface. The unique feature of  $^{210}\text{Pb}$ , when compared with  $^7\text{Be}$ , suggests that due to altitudinal distinct sources, they might allow assessments of the relative importance of stratospheric and tropospheric transport pathways to surface air, which makes them ideal tools to depict transport processes in the whole atmosphere [12]. Therefore, high  $^7\text{Be}/^{210}\text{Pb}$  ratios may be an indication of stratosphere-troposphere exchange, or of an air mass with components originating from the open ocean.

$^7\text{Be}$  is also subject to wet deposition, the most significant mechanism for its removal from the atmosphere. The concentrations of  $^7\text{Be}$  in the surface air and rainwater have been frequently used to estimate the deposition flux of  $^7\text{Be}$ , which is affected by both dry and wet processes. In wet deposition, precipitation transports  $^7\text{Be}$  from the upper troposphere to the ground. This process usually occurs in the spring and summer, when air transport from the stratosphere to the troposphere is easily induced by the heating of the earth's surface [26]. The deposition velocity of aerosols can be affected by precipitation and seasonal factors. However, the deposition velocity reflects the effectiveness of aerosol scavenging by precipitation. Thus, both the amount of precipitation and duration of rainfall are of relevant importance. Rainfall reduces the air concentration of  $^7\text{Be}$  and increases the deposition

velocity, which provides important information on the behaviour of atmospheric particulates in the environment. Typically, the Beryllium 7 concentration of air is inversely related to rainfall. High volumes of precipitation can reduce the  $^7\text{Be}$  concentration of air by washout. Relative humidity has also been found to be inversely correlated with  $^7\text{Be}$  [27] since both precipitation and relative humidity are related to the amount of water in the air.

To further explain the behaviour of  $^7\text{Be}$  in surface air, its relation to local climate variables has been extensively studied. Results show a great variability, mostly depending on the measurement site [12, 28, 29, 30, 31, 32, 33, 34, 35, 36]. Thus, local meteorological parameters affect differently  $^7\text{Be}$  concentrations in different locations.

The analysis of Beryllium 7 time series (Chapter 3 and Chapter 4) also focuses on a comparison with meteorological parameters, and confirms some of the characteristics of  $^7\text{Be}$ .

Time series analysis is a very wide topic spanning many different fields. In this Chapter, a procedure for the analysis is defined. The procedure is composed of different steps, and every step is explained giving details about the mathematical tools. It is based on time series analysis and uses different well-established methods, organised in such a way to best describe the properties of the time series. Moreover, some of the methods need to be modified in order to take into account the possible presence of missing data. The extension to missing data will be presented at the beginning of Chapter 3. In this Chapter instead, results coming from the application of the method to synthetic time series are shown, in order to validate the procedure and to test its reliability, by means of the analysis of artificial data with known properties.

### 2.1 Logical scheme

A time series is a collection of chronologically ordered data and can be considered as made up of three terms [37],

$$X_t = T_t + S_t + N_t \quad (2.1)$$

with  $t = 1, \dots, N$ ,  $N$  being the length of the time series.  $T_t$  is called trend, is considered here as a monotonic function and represents the overall growth (or decrease) of  $X_t$ .  $S_t$  represents the sum of the periodicities within the time series and is therefore called the periodic term, given by

$$S_t = \sum_i A_i \sin(2\pi\nu_i t) \quad (2.2)$$

$N_t$  represents the residuals, considered as a stochastic process underlying the other two processes, and is therefore what remains of the time series once the deterministic part has been subtracted.

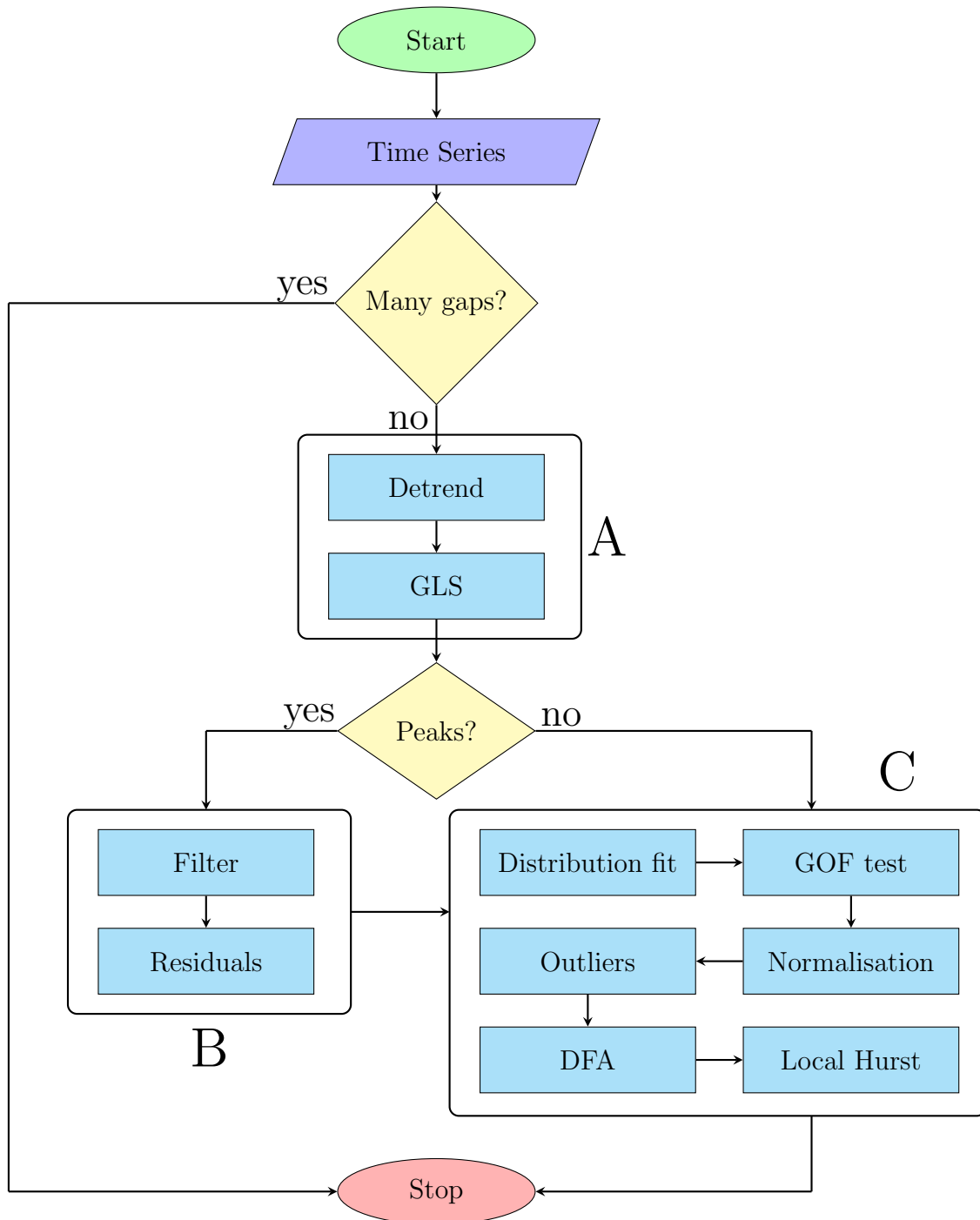


Figure 2.1: Flow chart for the method.

The logical scheme of the procedure is shown in Figure 2.1. It is composed of three main blocks, each one dealing with one of the terms in Equation (2.1). Moreover, since real-life time series often lack some data, it is not uncommon to

find gaps within the time series. Thus, when the time series is taken as input, it is first requested not to have a high number of missing data or not to have wide gaps. In fact, results could be not accurate, and a resampling of the time series should be considered. If  $X_t$  is suitable for the analysis, block *A* of Figure 2.1 is first executed.

## 2.2 Block A

### 2.2.1 Detrend

The first step of the analysis is the detrending procedure, i.e. the identification and removal of the trend from the time series. Trend  $T_t$  is considered as a monotonic function that describes the overall growth of the time series and could be modelled as, for instance, an  $n$ -degree polynomial. Though, if  $n$  is sufficiently high, the polynomial will fit too well to the time series, causing the removal of possible low frequencies present in the time series. As it will be seen in the next chapters, for some time series a linear trend is enough, while other ones do not have a trend at all. Thus, a fit is performed with the chosen function, and the result  $T_t$  is subtracted from  $X_t$ , giving us the detrended time series. In Figure 2.2 an example of synthetic time series is shown. The trend has been chosen linear, some periodicities are present, and also noise has been added. Referring to Equation (2.1), the synthetic time series chosen for testing the method is

$$X_t = 0.05 \cdot t + 2.0 \sin(2\pi \cdot 0.003 \cdot t) + 5.0 \sin(2\pi \cdot 0.020 \cdot t) + 2.5 \sin(2\pi \cdot 0.060 \cdot t) + \eta_t \quad (2.3)$$

with  $\eta_t$  a coloured noise time series generated starting from its power spectrum. Thus, a straight line has been fitted to the original time series, and subsequently subtracted from  $X_t$ , giving the detrended time series  $X_t - T_t$ .

Instead, if the presence of a trend is clear, but it is not straightforward how to model it, Empirical Mode Decomposition (EMD) can be employed [38]. EMD is an adaptive method and does not imply an *a priori* choice for the trend. The goal of the EMD is to decompose the time series in the so-called intrinsic mode functions (IMFs). An IMF is a function that satisfies two conditions:

- in the whole data set, the number of extrema and the number of zero crossings must either equal or differ at most by one;
- at any point, the mean value of the envelope defined by the local maxima and the envelope defined by the local minima is zero.

Hence, IMFs represent the oscillation modes of the data and the IMF in each cycle involves only one mode of oscillation. Thus, an IMF can be both amplitude and frequency modulated. In fact, it can be non-stationary. To decompose the data into IMF components, three assumptions are made:

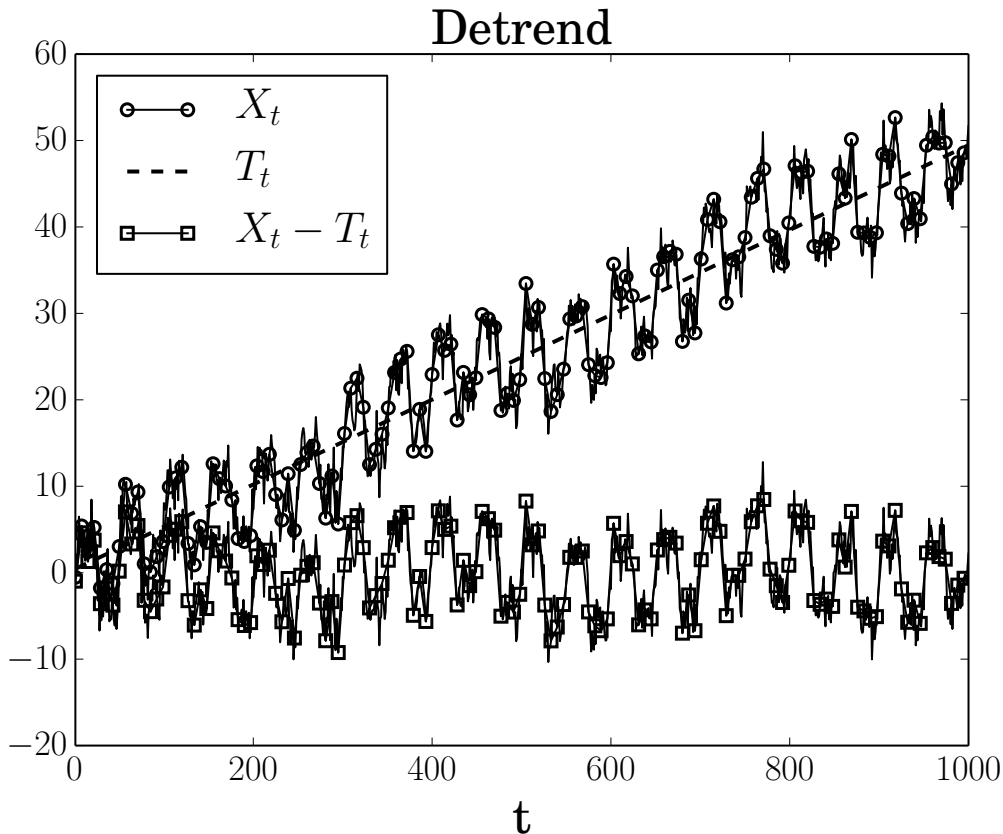


Figure 2.2: Detrend: Synthetic time series  $X_t$  ( $\circ$ ) is composed by a linear trend, periodicities, and noise. The dashed line represent the linear fit performed on the time series. Subtraction of the trend from  $X_t$  gives the detrended time series ( $\square$ ).

- the signal has at least two extrema, one maximum and one minimum;
- the characteristic time scale is defined by the time lapse between the extrema;
- if the data were totally devoid of extrema but contained only inflection points, then the signal can be differentiated once or more times to reveal the extrema. Final results can be obtained by integrations of the components.

Then, the sifting procedure is implemented as follows. The sifting procedure serves two purposes, to eliminate riding waves and to make the wave profiles more symmetric with respect to zero. The local maxima of  $X_t$  are connected by a cubic spline to form the upper envelope, and the same is done with the local minima to form the lower envelope. Then the mean of the envelopes  $m_1$  is computed, and subtracted from the time series, obtaining a proto-mode function  $h_1$  [39],

$$h_1 = X_t - m_1 \quad (2.4)$$

In Figure 2.3 an example of the sifting procedure for the extraction of  $h_1$  is shown. Now,  $h_1$  is treated as the time series, and the sifting procedure is repeated until the

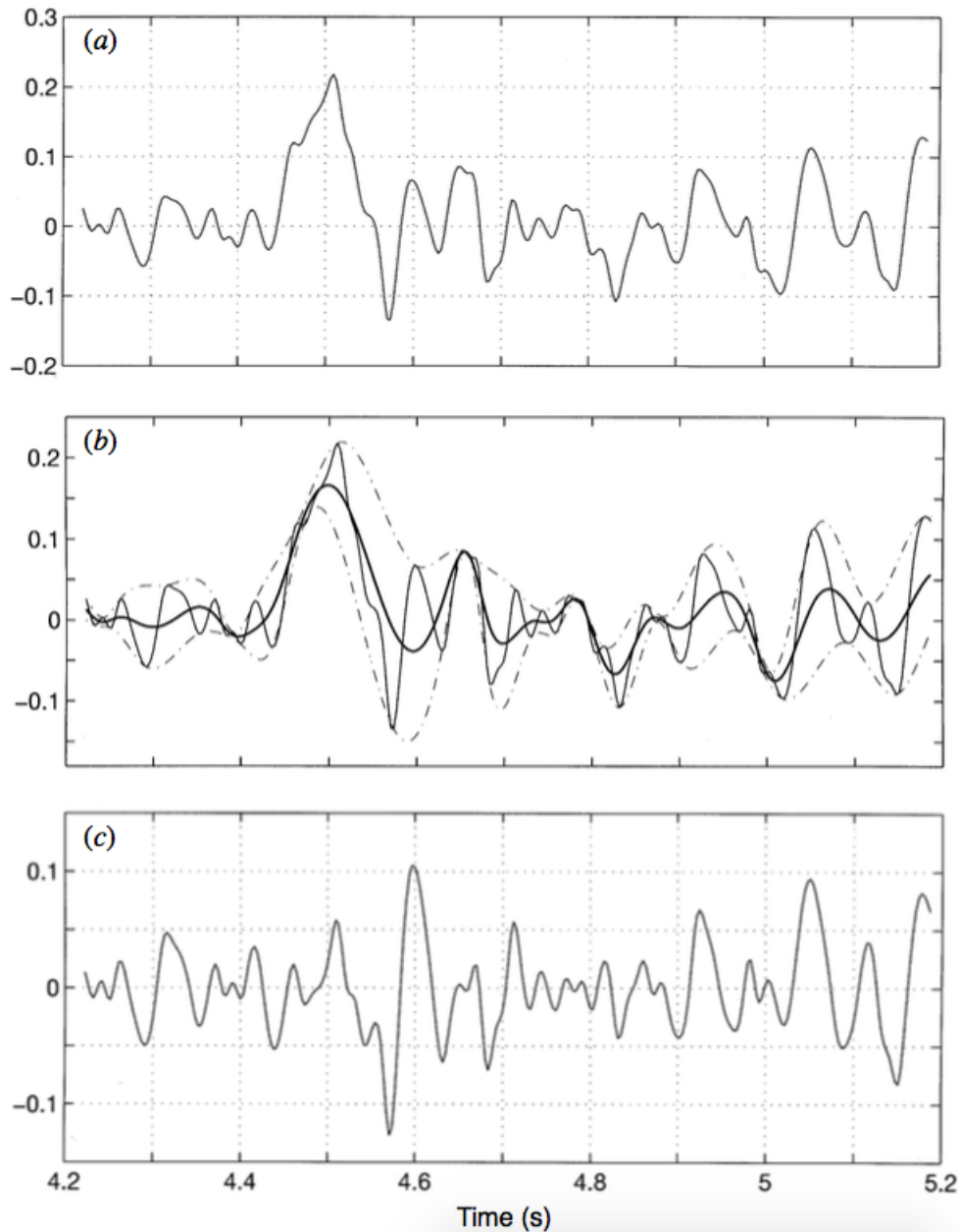


Figure 2.3: Example of the sifting procedure. (a): Original time series  $X_t$ . (b): Upper and lower envelopes obtained connecting local maxima and local minima with a cubic spline (dashed lines) and their mean  $m_1$  (solid line). (c): Proto-mode function  $h_1$  after the subtraction of  $m_1$  from the original time series  $X_t$ . Figure can be found in [38].

number of extrema and the number of zero crossings are either equal or differ at most by one. Then, the sifting procedure continues to be applied, and it is stopped when the number of zero crossings and extrema is the same for  $S$  successive sifting steps. A high  $S$  produce over-sifting, that can have a detrimental effect on the results. Huang et al. [39] recommend using for  $S$  a value in the range between 3 and 5. Once the first IMF  $c_1$  is obtained, it is subtracted from the time series, and

the residue  $r_1$  is now considered as the original time series,

$$r_1 = X_t - c_1 \quad (2.5)$$

The procedure is repeated for all the  $r_i$  values until the residue  $r_n$  becomes a constant value, a monotonic function or a function with only one extremum from which no more IMFs can be extracted. If the data have a trend, the final residue can be considered as the trend [40]. The time series is finally decomposed as

$$X_t = \sum_{i=1}^n c_i + r_n \quad (2.6)$$

with  $r_n = T_t$ .

To choose the best number to stop the sifting, the procedure described above is implemented for different values of  $S$ , producing different sets of IMFs. Then, each set is tested for orthogonality by means of the orthogonal index [39, 41]

$$OI = \frac{\sum_{j=1}^{n+1} \sum_{\substack{k=1 \\ j \neq k}}^{n+1} \sum_{t=1}^N c_{jt} c_{kt}}{\sum_{t=1}^N X_t^2} \quad (2.7)$$

The set with the lower value of  $OI$  is chosen, and hence the trend  $T_t$ .

## 2.2.2 GLS

Then the spectrum of the detrended time series can be computed since the trend has been removed as it will have obscured the frequency content of the time series during the spectrum estimation. With the spectrum, it is possible to analyse the time series in the frequency domain. The most common procedure to pass from time to frequency domain is by means of the Fourier transform, i.e. implementing the FFT (Fast Fourier Transform) algorithm [42]. However, in our case, we can not compute the FFT, for the time series generally has missing data and FFT requires evenly spaced data. Interpolation could be done in the case of missing data, but instead of introducing synthetic data, the Lomb-Scargle (LS) spectrum [43, 44] can be employed. It can handle the case of missing data, and in case of evenly spaced data, LS spectrum and FFT give the same result. The LS spectrum is based on least squares analysis and, as it will be proven later, it is given by

$$P(\omega) = \frac{1}{2\sigma^2} \left\{ \frac{[\sum_j (X_j - \langle X \rangle) \cos(\omega(t_j - \tau))]^2}{\sum_j \cos^2(\omega(t_j - \tau))} + \frac{[\sum_j (X_j - \langle X \rangle) \sin(\omega(t_j - \tau))]^2}{\sum_j \sin^2(\omega(t_j - \tau))} \right\} \quad (2.8)$$

with  $\omega = 2\pi\nu$ ,  $\nu$  the frequency,  $\sigma^2$  the variance of the data,  $N$  the length of the time series,  $\langle X \rangle$  the mean of the data, and  $\tau$  given by

$$\tau = \frac{1}{2\omega} \arctan \left\{ \frac{\sum_j \sin(2\omega t_j)}{\sum_j \cos(2\omega t_j)} \right\} \quad (2.9)$$

$\tau$  is a time shift that can be chosen arbitrarily since the fit is time translation invariant, and simplifies the form of Equation (2.8). The principal drawback of the LS spectrum is that it assumes all the fitted sinusoids to have zero mean, so it needs to be slightly modified in order to take into account the presence of a possible offset during the fit. The generalised Lomb-Scargle spectrum (GLS) has been introduced by Zechmeister et al. [45] to overcome this problem. Following [45] (with a slightly modified notation, for errors are not taken into account here), a general sinusoid with a non-zero mean can be written as

$$y(t) = a \cos(\omega t) + b \sin(\omega t) + c \quad (2.10)$$

From least squares analysis, the squared difference between the data  $y_i$  and  $y(t)$ ,

$$\chi^2 = \sum_i (y_i - y(t_i))^2 \quad i = 1, \dots, N \quad (2.11)$$

has to be minimised. Substituting (2.10) into (2.11), and computing the derivatives with respect to the three parameters  $a$ ,  $b$  and  $c$ , three equations are obtained (derivatives equal to zero),

$$\begin{cases} \partial_a \chi^2 = -2 \sum_i (y_i - y(t_i)) \cos(\omega t_i) = 0 \\ \partial_b \chi^2 = -2 \sum_i (y_i - y(t_i)) \sin(\omega t_i) = 0 \\ \partial_c \chi^2 = -2 \sum_i (y_i - y(t_i)) = 0 \end{cases} \quad (2.12)$$

With the insertion of (2.10), the three equations become

$$\begin{cases} \sum_i y_i \cos(\omega t_i) = a \sum_i \cos^2(\omega t_i) + b \sum_i \cos(\omega t_i) \sin(\omega t_i) + c \sum_i \cos(\omega t_i) \\ \sum_i y_i \sin(\omega t_i) = a \sum_i \cos(\omega t_i) \sin(\omega t_i) + b \sum_i \sin^2(\omega t_i) + c \sum_i \sin(\omega t_i) \\ \sum_i y_i = a \sum_i \cos(\omega t_i) + b \sum_i \sin(\omega t_i) + Nc \end{cases} \quad (2.13)$$

and can be rewritten in a matrix form (see [45] for the notation)

$$\begin{bmatrix} \hat{Y}C \\ \hat{Y}S \\ Y \end{bmatrix} = \begin{bmatrix} \hat{C}C & \hat{C}S & C \\ \hat{C}S & \hat{S}S & S \\ C & S & N \end{bmatrix} \begin{bmatrix} a \\ b \\ c \end{bmatrix} \quad (2.14)$$

The third equation of (2.13) gives

$$c = \frac{1}{N} \left[ \sum_i y_i - a \sum_i \cos(\omega t_i) - b \sin(\omega t_i) \right] \quad (2.15)$$

or

$$c = \frac{1}{N} \left[ Y - aC - bS \right] \quad (2.16)$$

and inserting it in the other two equations reduces the system to

$$\begin{bmatrix} \hat{Y}C - \frac{1}{N}Y \cdot C \\ \hat{Y}S - \frac{1}{N}Y \cdot S \end{bmatrix} = \begin{bmatrix} \hat{C}C - \frac{1}{N}C \cdot C & \hat{C}S - \frac{1}{N}C \cdot S \\ \hat{C}S - \frac{1}{N}C \cdot S & \hat{S}S - \frac{1}{N}S \cdot S \end{bmatrix} \begin{bmatrix} a \\ b \end{bmatrix} \quad (2.17)$$

or, to simplify the notation,

$$\begin{bmatrix} YC \\ YS \end{bmatrix} = \begin{bmatrix} CC & CS \\ CS & SS \end{bmatrix} \begin{bmatrix} a \\ b \end{bmatrix} \quad (2.18)$$

The solutions of (2.18) are

$$a = \frac{YC \cdot SS - YS \cdot CS}{CC \cdot SS - CS^2} \quad ; \quad b = \frac{YS \cdot CC - YC \cdot CS}{CC \cdot SS - CS^2} \quad (2.19)$$

Substituting the values of  $a$ ,  $b$  and  $c$  in (2.11) gives

$$\chi^2 = Y\hat{Y} - aY\hat{C} - bY\hat{S} - cY \quad (2.20)$$

or

$$\chi^2 = YY - aYC - bYS \quad (2.21)$$

with  $Y\hat{Y} = \sum_i y_i^2$  and  $YY = Y\hat{Y} - Y \cdot Y/N$ . Substituting the values (2.19) for  $a$  and  $b$ ,

$$\chi^2 = YY - \frac{YC^2 \cdot SS}{CC \cdot SS - CS^2} - \frac{YS^2 \cdot CC}{CC \cdot SS - CS^2} - 2 \frac{YC \cdot YS \cdot CS}{CC \cdot SS - CS^2} \quad (2.22)$$

As said earlier for the LS spectrum, the fit with Equation (2.10) is time translation invariant, and an arbitrary time reference  $\tau$  can be introduced (to be subtracted from  $t_i$  in the previous equations). Choosing

$$\tau = \frac{1}{2\omega} \arctan \left\{ \frac{2CS}{CC - SS} \right\} \quad (2.23)$$

the last term in Equation (2.22) disappears. Now, the spectrum is

$$P(\omega) = \frac{\chi_0^2 - \chi^2}{\chi_0^2} \quad (2.24)$$

with  $\chi_0^2 = \sum_i (y_i - \langle y \rangle)^2 = N\sigma^2 = YY$ ,  $\langle y \rangle = \sum_i y_i/N$ . Substituting the full form of the parameters in Equation (2.22), multiplying for  $N/2$  to ensure the same normalisation of the LS spectrum (2.8), and coming back to the notation of Equation (2.1) for the time series, the final form of the spectrum is

$$P(\omega) = \frac{1}{2\sigma^2} \left\{ \frac{N[\sum_j (X_j - \langle X \rangle) \cos(\omega(t_j - \tau))]^2}{N \sum_j \cos^2(\omega(t_j - \tau)) - [\sum_j \cos(\omega(t_j - \tau))]^2} + \frac{N[\sum_j (X_j - \langle X \rangle) \sin(\omega(t_j - \tau))]^2}{N \sum_j \sin^2(\omega(t_j - \tau)) - [\sum_j \sin(\omega(t_j - \tau))]^2} \right\} \quad (2.25)$$

with  $\omega = 2\pi\nu$ ,  $\nu$  the frequency,  $\sigma^2$  the variance of the data,  $N$  the length of the time series,  $\langle X \rangle$  the mean of the data.  $\tau$  is given by [45, 46]

$$\tau = \frac{1}{2\omega} \arctan \left\{ \frac{N \sum_j \sin(2\omega t_j) - 2 \sum_j \cos(\omega t_j) \sum_j \sin(\omega t_j)}{N \sum_j \cos(2\omega t_j) - [\sum_j \cos(\omega t_j)]^2 + [\sum_j \sin(\omega t_j)]^2} \right\} \quad (2.26)$$

The LS spectrum, and also the GLS spectrum, are associated with a threshold that allows to discriminate between a periodic frequency and a random fluctuation with probability  $p_0$ ,

$$z_{p_0} = -\ln[1 - (1 - p_0)^{1/N_\nu}] \quad (2.27)$$

Scargle [44] found Equation (2.27) for the LS spectrum of uncorrelated gaussian noise, showing that it has an exponential distribution with mean 1. So, if the data are corrupted by uncorrelated gaussian noise, there is a probability  $p_0$  that a peak in the spectrum greater than  $z_{p_0}$  is not noise. If the noise is not gaussian, Equation (2.27) is a good indicator of the noise level in the LS or GLS spectrum [47]. If the time series is sampled at every  $\Delta t$ , given  $f_s = 1/\Delta t$  as the sampling frequency, in Equation (2.27)  $N_\nu$  is the number of frequencies at which the spectrum is evaluated, i.e. positive and evenly spaced frequencies up to  $f_s/2$ , the Nyquist frequency [37], and is equal to half the number of the samples that compose  $X_t$ . An oversampling factor can also be taken, and the spectrum will be evaluated at more frequencies, namely  $N_\nu$  times the oversampling factor. Frequencies will still range up to the Nyquist frequency, but the spacing between two subsequent frequencies will be narrower. The oversampling factor is a sort of interpolation and no information is added to the spectrum, whereas it helps the plot look smoother [44] (the equivalent of zero padding in FFT [42]). An example of the GLS spectrum is shown in Figure 2.4. The  $S_t$  term of Equation (2.2) has been chosen to be composed of three periodicities, i.e. three sines with frequency  $\nu_1 = 0.003 \text{ Hz}$ ,  $\nu_2 = 0.020 \text{ Hz}$ , and  $\nu_3 = 0.060 \text{ Hz}$ , respectively. Peaks over the threshold correspond exactly to the three frequencies chosen for  $S_t$ .

Therefore, the block *A* gives in output the trend  $T_t$ , the detrended time series, and the GLS spectrum of  $X_t - T_t$ .

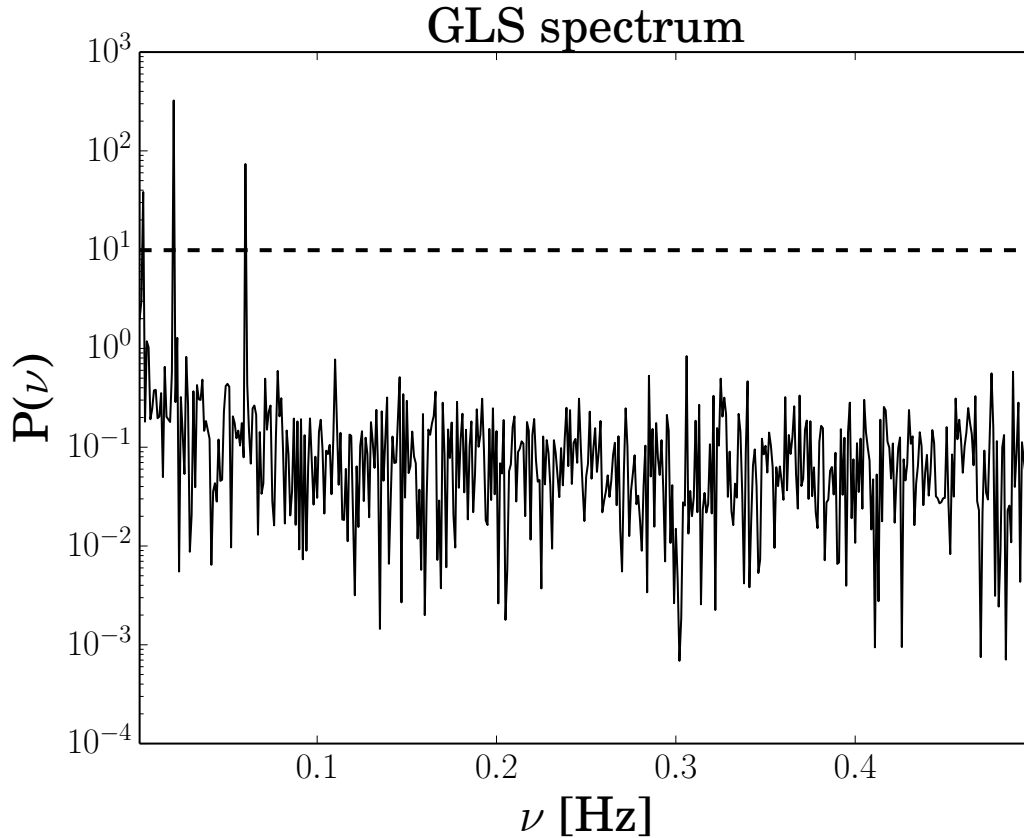


Figure 2.4: Generalised Lomb-Scargle spectrum for a synthetic time series made up of three sinusoids and noise. The dashed line represents the threshold for the detection of the peaks corresponding to periodicities. Three periodicities were introduced in the synthetic time series, and exactly three peaks over the threshold are found in the spectrum.

## 2.3 Block B

The spectrum and the threshold (2.27) are the inputs for the next step in the analysis, shown in block *B* of Figure 2.1. The term  $S_t$  is here characterised, i.e. the  $\nu_i$  of our time series corresponding to periodicities. If no periodicities are found, the analysis goes directly to block *C*, that will be described in the next section.

### 2.3.1 Filter

The first operation in this block is to construct a notch filter, to filter out frequencies corresponding to periodicities, i.e. those frequencies which contribute to the spectrum with a value higher than the threshold (2.27). The notch filter removes an interval of frequencies  $\Delta\nu$  around the  $\nu$  that corresponds to the selected peak in the GLS.  $\Delta\nu$  bounds are selected starting from  $\nu$  and going down on the spectrum as long as spectrum values keep decreasing. The last values of frequency on the right and on the left are respectively the right and left limit of  $\Delta\nu$ . Then, the contribution (in terms of percentage) of  $\Delta\nu$  to the entire spectrum is computed,

as the area under the peak, normalised to the total area of the spectrum. Table 2.1 summarises the results for the frequencies found in the particular case of the synthetic time series depicted in Figure 2.4.

	$\nu$ [Hz]	%
$\nu_1$	0.003	8.71
$\nu_2$	0.020	64.94
$\nu_3$	0.060	14.87

Table 2.1: Value of the frequency and corresponding percentage weight for the three frequencies inserted in the synthetic time series.

### 2.3.2 Residuals

When all  $\Delta\nu$  corresponding to peaks over the threshold have been filtered out, the periodic term  $S_t$  can be subtracted from the time series, and the remainder is exactly the term  $N_t$  of Equation (2.1). To come back from time to frequency domain, interpolation is needed in order to use the inverse FFT, for an inverse GLS spectrum cannot be computed. In case no peaks over the threshold were found, the term  $S_t$  is zero, and  $N_t$  is exactly equal to the detrended time series. Residuals are then what is beneath the time series once trend and periodicities are removed. Residuals for the synthetic time series after the filter application are shown in Figure 2.5.

## 2.4 Block C

The last step in the analysis is the block  $C$  of Figure 2.1, that aims at characterising the residuals. It focuses principally on persistence and noise characterisation, but also on outliers identification and on the probability distribution of the residuals.

### 2.4.1 Distribution fit

Residuals are organised in a histogram (normalised to the total area) and fitted to some known distributions, to see which one describes better the data. These distributions are:

- **Burr:** The Burr distribution is a three-parameter family of distributions on the positive real line. It can fit a wide range of empirical data, and is used in various fields such as finance, hydrology, and reliability to model a variety of data types. The Burr distribution depends on three parameters:  $\alpha > 0$ , the

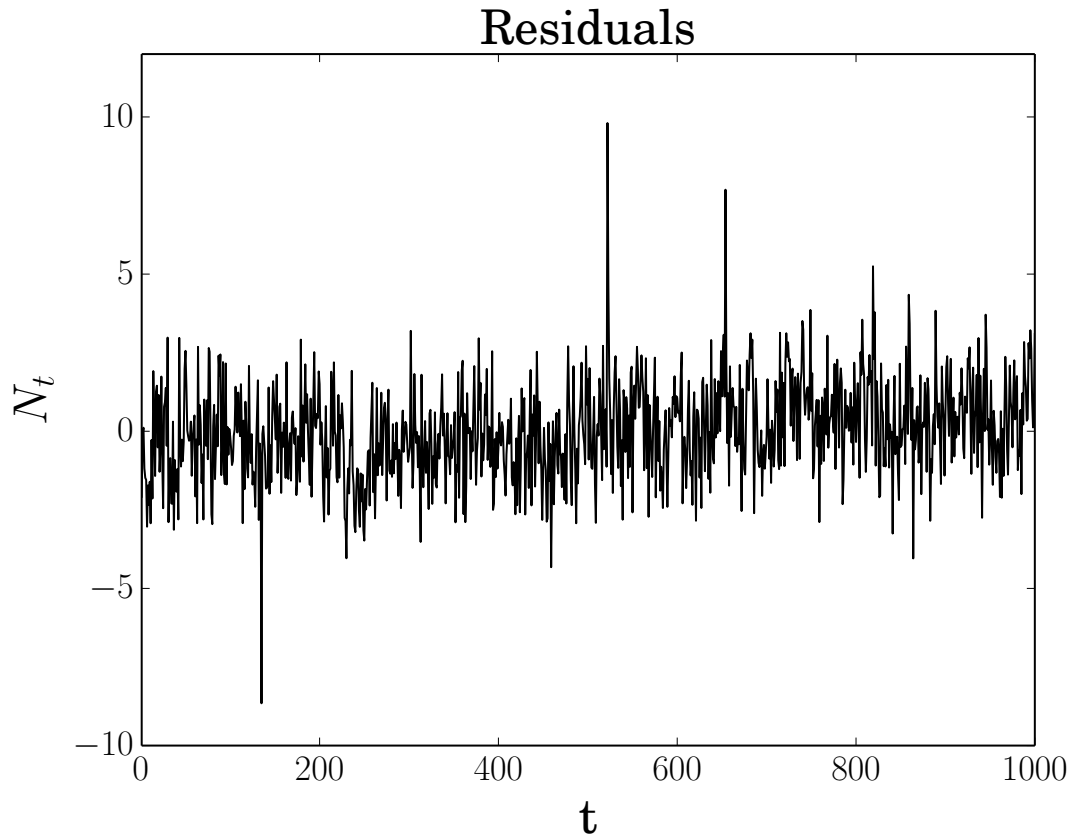


Figure 2.5: Residuals for the synthetic time series after the filter application and the periodicities removal.

scale parameter;  $c > 0$ , the first shape parameter;  $k > 0$ , the second shape parameter. The probability density function (PDF) is

$$f(x|\alpha, c, k) = \frac{\frac{kc}{\alpha} \left(\frac{x}{\alpha}\right)^{c-1}}{\left(1 + \left(\frac{x}{\alpha}\right)^c\right)^{k+1}} \quad (2.28)$$

- **Gamma:** The Gamma distribution is a two-parameter family of distributions used to model sums of exponentially distributed random variables. The Chi-square and the Exponential distributions, which are children of the Gamma distribution, are one-parameter distributions that fix one of the two gamma parameters. The Gamma distribution depends on two parameters:  $a > 0$ , the shape parameter;  $b \geq 0$ , the scale parameter. The PDF is

$$f(x|a, b) = \frac{1}{b^a \Gamma(a)} x^{a-1} e^{-x/b} \quad (2.29)$$

where  $\Gamma(\cdot)$  is the Gamma function.

- **Exponential:** The Exponential distribution is used to model events that occur randomly over time, and its main application area is studies of lifetimes.

It is a special case of the Gamma distribution with the shape parameter  $a = 1$ . The Exponential distribution depends on a single parameter, the mean  $\mu > 0$ . The PDF is

$$f(x|\mu) = \frac{1}{\mu} e^{-x/\mu} \quad (2.30)$$

- **Generalised Pareto:** The Generalised Pareto distribution is used to model the tails of another distribution. It allows a continuous range of possible shapes that include both the Exponential and Pareto distributions as special cases. The Generalised Pareto distribution depends on three parameters:  $-\infty < k < \infty$ , the shape parameter;  $\sigma \geq 0$ , the scale parameter;  $-\infty < \theta < \infty$ , the location parameter. The PDF is

$$f(x|k, \sigma, \theta) = \left(\frac{1}{\sigma}\right) \left(1 + k \frac{x - \theta}{\sigma}\right)^{-1 - \frac{1}{k}} \quad (2.31)$$

for  $k \neq 0$ ,  $x > \theta$  when  $k > 0$  or  $\theta < x < -\sigma/k$  when  $k < 0$ . For  $k = 0$  and  $x > \theta$  the PDF is

$$f(x|0, \sigma, \theta) = \left(\frac{1}{\sigma}\right) \exp\left(-\frac{x - \theta}{\sigma}\right) \quad (2.32)$$

- **Inverse Gaussian:** Also known as the Wald distribution, the inverse Gaussian is used to model nonnegative positively skewed data. Inverse Gaussian distributions have many similarities to standard Gaussian (Normal) distributions, which lead to applications in inferential statistics. The Inverse Gaussian distribution depends on two parameters:  $\mu > 0$ , the scale parameter;  $\lambda > 0$ , the shape parameter. The PDF is

$$f(x|\mu, \lambda) = \sqrt{\frac{\lambda}{2\pi x^3}} \exp\left(-\frac{\lambda}{2\mu^2 x}(x - \mu)^2\right) \quad (2.33)$$

- **Lognormal:** The Lognormal distribution is closely related to the normal distribution. If  $x$  is distributed lognormally with parameters  $\mu$  and  $\sigma$ , then  $\ln(x)$  is distributed normally with mean  $\mu$  and standard deviation  $\sigma$ . The Lognormal distribution is applicable when the quantity of interest must be positive, since  $\ln(x)$  exists only when  $x$  is positive. The Lognormal distribution depends on two parameters:  $-\infty < \mu < \infty$ , the log mean;  $\sigma \geq 0$ , the log standard deviation. The PDF is

$$f(x|\mu, \sigma) = \frac{1}{\sqrt{2\pi\sigma x}} \exp\left(\frac{-(\ln(x) - \mu)^2}{2\sigma^2}\right) \quad (2.34)$$

- **Poisson:** The Poisson distribution is appropriate for applications that involve counting the number of times a random event occurs in a given amount

of time, distance, area, etc. If the number of counts follows the Poisson distribution, then the interval between individual counts follows the exponential distribution. The Poisson distribution depends on a single parameter, the mean  $\lambda \geq 0$ . The PDF is

$$f(x|\lambda) = \frac{\lambda^x}{x!} e^{-\lambda} \quad (2.35)$$

- **Weibull:** The Weibull distribution is used in reliability and lifetime modelling, and to model the breaking strength of materials. The Weibull distribution depends on two parameters:  $a > 0$ , the scale parameter;  $b > 0$ , the shape parameter. The PDF is

$$f(x|a, b) = \frac{b}{a} \left(\frac{x}{a}\right)^{b-1} \exp\left[-\left(\frac{x}{a}\right)^b\right] \quad (2.36)$$

- **Rayleigh:** The Rayleigh distribution is a special case of the Weibull distribution. It is often used in communication theory to model scattered signals that reach a receiver by multiple paths. The Rayleigh distribution depends on a single parameter, the defining parameter  $b > 0$ . The PDF is

$$f(x|b) = \frac{x}{b^2} \exp\left(-\frac{x^2}{2b^2}\right) \quad (2.37)$$

- **Normal:** The Normal distribution, sometimes called the Gaussian distribution, is a two-parameter family of curves. The usual justification for using the Normal distribution for modelling is the Central Limit theorem, which states (roughly) that the sum of independent samples from any distribution with finite mean and variance converges to the Normal distribution as the sample size goes to infinity. The Normal distribution depends on two parameters:  $-\infty < \mu < \infty$ , the mean;  $\sigma \geq 0$ , the standard deviation. The PDF is

$$f(x|\mu, \sigma) = \frac{1}{\sqrt{2\pi}\sigma} \exp\left(\frac{-(x - \mu)^2}{2\sigma^2}\right) \quad (2.38)$$

- **t:** The t distribution is useful for modelling data distributions with heavier tails (more prone to outliers) than the normal distribution. It approaches the normal distribution as  $\nu$  approaches infinity, and smaller values of  $\nu$  yield heavier tails. The t distribution depends on three parameters:  $-\infty < \mu < \infty$ , the location parameter;  $\sigma > 0$ , the scale parameter;  $\nu > 0$ , the shape parameter. The PDF is

$$f(x|\mu, \sigma, \nu) = \frac{\Gamma(\frac{\nu+1}{2})}{\sqrt{\nu\pi}\sigma\Gamma(\nu/2)} \left[1 + \frac{(x-\mu)^2}{\nu\sigma^2}\right]^{-\frac{\nu+1}{2}} \quad (2.39)$$

Two histograms for each distribution are created, one for the residuals, and one

for the residuals without outliers (see subsection “Normalisation”). An example of histograms of residuals without outliers is shown in Figure 2.6, for the same residuals depicted in Figure 2.5. The left histogram is fitted with a Normal distribution (that passed the two tests with the highest p-value), while the right one is fitted with a Weibull distribution (that did not pass the tests).

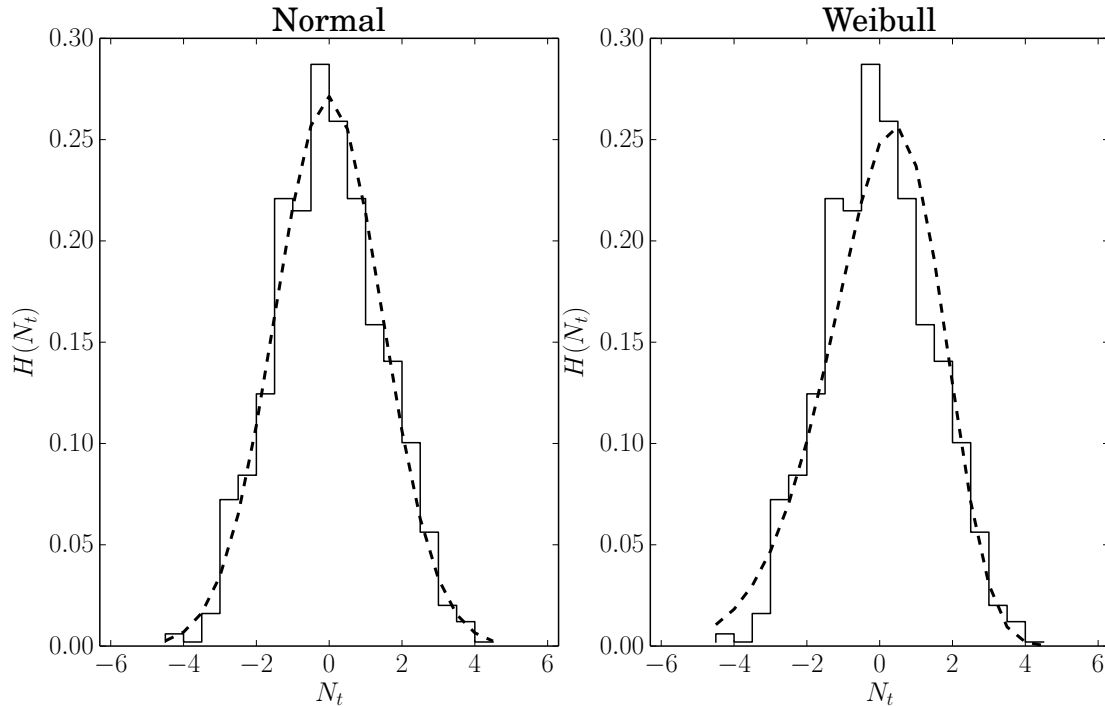


Figure 2.6: Histogram of residuals without outliers, fitted with a Normal distribution (left) and a Weibull distribution (right).

### 2.4.2 GOF test

Two goodness of fit (GOF) tests are implemented to discriminate the best-fitting distribution: the Kolmogorov-Smirnov (KS) test [48], whose statistic is given by

$$D_N = \sup_x |\Phi_N(x) - \Phi(x)| \quad (2.40)$$

where  $\Phi_N(x)$  is the empirical cumulative distribution function of the residuals and  $\Phi(x)$  is the hypothesised cumulative distribution function, and the Anderson-Darling (AD) test [49], whose statistic is given by

$$A^2 = -N - \sum_{i=1}^N \frac{2i-1}{N} [\ln(\Phi(x_i)) + \ln(1 - \Phi(x_{N+1-i}))] \quad (2.41)$$

From these two tests, it is possible to establish which distributions are suitable to describe the residuals. Among distributions that passed both the two tests, the

best fitting one is selected computing the p-value. The higher the p-value, the better the fit.

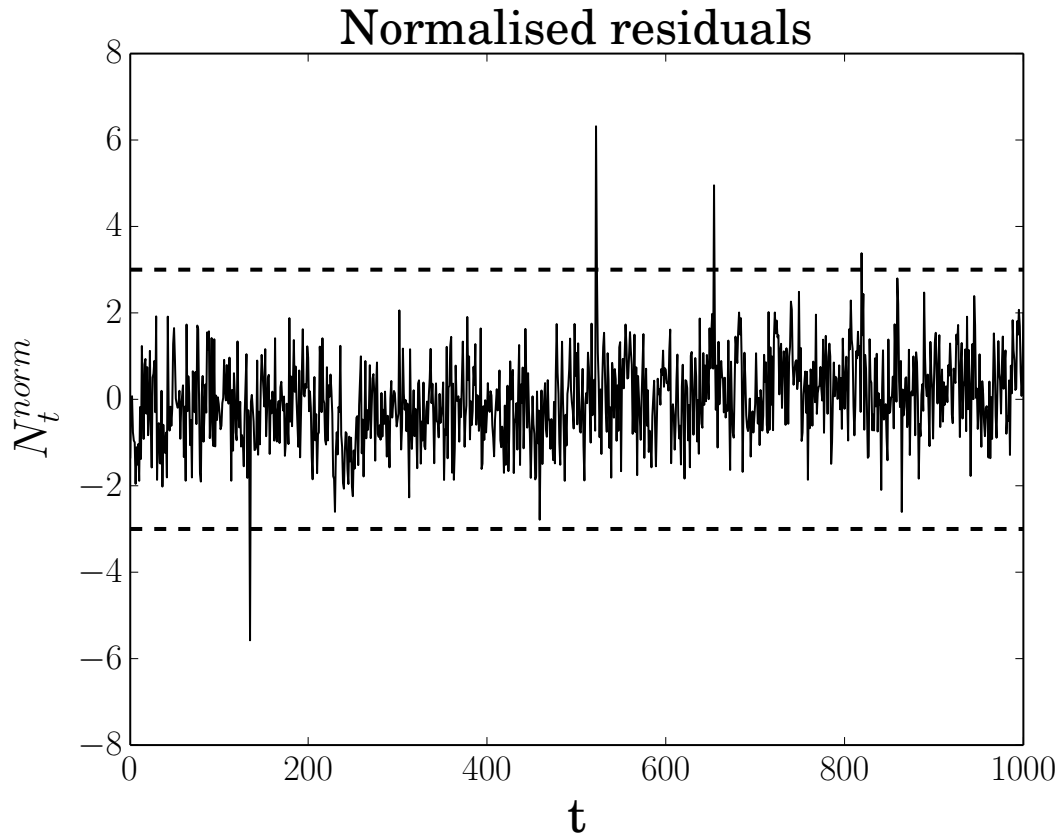


Figure 2.7: Residuals of Figure 2.5 for the synthetic time series, normalised to zero mean and unit variance. The dashed lines represent the  $\pm 3\sigma$  thresholds. The three outliers inserted in the synthetic time series at the beginning of the analysis are the three highest outliers in the figure.

### 2.4.3 Normalisation & Outliers

Mean  $\mu$  and variance  $\sigma^2$  of the residuals are computed, in order to normalise them to zero mean and unit variance and thus detect outliers, i.e. those values of the residuals greater than an arbitrary number of  $\sigma$  ( $3\sigma$  here). This is important since one would like to detect when an unusually high (or low) value of what he is measuring appears and also try to link it to a known process. It is also important to know the value of  $\sigma$ , for its value can help in assessing the significance of the outlier. In fact, a very small value of  $\sigma$  could mean that outliers are not significant. In Figure 2.7 normalised residuals of Figure 2.5 are shown. Three evident outliers can be noticed, that were introduced on purpose in the time series at the beginning of the analysis. A small, fourth outlier is also present but is only due to the statistics, since the time series has a length of approximately 1000 points.

### 2.4.4 DFA

The persistence of the residuals is finally inspected. Global persistence is evaluated by means of Detrended Fluctuation Analysis (DFA) [50], a method that aims at studying the scaling properties of a time series, i.e. its self-similarity, in terms of its fluctuations. It is known that self-similarity is exhibited by many physical [51, 52, 53, 54, 55, 56, 57, 58, 59, 60, 61, 62, 63, 64, 65, 66] and economic systems [67, 68, 69, 70, 71, 72, 73], where DFA has been widely applied. Fluctuations are computed at different time scales and are expected to scale exponentially, with the exponent expressing the self-similarity properties of the time series. DFA procedure is as follows. The mean  $\langle X \rangle$  is first subtracted from the residuals, which are secondly integrated, obtaining a new time series  $Y_t$ ,

$$Y_t = \sum_{t'=1}^t [X_{t'} - \langle X \rangle] \quad (2.42)$$

Subtraction of the mean is compulsory if  $\langle X \rangle$  is not zero [74], otherwise the inte-

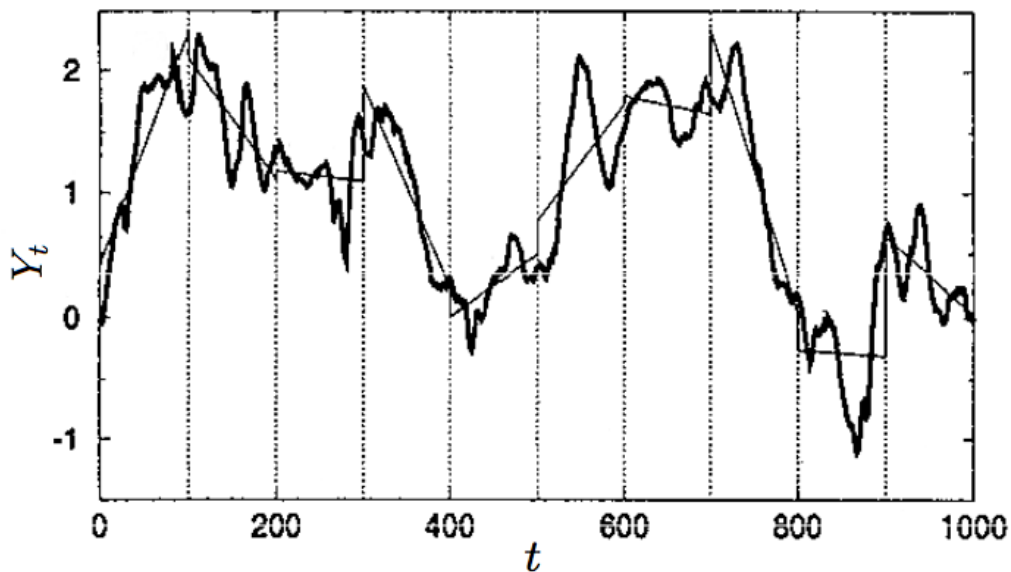


Figure 2.8: Integrated time series  $Y_t$ , divided in intervals of length  $n = 100$ . In each interval the time series is fitted with a least squares line  $Y_t^{fit}$ . Figure can be found in [76].

grated time series could only increase or decrease. Instead, the integration makes the physical process unbounded. Since in a self-similar process the fluctuations grow with the time window size in a power-law way, the fluctuations on large observation windows are exponentially larger than those of smaller windows, and the time series is unbounded. However, physical processes are bounded and cannot have arbitrarily large amplitudes no matter how long the data set is. Integration transforms the time series from a bounded to an unbounded process. One well-

known physical example is the dynamics of Brownian motion. In this case, the random force (noise) acting on particles is bounded, while the trajectory (an integration of all previous forces) of the Brownian particle is not bounded and exhibits properties that can be quantified by a self-similarity parameter.

$Y_t$  is then divided into  $N_n = \lfloor N/n \rfloor$  non-overlapping time intervals of length  $n$ . Since the length of the time series is often not a multiple of  $n$ , some data at the end of  $Y_t$  could be excluded. In order to not neglect them, the same procedure is repeated starting from the end of the integrated time series [75], and the total number of time intervals amounts to  $2N_n$ . The data in each interval  $s$  are fitted with a least squares line  $Y_s^{fit}$  (see Figure 2.8), and the variance is computed,

$$F^2(n, s) = \frac{1}{n} \sum_{i=1}^n [Y((s-1)n+i) - Y_s^{fit}(i)]^2 \quad (2.43)$$

for  $s = 1, \dots, N_n$ , and

$$F^2(n, s) = \frac{1}{n} \sum_{i=1}^n [Y(N - (s - N_n)n + i) - Y_s^{fit}(i)]^2 \quad (2.44)$$

for  $s = N_n + 1, \dots, 2N_n$ .  $Y_s^{fit}$  could also be a higher-order polynomial, as in Hu et al. [77], where they inspected the effects of trends on DFA. Since the residuals have already been detrended and periodicities have been removed, for the analysis regarding this thesis a straight line fit is employed.

The root mean square fluctuation  $F(n)$  is computed then for different  $n$  averaging over all the time intervals with the same length  $s$ ,

$$F(n) = \left[ \frac{1}{2N_n} \sum_{s=1}^{2N_n} F^2(n, s) \right]^{1/2} \quad (2.45)$$

If  $n = \mathcal{O}(N)$ , few time intervals constitute the average in Equation (2.45), leading to unreliable results. Thus, a maximum value less than or equal to  $N/4$  for  $n$  is often chosen [78]. On the other side, very small values of  $n$  introduce a bias in the fit of Equations (2.43) and (2.44). In this thesis, a minimum value of  $n = 10$  has been chosen.

The exponential scaling of the fluctuations is inspected in a log-log plot of  $\ln(F(n))$  versus  $\ln(n)$ , by means of a straight line fit.  $F(n)$  is expected to scale as  $n^H$ ,  $H$  being the Hurst exponent. It varies between 0.0 and 1.5, and it characterise the time series behaviour depending on its value:

- $0.0 < H < 0.5 \rightarrow$  anti-correlation, i.e. the process under study is anti-persistent and tends to show a decrease in values following a previous increase. An anti-persistent process appears very noisy;
- $H = 0.5 \rightarrow$  white noise;

- $0.5 < H < 1.0 \rightarrow$  positive correlation, i.e. the process under study is persistent. If the time series has been increasing (decreasing) for a period  $t$ , then it is expected to continue to increase (decrease) for a similar period. Persistent processes show then long-range correlations and exhibit relatively little noise;
- $H = 1.0 \rightarrow$  pink noise (i.e. power spectrum going as the inverse of the frequency);
- $H > 1.0 \rightarrow$  the time series is non-stationary and stronger long-range correlations are present.  $H = 1.5$  corresponds to brownian noise.

The slope of the fitted line could be not always the same, meaning that the time series has different scaling properties if seen at different time scales. The fit then determines the scaling properties of the residuals at different time scales.

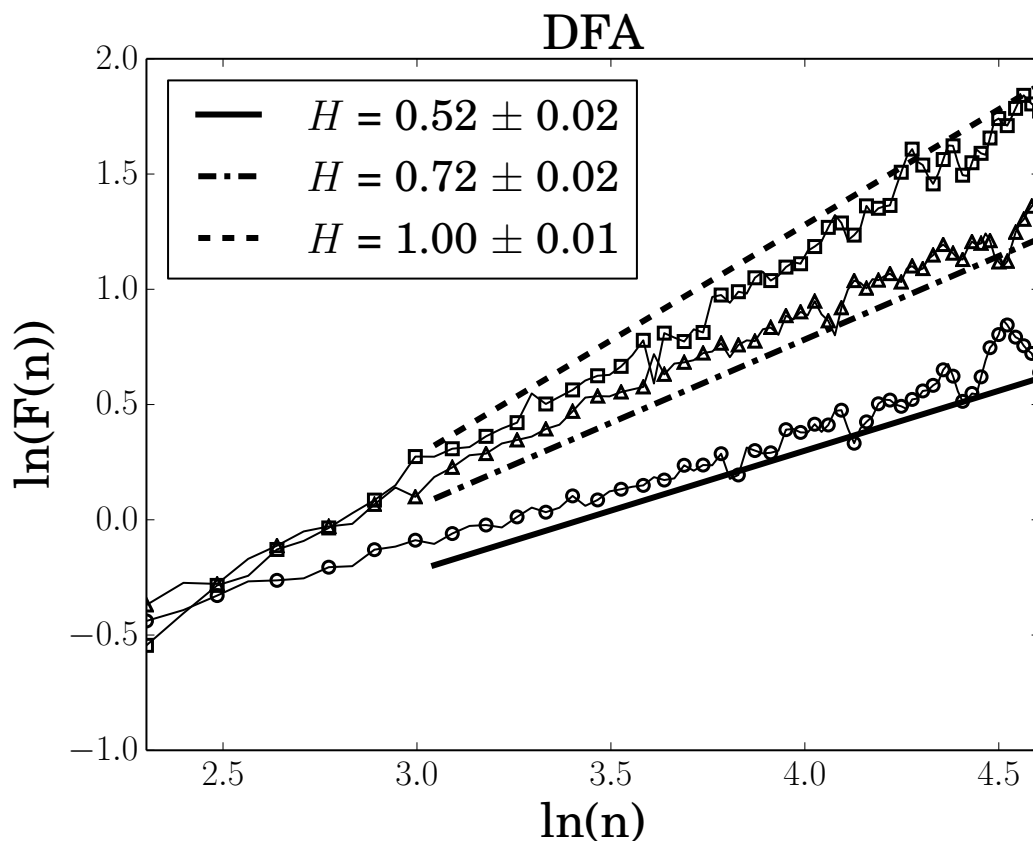


Figure 2.9: Detrended Fluctuations Analysis (DFA) for the residuals of three synthetic time series with the same terms  $T_t$  and  $S_t$ . The stochastic term  $N_t$  is different: white noise ( $\circ$ ), stochastic process with  $H = 0.75$  ( $\triangle$ ), and pink noise ( $\square$ ). The three lines represent the best fit and their slope gives the value of the Hurst exponent.

Three different synthetic time series have been simulated, with the same periodicities found previously but with three different stochastic terms, white noise, pink noise, and a stochastic process with  $H = 0.75$  respectively. Results are shown in Figure 2.9 for the residuals of the three time series, and they are in agreement

with the expected outcomes, except for the residuals with  $H = 0.75$ . The found Hurst exponent is  $H = 0.72 \pm 0.02$  and is slightly underestimated, but it should be remembered that simulations only approximate the stochastic process, due to its finite size [79].

### 2.4.5 Local Hurst

The Hurst exponent can also vary within the time series, that is it can change over time, and a local Hurst exponent  $H_t$  can be defined. To compute  $H_t$ , Multifractal Detrended Fluctuation Analysis (MFDFA) [75], a generalisation of Detrended Fluctuations Analysis, must be introduced first. The procedure is the same for DFA: First, Equations (2.43) and (2.44) are computed. Then, an average over all intervals is computed at various orders  $q$ ,

$$F_q(n) = \left[ \frac{1}{2N_n} \sum_{s=1}^{2N_n} [F^2(n, s)]^{q/2} \right]^{1/q} \sim n^{h(q)} \quad (2.46)$$

Comparing Equations (2.45) and (2.46), it is straightforward that DFA is MFDFA with  $q = 2$ , and  $h(2) = H$ . Finally,  $h(q)$  is determined by analysing the log-log plot of  $\ln(F_q(n))$  versus  $n$ , for each value of  $q$ .  $q$  can take any real value. For positive  $q$ , time intervals  $s$  with a large variance  $F^2(n, s)$  will dominate the average in Equation (2.46). Thus, for positive values of  $q$ ,  $h(q)$  describes the scaling behaviour of time intervals with large fluctuation. Instead, for negative values of  $q$ , time intervals with small variance  $F^2(n, s)$  will dominate the average  $F_q(n)$ . Hence, for negative values of  $q$ ,  $h(q)$  describes the scaling behaviour of time intervals with small fluctuations.  $h(q)$  for  $q < 0$  is usually larger than  $h(q)$  for  $q > 0$ . As a matter of fact, for the maximum scale  $n = N$  the fluctuation function  $F_q(n)$  is independent of  $q$  since the sum in Equation (2.46) runs over only two identical segments ( $N_n = 1$ ). For smaller scales  $n \ll N$ , the averaging procedure runs over several segments, and the average value  $F_q(n)$  will be dominated by the  $F^2(n, s)$  from the segments with small (large) fluctuations if  $q < 0$  ( $q > 0$ ). Thus, for  $n \ll N$ ,  $F_q(n)$  will be smaller than  $F_q(n)$  with  $q > 0$ , while both become equal for  $n = N$ . Hence, if we assume a homogeneous scaling behaviour of  $F_q(n)$ , the slope  $h(q)$  in a log-log plot of  $F_q(n)$  with  $q < 0$  versus  $n$  must be larger than the corresponding slope of  $F_q(n)$  with  $q > 0$ . Thus,  $h(q)$  for  $q < 0$  will usually be larger than  $h(q)$  for  $q > 0$ .

For  $q = 0$  Equation (2.46) is divergent and can be replaced by an exponential of a logarithmic sum

$$F_0(n) = \exp \left[ \frac{1}{4N_n} \sum_{s=1}^{2N_n} \ln(F^2(n, s)) \right] \sim n^{h(0)} \quad (2.47)$$

If  $h(q)$  is approximately constant for all the values of  $q$ , the time series is said to be monofractal, i.e. it exhibits the same scaling at all scales. Instead, if  $h(q)$  varies significantly, the time series is multifractal, i.e. it exhibits different scaling at different scales [80, 81].

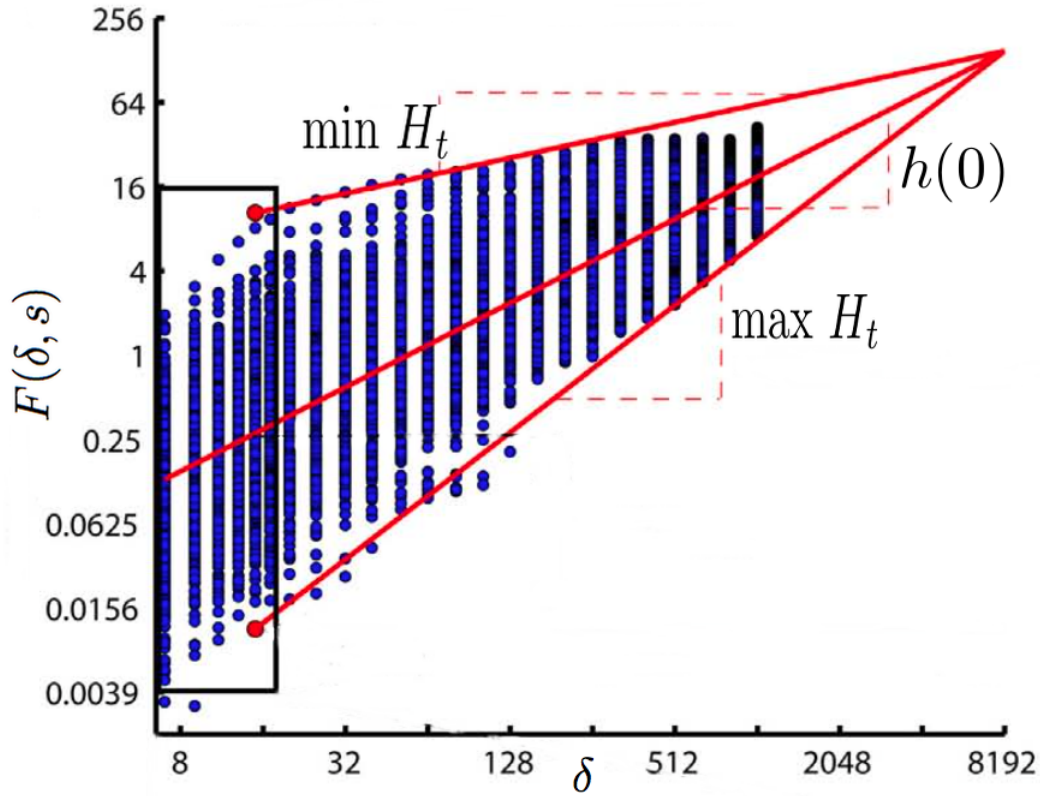


Figure 2.10:  $F(\delta, s)$  vs  $\delta$ . Every column of blue dots represents the value of the root mean square fluctuation computed in an interval of fixed length  $n$ . The local Hurst exponent is obtained from the slope of the line connecting each blue dot to  $F_q(N)$ , represented by the intersection point of the three red lines. Figure can be found in [82].

Following Ihlen [82], a local Hurst exponent  $H_t$  can now be defined. When  $n$  is equal to the total length of the time series  $N$ , Equation (2.46) is independent of  $q$ , and the value of  $F_q(N)$  is thus the same for all the orders  $q$ . Time series can be divided into small time intervals of length  $\delta$  (to appreciate variations of  $H_t$  on a small scale) and the square root of Equation (2.43) can be computed in order to obtain the values of the fluctuations as a function of time, i.e. in each small time window (Figure 2.10). However, this time the time intervals overlap, spanning the whole time series, and the fluctuations in every window are given by

$$F(\delta, s) = \sqrt{\frac{1}{\delta} \sum_{i=1}^{\delta} [Y((s-1) + i) - Y_s^{fit}(i)]^2} \quad (2.48)$$

with  $s = 1, \dots, N - \delta + 1$  the number of the time interval. Then, each value of the fluctuations and the value of  $F_q(N)$  can be connected with a straight line to obtain the local Hurst exponent  $H_t$  as the slope of the line [82], i.e. the Hurst exponent for a single time window.  $H_t$  expresses the behaviour of the correlations within the time series during the time. In Figure 2.11, the local Hurst exponent  $H_t$  for the residuals of three synthetic time series with the same terms  $T_t$  and  $S_t$  is presented. The stochastic term  $N_t$  is different for the three cases and corresponds to pink noise (top), a stochastic process with  $H = 0.75$  (middle), and white noise (bottom) respectively.  $H_t$  fluctuates as expected around the simulated  $H$ , for all the three cases.

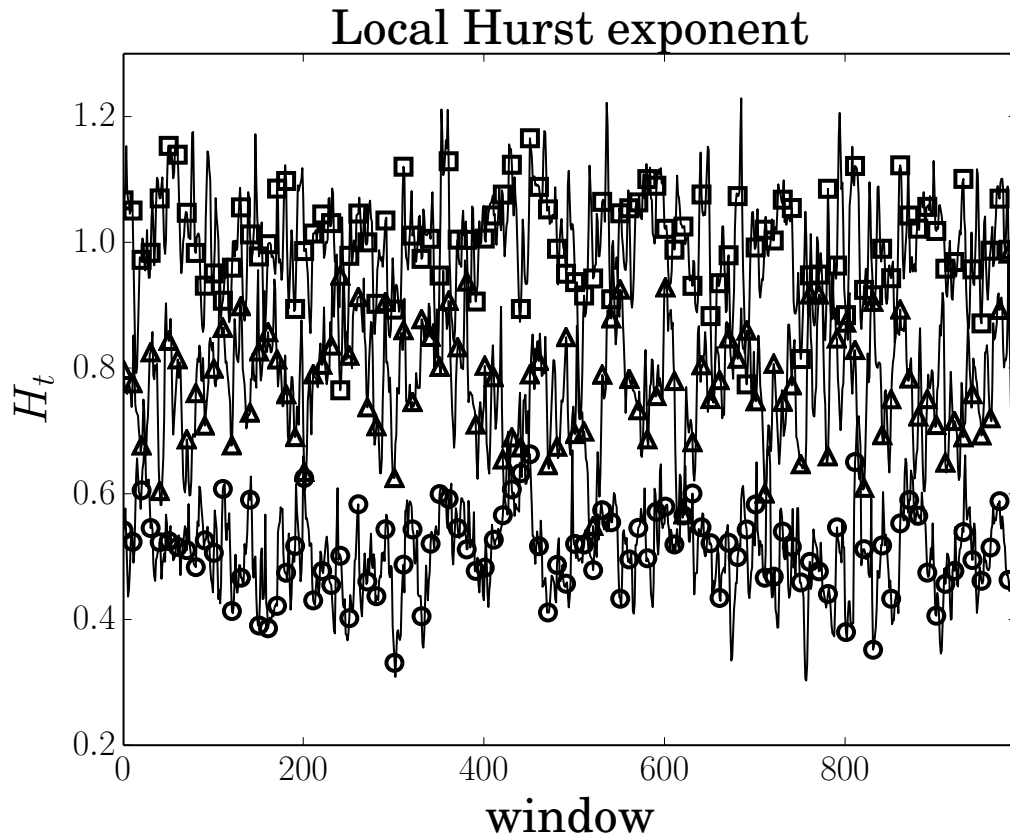


Figure 2.11: Local Hurst exponent  $H_t$  for the residuals of three synthetic time series with the same terms  $T_t$  and  $S_t$ . The stochastic term  $N_t$  is different: white noise ( $\circ$ ), stochastic process with  $H = 0.75$  ( $\triangle$ ), and pink noise ( $\square$ ).  $H_t$  fluctuates as expected around the simulated  $H$ , for all the three cases.

Finally, the Hurst exponent is also linked to the coefficient  $\beta$  that defines the kind of noise from the slope of the power spectrum [83]

$$P(\nu) \sim 1/\nu^\beta \quad (2.49)$$

by means of the relation

$$\beta = 2H - 1 \quad (2.50)$$

Thus, from the evolution of  $H_t$ , the evolution of noise coefficient  $\beta_t$  can also be recovered.

## 2.5 Detrended Cross-Correlation Analysis

Similar to DFA, Detrended Cross-Correlation Analysis (DCCA) can be employed to detect long-range correlations between two different time series  $x$  and  $y$ . Even if DCCA is not in the flowchart of Figure 2.1, as it requires two different time series to be employed, it is described here and will be used in Chapter 3 to find correlations between Beryllium 7 and meteorological parameters' residuals time series.

Provided the two series have the same length  $N$ , they are first integrated and then divided into  $N - n$  overlapping windows, each containing  $n + 1$  values [84]. The difference with DFA is that now the time windows can overlap, resulting in a higher number of points for the final fluctuation function at fixed scale. The same detrending procedure for the DFA is applied to both time series in each window, and the covariance is defined as

$$F_{xy}^2(n, i) = \frac{1}{n-1} \sum_{k=i}^{n+i} (Y_{xi} - Y_{xi}^{fit})(Y_{yi} - Y_{yi}^{fit}) \quad (2.51)$$

Finally, the detrended covariance is calculated summing over all the overlapping  $N - n$  windows of size  $n$ ,

$$F_{xy}^2(n) = \frac{1}{N-n} \sum_{i=1}^{N-n} F_{xy}^2(n, i) \quad (2.52)$$

with subscript  $x$  and  $y$  referring to the  $x$  and  $y$  time series, respectively. In a log-log plot of  $F_{xy}^2(n)$  versus  $n$ , the slope of the fitted line provides just a global characterisation of persistence [85, 86]. Equation (2.52) is computed for different  $n$ , and a cross-correlation coefficient (ranging between -1.0 and +1.0) can be defined this way [87, 88, 89, 90, 91, 92],

$$\rho_{DCCA}(n) = \frac{F_{xy}^2(n)}{F_{xx}(n)F_{yy}(n)} \quad (2.53)$$

Similar to standard cross-correlation coefficient,  $\rho_{DCCA} = 1.0$  indicates a perfect cross-correlation, while  $\rho_{DCCA} = -1.0$  means a perfect anti cross-correlation. If  $\rho_{DCCA} = 0.0$ , there is no cross-correlation between the two different time series. The cross-correlation coefficient depends on the time scale  $n$ , thus correlations could not be the same at all the time scales.  $\rho_{DCCA}$  can, therefore, identify where high or low correlation events occur.

---

## $^7\text{Be}$ worldwide time series analysis

---

In this Chapter, the analysis of all the available  $^7\text{Be}$  time series is presented. First, a modification of the algorithm of Chapter 2 is needed, because of the unavoidable presence of missing data in real-life time series. Then, time series suitable for the analysis are selected, and results are shown in detail station by station.

The main purpose of the analysis is to highlight differences and similarities between records of the same variable in different places of the world. It has been here applied to  $^7\text{Be}$ , but examples of applications to other observables will be described in the appendices. All the mathematical tools delineated in Chapter 2 have been written both in Matlab and Python code, and a software provided with a graphic user interface has been developed, for both the two languages.

### 3.1 Missing data

Mostly due to instruments' failures, missing data are an unavoidable feature of geophysical time series. Conversely, all the mathematical tools presented in Chapter 2 (with the exception of the generalised Lomb-Scargle spectrum, Equation (2.25)) have been developed not taking into account the possibility of unevenly sampled data. Thus, their modification is needed to perform the analysis.

For the detrending procedure with empirical mode decomposition, missing data are first interpolated with the nearest neighbour algorithm. At the end of the procedure, missing data are restored and values of the trend in correspondence of the missing data's original position are removed. The same interpolation is applied in the filter procedure to obtain the residuals time series since an inverse generalised Lomb-Scargle spectrum does not exist. For the Detrended Fluctuation Analysis instead, the problem arises when a time window contains missing data. A linear fit has to be performed, and it could be not accurate in the presence of too many or

too wide gaps. So, the value of the variance (2.43) or (2.44) is discarded if one-fifth of the data or more are missing data. It has to be noticed that this limit has been chosen arbitrarily. Obviously, the same applies to the local Hurst exponent and to the Detrended Cross-Correlation Analysis.

### 3.2 Data pre-processing

Time series of  $^7\text{Be}$  at the IMS stations are recorded daily and measured in  $\mu\text{Bq}/\text{m}^3$ . Every station also comes with daily meteorological parameters: relative humidity (%), temperature ( $^{\circ}\text{C}$ ), barometric pressure ( $\text{Pa}$ ), wind direction (degrees from the north,  $0^{\circ}$ - $360^{\circ}$ , clockwise), wind speed ( $\text{m}\cdot\text{s}^{-1}$ ) and precipitation ( $\text{mm}$ ). Precipitation has not been considered in this thesis.

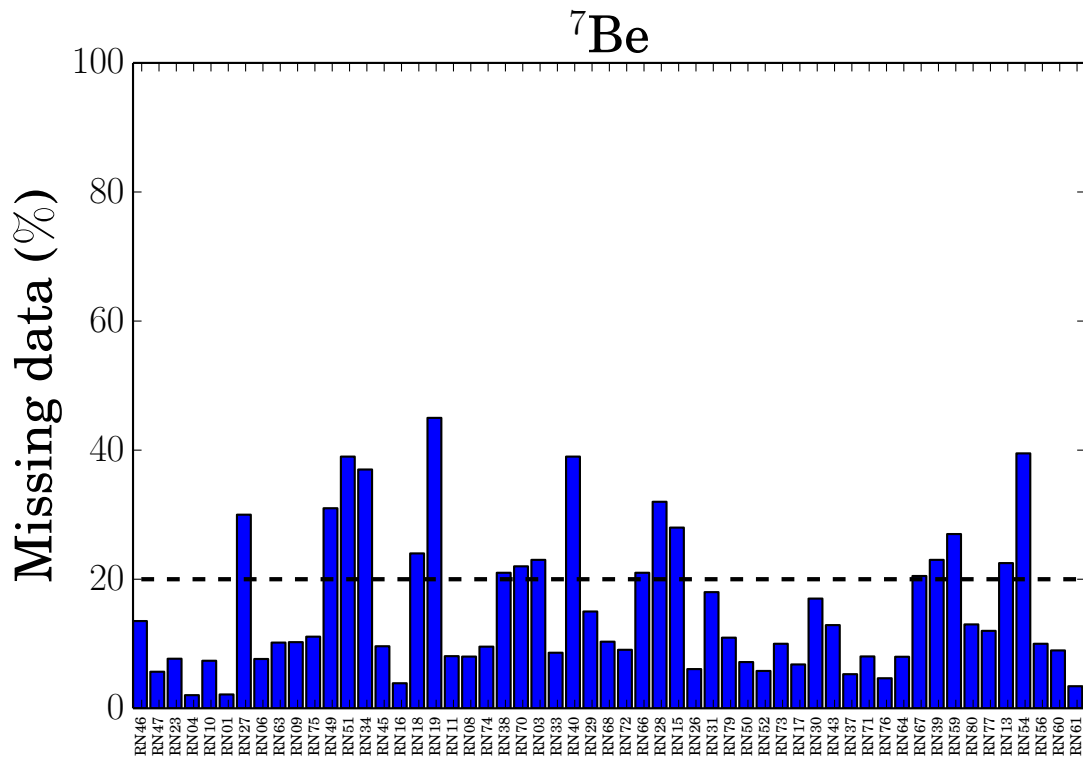


Figure 3.1: Total percentage of  $^7\text{Be}$  missing data in every station. The horizontal dashed line is the arbitrary threshold of 20% chosen for selecting the stations.

Before starting the analysis, data must be pre-processed, in order to remove spurious values. For instance, referring to Table 1.1, values of  $^7\text{Be}$  with a total air volume less than  $10800 \text{ m}^3$  ( $500 \text{ m}^3\text{h}^{-1}$  of airflow  $\times 24 \text{ h}$  of collection time) are replaced by a gap, in order to satisfy minimum requirements of the IMS stations. For what concerns meteorological parameters, values outside the physical bounds have been removed. Subsequently, stations with more than 20% of total missing data have been discarded. This limit is arbitrary but is chosen to have better results. Indeed, modified algorithms for the analysis and even the GLS spectrum can

be implemented even in the presence of too many or too wide gaps, but results will not be accurate. The total percentage of missing data in every station is shown in Figure 3.1. Time series with less than 20% of missing data have been then visually inspected in order to verify the suitability for the analysis. Five stations have been discarded among those with a percentage of missing data less than 20%: RN29 and RN73, for they had a gap of approximately six-months width; RN31 and RN30, for they had a gap of approximately one-year width; RN56, for its length is less than one year. Time series with wide gaps have not been considered since too much information is lost, while very short time series have not been considered as too little information is present in the data. Table 3.1 lists the stations employed for the analysis, along with the latitude and longitude coordinates. Once  $^7\text{Be}$  time

ID	Location	Latitude [ $^{\circ}N$ ]	Longitude [ $^{\circ}E$ ]
RN46	Chatham Island, New Zealand	-43.82	176.48
RN47	Kaitaia, New Zealand	-35.07	173.29
RN23	Rarotonga, Cook Islands	-21.20	-159.81
RN04	Melbourne, VIC, Australia	-37.73	145.10
RN10	Perth, WA, Australia	-31.93	115.98
RN01	Buenos Aires, Argentina	-34.54	-58.47
RN06	Townsville, QLD, Australia	-19.25	146.77
RN63	Stockholm, Sweden	59.41	17.95
RN09	Darwin, NT, Australia	-12.43	130.89
RN75	Charlottesville, VA, USA	38.00	-78.40
RN45	Ulaanbaatar, Mongolia	47.89	106.33
RN16	Yellowknife, N.W.T., Canada	62.48	-114.47
RN11	Rio de Janeiro, Brazil	-22.99	-43.42
RN08	Cocos Islands, Australia	-12.19	96.83
RN74	Ashland, KS, USA	37.17	-99.77
RN33	Schauinsland/Freiburg, Germany	47.92	7.91
RN68	Tristan da Cunha, United Kingdom	-37.07	-12.31
RN72	Melbourne, FL, USA	28.10	-80.65
RN26	Nadi, Fiji	-17.76	177.45
RN79	Oahu, Hawaii, USA	21.52	-157.99
RN50	Panama City, Panama	8.98	-79.53
RN52	Tanay, Philippines	14.58	121.37
RN17	St. John's, N.L., Canada	47.59	-52.74
RN43	Nouakchott, Mauritania	18.14	-15.92
RN37	Okinawa, Japan	26.50	127.90
RN71	Sand Point, Alaska, USA	55.34	-160.49
RN76	Salchaket, Alaska, USA	64.67	-147.10
RN64	Dar Es Salaam, Tanzania	-6.78	39.20
RN60	Petropavlovsk, Russian Federation	53.05	158.78
RN61	Dubna, Russian Federation	56.74	37.25

Table 3.1: Stations' ID and their exact location.

series are selected, the percentage of missing data is computed for the meteorological parameters' time series. Figure 3.2 shows the percentage of missing data for the meteorological parameters corresponding to the selected Beryllium 7 stations. Time series with over 20% of missing data have not been considered, hence not every <sup>7</sup>Be time series can be compared to all the meteorological parameters when the detrended cross-correlation coefficient is computed. Moreover, since meteorological parameters are not of primary interest for the IMS, their time series can sometimes be of poor quality [93], and even if their percentage of missing data is below 20%, they have not been analysed. Examples of meteorological time series not suitable for the analysis are shown in Figure 3.3, for wind speed (RN01), humidity (RN50), and wind direction (RN52).

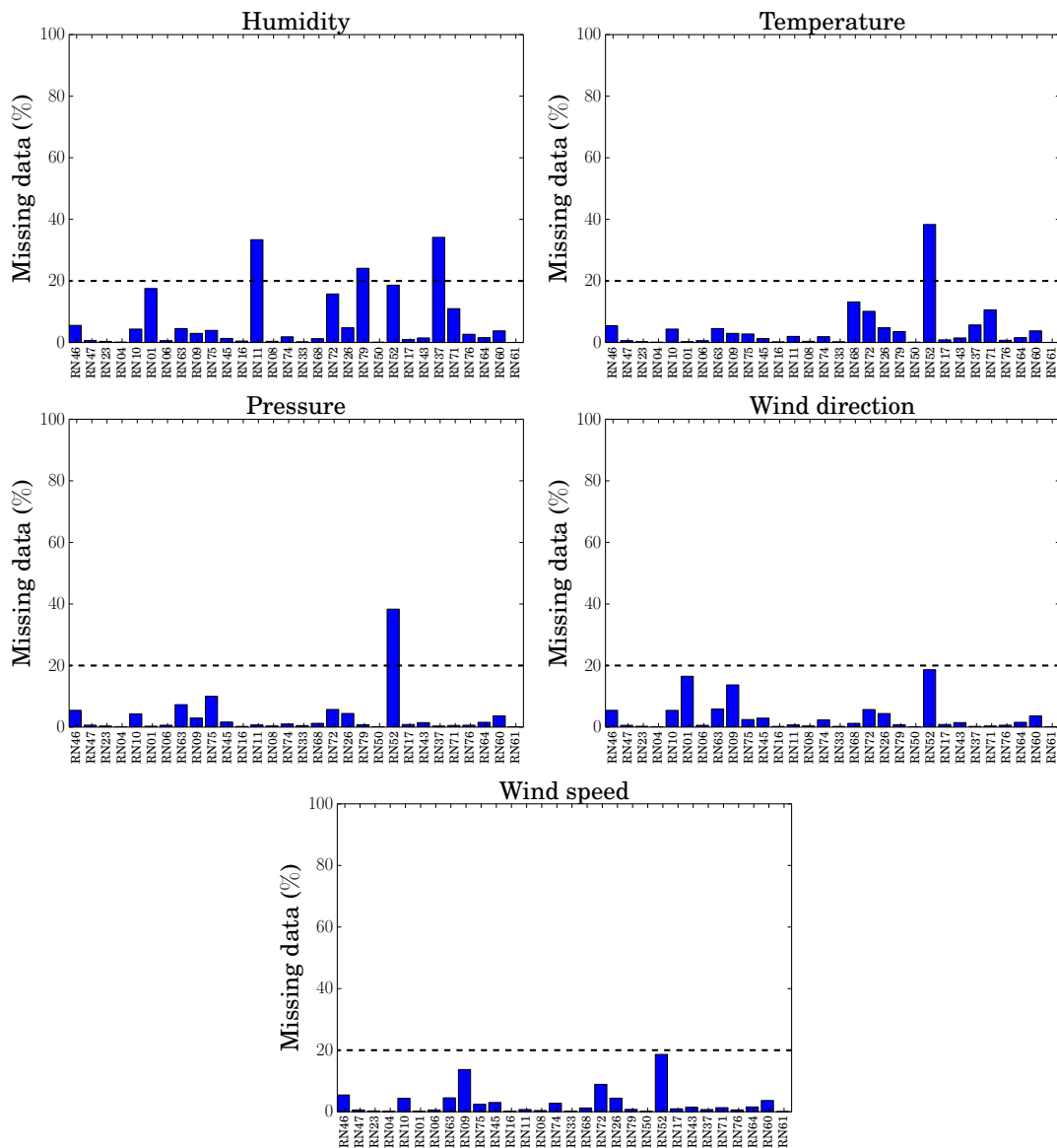


Figure 3.2: Total percentage of meteorological parameters' missing data in every station. The horizontal dashed line is the arbitrary threshold of 20% chosen for selecting the stations.

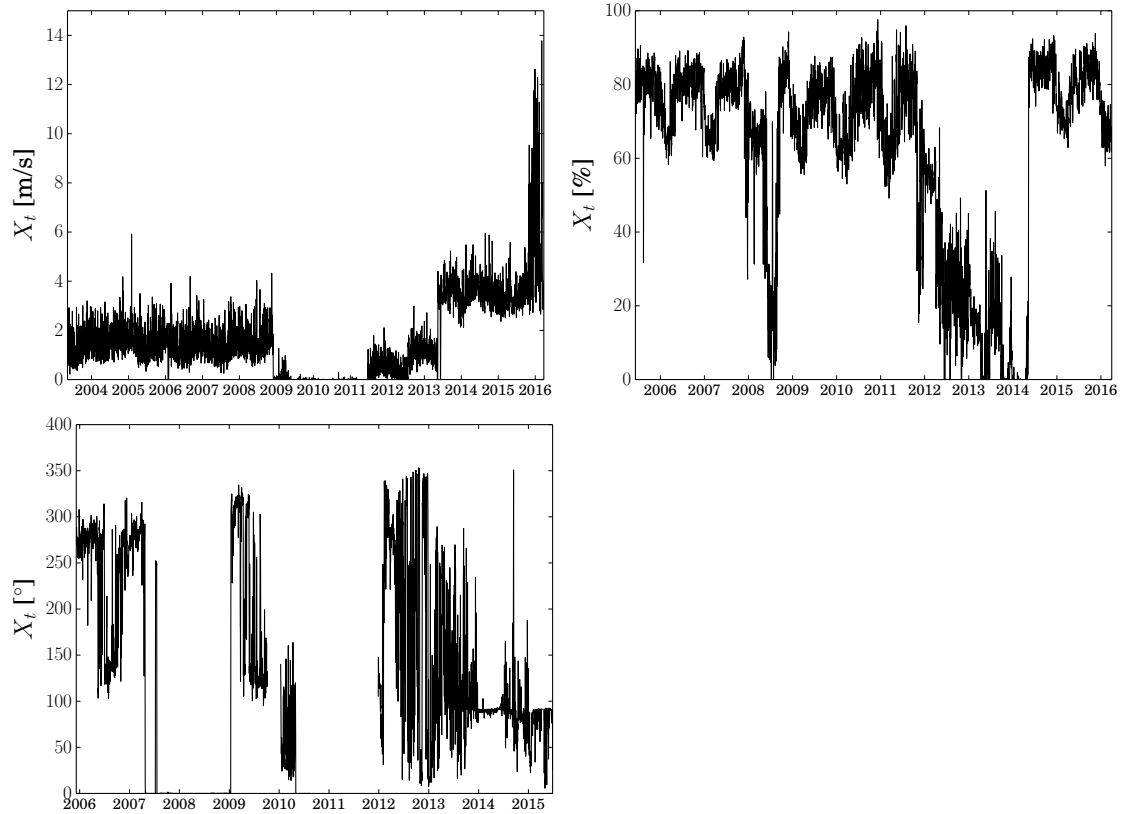


Figure 3.3: Examples of poor quality time series of meteorological parameters: wind speed (top left, station RN01), humidity (top right, station RN50), and wind direction (bottom, station RN52).

### 3.3 Analysis of ${}^7\text{Be}$ time series

The analysis is here presented in details, showing the results individually for each of the selected stations. Besides what described in Chapter 2, the analysis has been also performed dynamically. First, the initial year of data of the time series is analysed. Then, a year of data is added and the analysis is performed again, and so on until the total length of the time series is reached. Thus, the variability of the percentage weight of the annual periodicity (the most prominent in the spectrum) can be evaluated.

The following figures will be shown for each station: Time series with trend superimposed, GLS spectrum, normalised residuals, the histogram of the residuals, DFA, local Hurst exponent for a time window of two weeks, dynamics of the one-year harmonic percentage weight, and the detrended cross-correlations with available meteorological parameters. Moreover, tables of periodicities and outliers are shown.

### 3.3.1 Chatham Island, New Zealand (RN46)

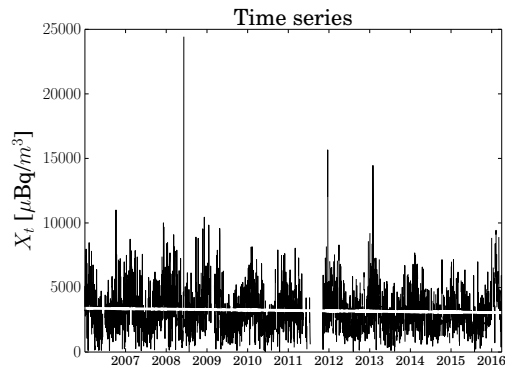


Figure 3.4: Time series with trend superimposed (solid white line).

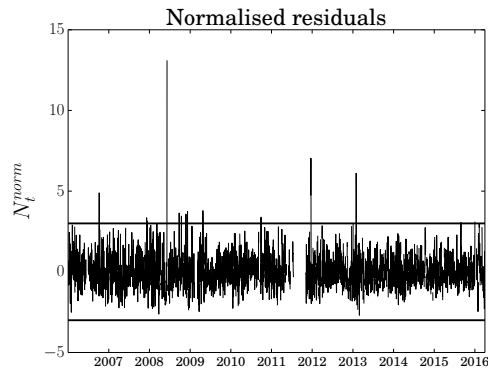


Figure 3.5: Normalised residual time series with the  $\pm 3\sigma$  thresholds (solid black lines).

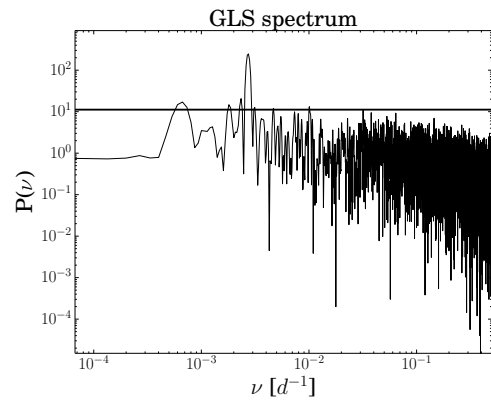


Figure 3.6: Log-log plot of the GLS spectrum with the associated threshold (solid black line).

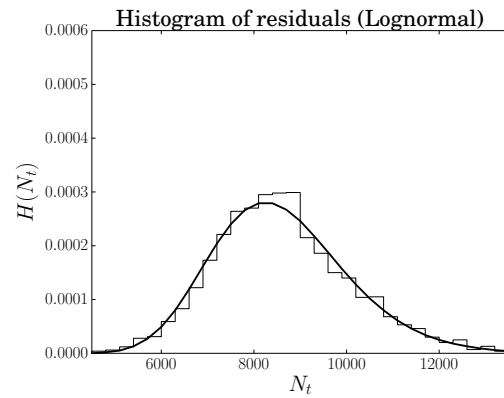


Figure 3.7: Histogram of residuals with the best-fitting distribution (no outliers).

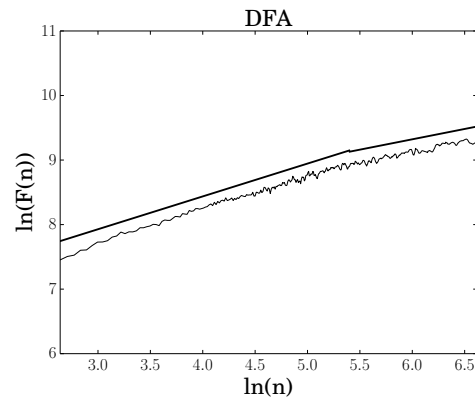


Figure 3.8: Detrended fluctuation analysis. The solid black lines are the best fit at different scales.

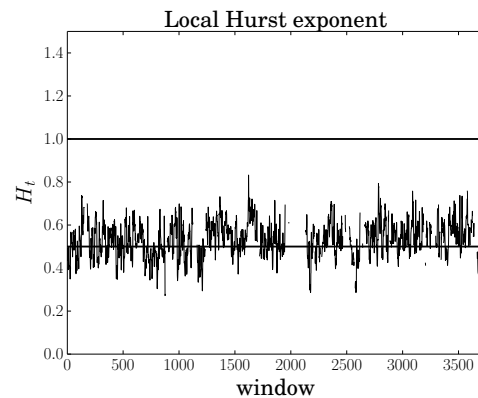


Figure 3.9: Local Hurst exponent  $H_t$  for a time window of two weeks. Solid lines represent the values of pink noise (top) and white noise (bottom).

Periodicity	Percentage
3 months	1.11
6 months	0.50
1 year	13.17
1.5 years	0.62
4 years	0.85

Table 3.2: Periodicities as frequencies corresponding to peaks in the spectrum higher than the threshold.

Value	Date
4.890	2006/10/07
13.075	2008/06/07
4.767	2011/12/20
7.041	2011/12/21
6.106	2013/01/30
4.623	2013/01/31

Table 3.3: Outliers as values in the normalised residuals greater (less) than + (-)  $3\sigma$ . Only very high or very low outliers are listed.

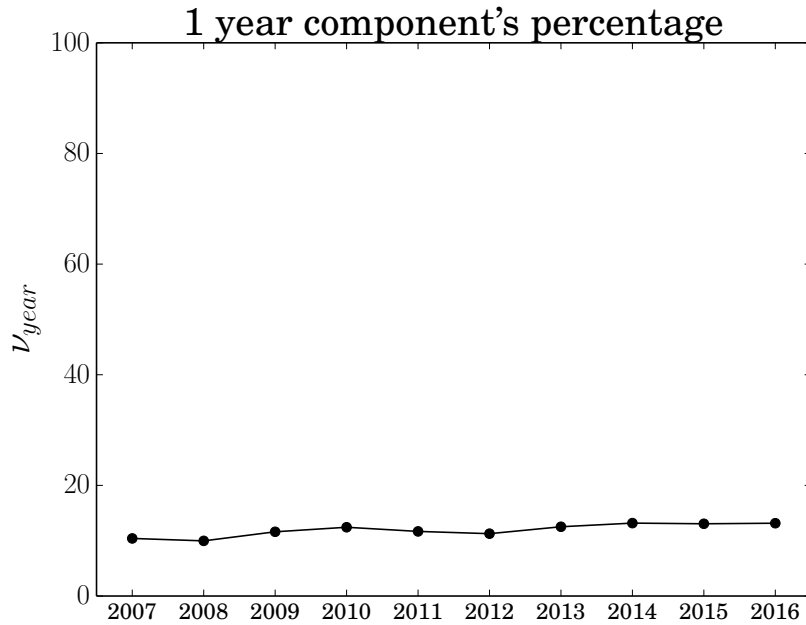


Figure 3.10: Dynamic analysis of the percentage of the one-year periodicity.

Station RN46 exhibits a predominant periodicity of one year, with a percentage weight of 13.17%, much higher than the other periodicities. The trend is linear and data are approximately regular except for a period in the second half of 2011. Three very high outliers occur in the residual time series, with values of  $\sim 6, 7, 13\sigma$  respectively. Residuals without outliers are best described by a Lognormal distribution. From DFA plot, two scaling regimes are found: The first, from 14 days to  $\sim 221$  days, has a Hurst exponent  $H = 0.5087 \pm 0.0032$ ; the second, from  $\sim 221$  days to the end of the series, has a Hurst exponent  $H = 0.3207 \pm 0.0040$ . The different regimes show a change in correlation properties of the residuals, from uncorrelated (white noise) to anti-correlated. This is also an evidence of multifractality. The local Hurst exponent  $H_t$  is computed at a time window of

two weeks and oscillates first around a value compatible with white noise, while tends to assume higher values at the end of the series. The one-year component's percentage does not show great variability and its value remains constant at  $\sim 10\%$  when adding new years.

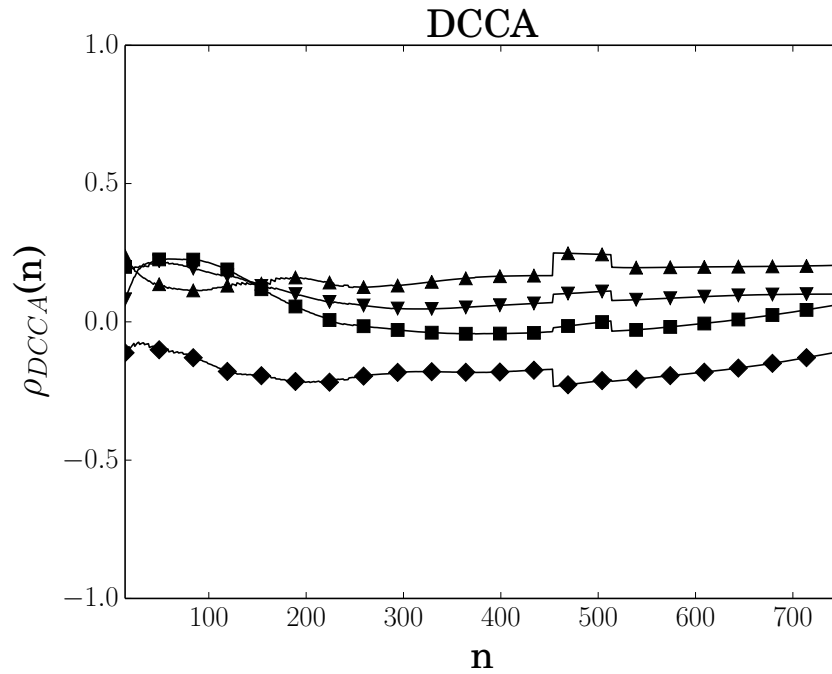


Figure 3.11: Detrended cross correlation between  ${}^7\text{Be}$  and available meteorological parameters (humidity (○), temperature (△), pressure (□), wind direction (▽), and wind speed (◇)).

Station RN46 does not exhibit significant cross-correlations with the available meteorological parameters. Humidity time series was not suitable for the analysis.

### 3.3.2 Kaitaia, New Zealand (RN47)

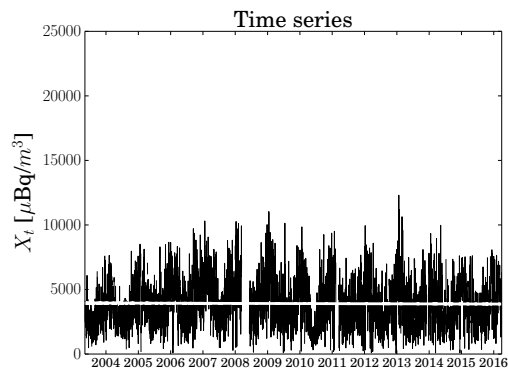


Figure 3.12: Time series with trend superimposed (solid white line).

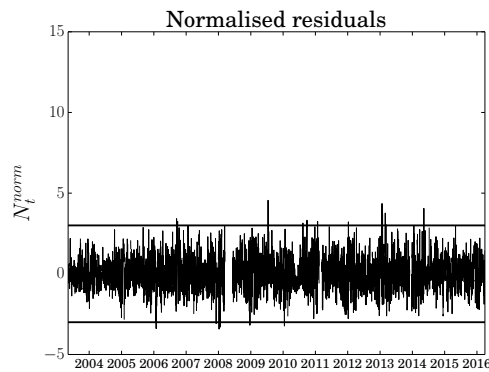


Figure 3.13: Normalised residual time series with the  $\pm 3\sigma$  thresholds (solid black lines).

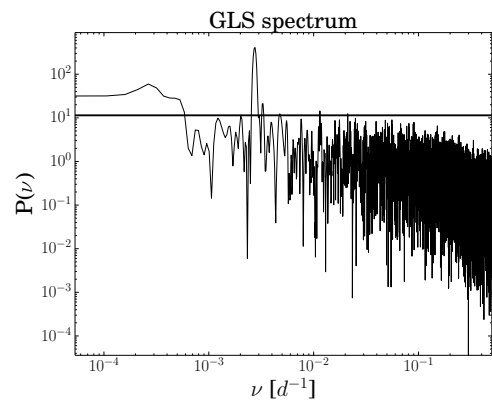


Figure 3.14: Log-log plot of the GLS spectrum with the associated threshold (solid black line).

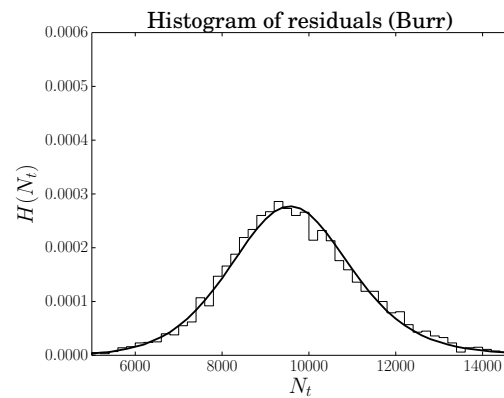


Figure 3.15: Histogram of residuals with the best-fitting distribution (no outliers).

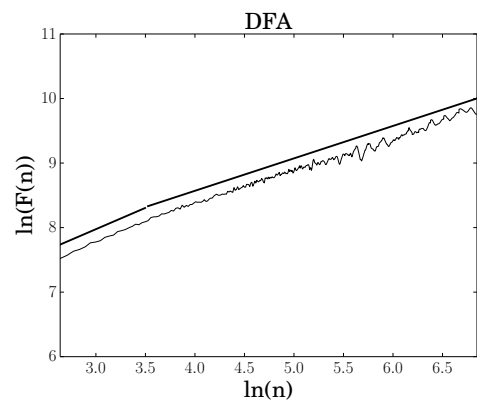


Figure 3.16: Detrended fluctuation analysis. The solid black lines are the best fit at different scales.

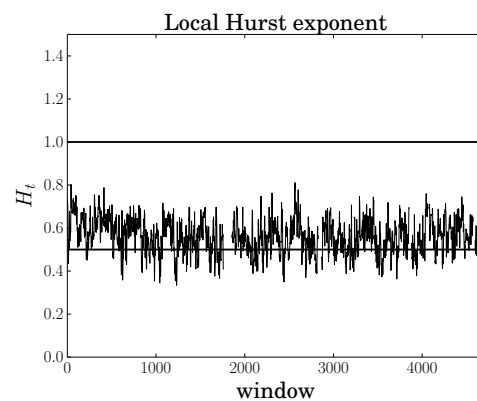


Figure 3.17: Local Hurst exponent  $H_t$  for a time window of two weeks. Solid lines represent the values of pink noise (top) and white noise (bottom).

Periodicity	Percentage	Value	Date
2 months	0.51	4.556	2009/07/15
3 months	0.63	4.356	2013/01/23
6 months	1.08	4.054	2014/05/11
1 year	17.98		
10.5 years	4.03		

Table 3.4: Periodicities as frequencies corresponding to peaks in the spectrum higher than the threshold.

Table 3.5: Outliers as values in the normalised residuals greater (less) than + (-)  $3\sigma$ . Only very high or very low outliers are listed.

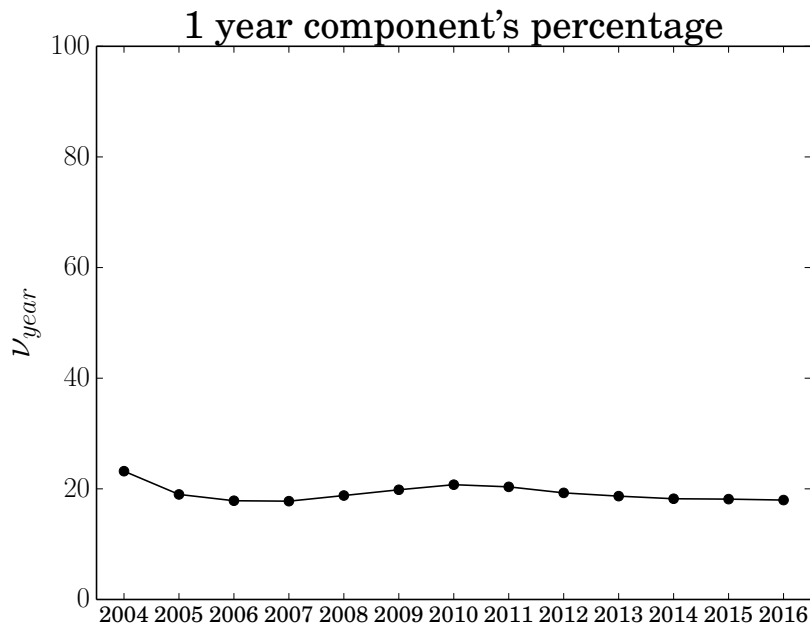


Figure 3.18: Dynamic analysis of the percentage of the one-year periodicity.

Station RN47 exhibits a predominant periodicity of one year, with a percentage weight of 17.98%, much higher than the other periodicities. With a percentage weight of 4.03%, a periodicity of 10.5 years is present and can be associated with the solar cycle. The trend is linear and data are approximately regular except for a period in the second half of 2008. High outliers do not occur in the residual time series, as confirmed by the absence of great variations in the time series. Residuals without outliers are best described by a Burr distribution. From DFA plot, two scaling regimes are found: The first, from 14 days to  $\sim 33$  days, has a Hurst exponent  $H = 0.6604 \pm 0.010$ ; the second, from  $\sim 33$  days to the end of the series, has a Hurst exponent  $H = 0.5025 \pm 0.0024$ . The different regimes show a change in correlation properties of the residuals, from correlated at very small scales to uncorrelated (white noise). This is also an evidence of multifractality. The local Hurst exponent  $H_t$  is computed at a time window of two weeks and

oscillates around a value compatible with long-range correlations ( $\sim 0.6$ ). The one-year component's percentage does not show great variability and its value remains constant at  $\sim 20\%$  when adding new years.

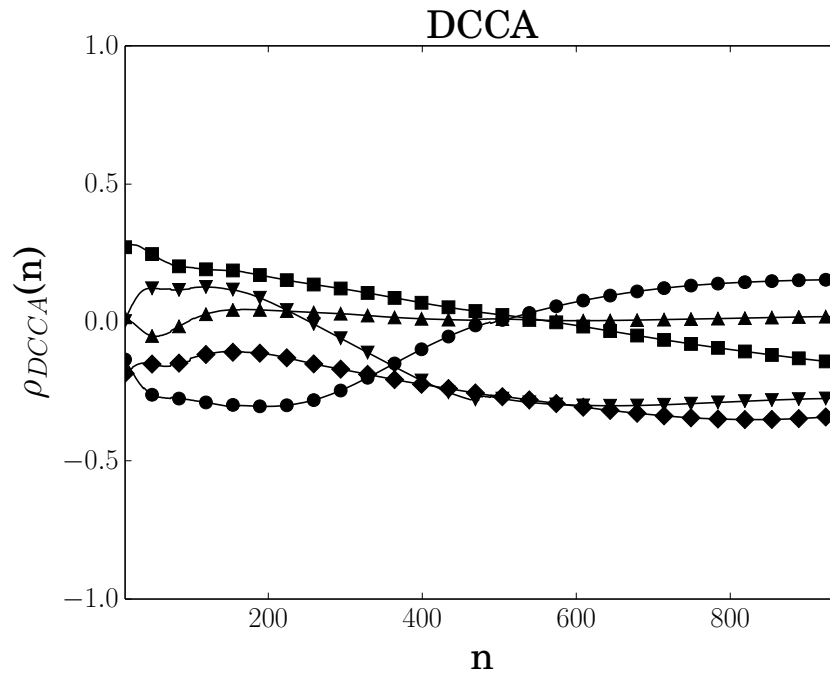


Figure 3.19: Detrended cross correlation between <sup>7</sup>Be and available meteorological parameters (humidity (○), temperature (△), pressure (□), wind direction (▽), and wind speed (◇)).

Station RN47 exhibits negative cross-correlations with humidity at small scales ( $< 200$  days) and positive cross-correlations with pressure at very small scales ( $< 50$  days). There are no cross-correlations with temperature. <sup>7</sup>Be shows instead negative cross-correlations with both wind direction and speed at big scales ( $> 500$  days).

### 3.3.3 Rarotonga, Cook Islands (RN23)

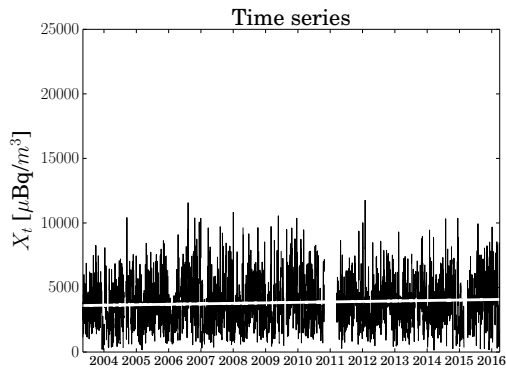


Figure 3.20: Time series with trend superimposed (solid white line).

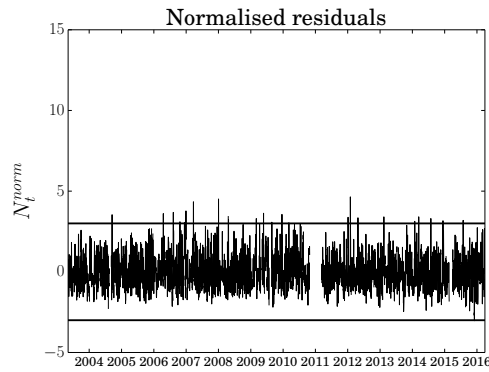


Figure 3.21: Normalised residual time series with the  $\pm 3\sigma$  thresholds (solid black lines).

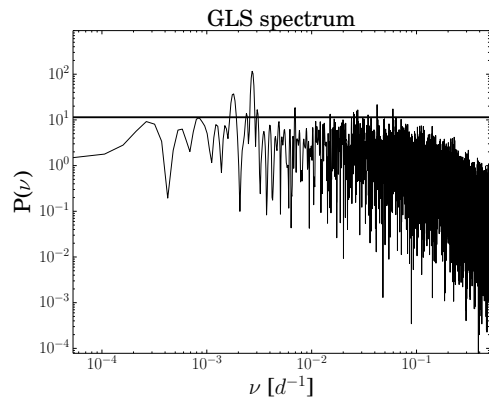


Figure 3.22: Log-log plot of the GLS spectrum with the associated threshold (solid black line).

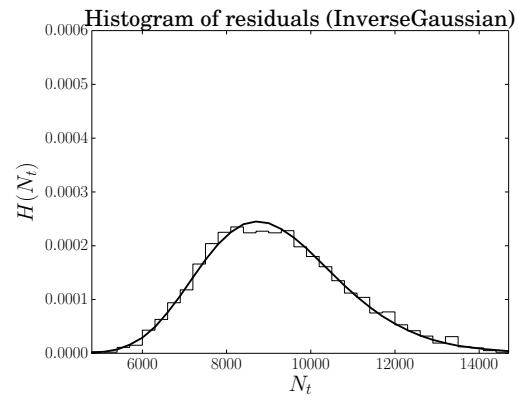


Figure 3.23: Histogram of residuals with the best-fitting distribution (no outliers).

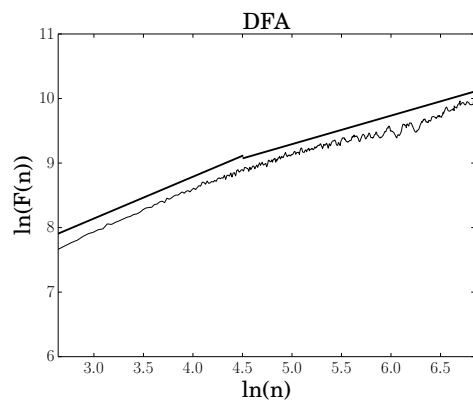


Figure 3.24: Detrended fluctuation analysis. The solid black lines are the best fit at different scales.

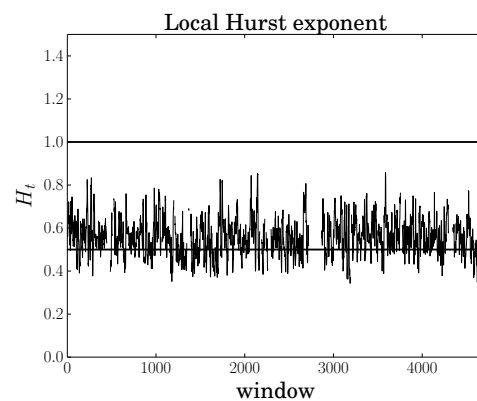


Figure 3.25: Local Hurst exponent  $H_t$  for a time window of two weeks. Solid lines represent the values of pink noise (top) and white noise (bottom).

Periodicity	Percentage	Value	Date
2 weeks	1.39	4.341	2007/03/24
1 month	3.52	4.322	2007/03/25
2 months	0.53	4.514	2008/01/02
4 months	0.68	4.643	2012/01/31
1 year	5.42		
1.5 years	1.62		

Table 3.6: Periodicities as frequencies corresponding to peaks in the spectrum higher than the threshold.

Table 3.7: Outliers as values in the normalised residuals greater (less) than + (-)  $3\sigma$ . Only very high or very low outliers are listed.

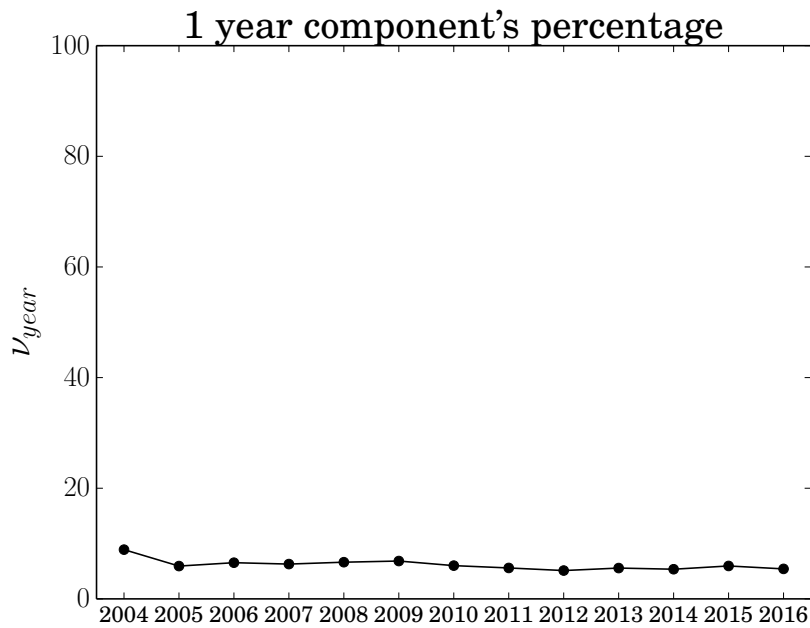


Figure 3.26: Dynamic analysis of the percentage of the one-year periodicity.

Station RN23 exhibits a predominant periodicity of one year, with a percentage weight of 5.42%, comparable with the other periodicities, especially the one-month periodicity. The trend is linear and data are approximately regular except for a period ranging from the end of 2010 and the beginning of 2011. High outliers do not occur in the residual time series, as confirmed by the absence of great variations in the time series. Residuals without outliers are best described by an Inverse Gaussian distribution. From DFA plot, two scaling regimes are found: The first, from 14 days to  $\sim 90$  days, has a Hurst exponent  $H = 0.6477 \pm 0.0051$ ; the second, from  $\sim 90$  days to the end of the series, has a Hurst exponent  $H = 0.4421 \pm 0.0034$ . The different regimes show a change in correlation properties of the residuals, from correlated at small scales to anti-correlated. This is also an evidence of multifractality. The local Hurst exponent  $H_t$  is computed at a time window of

two weeks and oscillates around a value compatible with long-range correlations ( $\sim 0.6$ ). The one-year component's percentage does not show great variability and its value remains at less than 10% when adding new years.

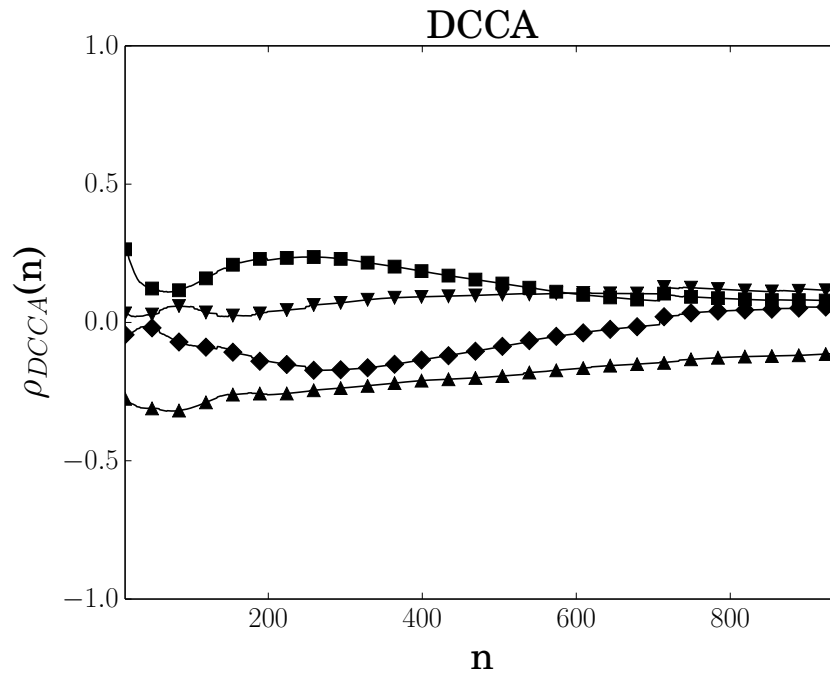


Figure 3.27: Detrended cross correlation between <sup>7</sup>Be and available meteorological parameters (humidity (○), temperature (△), pressure (□), wind direction (▽), and wind speed (◇)).

Station RN23 exhibits negative cross-correlations with temperature at small scales ( $< 200$  days) and positive cross-correlations with pressure at scales between 200 and 300 days. There are no cross-correlations with the other parameters. Humidity time series was not suitable for the analysis.

### 3.3.4 Melbourne, VIC, Australia (RN04)

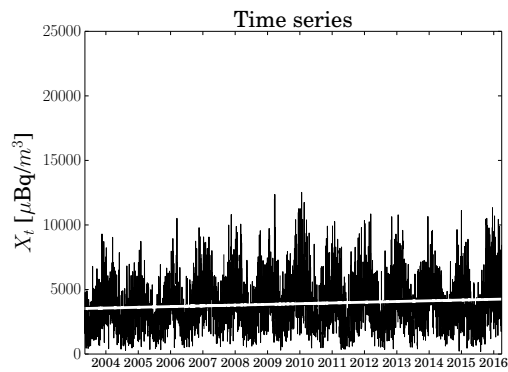


Figure 3.28: Time series with trend superimposed (solid white line).

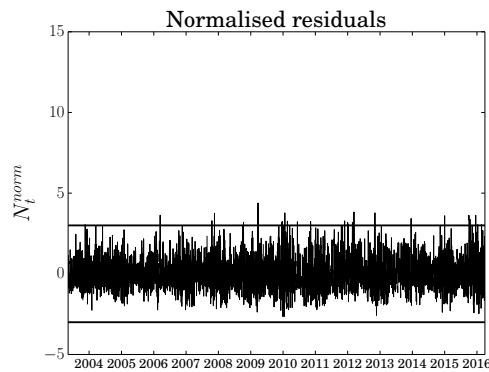


Figure 3.29: Normalised residual time series with the  $\pm 3\sigma$  thresholds (solid black lines).

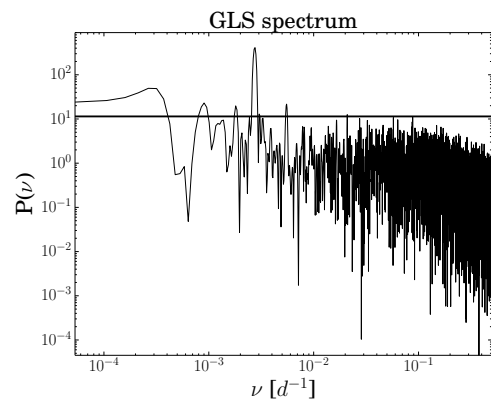


Figure 3.30: Log-log plot of the GLS spectrum with the associated threshold (solid black line).

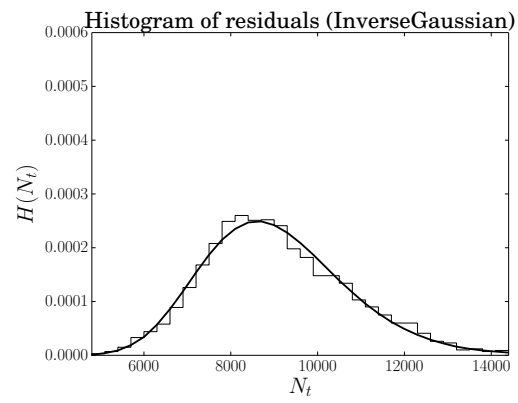


Figure 3.31: Histogram of residuals with the best-fitting distribution (no outliers).

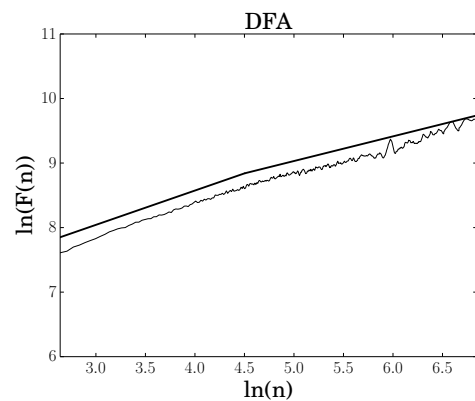


Figure 3.32: Detrended fluctuation analysis. The solid black lines are the best fit at different scales.

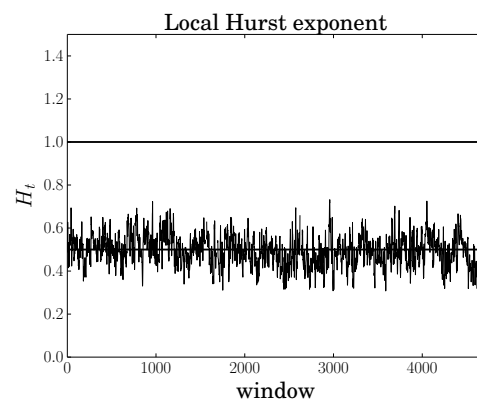


Figure 3.33: Local Hurst exponent  $H_t$  for a time window of two weeks. Solid lines represent the values of pink noise (top) and white noise (bottom).

Periodicity	Percentage	Value	Date
2 months	0.45	4.128	2009/03/20
6 months	1.03	4.388	2009/03/24
1 year	16.63		
1.5 years	0.60		
3 years	0.93		
10.5 years	2.68		

Table 3.9: Outliers as values in the normalised residuals greater (less) than + (-)  $3\sigma$ . Only very high or very low outliers are listed.

Table 3.8: Periodicities as frequencies corresponding to peaks in the spectrum higher than the threshold.

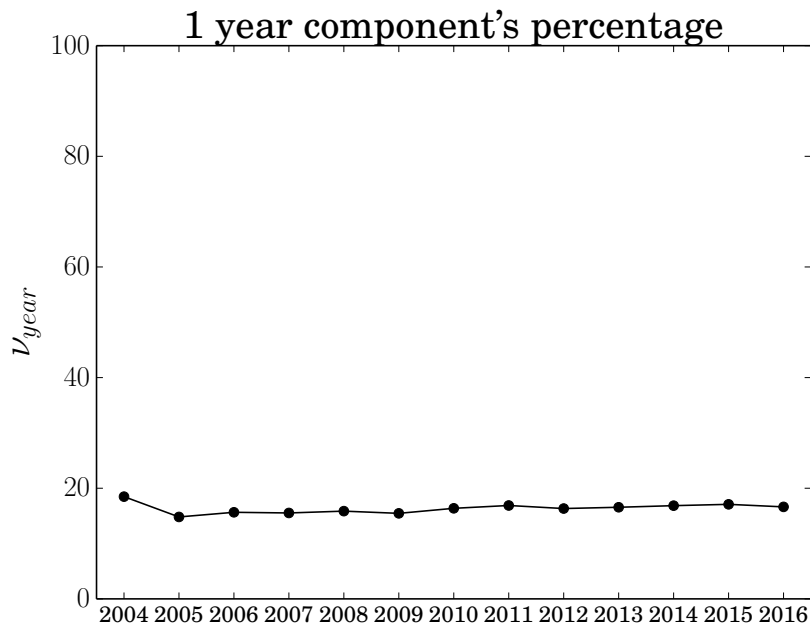


Figure 3.34: Dynamic analysis of the percentage of the one-year periodicity.

Station RN04 exhibits a predominant periodicity of one year, with a percentage weight of 16.63%, much higher than the other periodicities. With a percentage weight of 2.68%, a periodicity of 10.5 years is present and can be associated with the solar cycle. The trend is linear and data are approximately regular. High outliers do not occur in the residual time series, as confirmed by the absence of great variations in the time series. Residuals without outliers are best described by an Inverse Gaussian distribution. From DFA plot, two scaling regimes are found: The first, from 14 days to  $\sim 90$  days, has a Hurst exponent  $H = 0.5316 \pm 0.0040$ ; the second, from  $\sim 90$  days to the end of the series, has a Hurst exponent  $H = 0.3823 \pm 0.0059$ . The different regimes show a change in correlation properties of the residuals, from uncorrelated (white noise) to anti-correlated. This is also an evidence of multifractality. The local Hurst exponent  $H_t$  is computed at a time

window of two weeks and oscillates around a value compatible with white noise ( $\sim 0.5$ ). The one-year component's percentage does not show great variability and its value remains constant at  $\sim 20\%$  when adding new years.

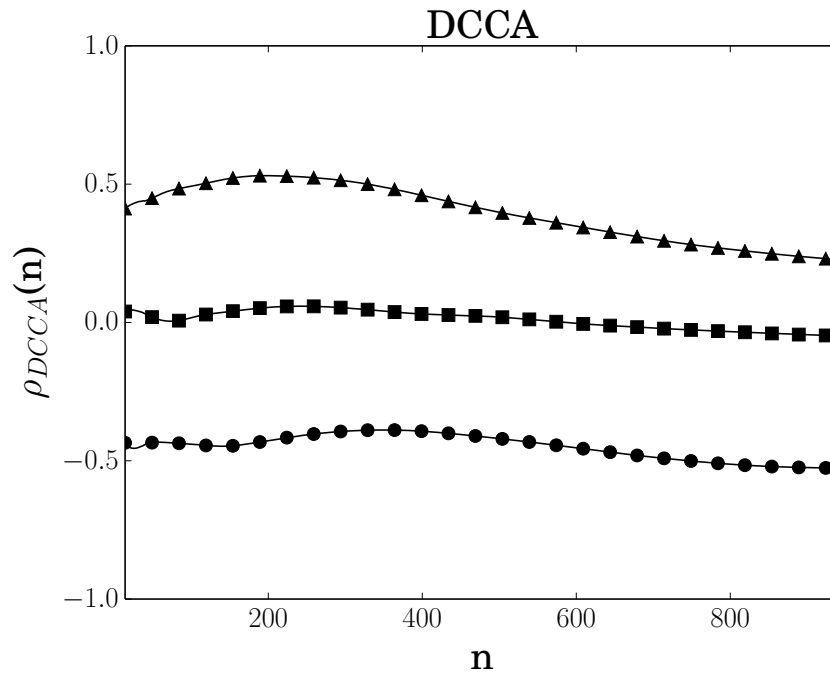


Figure 3.35: Detrended cross correlation between <sup>7</sup>Be and available meteorological parameters (humidity (○), temperature (Δ), pressure (□), wind direction (∇), and wind speed (◇)).

Station RN04 exhibits negative cross-correlations with humidity at all scales and positive cross-correlations with temperature at all scales (stronger at small scales). There are no cross-correlations with pressure. Wind direction and speed time series were not suitable for the analysis.

### 3.3.5 Perth, WA, Australia (RN10)

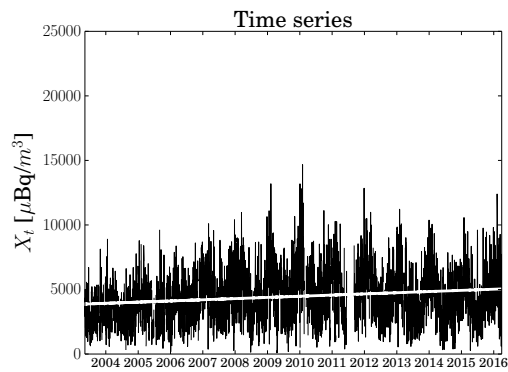


Figure 3.36: Time series with trend superimposed (solid white line).

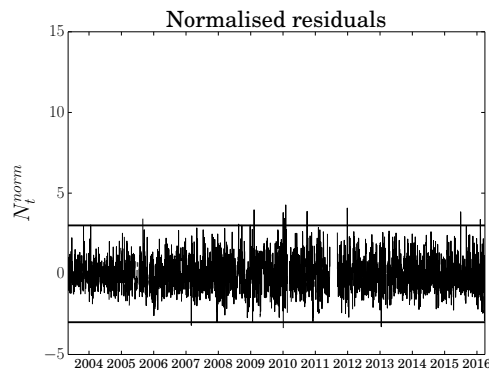


Figure 3.37: Normalised residual time series with the  $\pm 3\sigma$  thresholds (solid black lines).

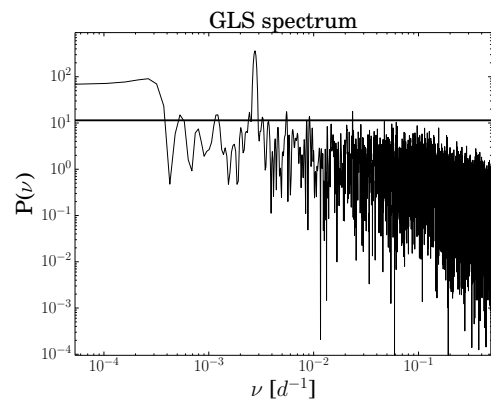


Figure 3.38: Log-log plot of the GLS spectrum with the associated threshold (solid black line).

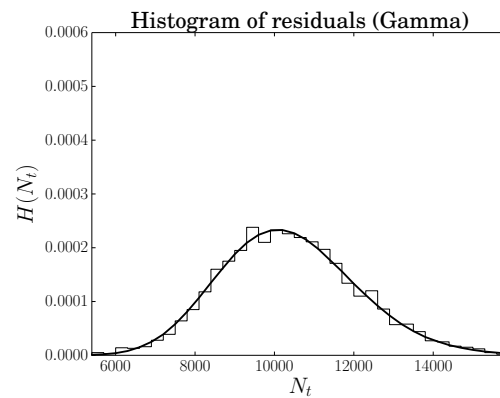


Figure 3.39: Histogram of residuals with the best-fitting distribution (no outliers).

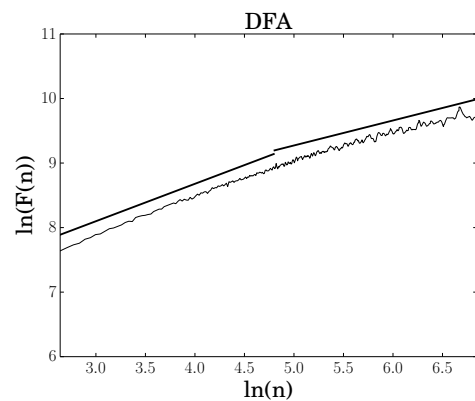


Figure 3.40: Detrended fluctuation analysis. The solid black lines are the best fit at different scales.

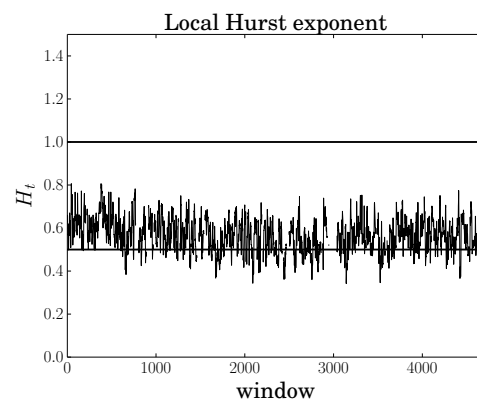


Figure 3.41: Local Hurst exponent  $H_t$  for a time window of two weeks. Solid lines represent the values of pink noise (top) and white noise (bottom).

Periodicity	Percentage	Value	Date
1 month	0.74	4.168	2010/01/31
4 months	0.77	4.269	2010/02/01
6 months	0.83	4.076	2011/12/28
1 year	16.10		
2 years	0.65		
5 years	0.36		
10.5 years	5.08		

Table 3.11: Outliers as values in the normalised residuals greater (less) than + (-)  $3 \sigma$ . Only very high or very low outliers are listed.

Table 3.10: Periodicities as frequencies corresponding to peaks in the spectrum higher than the threshold.

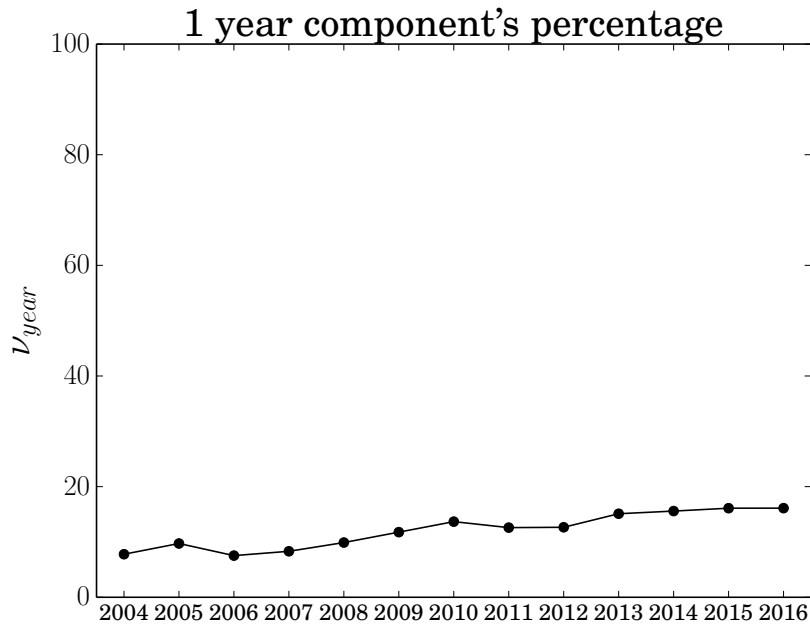


Figure 3.42: Dynamic analysis of the percentage of the one-year periodicity.

Station RN10 exhibits a predominant periodicity of one year, with a percentage weight of 16.10%, much higher than the other periodicities. With a percentage weight of 5.08%, a periodicity of 10.5 years is present and can be associated with the solar cycle. Time series shows a slightly upward trend and data are approximately regular except for a period in mid-2011. High outliers do not occur in the residual time series, as confirmed by the absence of great variations in the time series. Residuals without outliers are best described by a Gamma distribution. From DFA plot, two scaling regimes are found: The first, from 14 days to  $\sim 120$  days, has a Hurst exponent  $H = 0.5798 \pm 0.0034$ ; the second, from  $\sim 120$  days to the end of the series, has a Hurst exponent  $H = 0.3873 \pm 0.0030$ . The different regimes show a change in correlation properties of the residuals, from correlated

to anti-correlated. This is also an evidence of multifractality. The local Hurst exponent  $H_t$  is computed at a time window of two weeks and oscillates around a value compatible with long-range correlations ( $\sim 0.6$ ). The one-year component's percentage shows great variability and its value goes from  $\sim 10\%$  to  $\sim 20\%$  when adding new years.

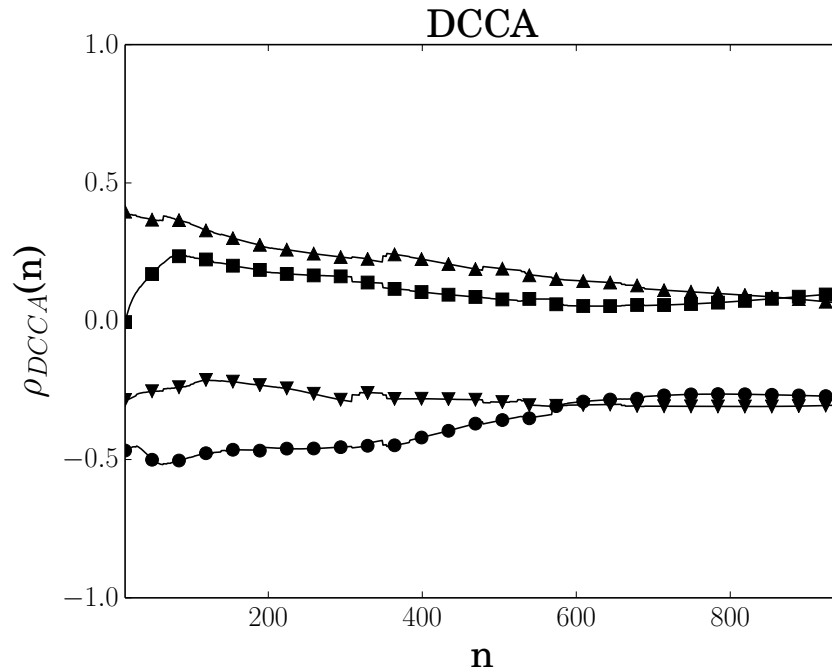


Figure 3.43: Detrended cross correlation between  $^7\text{Be}$  and available meteorological parameters (humidity ( $\circ$ ), temperature ( $\triangle$ ), pressure ( $\square$ ), wind direction ( $\nabla$ ), and wind speed ( $\diamond$ )).

Station RN10 exhibits negative cross-correlations with humidity and wind direction at all scales (stronger at small scales) and positive cross-correlations with temperature at small scales ( $< 300$  days). There are no cross-correlations with pressure. Wind speed time series was not suitable for the analysis.

### 3.3.6 Buenos Aires, Argentina (RN01)

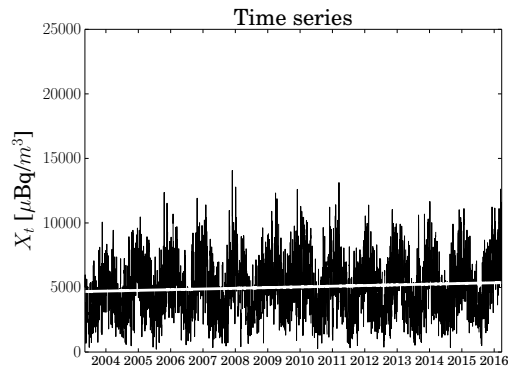


Figure 3.44: Time series with trend superimposed (solid white line).

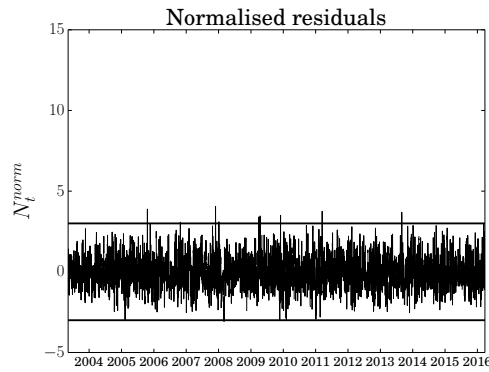


Figure 3.45: Normalised residual time series with the  $\pm 3\sigma$  thresholds (solid black lines).

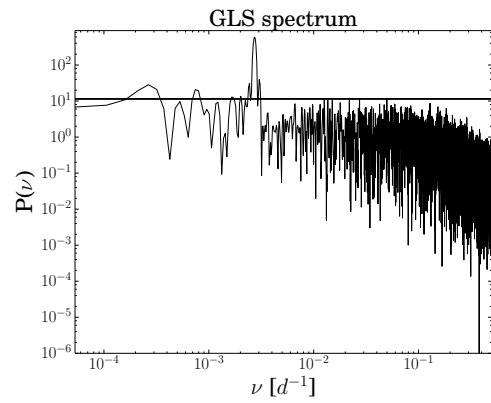


Figure 3.46: Log-log plot of the GLS spectrum with the associated threshold (solid black line).

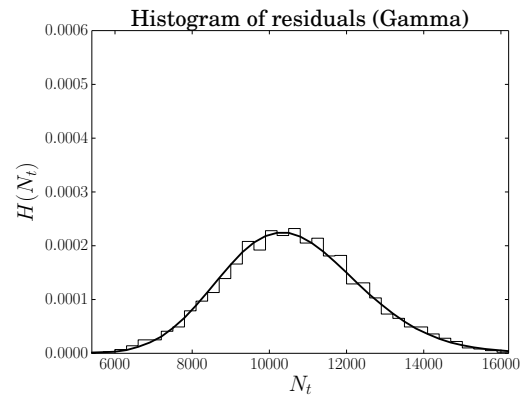


Figure 3.47: Histogram of residuals with the best-fitting distribution (no outliers).

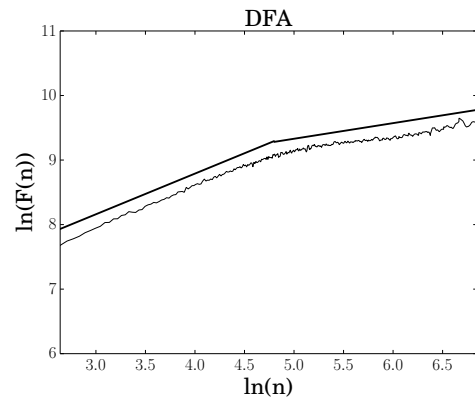


Figure 3.48: Detrended fluctuation analysis. The solid black lines are the best fit at different scales.

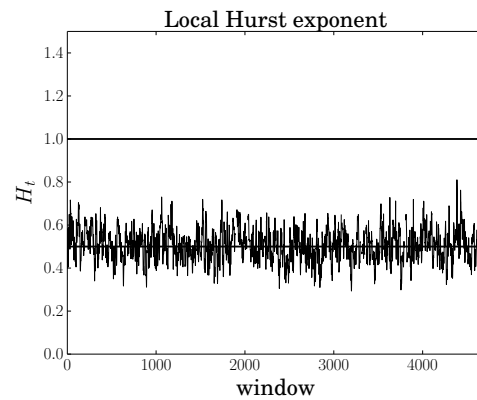


Figure 3.49: Local Hurst exponent  $H_t$  for a time window of two weeks. Solid lines represent the values of pink noise (top) and white noise (bottom).

Periodicity	Percentage	Value	Date
2 weeks	0.53	4.046	2007/11/28
1 month	0.61		
1 year	25.06		
1.5 years	0.94		
3.5 years	0.68		
10.5 years	1.07		

Table 3.13: Outliers as values in the normalised residuals greater (less) than + (-)  $3\sigma$ . Only very high or very low outliers are listed.

Table 3.12: Periodicities as frequencies corresponding to peaks in the spectrum higher than the threshold.

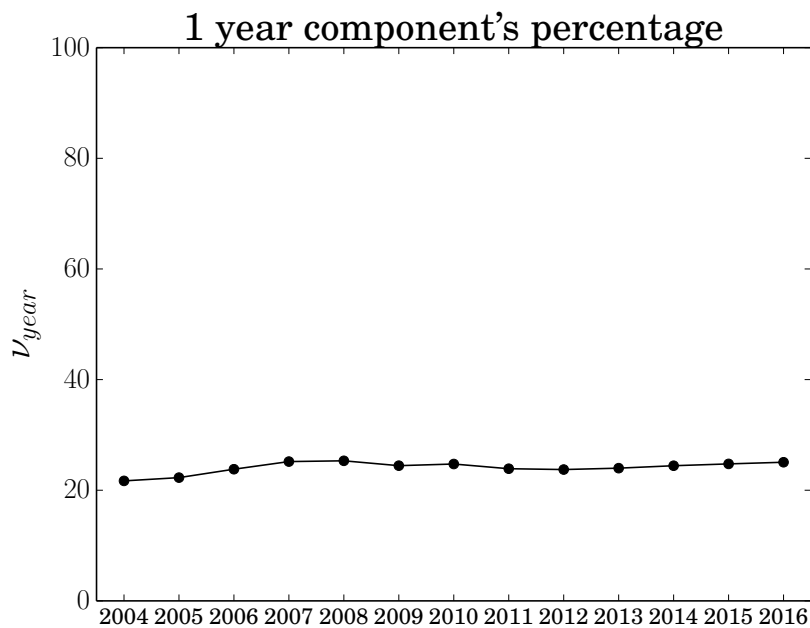


Figure 3.50: Dynamic analysis of the percentage of the one-year periodicity.

Station RN01 exhibits a predominant periodicity of one year, with a percentage weight of 25.06%, much higher than the other periodicities. With a percentage weight of 1.07%, a periodicity of 10.5 years is present and can be associated with the solar cycle. Time series shows a slightly upward trend and data are approximately regular. High outliers do not occur in the residual time series, as confirmed by the absence of great variations in the time series. Residuals without outliers are best described by a Gamma distribution. From DFA plot, two scaling regimes are found: The first, from 14 days to  $\sim 120$  days, has a Hurst exponent  $H = 0.6303 \pm 0.0037$ ; the second, from  $\sim 120$  days to the end of the series, has a Hurst exponent  $H = 0.2420 \pm 0.0021$ . The different regimes show a change in correlation properties of the residuals, from correlated to anti-correlated. This is also an evidence of multifractality. The local Hurst exponent  $H_t$  is computed at a time window of two

weeks and oscillates around a value compatible with white noise ( $\sim 0.5$ ). The one-year component's percentage does not show great variability and, starting from a value of 20%, it increases a little when adding new years.

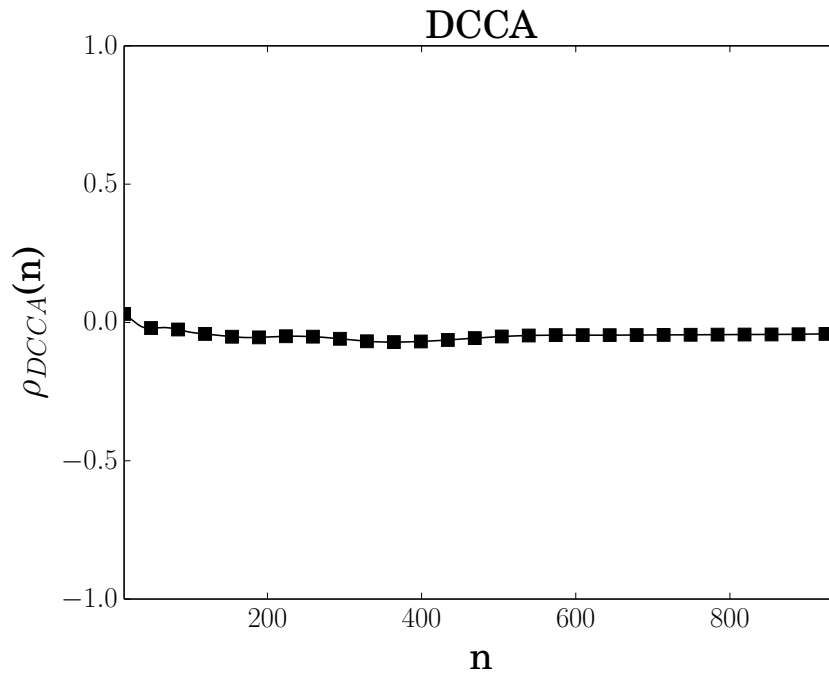


Figure 3.51: Detrended cross correlation between <sup>7</sup>Be and available meteorological parameters (humidity (○), temperature (△), pressure (□), wind direction (▽), and wind speed (◇)).

Station RN01 does not exhibit cross-correlations with pressure. All the other parameters were not suitable for the analysis.

### 3.3.7 Townsville, QLD, Australia (RN06)

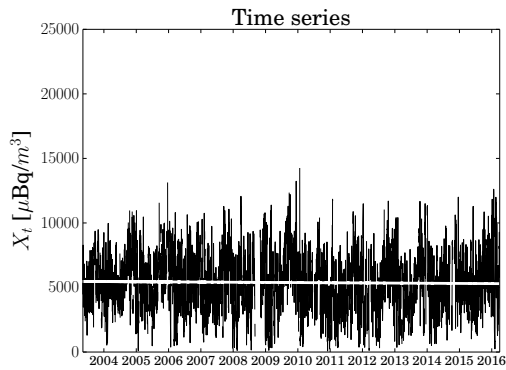


Figure 3.52: Time series with trend superimposed (solid white line).

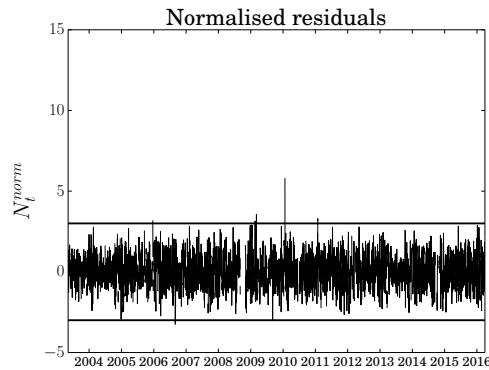


Figure 3.53: Normalised residual time series with the  $\pm 3\sigma$  thresholds (solid black lines).

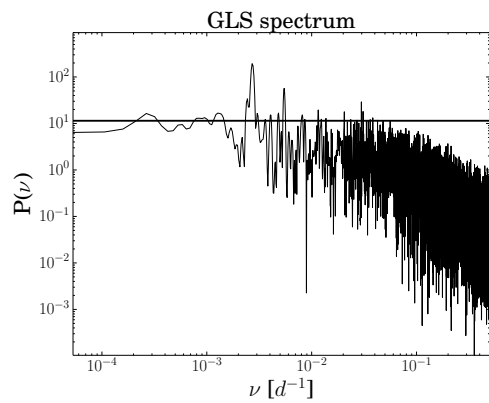


Figure 3.54: Log-log plot of the GLS spectrum with the associated threshold (solid black line).

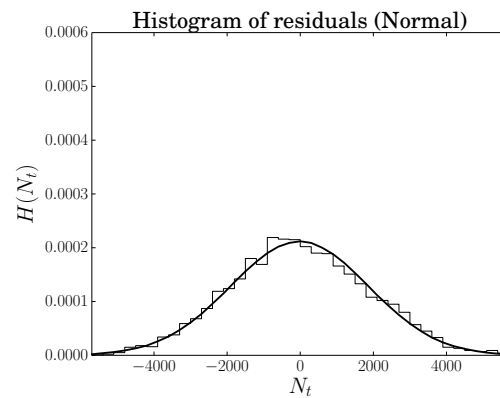


Figure 3.55: Histogram of residuals with the best-fitting distribution (no outliers).

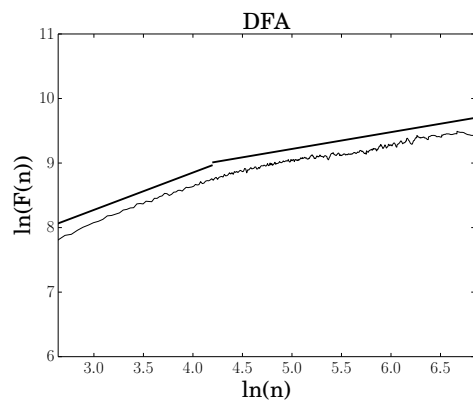


Figure 3.56: Detrended fluctuation analysis. The solid black lines are the best fit at different scales.

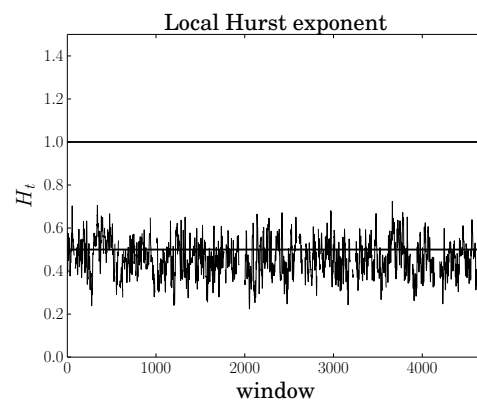


Figure 3.57: Local Hurst exponent  $H_t$  for a time window of two weeks. Solid lines represent the values of pink noise (top) and white noise (bottom).

Periodicity	Percentage	Value	Date
1 month	5.47	5.776	2010/01/22
2 months	1.53		
3 months	2.14		
4 months	1.99		
6 months	3.90		
1 year	10.19		
2 years	1.17		
3 years	1.17		
10.5 years	0.82		

Table 3.15: Outliers as values in the normalised residuals greater (less) than  $\pm 3 \sigma$ . Only very high or very low outliers are listed.

Table 3.14: Periodicities as frequencies corresponding to peaks in the spectrum higher than the threshold.

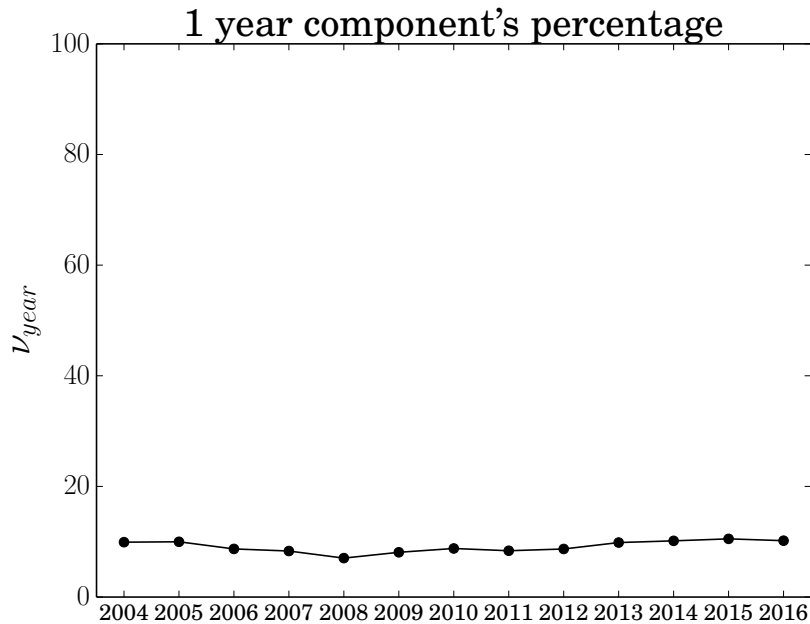


Figure 3.58: Dynamic analysis of the percentage of the one-year periodicity.

Station RN06 exhibits a predominant periodicity of one year, with a percentage weight of 10.09%. With a percentage weight of 0.82%, a periodicity of 10.5 years is present and can be associated with the solar cycle. Time series shows an approximately constant linear trend and data are approximately regular, except for a small period in mid-2008. A high outlier occurs in the residual time series at the beginning of 2010, in correspondence of the maximum of the time series. Residuals without outliers are best described by a Normal distribution. From DFA plot, two scaling regimes are found: The first, from 14 days to  $\sim 67$  days, has a Hurst exponent  $H = 0.5786 \pm 0.0066$ ; the second, from  $\sim 67$  days to the end of the series, has

a Hurst exponent  $H = 0.2603 \pm 0.0016$ . The different regimes show a change in correlation properties of the residuals, from correlated to anti-correlated. This is also an evidence of multifractality. The local Hurst exponent  $H_t$  is computed at a time window of two weeks and oscillates around a value compatible with white noise ( $\sim 0.5$ ). The one-year component's percentage does not show great variability and remains at  $\sim 10\%$  when adding new years.

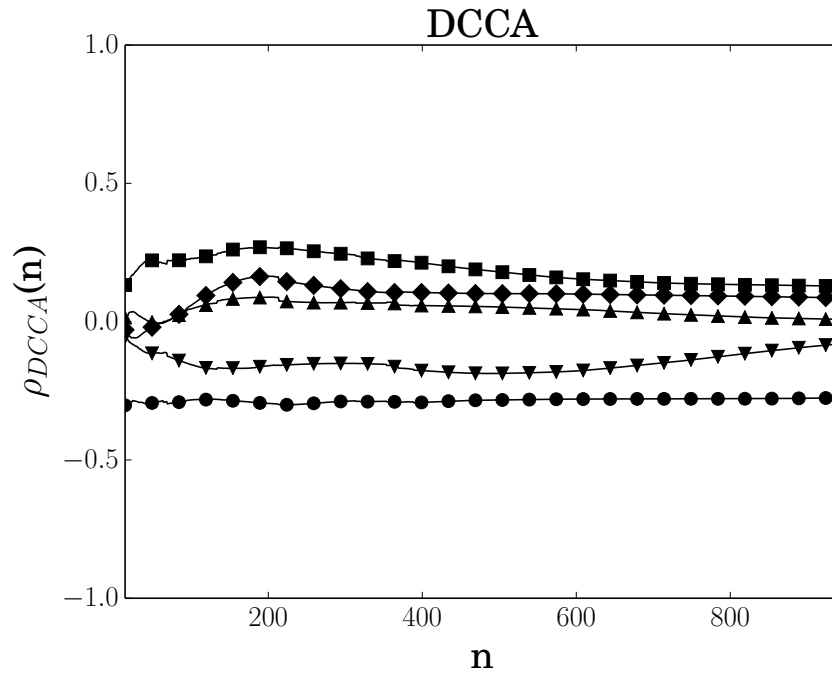


Figure 3.59: Detrended cross correlation between  $^7\text{Be}$  and available meteorological parameters (humidity ( $\circ$ ), temperature ( $\triangle$ ), pressure ( $\square$ ), wind direction ( $\nabla$ ), and wind speed ( $\diamond$ )).

Station RN06 exhibits negative cross-correlations with humidity at all scales, while there are no cross-correlations with the other parameters.

### 3.3.8 Stockholm, Sweden (RN63)

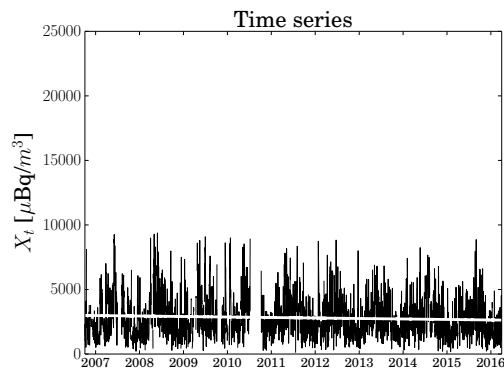


Figure 3.60: Time series with trend superimposed (solid white line).

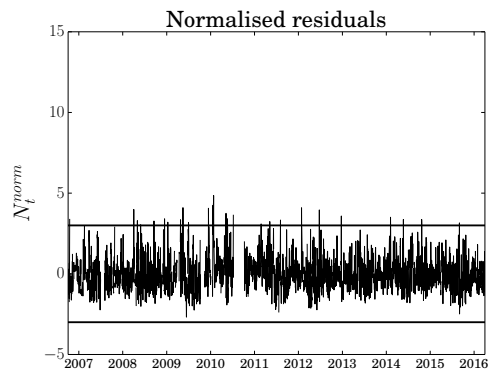


Figure 3.61: Normalised residual time series with the  $\pm 3\sigma$  thresholds (solid black lines).

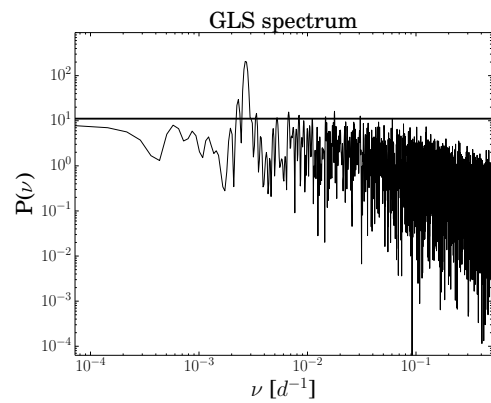


Figure 3.62: Log-log plot of the GLS spectrum with the associated threshold (solid black line).

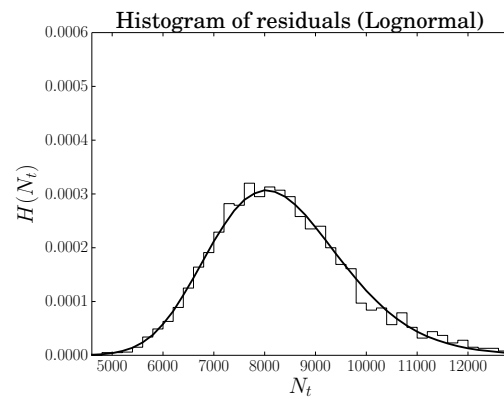


Figure 3.63: Histogram of residuals with the best-fitting distribution (no outliers).

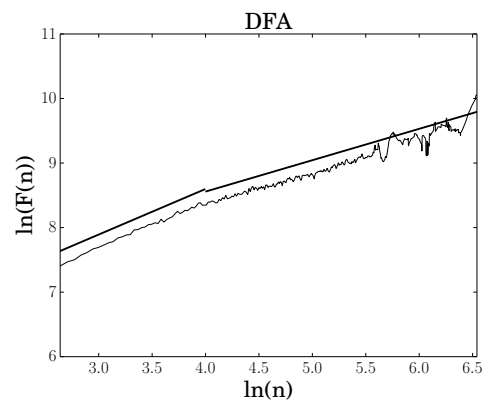


Figure 3.64: Detrended fluctuation analysis. The solid black lines are the best fit at different scales.

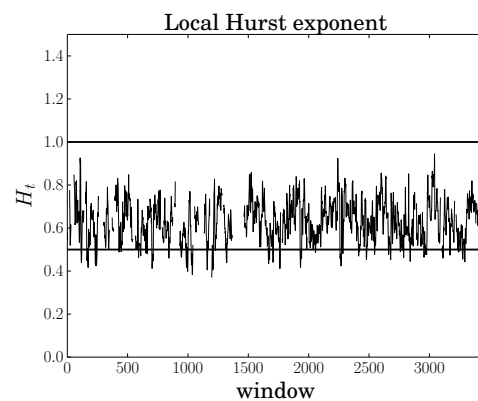


Figure 3.65: Local Hurst exponent  $H_t$  for a time window of two weeks. Solid lines represent the values of pink noise (top) and white noise (bottom).

Periodicity	Percentage	Value	Date
2 weeks	0.62	4.064	2009/12/14
1 month	0.82	4.237	2010/01/20
2 months	1.46	4.327	2010/01/24
4 months	1.54	4.851	2010/01/26
6 months	0.67	4.092	2012/01/27
1 year	13.00		

Table 3.16: Periodicities as frequencies corresponding to peaks in the spectrum higher than the threshold.

Table 3.17: Outliers as values in the normalised residuals greater (less) than  $+ (-) 3 \sigma$ . Only very high or very low outliers are listed.

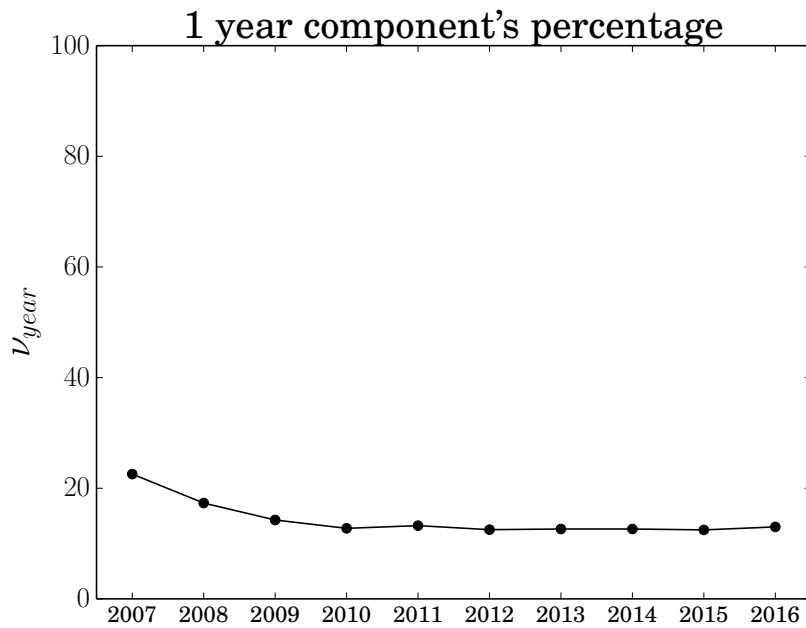


Figure 3.66: Dynamic analysis of the percentage of the one-year periodicity.

Station RN63 exhibits a predominant periodicity of one year, with a percentage weight of 13.00%, much higher than the other periodicities. Time series shows an approximately constant linear trend and data are approximately regular, except for a small period in mid-2010. High outliers do not occur in the residual time series, as confirmed by the absence of great variations in the time series. Residuals without outliers are best described by a Lognormal distribution. From DFA plot, two scaling regimes are found: The first, from 14 days to  $\sim 55$  days, has a Hurst exponent  $H = 0.7064 \pm 0.0084$ ; the second, from  $\sim 55$  days to the end of the series, has a Hurst exponent  $H = 0.4862 \pm 0.0047$ . The different regimes show a change in correlation properties of the residuals, from correlated to uncorrelated (white noise). This is also an evidence of multifractality. The local Hurst exponent  $H_t$  is computed at a time window of two weeks and oscillates around a value compatible

with long-range correlations ( $\sim 0.7$ ). The one-year component's percentage goes from over 20% to approximately 15% when adding new years.

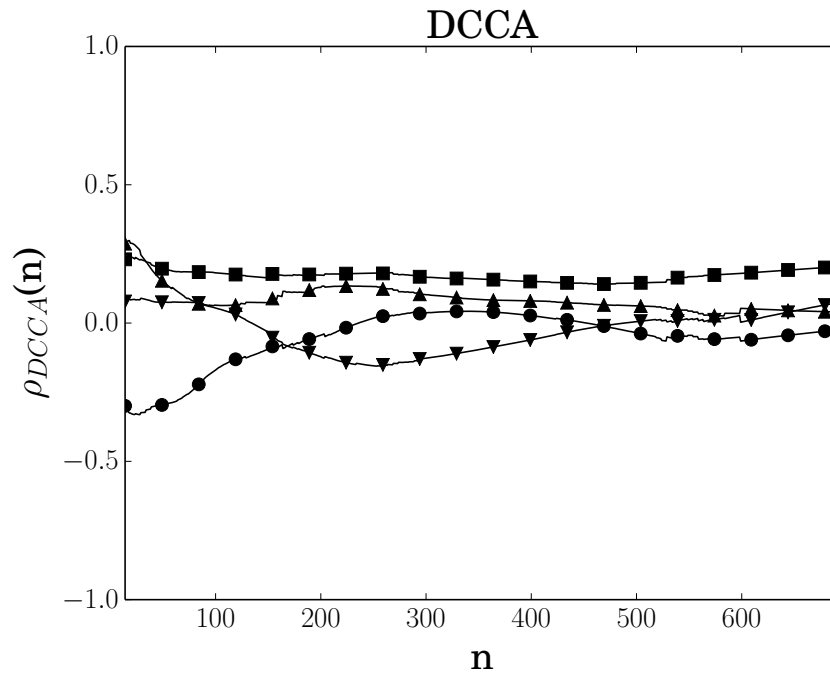


Figure 3.67: Detrended cross correlation between <sup>7</sup>Be and available meteorological parameters (humidity (○), temperature (△), pressure (□), wind direction (▽), and wind speed (◇)).

Station RN63 exhibits negative cross-correlations with humidity at small scales (< 100 days) and positive cross-correlations with temperature at very small scales (< 50 days) and pressure at all scales. There are no cross-correlations with wind direction. Wind speed time series was not suitable for the analysis.

### 3.3.9 Darwin, NT, Australia (RN09)

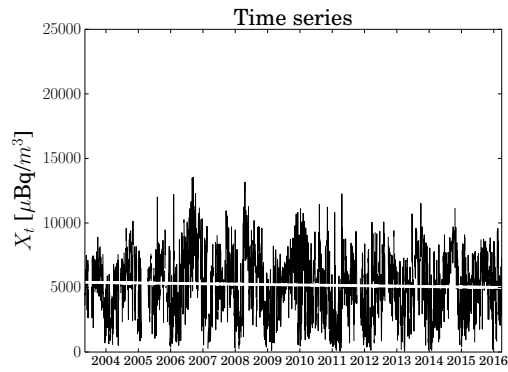


Figure 3.68: Time series with trend superimposed (solid white line).

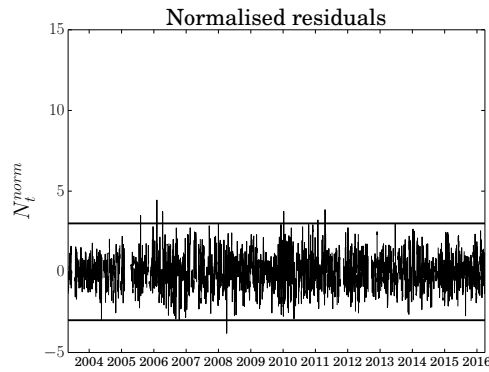


Figure 3.69: Normalised residual time series with the  $\pm 3\sigma$  thresholds (solid black lines).

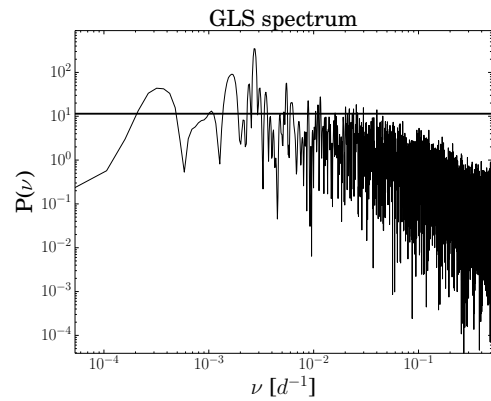


Figure 3.70: Log-log plot of the GLS spectrum with the associated threshold (solid black line).

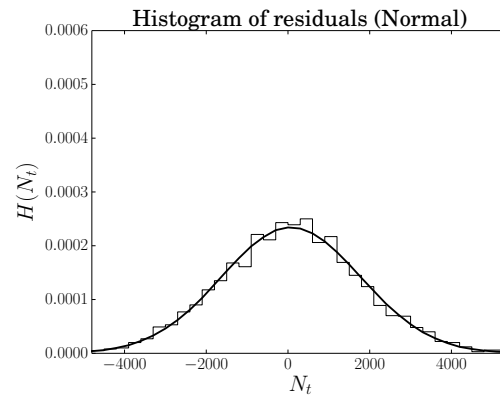


Figure 3.71: Histogram of residuals with the best-fitting distribution (no outliers).

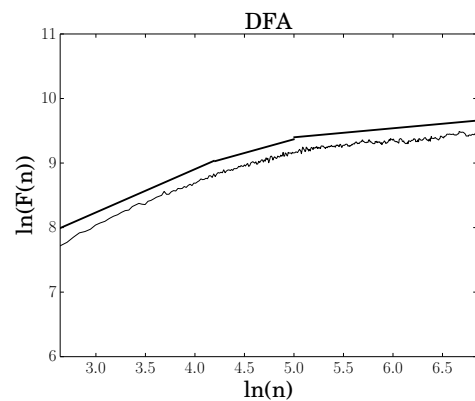


Figure 3.72: Detrended fluctuation analysis. The solid black lines are the best fit at different scales.

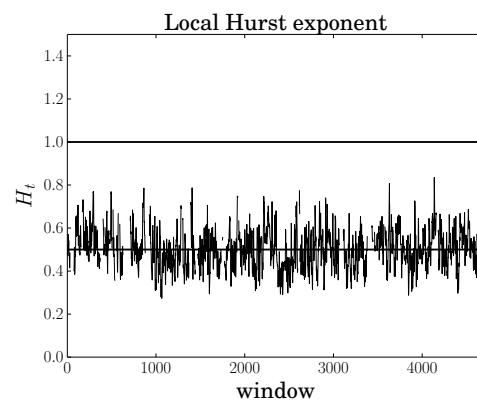


Figure 3.73: Local Hurst exponent  $H_t$  for a time window of two weeks. Solid lines represent the values of pink noise (top) and white noise (bottom).

Periodicity	Percentage	Value	Date
1 month	4.42	4.446	2006/02/04
2 months	2.65		
3 months	3.29		
4 months	1.09		
6 months	4.74		
1 year	18.55		
1.5 years	6.71		
2.5 years	0.99		
8.5 years	2.00		

Table 3.19: Outliers as values in the normalised residuals greater (less) than + (-)  $3\sigma$ . Only very high or very low outliers are listed.

Table 3.18: Periodicities as frequencies corresponding to peaks in the spectrum higher than the threshold.

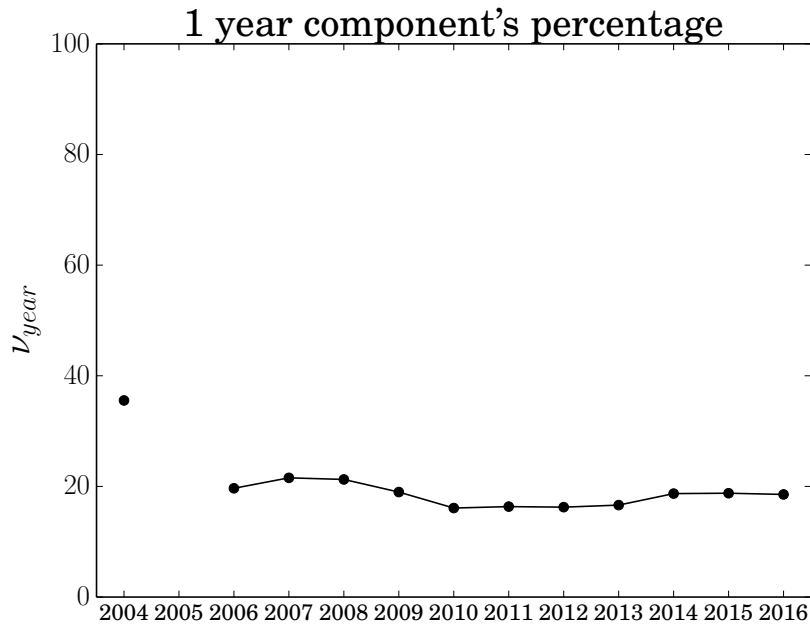


Figure 3.74: Dynamic analysis of the percentage of the one-year periodicity.

Station RN09 exhibits a predominant periodicity of one year, with a percentage weight of 18.55%, much higher than the other periodicities. With a percentage weight of 2.00%, a periodicity of 8.5 years is present and can be associated with the solar cycle. Time series shows an approximately constant linear trend and data are approximately regular, except for a period at the beginning of 2005. High outliers do not occur in the residual time series, as confirmed by the absence of great variations in the time series. Residuals without outliers are best described by a Normal distribution. From DFA plot, three scaling regimes are found: The first, from 14 days to  $\sim 67$  days, has a Hurst exponent  $H = 0.6707 \pm 0.0085$ ; the second,

from  $\sim 67$  days to  $\sim 148$  days, has a Hurst exponent  $H = 0.4258 \pm 0.0091$ ; the third, from  $\sim 148$  days to the end of the series, has a Hurst exponent  $H = 0.1399 \pm 0.0017$ . The first two regimes show a change in correlation properties of the residuals, from correlated to anti-correlated. This is also an evidence of multifractality. The third regimes instead, indicates an anti-correlated regime or it probably expresses the limitations of the algorithm in accurately estimating the degree of correlations in the residual time series [94]. The local Hurst exponent  $H_t$  is computed at a time window of two weeks and oscillates around a value compatible with white noise ( $\sim 0.5$ ). The one-year component's percentage has a value of approximately 40% when adding the first year and then remains constant at approximately 20% when adding the other years. Adding the year 2005 makes the total number of missing data exceed the threshold of 20%, hence the series is not analysed.

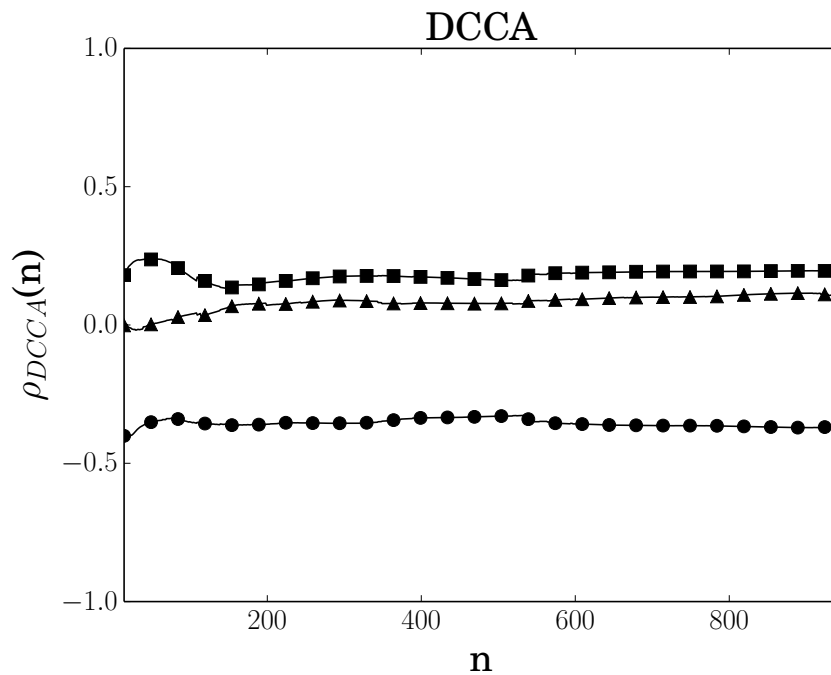


Figure 3.75: Detrended cross correlation between <sup>7</sup>Be and available meteorological parameters (humidity (○), temperature (△), pressure (□), wind direction (▽), and wind speed (◇)).

Station RN09 exhibits negative cross-correlations with humidity at all scales and slightly positive cross-correlations with pressure. There are no cross-correlations with temperature. Wind direction and speed time series were not suitable for the analysis.

### 3.3.10 Charlottesville, VA, USA (RN75)

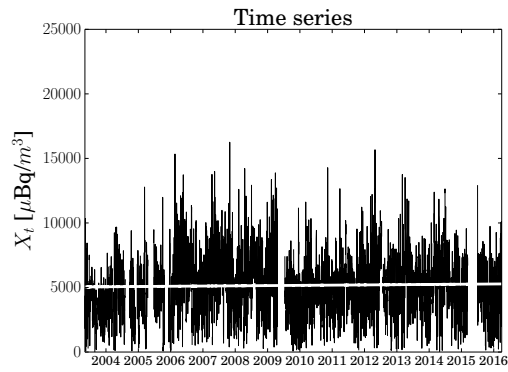


Figure 3.76: Time series with trend superimposed (solid white line).

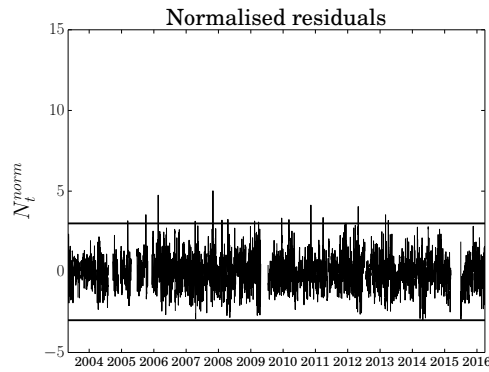


Figure 3.77: Normalised residual time series with the  $\pm 3\sigma$  thresholds (solid black lines).

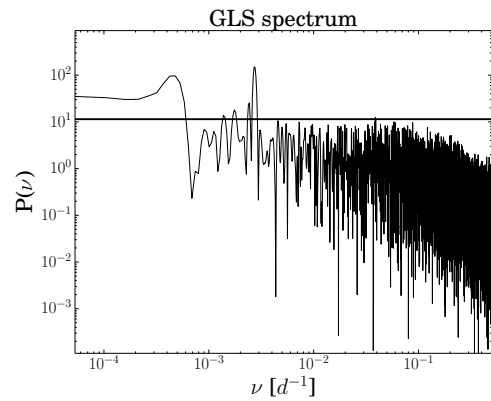


Figure 3.78: Log-log plot of the GLS spectrum with the associated threshold (solid black line).

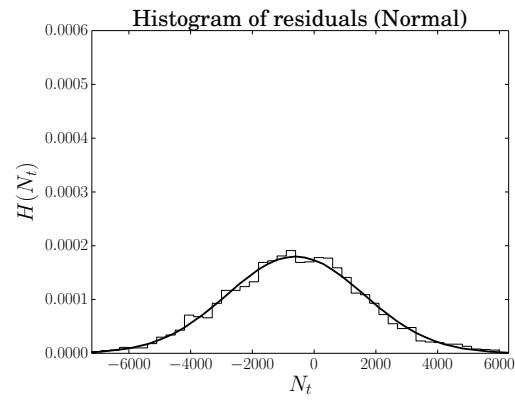


Figure 3.79: Histogram of residuals with the best-fitting distribution (no outliers).

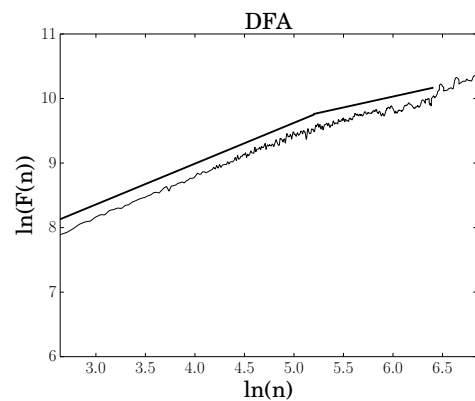


Figure 3.80: Detrended fluctuation analysis. The solid black lines are the best fit at different scales.

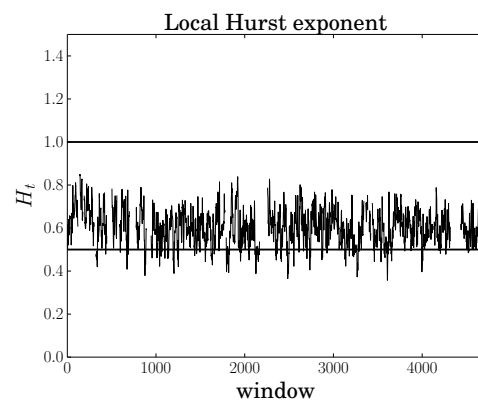


Figure 3.81: Local Hurst exponent  $H_t$  for a time window of two weeks. Solid lines represent the values of pink noise (top) and white noise (bottom).

Periodicity	Percentage	Value	Date
1 month	1.02	4.750	2006/02/19
1 year	6.73	5.020	2007/10/31
1.5 years	0.77	4.134	2010/11/11
2 years	0.46	4.043	2012/04/29
5.5 years	5.22		
14 years	0.71		

Table 3.20: Periodicities as frequencies corresponding to peaks in the spectrum higher than the threshold.

Table 3.21: Outliers as values in the normalised residuals greater (less) than + (-)  $3\sigma$ . Only very high or very low outliers are listed.

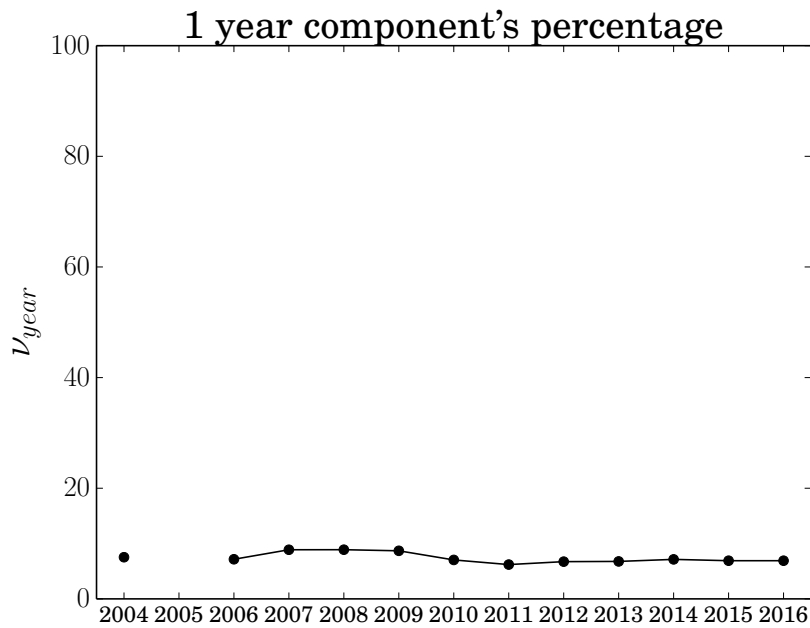


Figure 3.82: Dynamic analysis of the percentage of the one-year periodicity.

Station RN75 exhibits a predominant periodicity of one year, with a percentage weight of 6.73%. With a percentage weight of 0.71%, a periodicity of 14 years is present and could be associated with the solar cycle. Time series shows an approximately constant linear trend and data are approximately regular, except for periods in mid-2005 and in mid-2015. High outliers do not occur in the residual time series, as confirmed by the absence of great variations in the time series. Residuals without outliers are best described by a Normal distribution. From DFA plot, two scaling regimes are found: The first, from 14 days to  $\sim 180$  days, has a Hurst exponent  $H = 0.6326 \pm 0.0037$ ; the second, from  $\sim 180$  days to the end of the series, has a Hurst exponent  $H = 0.3375 \pm 0.0054$ . The different regimes show a change in correlation properties of the residuals, from correlated to anti-correlated. This is also an evidence of multifractality. The local Hurst

---

exponent  $H_t$  is computed at a time window of two weeks and oscillates around a value compatible with long-range correlations ( $\sim 0.6$ ). The one-year component's percentage remains at approximately 10% when adding new years. Adding the year 2005 makes the total number of missing data exceed the threshold of 20%, hence the series is not analysed. All meteorological parameters were not suitable for the detrended cross-correlation analysis.

### 3.3.11 Ulaanbaatar, Mongolia (RN45)

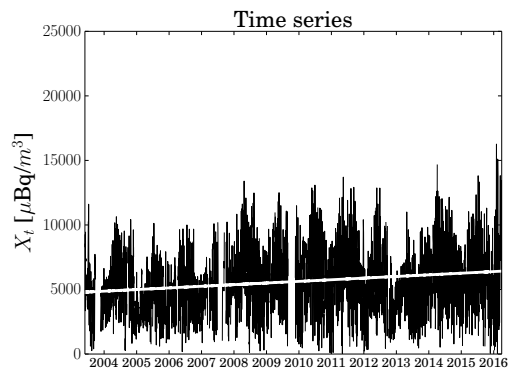


Figure 3.83: Time series with trend superimposed (solid white line).

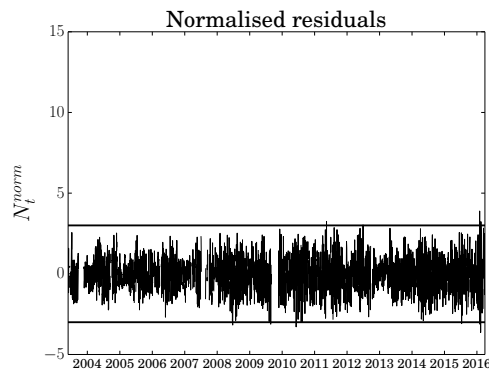


Figure 3.84: Normalised residual time series with the  $\pm 3\sigma$  thresholds (solid black lines).

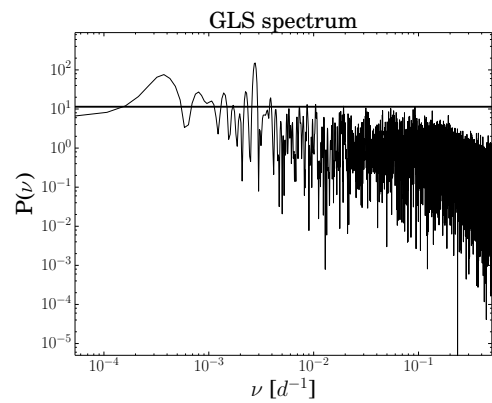


Figure 3.85: Log-log plot of the GLS spectrum with the associated threshold (solid black line).

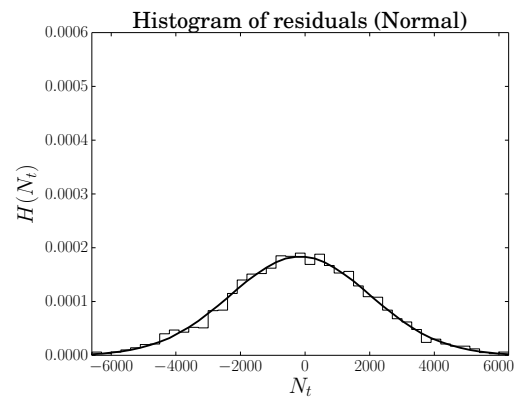


Figure 3.86: Histogram of residuals with the best-fitting distribution (no outliers).

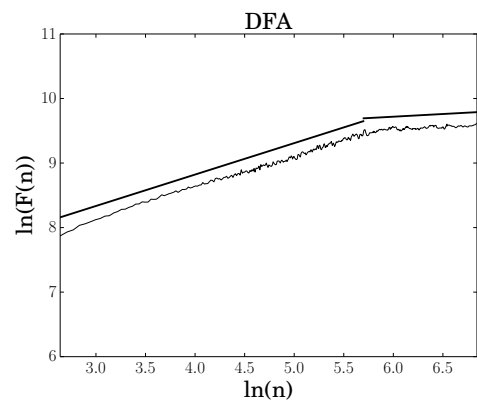


Figure 3.87: Detrended fluctuation analysis. The solid black lines are the best fit at different scales.

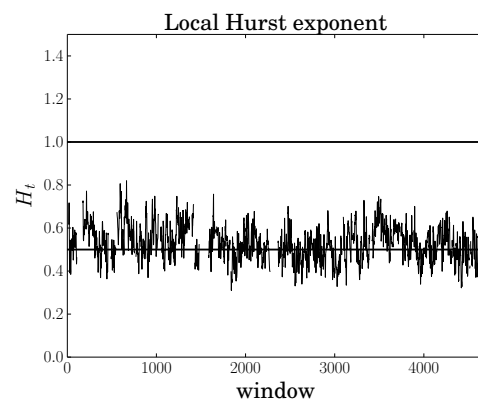


Figure 3.88: Local Hurst exponent  $H_t$  for a time window of two weeks. Solid lines represent the values of pink noise (top) and white noise (bottom).

Periodicity	Percentage
2 months	0.51
3 months	0.67
4 months	1.16
6 months	0.80
1 year	7.34
1.5 years	0.38
2 years	0.92
2.5 years	0.56
3.5 years	1.29
7.5 years	3.69

Value	Date
3.891	2016/02/01

Table 3.23: Outliers as values in the normalised residuals greater (less) than + (-)  $3\sigma$ . Only very high or very low outliers are listed.

Table 3.22: Periodicities as frequencies corresponding to peaks in the spectrum higher than the threshold.

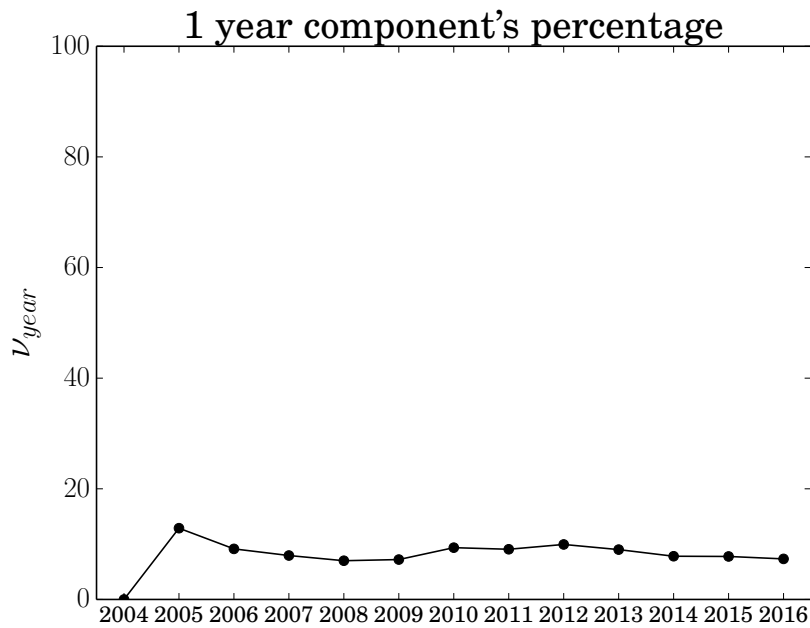


Figure 3.89: Dynamic analysis of the percentage of the one-year periodicity.

Station RN45 exhibits a predominant periodicity of one year, with a percentage weight of 7.34%. Time series shows an upward linear trend and data are approximately regular, except for a period at the end of 2009. High outliers do not occur in the residual time series, as confirmed by the absence of great variations in the time series. Residuals without outliers are best described by a Normal distribution. From DFA plot, two scaling regimes are found: The first, from 14 days to  $\sim 300$  days, has a Hurst exponent  $H = 0.4870 \pm 0.0021$ ; the second, from  $\sim 300$  days to the end of the series, has a Hurst exponent  $H = 0.0837 \pm 0.0023$ . The

first regime shows an uncorrelated behaviour of the series, while the second regime probably expresses the limitations of the algorithm in accurately estimating the degree of correlations in the residual time series [94]. The local Hurst exponent  $H_t$  is computed at a time window of two weeks and oscillates initially around a value compatible with long-range correlations ( $\sim 0.6$ ), then oscillates around a value compatible with white noise ( $\sim 0.5$ ). The one-year component's percentage remains constant at approximately 10% when adding new years. When the year 2004 is added, no one-year periodicity is found.

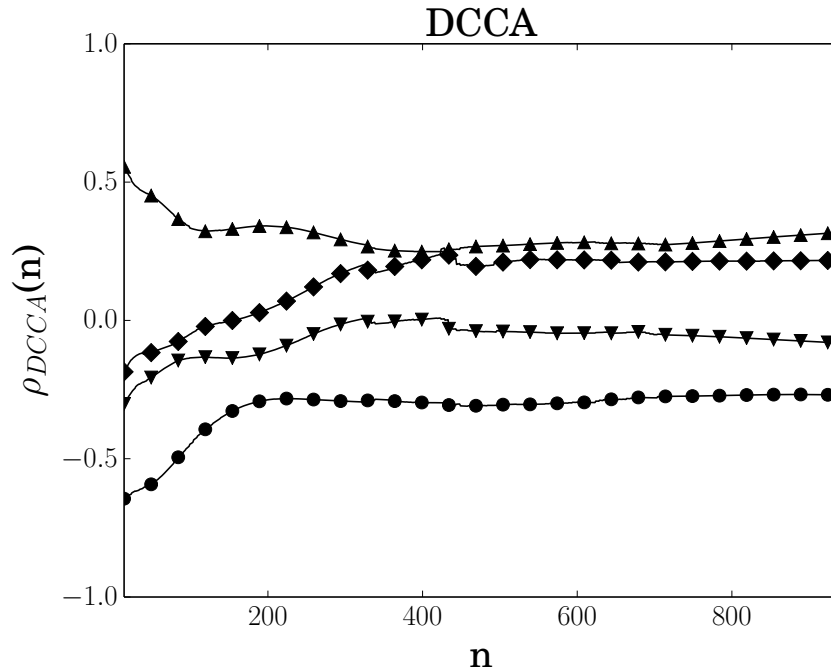


Figure 3.90: Detrended cross correlation between <sup>7</sup>Be and available meteorological parameters (humidity (○), temperature (△), pressure (□), wind direction (▽), and wind speed (◇)).

Station RN45 exhibits negative cross-correlations with humidity at all scales and positive cross-correlations with temperature at all scales and wind speed at big scales ( $> 400$  days). There are no cross-correlations with wind direction. Pressure time series was not suitable for the analysis.

### 3.3.12 Yellowknife, N.W.T., Canada (RN16)

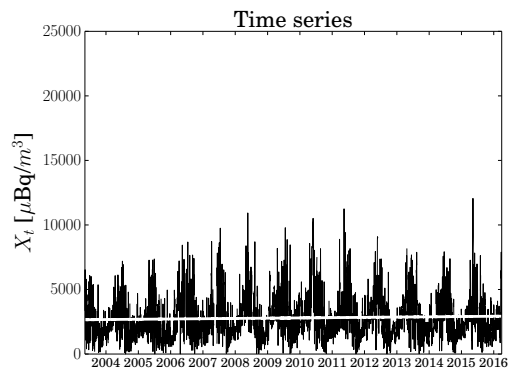


Figure 3.91: Time series with trend superimposed (solid white line).

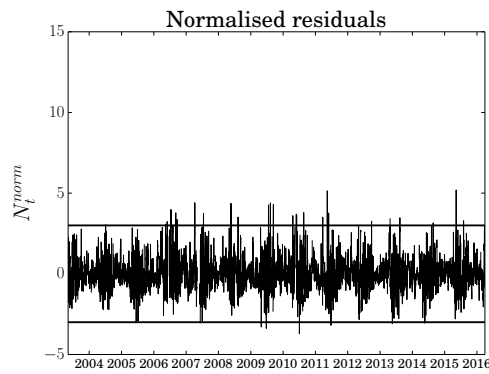


Figure 3.92: Normalised residual time series with the  $\pm 3\sigma$  thresholds (solid black lines).

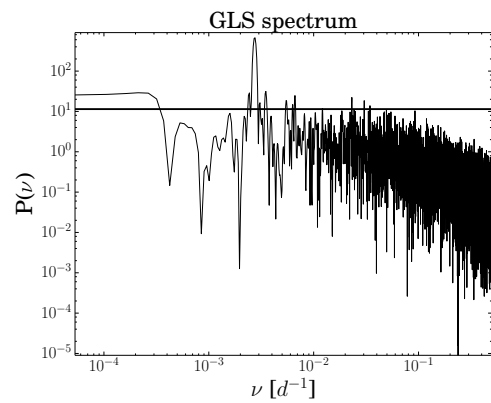


Figure 3.93: Log-log plot of the GLS spectrum with the associated threshold (solid black line).

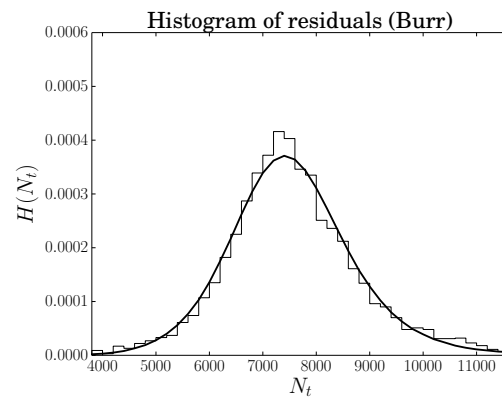


Figure 3.94: Histogram of residuals with the best-fitting distribution (no outliers).

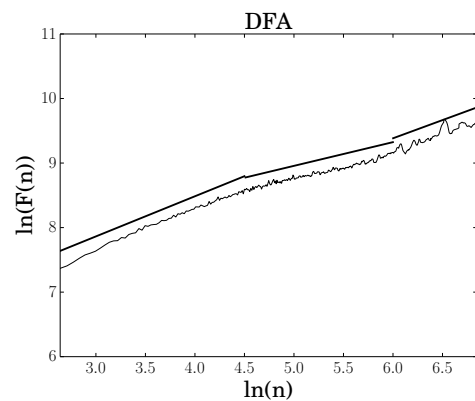


Figure 3.95: Detrended fluctuation analysis. The solid black lines are the best fit at different scales.

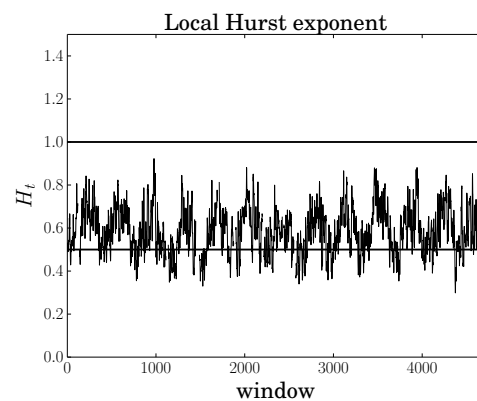


Figure 3.96: Local Hurst exponent  $H_t$  for a time window of two weeks. Solid lines represent the values of pink noise (top) and white noise (bottom).

Periodicity	Percentage	Value	Date
1 month	2.47	4.406	2007/04/09
3 months	0.53	4.371	2008/05/22
6 months	2.34	4.268	2009/07/20
1 year	29.83	4.394	2009/08/10
13 years	1.72	4.301	2009/09/13
		5.143	2011/05/15
		5.199	2015/05/11

Table 3.24: Periodicities as frequencies corresponding to peaks in the spectrum higher than the threshold.

Table 3.25: Outliers as values in the normalised residuals greater (less) than + (-)  $3 \sigma$ . Only very high or very low outliers are listed.

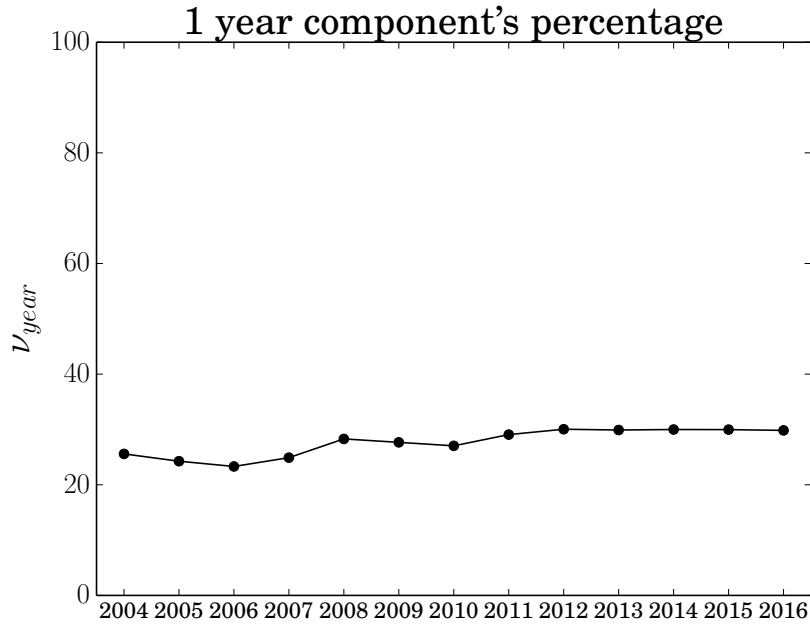


Figure 3.97: Dynamic analysis of the percentage of the one-year periodicity.

Station RN16 exhibits a predominant periodicity of one year, with a percentage weight of 29.83%, much higher than the other periodicities. With a percentage weight of 1.72%, a periodicity of 13 years is present and can be associated with the solar cycle. Time series shows a constant linear trend and data are approximately regular. The highest outlier occurs in 2015, in correspondence of the maximum of the time series. Residuals without outliers are best described by a Burr distribution. From DFA plot, three scaling regimes are found: The first, from 14 days to  $\sim 90$  days, has a Hurst exponent  $H = 0.6220 \pm 0.0060$ ; the second, from  $\sim 90$  days to  $\sim 400$  days, has a Hurst exponent  $H = 0.3676 \pm 0.0033$ ; the third, from  $\sim 400$  days to the end of the series, has a Hurst exponent  $H = 0.5642 \pm 0.0108$ .

The first two regimes show a change in the time series behaviour, from correlated to anti-correlated, while the second two regimes express the return of long-range correlations. The local Hurst exponent  $H_t$  is computed at a time window of two weeks and oscillates (almost periodically) around a value compatible with long-range correlations ( $\sim 0.65$ ). The one-year component's percentage increases from a value of approximately 25% to a value of 30% when adding new years.

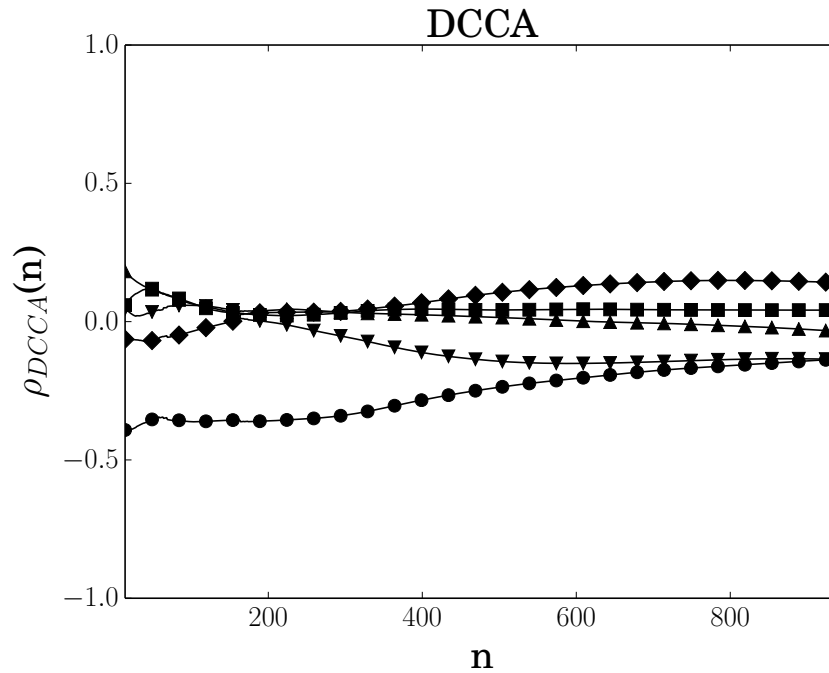


Figure 3.98: Detrended cross correlation between  $^7\text{Be}$  and available meteorological parameters (humidity ( $\circ$ ), temperature ( $\triangle$ ), pressure ( $\square$ ), wind direction ( $\nabla$ ), and wind speed ( $\diamond$ )).

Station RN16 exhibits negative cross-correlations with humidity at scales less than 400 days. There are no cross-correlations with the other meteorological parameters.

### 3.3.13 Rio de Janeiro, Brazil (RN11)

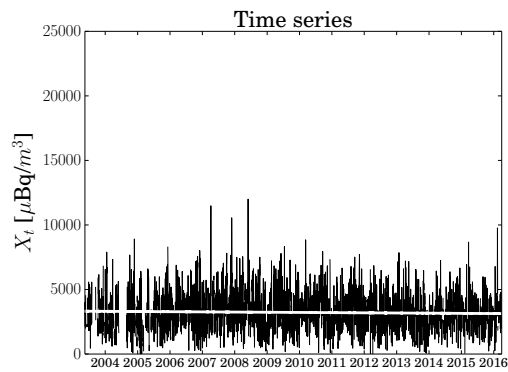


Figure 3.99: Time series with trend superimposed (solid white line).

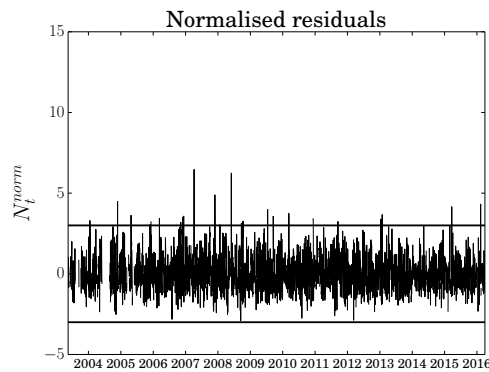


Figure 3.100: Normalised residual time series with the  $\pm 3\sigma$  thresholds (solid black lines).

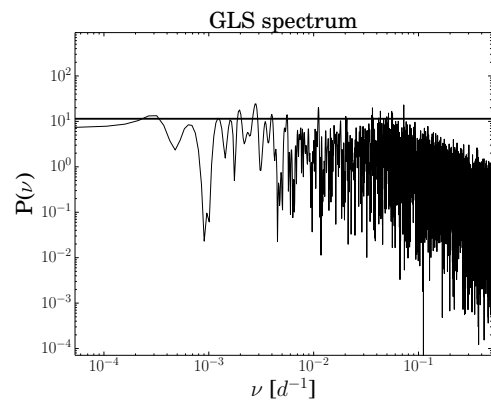


Figure 3.101: Log-log plot of the GLS spectrum with the associated threshold (solid black line).

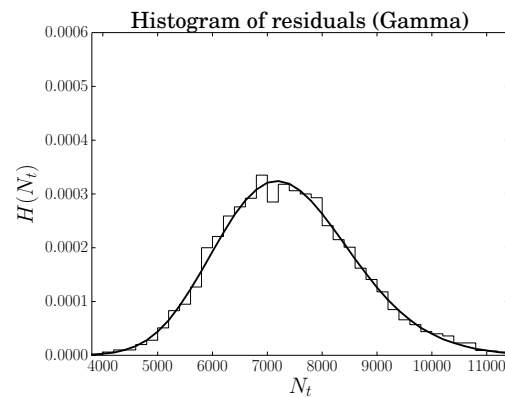


Figure 3.102: Histogram of residuals with the best-fitting distribution (no outliers).

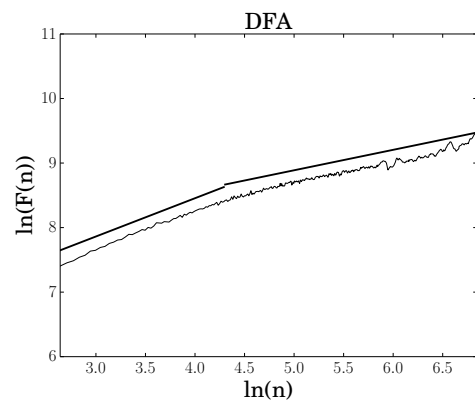


Figure 3.103: Detrended fluctuation analysis. The solid black lines are the best fit at different scales.

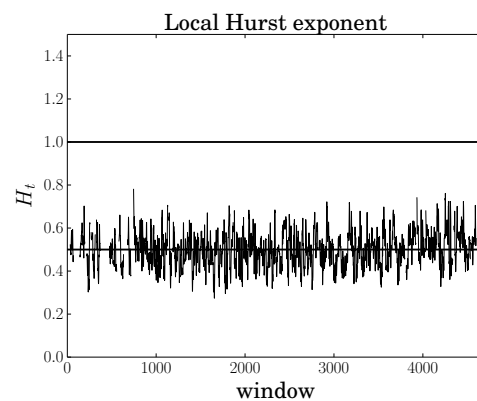


Figure 3.104: Local Hurst exponent  $H_t$  for a time window of two weeks. Solid lines represent the values of pink noise (top) and white noise (bottom).

Periodicity	Percentage	Value	Date
2 weeks	3.87	4.489	2004/11/25
1 month	3.28	6.467	2007/04/07
2 months	1.18	4.892	2007/11/28
3 months	1.32	6.243	2008/05/31
6 months	1.52	4.156	2015/03/23
1 year	1.60	4.322	2016/02/12
1.5 years	0.81		
2 years	0.52		
8.5 years	0.80		

Table 3.27: Outliers as values in the normalised residuals greater (less) than  $+ (-) 3 \sigma$ . Only very high or very low outliers are listed.

Table 3.26: Periodicities as frequencies corresponding to peaks in the spectrum higher than the threshold.

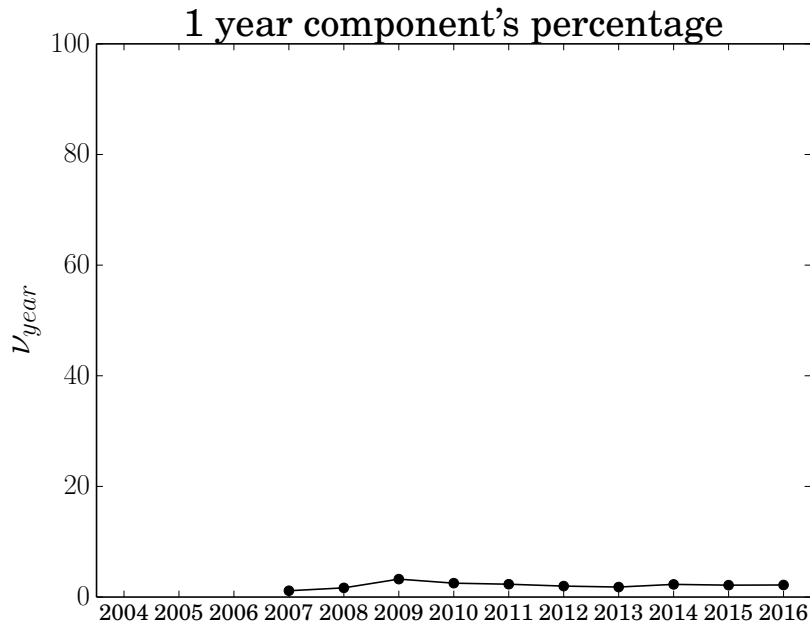


Figure 3.105: Dynamic analysis of the percentage of the one-year periodicity.

Station RN11 exhibits a predominant periodicity of two weeks, with a percentage weight of 3.87%, comparable with the other periodicities. With a percentage weight of 0.80%, a periodicity of 8.5 years is present and could be associated with the solar cycle. Time series shows a constant linear trend and data are approximately regular, except for a period in mid-2004. Two high outliers occur in mid-2007 and mid-2008. Residuals without outliers are best described by a Gamma distribution. From DFA plot, two scaling regimes are found: The first, from 14 days to  $\sim 74$  days, has a Hurst exponent  $H = 0.5930 \pm 0.0056$ ; the second, from  $\sim 74$  days to the end of the series, has a Hurst exponent  $H = 0.3169 \pm 0.0021$ . The two regimes

show a change in the time series behaviour, from correlated to anti-correlated. This is also an evidence of multifractality. The local Hurst exponent  $H_t$  is computed at a time window of two weeks and oscillates around a value compatible with white noise ( $\sim 0.5$ ). The one-year component's percentage remains approximately constant at a value of 2% when adding new years.

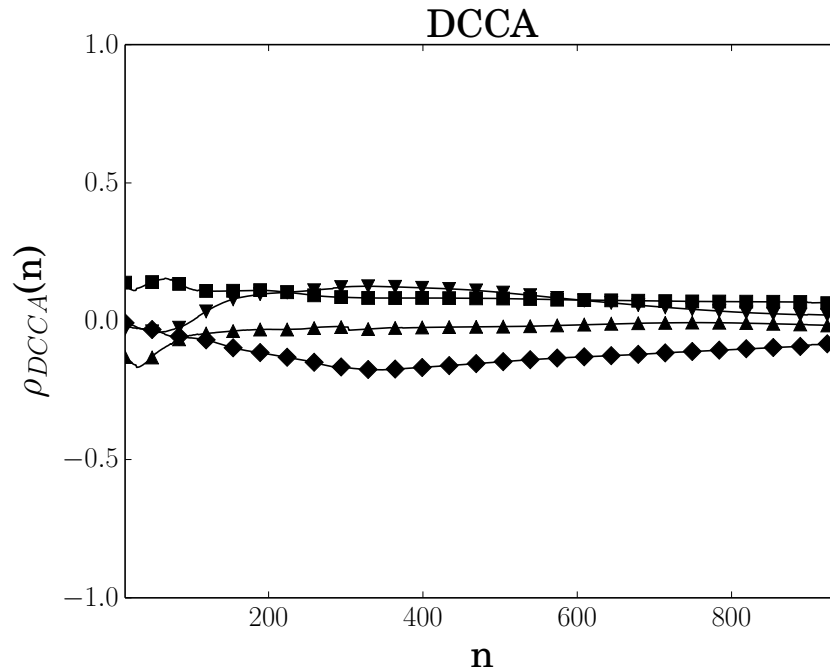


Figure 3.106: Detrended cross correlation between <sup>7</sup>Be and available meteorological parameters (humidity (○), temperature (△), pressure (□), wind direction (▽), and wind speed (◇)).

Station RN11 does not exhibit cross-correlations with the available meteorological parameters. Humidity time series was not suitable for the analysis.

### 3.3.14 Cocos Islands, Australia (RN08)

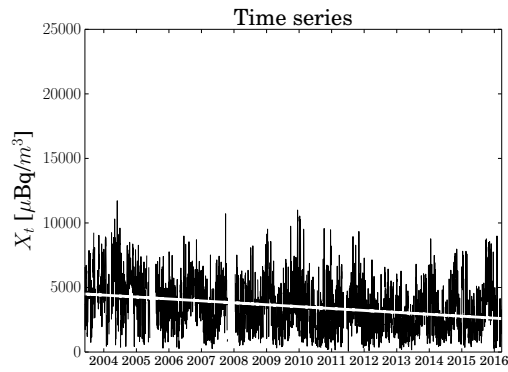


Figure 3.107: Time series with trend superimposed (solid white line).

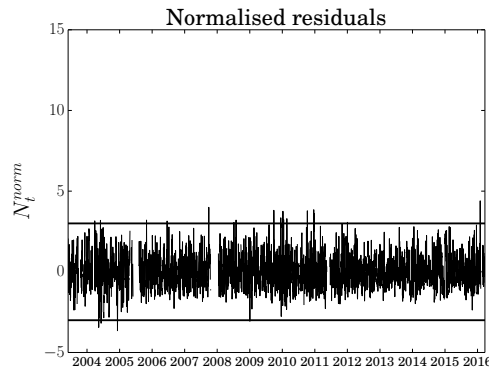


Figure 3.108: Normalised residual time series with the  $\pm 3\sigma$  thresholds (solid black lines).

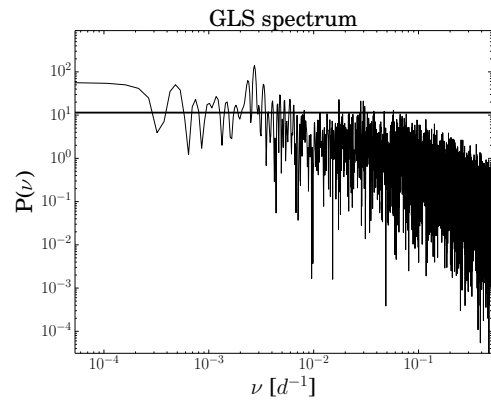


Figure 3.109: Log-log plot of the GLS spectrum with the associated threshold (solid black line).

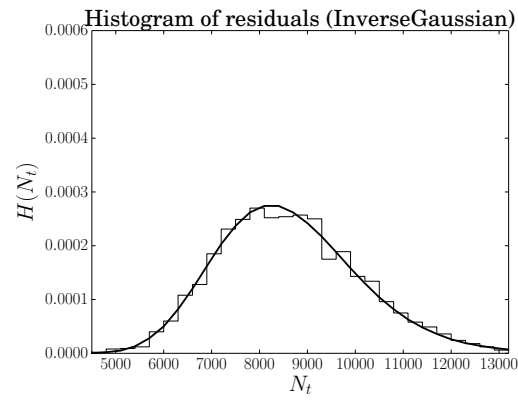


Figure 3.110: Histogram of residuals with the best-fitting distribution (no outliers).

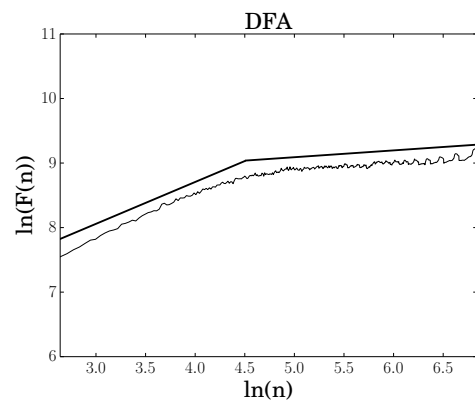


Figure 3.111: Detrended fluctuation analysis. The solid black lines are the best fit at different scales.

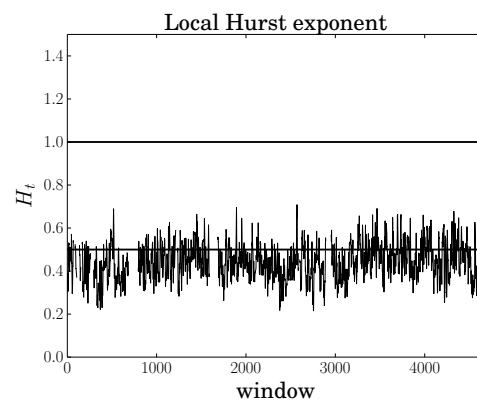


Figure 3.112: Local Hurst exponent  $H_t$  for a time window of two weeks. Solid lines represent the values of pink noise (top) and white noise (bottom).

Periodicity	Percentage
2 weeks	1.27
1 month	3.33
2 months	0.69
4 months	0.43
6 months	4.98
1 year	10.92
1.5 years	0.76
2 years	0.68
2.5 years	1.46
3.5 years	0.56
5.5 years	1.52
14 years	2.39

Value	Date
4.399	2016/01/31

Table 3.29: Outliers as values in the normalised residuals greater (less) than + (-) 3  $\sigma$ . Only very high or very low outliers are listed.

Table 3.28: Periodicities as frequencies corresponding to peaks in the spectrum higher than the threshold.

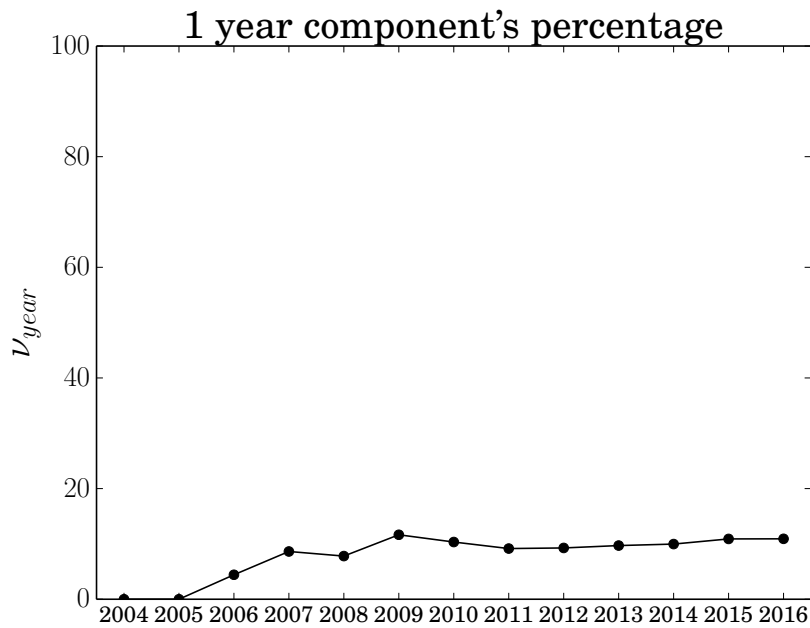


Figure 3.113: Dynamic analysis of the percentage of the one-year periodicity.

Station RN08 exhibits a predominant periodicity of one year, with a percentage weight of 10.92%, higher than the other periodicities. With a percentage weight of 2.39%, a periodicity of 14 years is present and could be associated with the solar cycle. Time series shows a downward linear trend and data are approximately regular, except for a period in mid-2005 and another one at the end of 2007. High outliers do not occur in the residual time series, as confirmed by the absence of

great variations in the time series. Residuals without outliers are best described by an Inverse Gaussian distribution. From DFA plot, two scaling regimes are found: The first, from 14 days to  $\sim 90$  days, has a Hurst exponent  $H = 0.6485 \pm 0.0075$ ; the second, from  $\sim 90$  days to the end of the series, has a Hurst exponent  $H = 0.1056 \pm 0.0023$ . The first regime shows a correlated behaviour of the series, while the second regime probably expresses the limitations of the algorithm in accurately estimating the degree of correlations in the residual time series [94]. The local Hurst exponent  $H_t$  is computed at a time window of two weeks and oscillates first around a value compatible with long-range anti-correlations ( $\sim 0.4$ ), then oscillates around a value compatible with white noise ( $\sim 0.5$ ). The one-year component's percentage goes from 0% to 10% and then remains approximately constant when adding the other years.

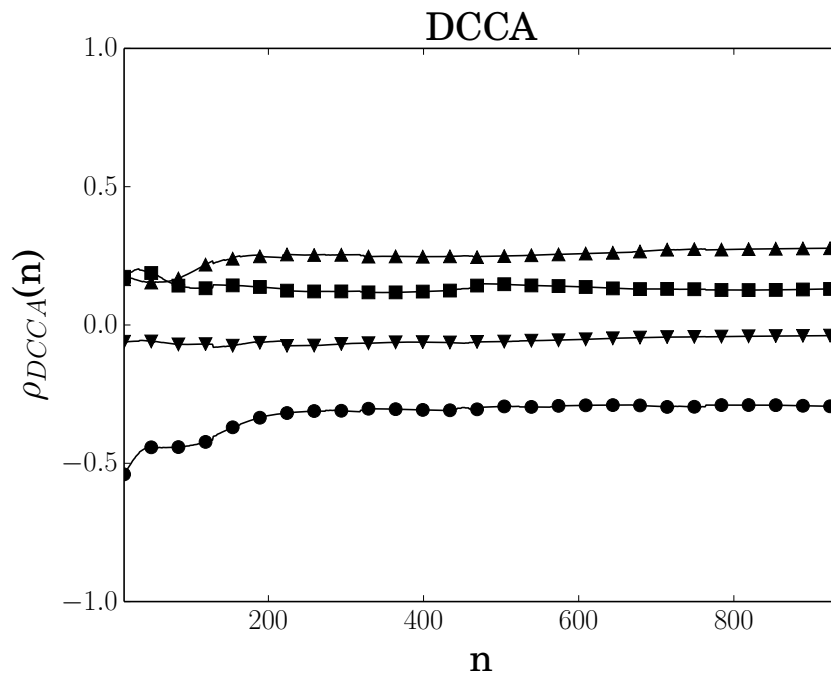


Figure 3.114: Detrended cross correlation between <sup>7</sup>Be and available meteorological parameters (humidity (○), temperature (△), pressure (□), wind direction (▽), and wind speed (◇)).

Station RN08 exhibits negative cross-correlations with humidity at all scales and positive cross-correlations with temperature at all scales. There are no cross-correlations with pressure and wind direction. Wind speed time series was not available for the analysis.

### 3.3.15 Ashland, KS, USA (RN74)

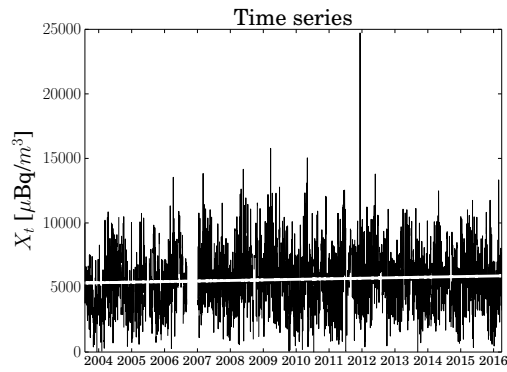


Figure 3.115: Time series with trend superimposed (solid white line).

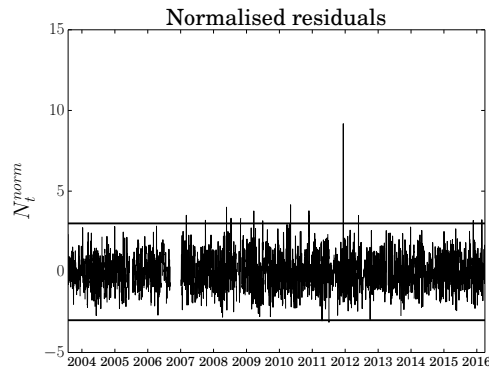


Figure 3.116: Normalised residual time series with the  $\pm 3\sigma$  thresholds (solid black lines).

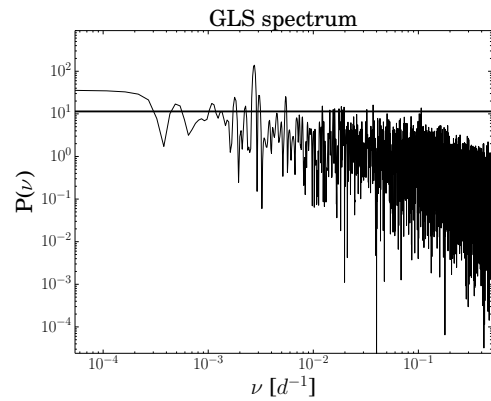


Figure 3.117: Log-log plot of the GLS spectrum with the associated threshold (solid black line).

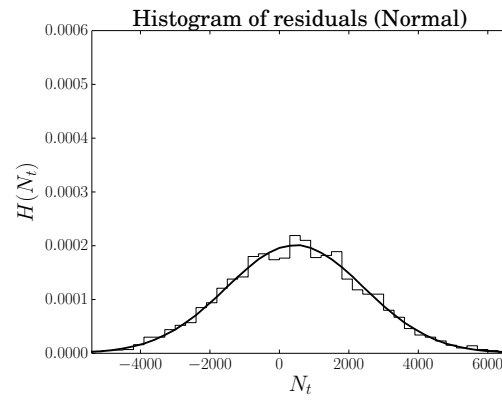


Figure 3.118: Histogram of residuals with the best-fitting distribution (no outliers).

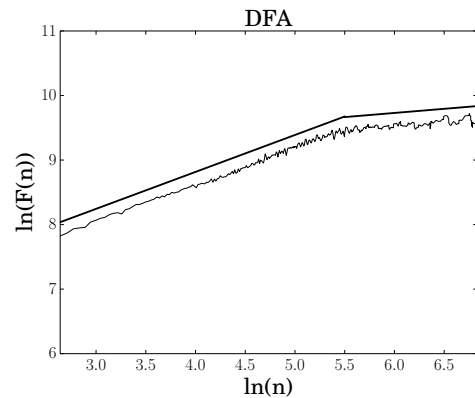


Figure 3.119: Detrended fluctuation analysis. The solid black lines are the best fit at different scales.

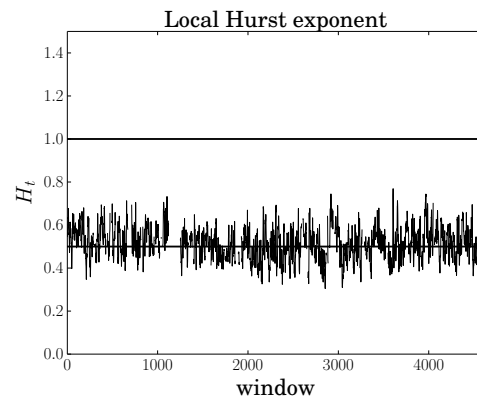


Figure 3.120: Local Hurst exponent  $H_t$  for a time window of two weeks. Solid lines represent the values of pink noise (top) and white noise (bottom).

Periodicity	Percentage	Value	Date
1 week	0.57	4.005	2008/05/24
1 month	1.25	9.180	2011/12/11
2 months	4.31		
3 months	0.67		
6 months	1.12		
1 year	6.54		
1.5 years	0.74		
2 years	0.38		
2.5 years	0.84		
5.5 years	0.59		
14 years	1.73		

Table 3.31: Outliers as values in the normalised residuals greater (less) than + (-) 3  $\sigma$ . Only very high or very low outliers are listed.

Table 3.30: Periodicities as frequencies corresponding to peaks in the spectrum higher than the threshold.

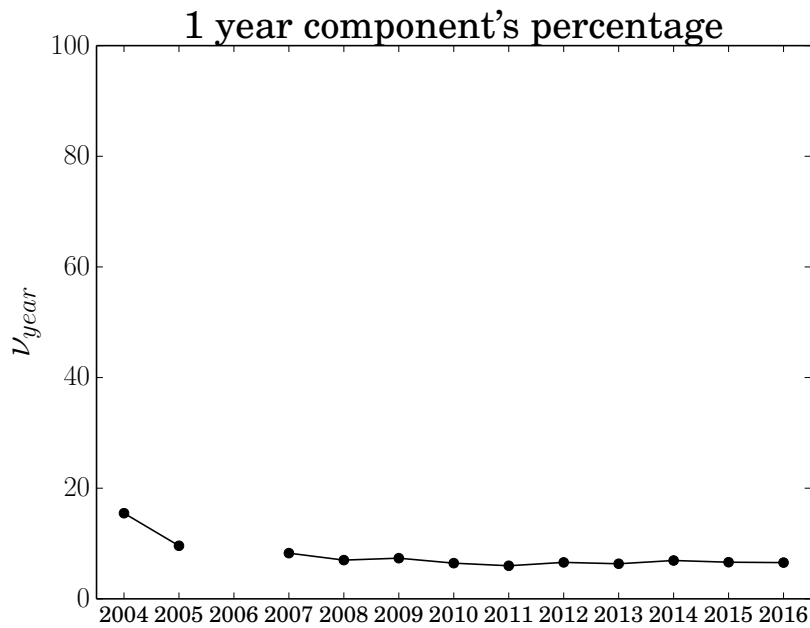


Figure 3.121: Dynamic analysis of the percentage of the one-year periodicity.

Station RN74 exhibits a predominant periodicity of one year, with a percentage weight of 6.54%, higher than the other periodicities. With a percentage weight of 1.73%, a periodicity of 14 years is present and could be associated with the solar cycle. Time series shows a slightly upward linear trend and data are approximately regular, except for a period at the end of 2006. An evidently high outlier occurs in the residual time series, in correspondence of the maximum of the time series. Residuals without outliers are best described by a Normal distribution. From DFA

plot, two scaling regimes are found: The first, from 14 days to  $\sim 245$  days, has a Hurst exponent  $H = 0.5724 \pm 0.0030$ ; the second, from  $\sim 245$  days to the end of the series, has a Hurst exponent  $H = 0.1281 \pm 0.0044$ . The first regime shows a correlated behaviour of the series, while the second regime probably expresses the limitations of the algorithm in accurately estimating the degree of correlations in the residual time series [94]. The local Hurst exponent  $H_t$  is computed at a time window of two weeks and oscillates around a value compatible with white noise ( $\sim 0.5$ ). The one-year component's percentage goes from a value of  $\sim 20\%$  to one of  $\sim 7\%$  and then remains approximately constant when adding the other years. Adding the year 2006 makes the total number of missing data exceed the threshold of 20%, hence the series is not analysed.

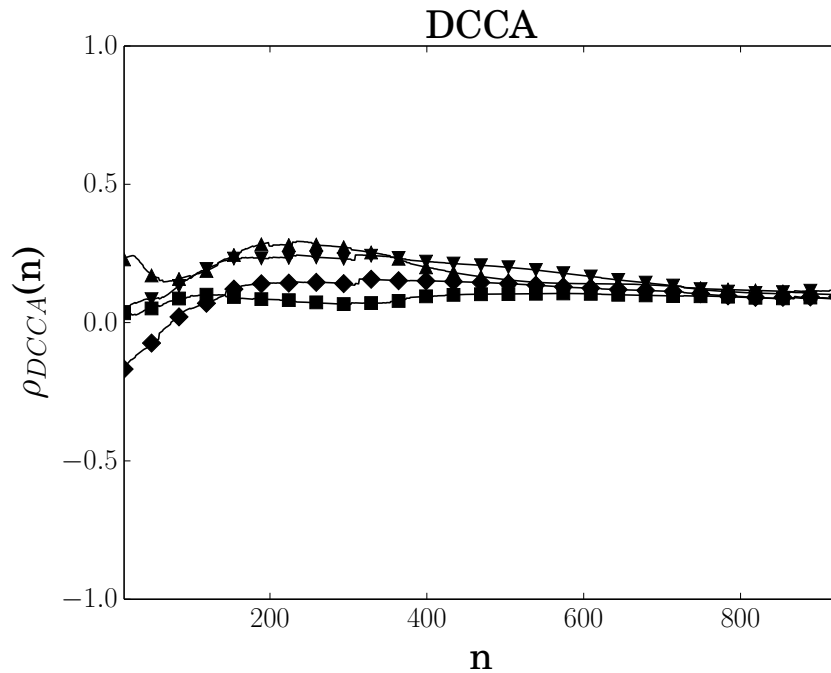


Figure 3.122: Detrended cross correlation between <sup>7</sup>Be and available meteorological parameters (humidity (○), temperature (△), pressure (□), wind direction (▽), and wind speed (◇)).

Station RN74 exhibits positive cross-correlations with temperature and wind direction at scales between 200 and 400 days. There are no cross-correlations with pressure and wind speed. Humidity time series was not suitable for the analysis.

### 3.3.16 Schauinsland/Freiburg, Germany (RN33)

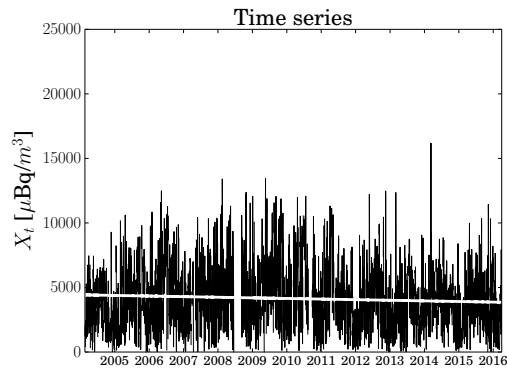


Figure 3.123: Time series with trend superimposed (solid white line).

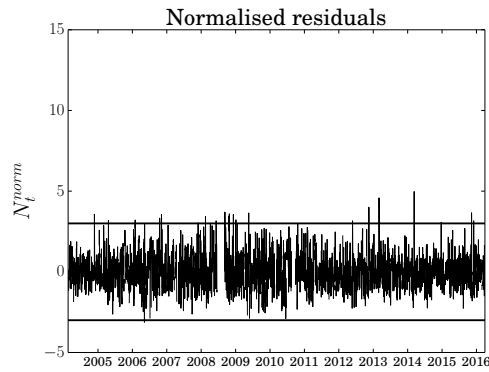


Figure 3.124: Normalised residual time series with the  $\pm 3\sigma$  thresholds (solid black lines).

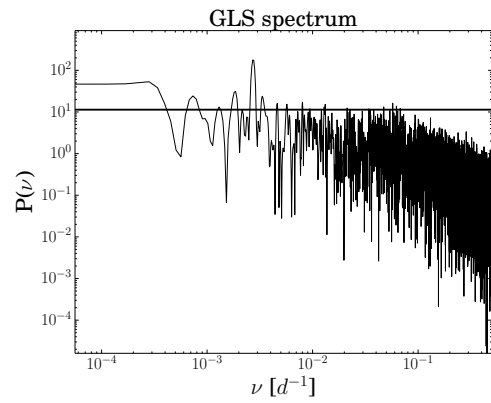


Figure 3.125: Log-log plot of the GLS spectrum with the associated threshold (solid black line).

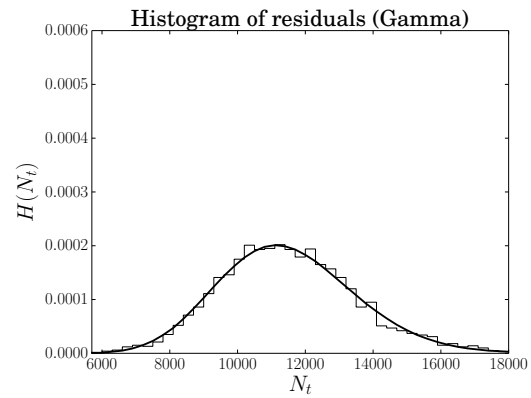


Figure 3.126: Histogram of residuals with the best-fitting distribution (no outliers).

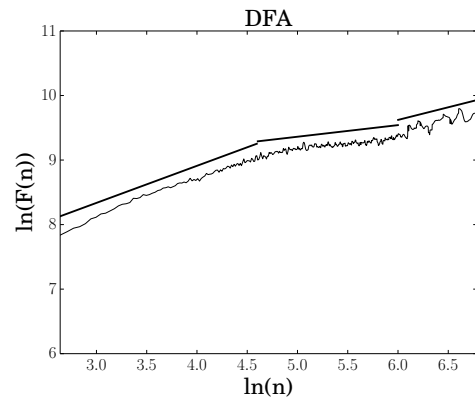


Figure 3.127: Detrended fluctuation analysis. The solid black lines are the best fit at different scales.

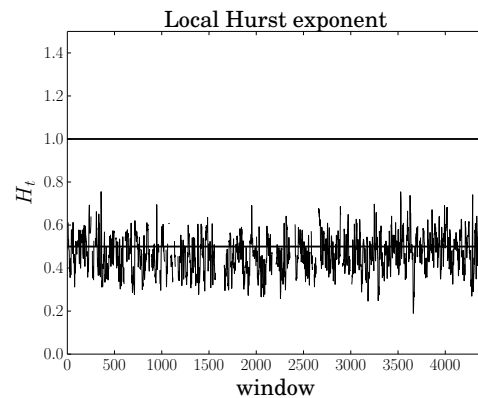


Figure 3.128: Local Hurst exponent  $H_t$  for a time window of two weeks. Solid lines represent the values of pink noise (top) and white noise (bottom).

Periodicity	Percentage	Value	Date
2 weeks	2.50	5.021	2012/02/10
1 month	1.07	4.008	2012/11/15
2 months	0.58	4.582	2013/03/03
3 months	1.77	4.974	2014/03/11
4 months	1.17		
6 months	1.42		
1 year	9.47		
1.5 years	1.83		
2 years	0.55		
3.5 years	1.00		
9.5 years	3.43		

Table 3.33: Outliers as values in the normalised residuals greater (less) than + (-)  $3\sigma$ . Only very high or very low outliers are listed.

Table 3.32: Periodicities as frequencies corresponding to peaks in the spectrum higher than the threshold.

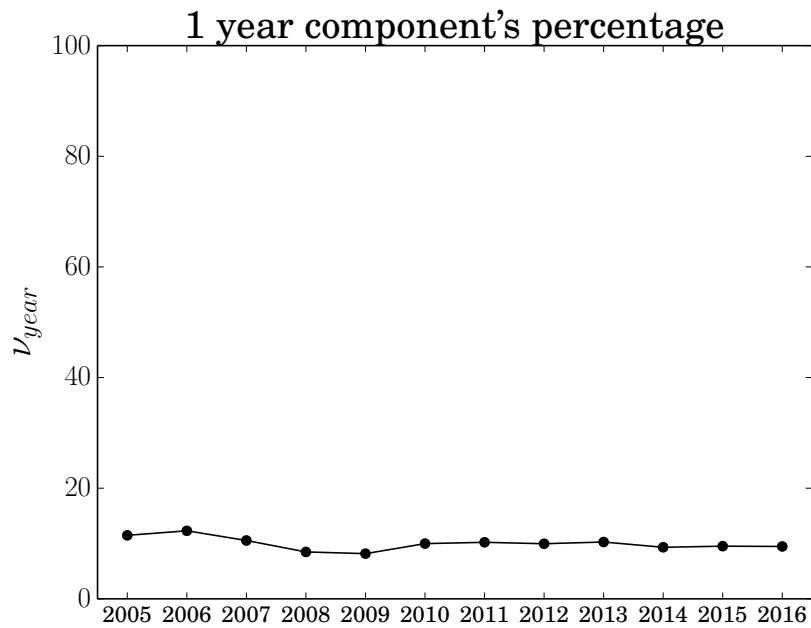


Figure 3.129: Dynamic analysis of the percentage of the one-year periodicity.

Station RN33 exhibits a predominant periodicity of one year, with a percentage weight of 9.47%, higher than the other periodicities. With a percentage weight of 3.43%, a periodicity of 9.5 years is present and can be associated with the solar cycle. Time series shows a constant linear trend and data are approximately regular, except for a period in mid-2008. High outliers do not occur in the residual time series, as confirmed by the absence of great variations in the time series. Residuals without outliers are best described by a Gamma distribution. From

DFA plot, three scaling regimes are found: The first, from 14 days to  $\sim 100$  days, has a Hurst exponent  $H = 0.5745 \pm 0.0065$ ; the second, from  $\sim 100$  days to  $\sim 400$  days, has a Hurst exponent  $H = 0.1800 \pm 0.0045$ ; the third, from  $\sim 400$  days to the end of the series, has a Hurst exponent  $H = 0.3918 \pm 0.0128$ . The first two regimes show a change in the series from a correlated behaviour to an anti-correlated one, while the third regime shows a less anti-correlated behaviour of the residuals at big time scales. The local Hurst exponent  $H_t$  is computed at a time window of two weeks and oscillates around a value compatible with white noise ( $\sim 0.5$ ). The one-year component's percentage remains approximately constant around a value of 10% when adding new years.

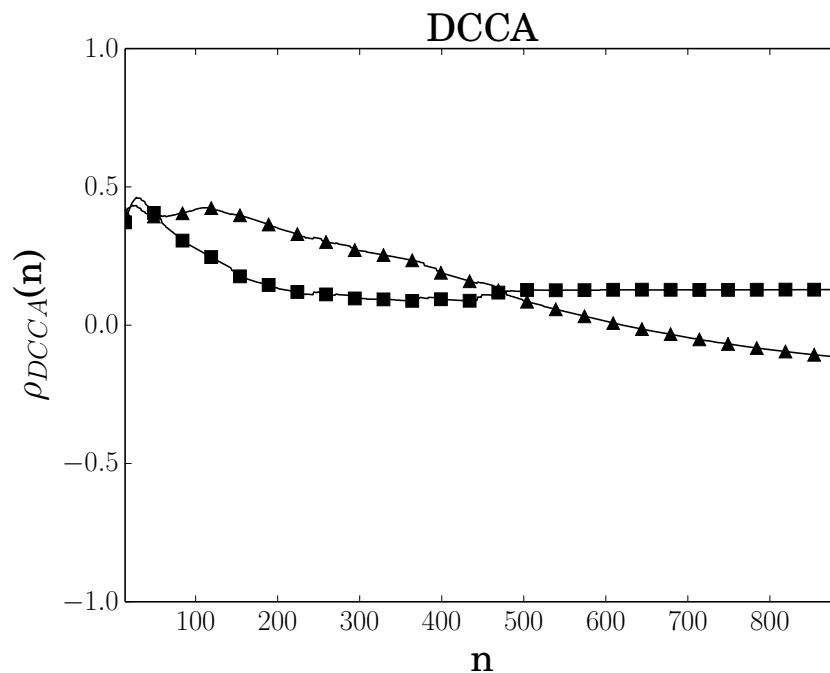


Figure 3.130: Detrended cross correlation between <sup>7</sup>Be and available meteorological parameters (humidity (○), temperature (△), pressure (□), wind direction (▽), and wind speed (◇)).

Station RN33 exhibits positive cross-correlations with pressure at very small scales ( $< 50$  days) and with temperature at scales less than 400 days. The other meteorological parameters time series were not suitable for the analysis.

### 3.3.17 Tristan da Cunha, United Kingdom (RN68)

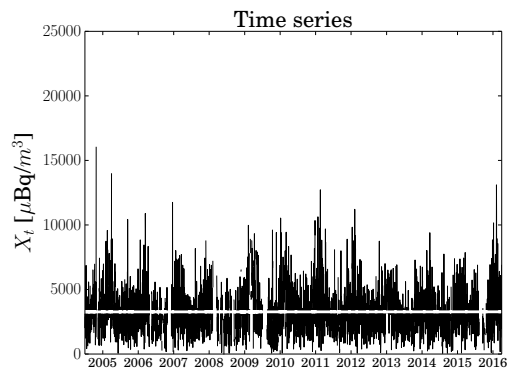


Figure 3.131: Time series with trend superimposed (solid white line).

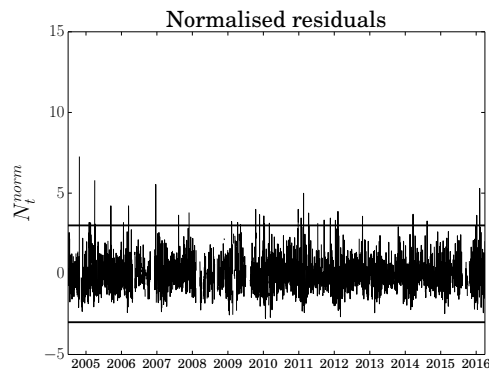


Figure 3.132: Normalised residual time series with the  $\pm 3\sigma$  thresholds (solid black lines).

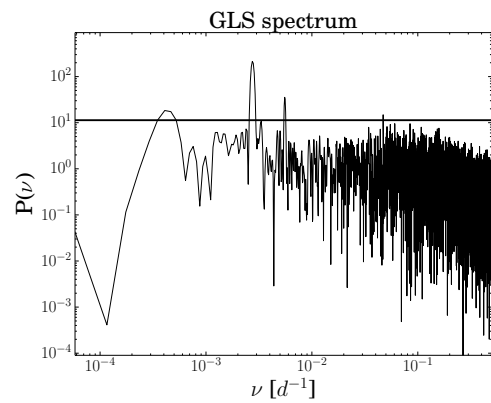


Figure 3.133: Log-log plot of the GLS spectrum with the associated threshold (solid black line).

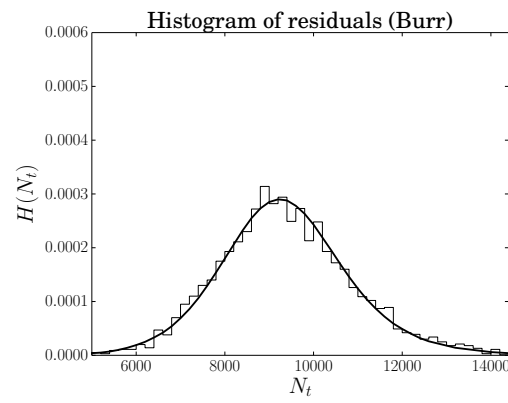


Figure 3.134: Histogram of residuals with the best-fitting distribution (no outliers).

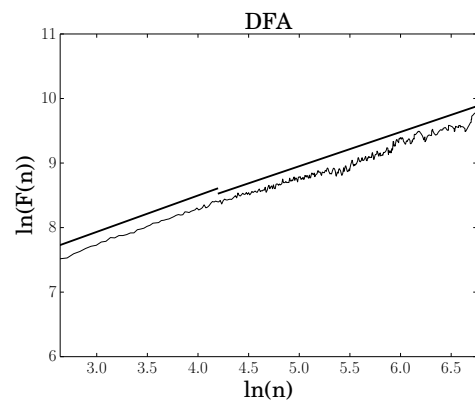


Figure 3.135: Detrended fluctuation analysis. The solid black lines are the best fit at different scales.

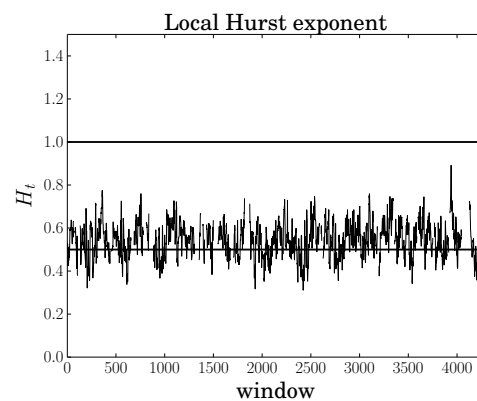


Figure 3.136: Local Hurst exponent  $H_t$  for a time window of two weeks. Solid lines represent the values of pink noise (top) and white noise (bottom).

Periodicity	Percentage	Value	Date
2 weeks	1.15	7.238	2004/10/25
6 months	1.39	5.764	2005/04/01
1 year	9.66	4.213	2005/09/14
6.5 years	0.79	4.209	2006/03/15
		5.540	2006/12/20
		4.992	2011/02/19
		5.296	2016/02/06
		4.047	2016/02/07

Table 3.34: Periodicities as frequencies corresponding to peaks in the spectrum higher than the threshold.

Table 3.35: Outliers as values in the normalised residuals greater (less) than + (-)  $3\sigma$ . Only very high or very low outliers are listed.

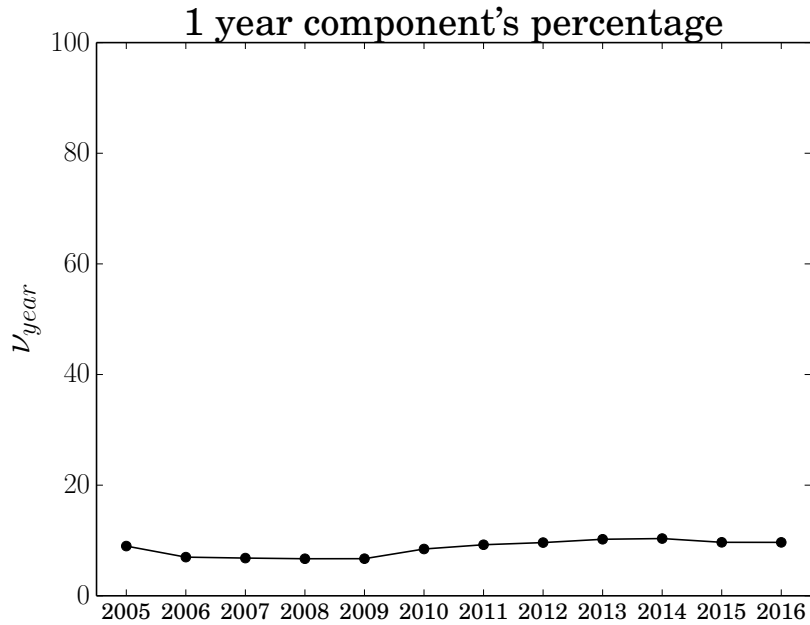


Figure 3.137: Dynamic analysis of the percentage of the one-year periodicity.

Station RN68 exhibits a predominant periodicity of one year, with a percentage weight of 9.66%, higher than the other periodicities. Time series shows a constant linear trend and data are approximately regular, except for a small period in mid-2009. A high outlier ( $\sim 7\sigma$ ) occurs in the residual time series at the end of 2004, in correspondence of the maximum of the time series. Residuals without outliers are best described by a Burr distribution. From DFA plot, two scaling regimes are found: The first, from 14 days to  $\sim 67$  days, has a Hurst exponent  $H = 0.5641 \pm 0.0051$ ; the second, from  $\sim 67$  days to the end of the series, has a Hurst exponent  $H = 0.5300 \pm 0.0032$ . The first two regimes show a change in

the series from a correlated behaviour to an uncorrelated one. The local Hurst exponent  $H_t$  is computed at a time window of two weeks and oscillates around a value compatible with long-range correlations ( $\sim 0.55$ ). The one-year component's percentage remains approximately constant around a value of 10% when adding new years.

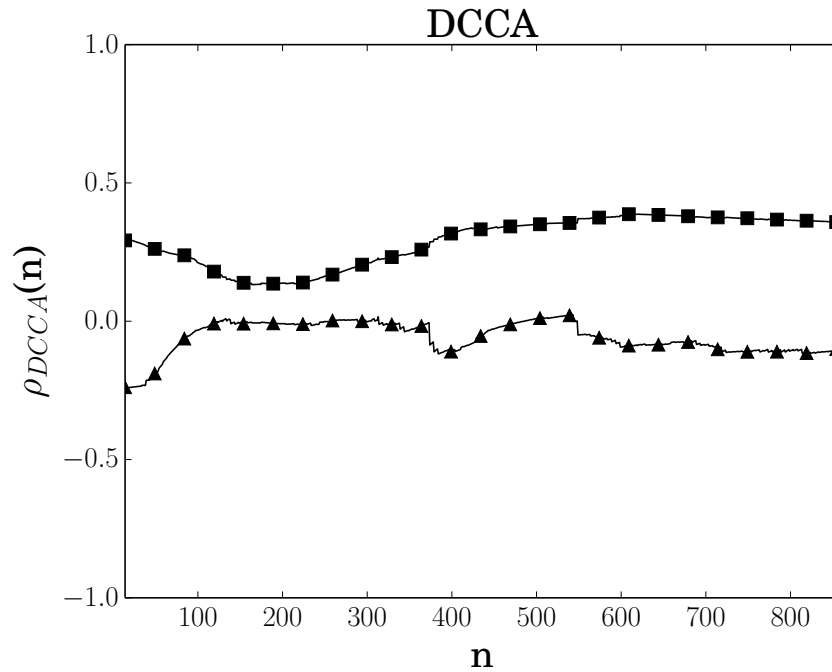


Figure 3.138: Detrended cross correlation between  $^7\text{Be}$  and available meteorological parameters (humidity ( $\circ$ ), temperature ( $\triangle$ ), pressure ( $\square$ ), wind direction ( $\nabla$ ), and wind speed ( $\diamond$ )).

Station RN68 exhibits positive cross-correlations with pressure at very small scales ( $< 50$  days) and at scales greater than 400 days. There are no cross-correlations with temperature. The other meteorological parameters time series were not suitable for the analysis.

### 3.3.18 Melbourne, FL, USA (RN72)

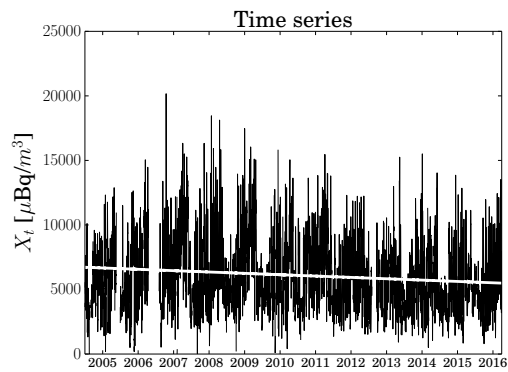


Figure 3.139: Time series with trend superimposed (solid white line).

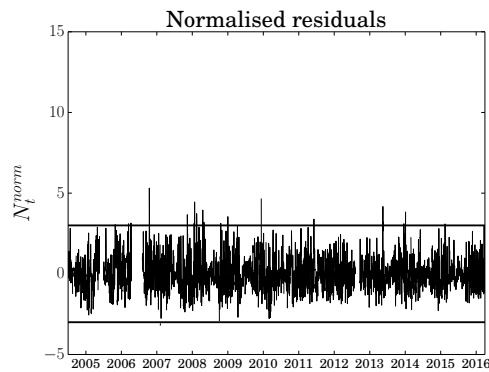


Figure 3.140: Normalised residual time series with the  $\pm 3\sigma$  thresholds (solid black lines).

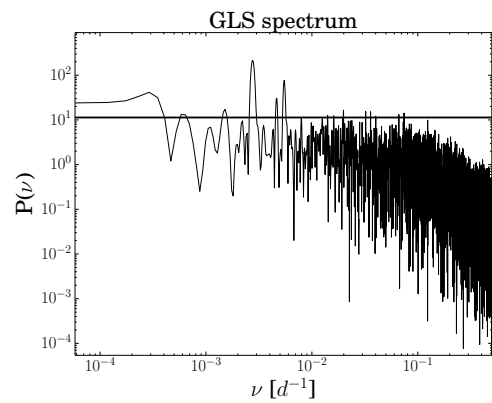


Figure 3.141: Log-log plot of the GLS spectrum with the associated threshold (solid black line).

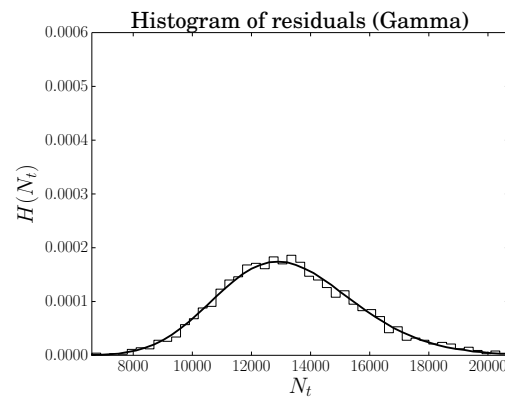


Figure 3.142: Histogram of residuals with the best-fitting distribution (no outliers).

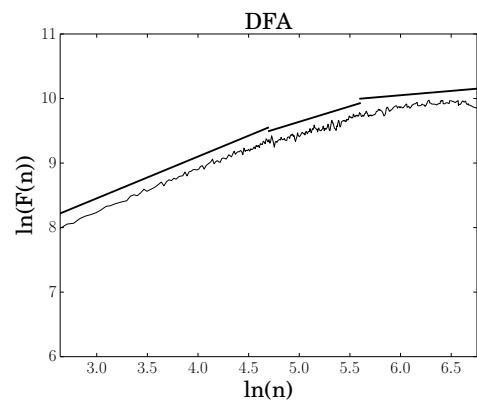


Figure 3.143: Detrended fluctuation analysis. The solid black lines are the best fit at different scales.

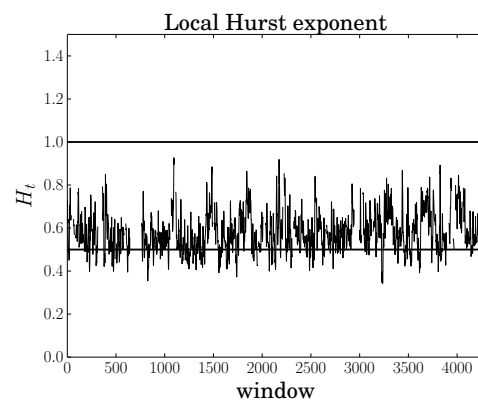


Figure 3.144: Local Hurst exponent  $H_t$  for a time window of two weeks. Solid lines represent the values of pink noise (top) and white noise (bottom).

Periodicity	Percentage	Value	Date
2 weeks	1.25	5.311	2006/10/16
1 month	2.25	4.452	2008/01/25
2 months	1.99	4.637	2009/12/11
6 months	5.49	4.170	2013/05/16
1 year	10.29		
2 years	0.77		
4.5 years	0.51		
9.5 years	2.25		

Table 3.37: Outliers as values in the normalised residuals greater (less) than + (-) 3  $\sigma$ . Only very high or very low outliers are listed.

Table 3.36: Periodicities as frequencies corresponding to peaks in the spectrum higher than the threshold.

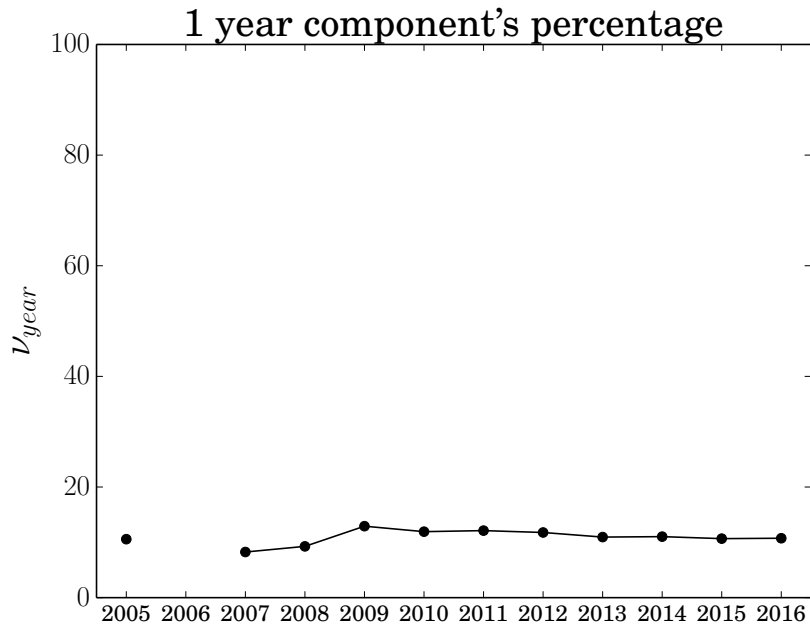


Figure 3.145: Dynamic analysis of the percentage of the one-year periodicity.

Station RN72 exhibits a predominant periodicity of one year, with a percentage weight of 10.29%, higher than the other periodicities. With a percentage weight of 2.25%, a periodicity of 9.5 years is present and could be associated with the solar cycle. Time series shows a slightly downward linear trend and data are approximately regular, except for a period in mid-2006. A high outlier occurs in the residual time series at the end of 2006, in correspondence of the maximum of the time series. Residuals without outliers are best described by a Gamma distribution. From DFA plot, three scaling regimes are found: The first, from 14 days to  $\sim 110$  days, has a Hurst exponent  $H = 0.6472 \pm 0.0046$ ; the second, from  $\sim 110$  days to  $\sim 270$  days, has a Hurst exponent  $H = 0.4801 \pm 0.0111$ ; the third, from

$\sim 270$  days to the end of the series, has a Hurst exponent  $H = 0.1341 \pm 0.0054$ . The first two regimes show a change in the series from a correlated behaviour to an uncorrelated one, while the third regime shows an anti-correlated behaviour of the residuals at big time scales, or it probably expresses the limitations of the algorithm in accurately estimating the degree of correlations in the residual time series [94]. The local Hurst exponent  $H_t$  is computed at a time window of two weeks and oscillates around a value compatible with long-range correlations ( $\sim 0.6$ ). The one-year component's percentage remains approximately constant around a value of 10% when adding new years. Adding the year 2006 makes the total number of missing data exceed the threshold of 20%, hence the series is not analysed.

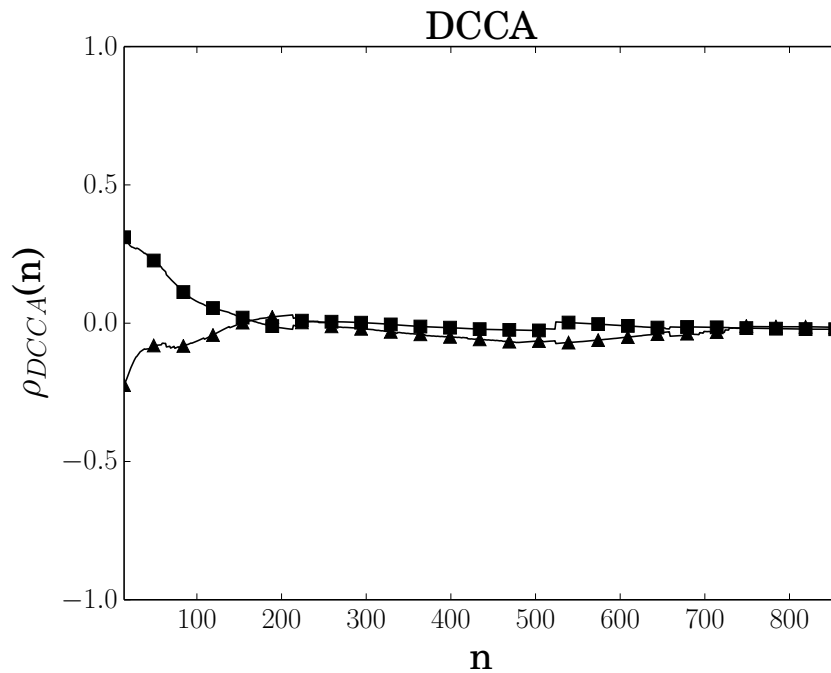


Figure 3.146: Detrended cross correlation between <sup>7</sup>Be and available meteorological parameters (humidity (○), temperature (△), pressure (□), wind direction (▽), and wind speed (◇)).

Station RN72 exhibits positive cross-correlations with pressure at very small scales ( $< 50$  days). There are no cross-correlations with temperature. The other meteorological parameters time series were not suitable for the analysis.

### 3.3.19 Nadi, Fiji (RN26)

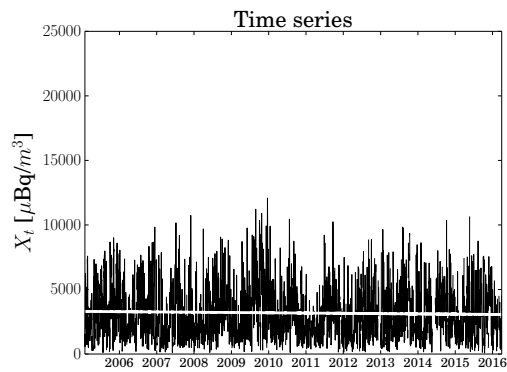


Figure 3.147: Time series with trend superimposed (solid white line).

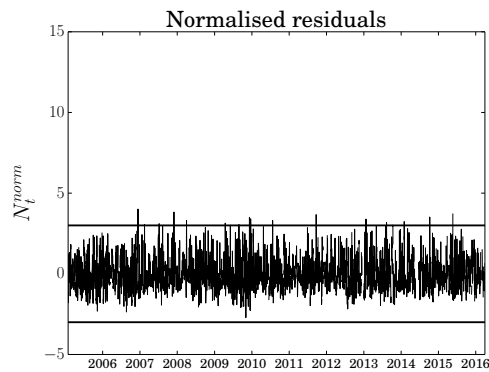


Figure 3.148: Normalised residual time series with the  $\pm 3\sigma$  thresholds (solid black lines).

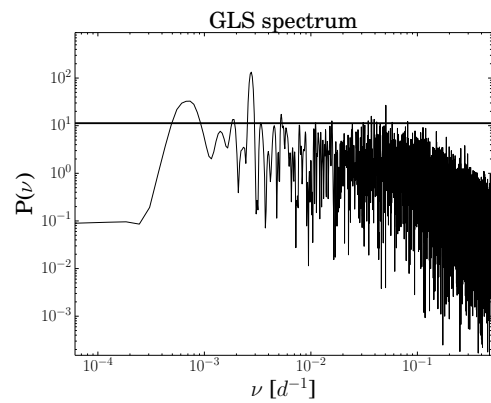


Figure 3.149: Log-log plot of the GLS spectrum with the associated threshold (solid black line).

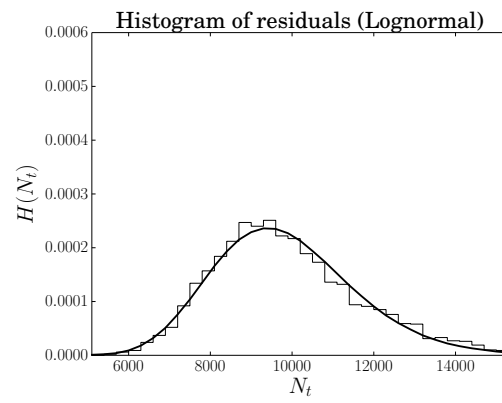


Figure 3.150: Histogram of residuals with the best-fitting distribution (no outliers).

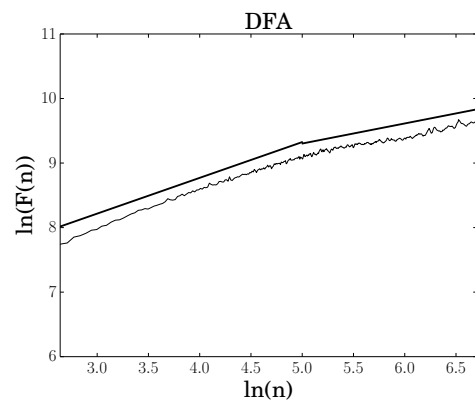


Figure 3.151: Detrended fluctuation analysis. The solid black lines are the best fit at different scales.

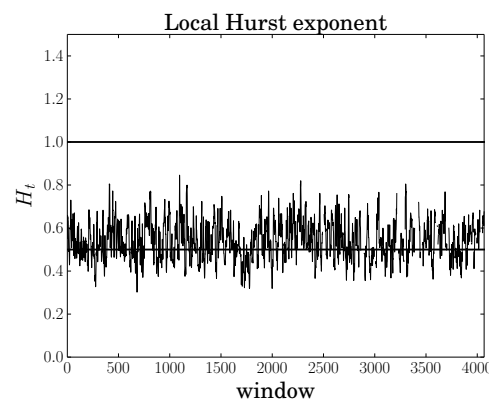


Figure 3.152: Local Hurst exponent  $H_t$  for a time window of two weeks. Solid lines represent the values of pink noise (top) and white noise (bottom).

Periodicity	Percentage	Value	Date
2 weeks	2.34	4.013	2006/12/13
1 month	3.98		
2 months	0.91		
3 months	0.51		
6 months	0.87		
1 year	7.39		
1.5 years	0.68		
3.5 years	2.52		

Table 3.39: Outliers as values in the normalised residuals greater (less) than + (-)  $3\sigma$ . Only very high or very low outliers are listed.

Table 3.38: Periodicities as frequencies corresponding to peaks in the spectrum higher than the threshold.

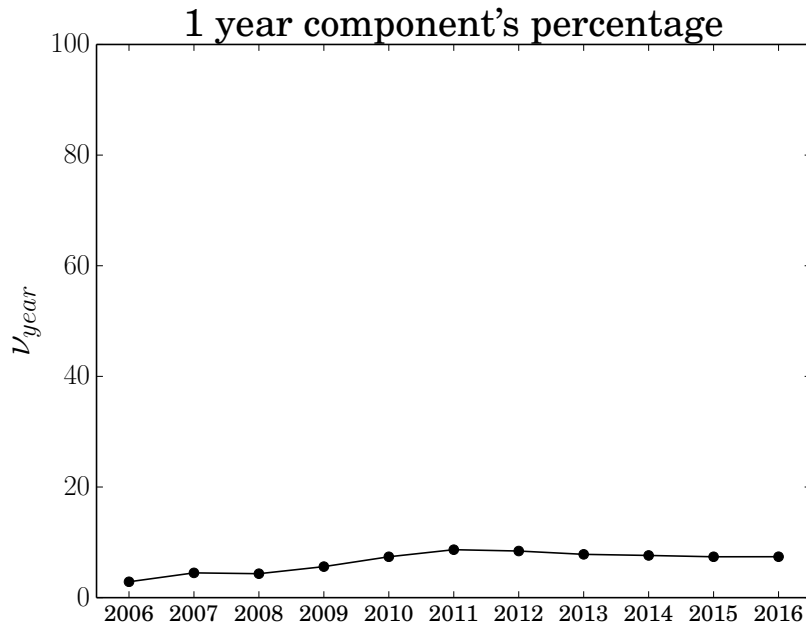


Figure 3.153: Dynamic analysis of the percentage of the one-year periodicity.

Station RN26 exhibits a predominant periodicity of one year, with a percentage weight of 7.39%, higher than the other periodicities. Time series shows a constant linear trend and data are approximately regular. High outliers do not occur in the residual time series, as confirmed by the absence of great variations in the time series. Residuals without outliers are best described by a Lognormal distribution. From DFA plot, two scaling regimes are found: The first, from 14 days to  $\sim 150$  days, has a Hurst exponent  $H = 0.5542 \pm 0.0035$ ; the second, from  $\sim 150$  days to the end of the series, has a Hurst exponent  $H = 0.3110 \pm 0.0023$ . The different regimes show a change in correlation properties of the residuals, from slightly correlated to anti-correlated. This is also an evidence of multifractality.

The local Hurst exponent  $H_t$  is computed at a time window of two weeks and oscillates around a value compatible with long-range correlations ( $\sim 0.6$ ). The one-year component's percentage has initially small values and eventually remains approximately constant around a value of 8% when adding new years.

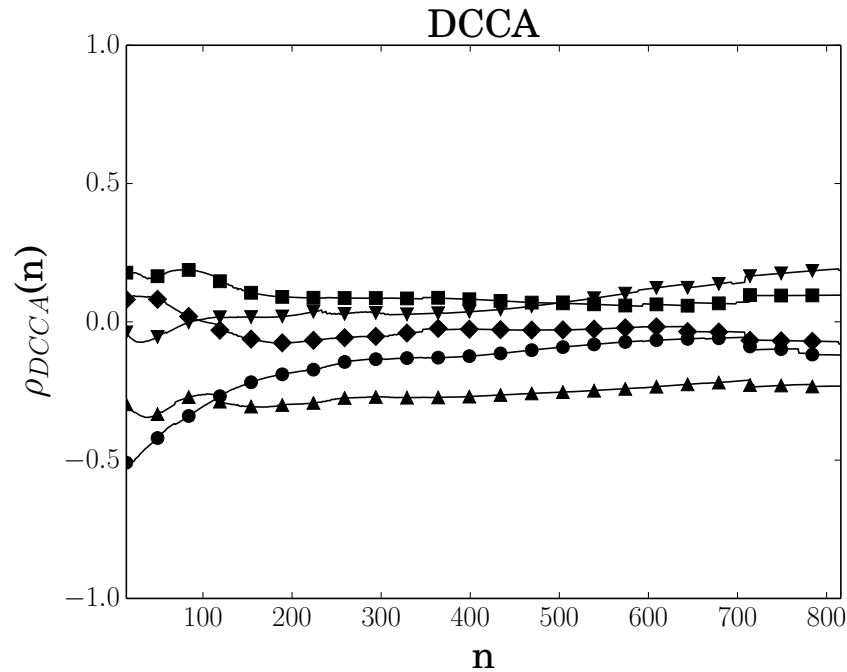


Figure 3.154: Detrended cross correlation between  $^7\text{Be}$  and available meteorological parameters (humidity (○), temperature (△), pressure (□), wind direction (▽), and wind speed (◇)).

Station RN26 exhibits negative cross-correlations with humidity at small scales ( $< 200$  days) and with temperature at all scales. There are no cross-correlations with the other meteorological parameters.

### 3.3.20 Oahu, Hawaii, USA (RN79)

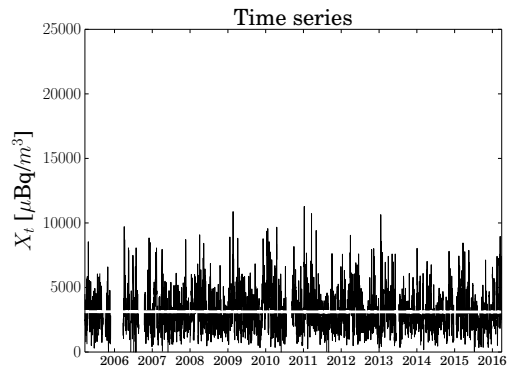


Figure 3.155: Time series with trend superimposed (solid white line).

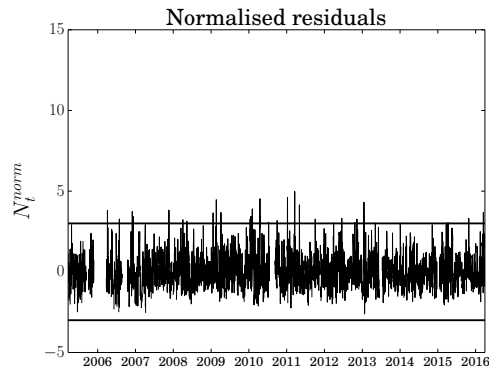


Figure 3.156: Normalised residual time series with the  $\pm 3\sigma$  thresholds (solid black lines).

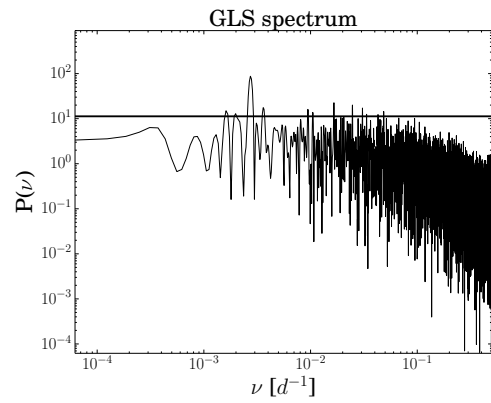


Figure 3.157: Log-log plot of the GLS spectrum with the associated threshold (solid black line).

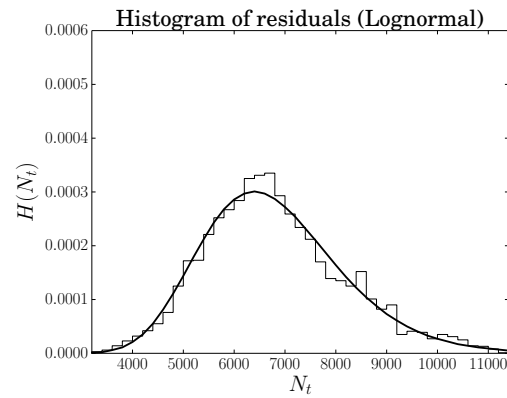


Figure 3.158: Histogram of residuals with the best-fitting distribution (no outliers).

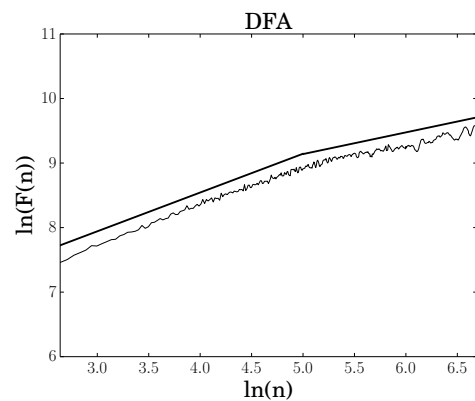


Figure 3.159: Detrended fluctuation analysis. The solid black lines are the best fit at different scales.

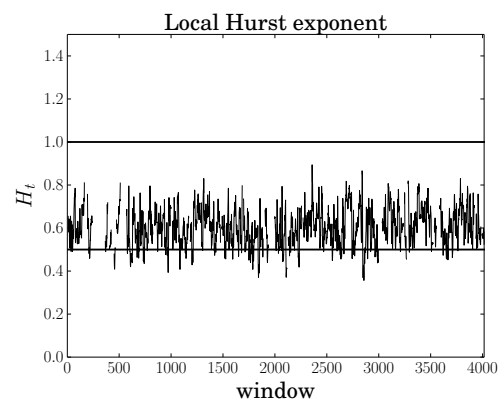


Figure 3.160: Local Hurst exponent  $H_t$  for a time window of two weeks. Solid lines represent the values of pink noise (top) and white noise (bottom).

Periodicity	Percentage	Value	Date
2 weeks	0.95	4.468	2009/02/20
1 month	3.37	4.528	2010/04/18
2 months	1.29	4.598	2011/01/09
3 months	0.66	4.982	2011/03/20
4 months	0.82	4.148	2011/05/04
1 year	4.95	4.311	2013/01/17
1.5 years	1.32		

Table 3.40: Periodicities as frequencies corresponding to peaks in the spectrum higher than the threshold.

Table 3.41: Outliers as values in the normalised residuals greater (less) than  $+ (-) 3 \sigma$ . Only very high or very low outliers are listed.

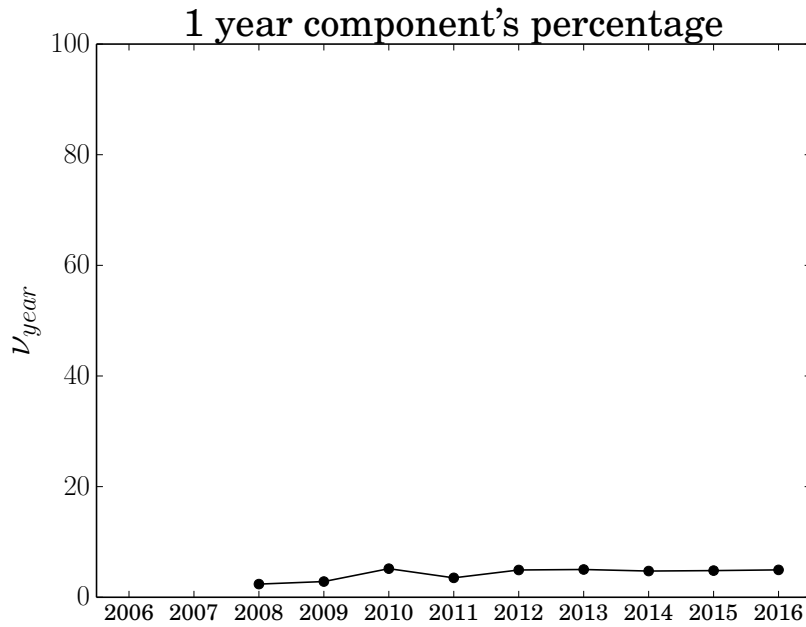


Figure 3.161: Dynamic analysis of the percentage of the one-year periodicity.

Station RN79 exhibits a predominant periodicity of one year, with a percentage weight of 4.95%, comparable with some of the other periodicities. Time series shows a constant linear trend and data are approximately regular, except for a period at the beginning of 2006, and two other small periods in mid-2006 and mid-2010, respectively. High outliers do not occur in the residual time series, as confirmed by the absence of great variations in the time series. Residuals without outliers are best described by a Lognormal distribution. From DFA plot, two scaling regimes are found: The first, from 14 days to  $\sim 150$  days, has a Hurst exponent  $H = 0.6010 \pm 0.0041$ ; the second, from  $\sim 150$  days to the end of the series, has a Hurst exponent  $H = 0.3362 \pm 0.0039$ . The different regimes show a change in correlation properties of the residuals, from correlated to anti-correlated. This is

also an evidence of multifractality. The local Hurst exponent  $H_t$  is computed at a time window of two weeks and oscillates around a value compatible with long-range correlations ( $\sim 0.6$ ). The one-year component's percentage remains approximately constant around a value of 5% when adding new years. Adding the year 2006 makes the total number of missing data exceed the threshold of 20%, even when 2007 data are added, hence the series are not analysed.

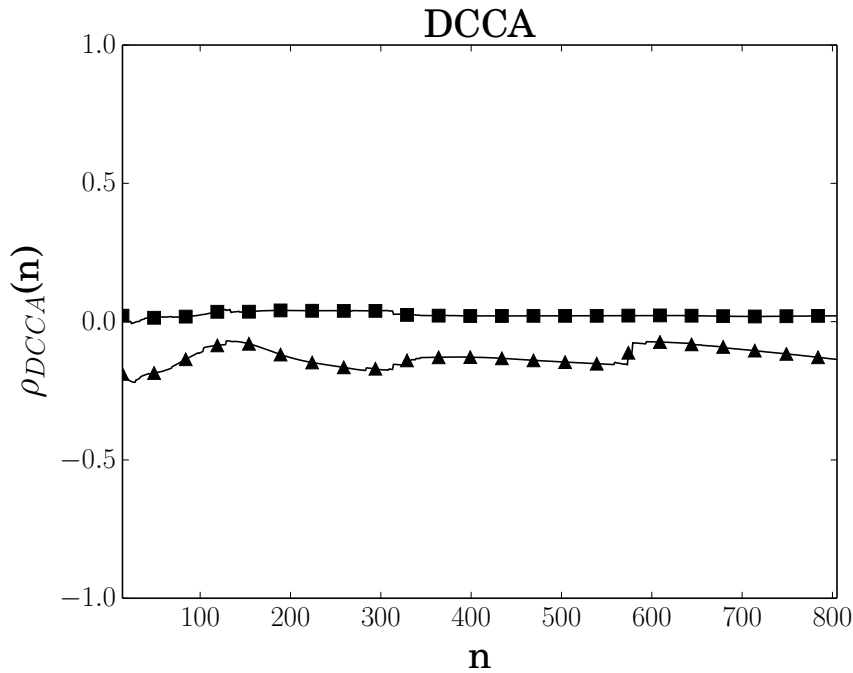


Figure 3.162: Detrended cross correlation between <sup>7</sup>Be and available meteorological parameters (humidity (○), temperature (△), pressure (□), wind direction (▽), and wind speed (◇)).

Station RN79 exhibits slightly negative cross-correlations with temperature at all scales and no cross-correlations with pressure. The other meteorological parameters were not suitable for the analysis.

### 3.3.21 Panama City, Panama (RN50)

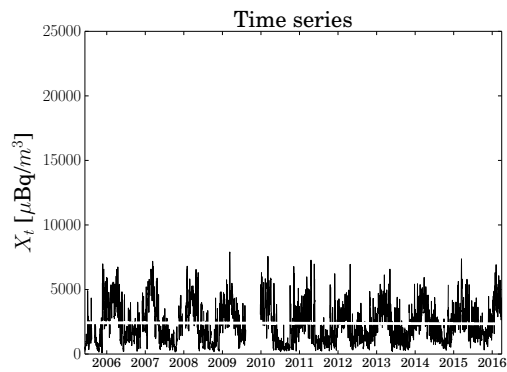


Figure 3.163: Time series with trend superimposed (solid white line).

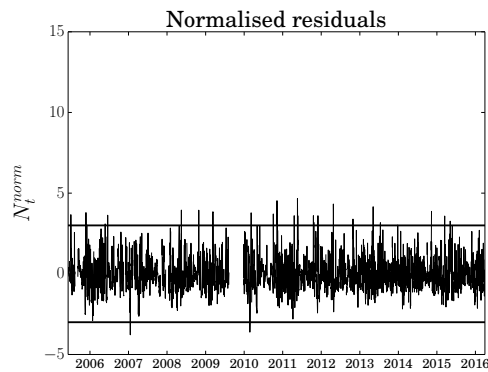


Figure 3.164: Normalised residual time series with the  $\pm 3\sigma$  thresholds (solid black lines).

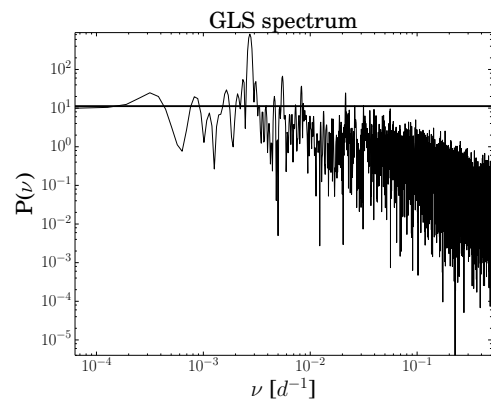


Figure 3.165: Log-log plot of the GLS spectrum with the associated threshold (solid black line).

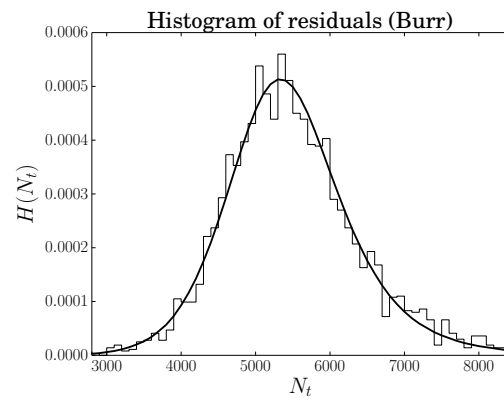


Figure 3.166: Histogram of residuals with the best-fitting distribution (no outliers).

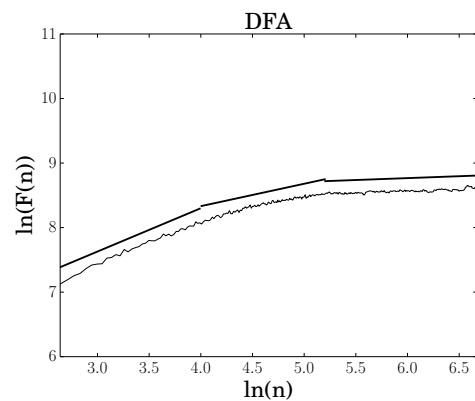


Figure 3.167: Detrended fluctuation analysis. The solid black lines are the best fit at different scales.

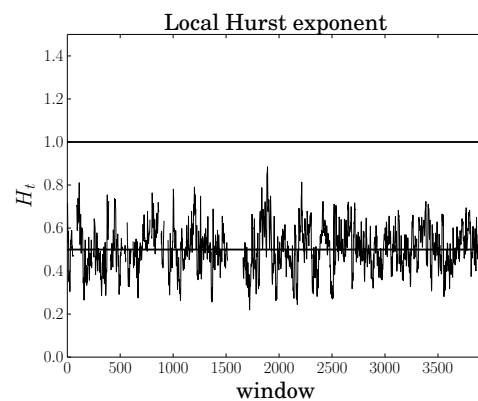


Figure 3.168: Local Hurst exponent  $H_t$  for a time window of two weeks. Solid lines represent the values of pink noise (top) and white noise (bottom).

Periodicity	Percentage	Value	Date
1 month	1.58	4.531	2010/11/08
2 months	1.57	4.662	2011/05/21
4 months	2.74	4.113	2012/04/24
6 months	4.28	4.327	2012/04/25
1 year	40.72	4.156	2013/05/07
1.5 years	2.32		
3.5 years	0.75		
8.5 years	1.39		

Table 3.43: Outliers as values in the normalised residuals greater (less) than + (-) 3  $\sigma$ . Only very high or very low outliers are listed.

Table 3.42: Periodicities as frequencies corresponding to peaks in the spectrum higher than the threshold.

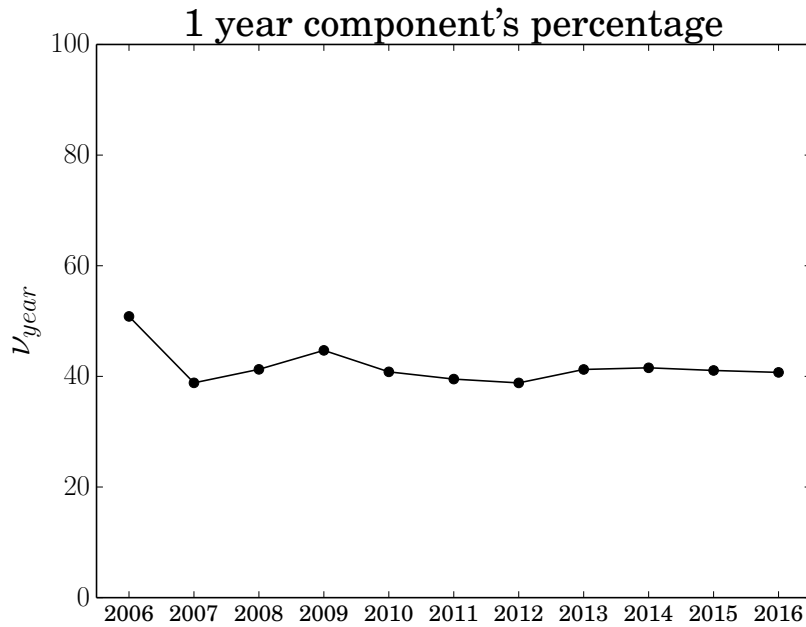


Figure 3.169: Dynamic analysis of the percentage of the one-year periodicity.

Station RN50 exhibits a predominant periodicity of one year, with a percentage weight of 40.72%, much higher than the other periodicities. Time series shows a constant linear trend and data are approximately regular, except for a period at the end of 2009. High outliers do not occur in the residual time series, as confirmed by the absence of great variations in the time series. Residuals without outliers are best described by a Burr distribution. From DFA plot, three scaling regimes are found: The first, from 14 days to  $\sim 55$  days, has a Hurst exponent  $H = 0.6716 \pm 0.0105$ ; the second, from  $\sim 55$  days to  $\sim 180$  days, has a Hurst exponent  $H = 0.3472 \pm 0.0061$ ; the third, from  $\sim 180$  days to the end of the series, has a Hurst exponent  $H = 0.0589 \pm 0.0017$ . The first two regimes show a change

in the series from a correlated behaviour to an anti-correlated one, while the third regime shows a more anti-correlated behaviour of the residuals at big time scales, or it probably expresses the limitations of the algorithm in accurately estimating the degree of correlations in the residual time series [94]. The local Hurst exponent  $H_t$  is computed at a time window of two weeks and oscillates around a value compatible with white noise ( $\sim 0.5$ ). The one-year component's percentage has initially a value of  $\sim 50\%$  and then remains approximately constant around a value of 40% when adding new years.

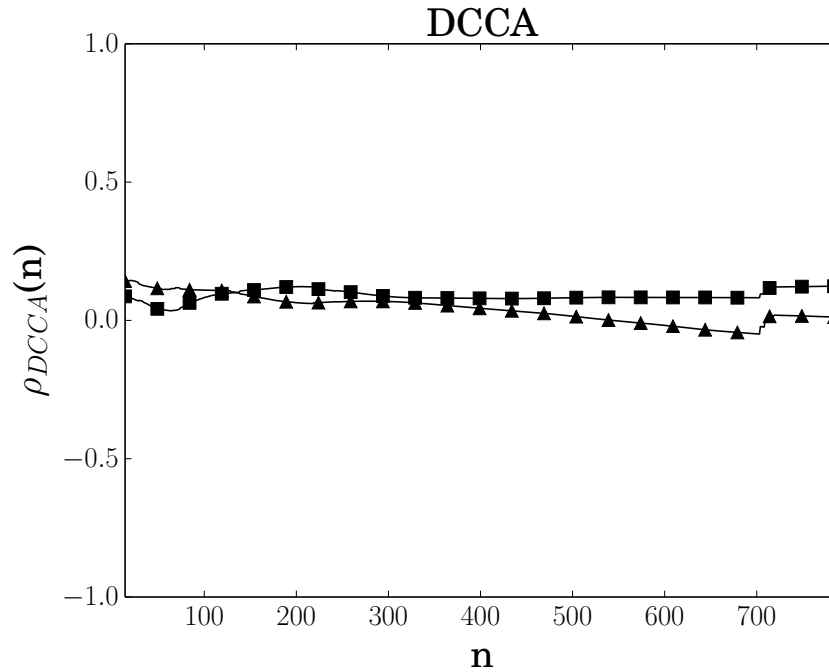


Figure 3.170: Detrended cross correlation between <sup>7</sup>Be and available meteorological parameters (humidity (○), temperature (△), pressure (□), wind direction (▽), and wind speed (◇)).

Station RN50 does not exhibit cross-correlations with both temperature and pressure. The other meteorological parameters were not suitable for the analysis.

### 3.3.22 Tanay, Philippines (RN52)

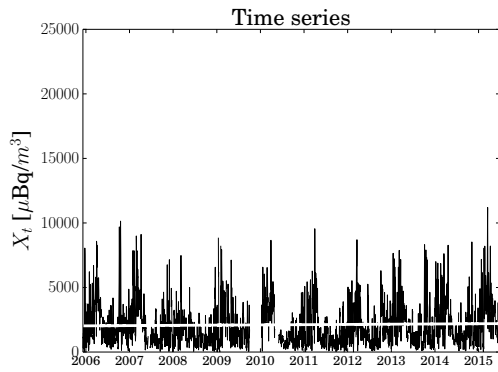


Figure 3.171: Time series with trend superimposed (solid white line).

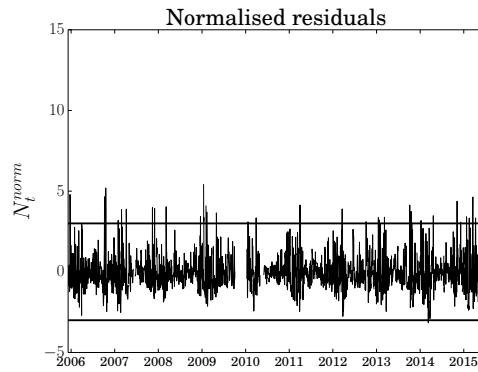


Figure 3.172: Normalised residual time series with the  $\pm 3\sigma$  thresholds (solid black lines).

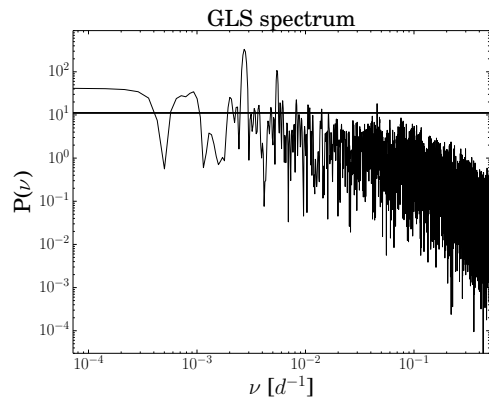


Figure 3.173: Log-log plot of the GLS spectrum with the associated threshold (solid black line).

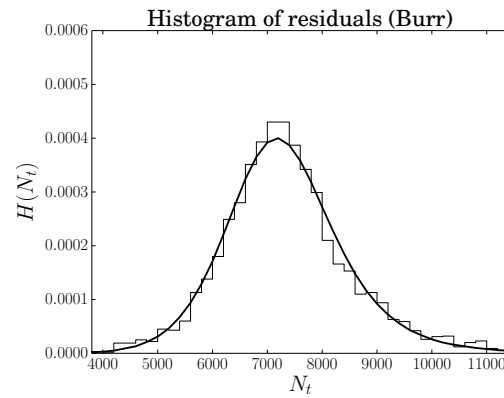


Figure 3.174: Histogram of residuals with the best-fitting distribution (no outliers).

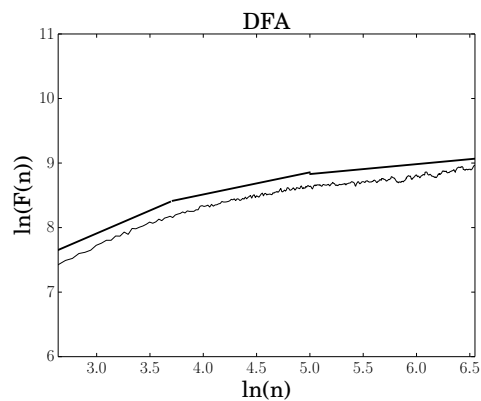


Figure 3.175: Detrended fluctuation analysis. The solid black lines are the best fit at different scales.

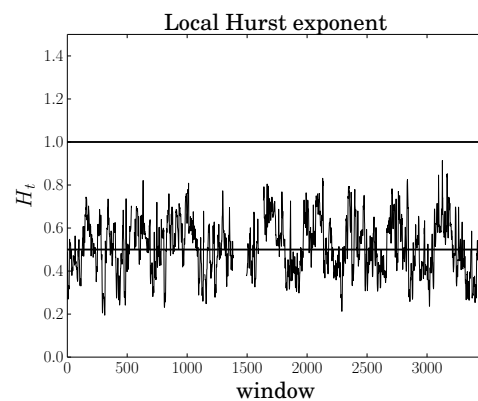


Figure 3.176: Local Hurst exponent  $H_t$  for a time window of two weeks. Solid lines represent the values of pink noise (top) and white noise (bottom).

Periodicity	Percentage	Value	Date
2 weeks	0.90	4.790	2005/12/23
2 months	1.61	4.389	2005/12/24
3 months	1.53	4.649	2006/10/08
4 months	1.01	5.194	2006/10/18
6 months	7.61	4.486	2006/10/19
1 year	17.81	4.030	2008/03/07
1.5 years	1.23	5.402	2009/01/14
3 years	1.41	4.078	2009/02/03
4 years	1.29	4.141	2011/04/01
		4.132	2013/10/06
		4.377	2014/11/06
		4.633	2015/03/18

Table 3.44: Periodicities as frequencies corresponding to peaks in the spectrum higher than the threshold.

Table 3.45: Outliers as values in the normalised residuals greater (less) than + (-) 3  $\sigma$ . Only very high or very low outliers are listed.

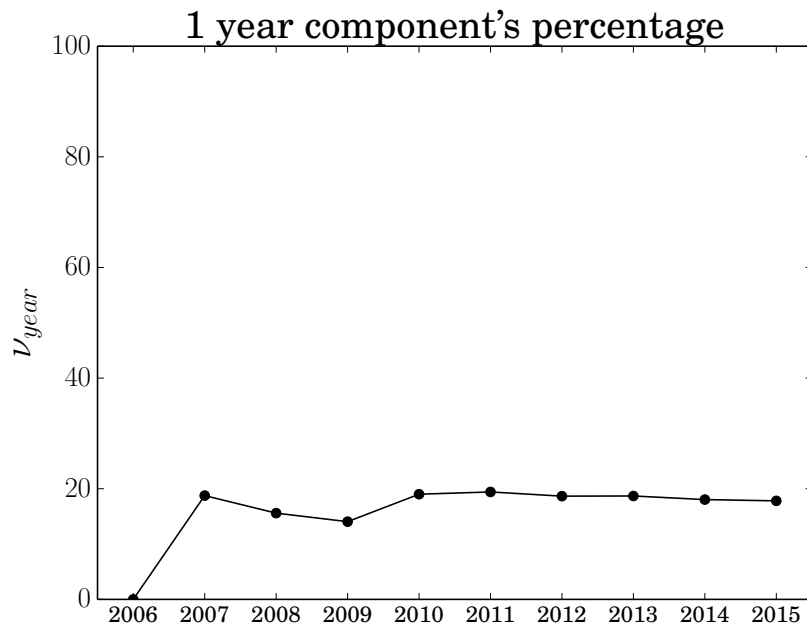


Figure 3.177: Dynamic analysis of the percentage of the one-year periodicity.

Station RN52 exhibits a predominant periodicity of one year, with a percentage weight of 17.81%, much higher than the other periodicities. Time series shows a constant linear trend and data are approximately regular, except for a period at the end of 2009. High outliers occur in the first half of the residual time series. Residuals without outliers are best described by a Burr distribution. From DFA

plot, three scaling regimes are found: The first, from 14 days to  $\sim 40$  days, has a Hurst exponent  $H = 0.7101 \pm 0.0140$ ; the second, from  $\sim 40$  days to  $\sim 150$  days, has a Hurst exponent  $H = 0.3426 \pm 0.0051$ ; the third, from  $\sim 150$  days to the end of the series, has a Hurst exponent  $H = 0.1537 \pm 0.0040$ . The first two regimes show a change in the series from a correlated behaviour to an anti-correlated one, while the third regime shows a more anti-correlated behaviour of the residuals at big time scales, or it probably expresses the limitations of the algorithm in accurately estimating the degree of correlations in the residual time series [94]. The local Hurst exponent  $H_t$  is computed at a time window of two weeks and oscillates around a value compatible with white noise ( $\sim 0.5$ ). The one-year component's percentage remains approximately constant around a value of 20% when adding new years. All the meteorological parameters were not suitable for the detrended cross-correlation analysis.

### 3.3.23 St. John's, N.L., Canada (RN17)

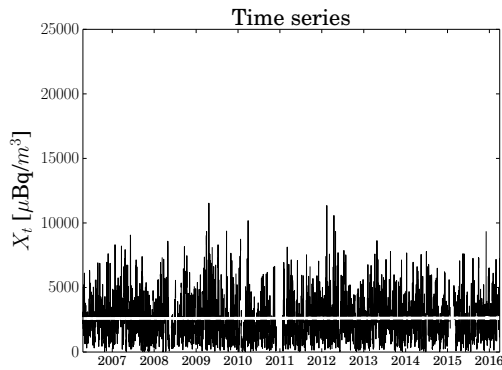


Figure 3.178: Time series with trend superimposed (solid white line).

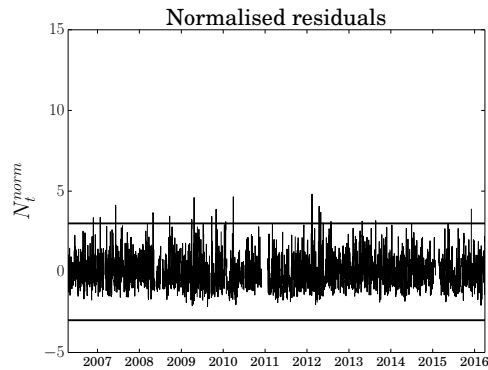


Figure 3.179: Normalised residual time series with the  $\pm 3\sigma$  thresholds (solid black lines).

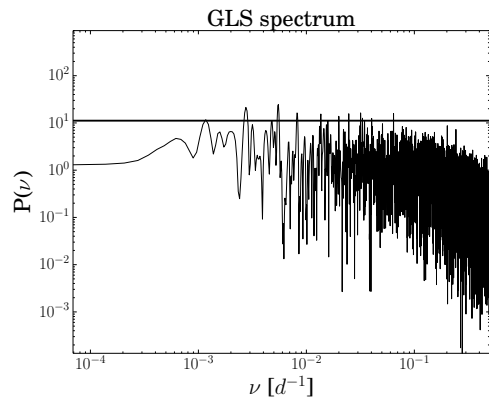


Figure 3.180: Log-log plot of the GLS spectrum with the associated threshold (solid black line).

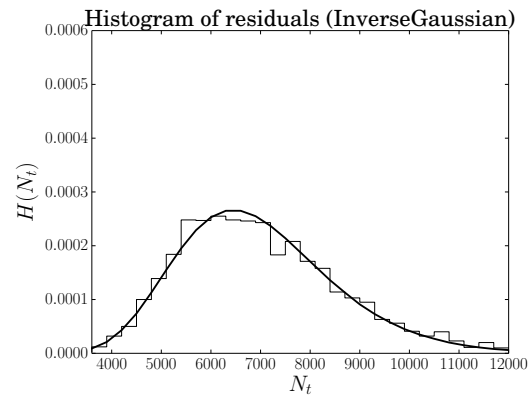


Figure 3.181: Histogram of residuals with the best-fitting distribution (no outliers).

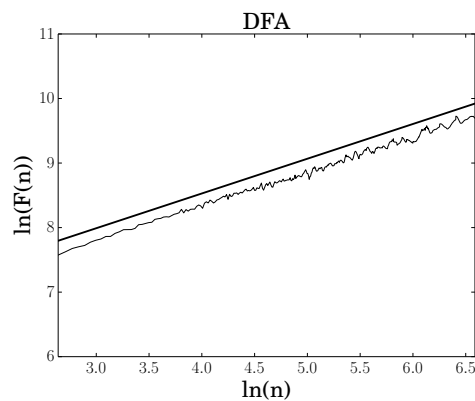


Figure 3.182: Detrended fluctuation analysis. The solid black lines are the best fit at different scales.

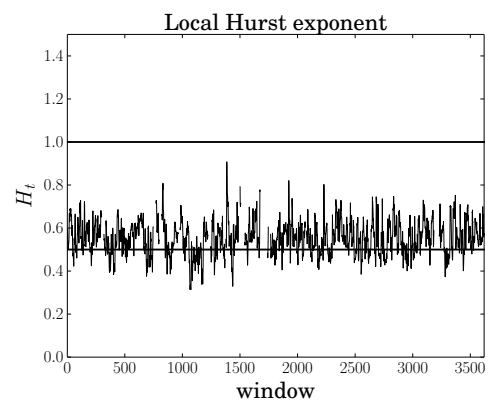


Figure 3.183: Local Hurst exponent  $H_t$  for a time window of two weeks. Solid lines represent the values of pink noise (top) and white noise (bottom).

Periodicity	Percentage	Value	Date
2 weeks	0.99	4.126	2007/06/08
1 month	3.24	4.002	2007/06/09
2 months	1.48	4.605	2009/04/22
4 months	1.01	4.647	2010/03/30
6 months	1.17	4.817	2012/02/14
1 year	1.05	4.060	2012/04/16
2.5 years	0.64		

Table 3.46: Periodicities as frequencies corresponding to peaks in the spectrum higher than the threshold.

Table 3.47: Outliers as values in the normalised residuals greater (less) than  $+ (-) 3 \sigma$ . Only very high or very low outliers are listed.

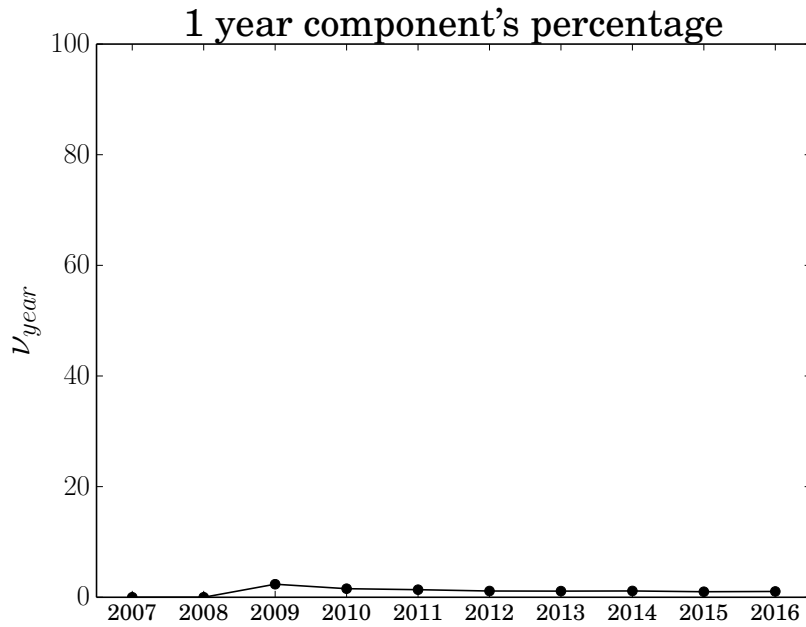


Figure 3.184: Dynamic analysis of the percentage of the one-year periodicity.

Station RN17 exhibits a predominant periodicity of one month, with a percentage weight of 3.24%, comparable with the other periodicities. Time series shows a constant linear trend and data are approximately regular, except for a small period at the beginning of 2011. High outliers do not occur in the residual time series, as confirmed by the absence of great variations in the time series. Residuals without outliers are best described by an Inverse Gaussian distribution. From DFA plot, a single scaling regime is found, with a Hurst exponent  $H = 0.5384 \pm 0.0017$ . Residual time series are then uncorrelated (white noise). The local Hurst exponent  $H_t$  is computed at a time window of two weeks and oscillates around a value compatible with long-range correlations ( $\sim 0.6$ ), with a period in the middle compatible with white noise ( $\sim 0.5$ ). The one-year component's percentage remains approximately

constant around a value of 1% when adding new years.

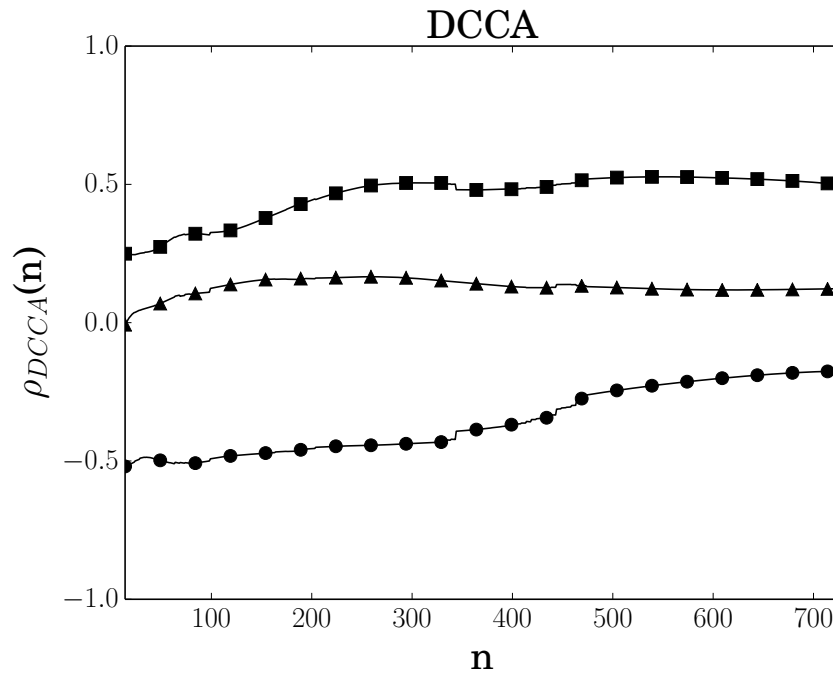


Figure 3.185: Detrended cross correlation between <sup>7</sup>Be and available meteorological parameters (humidity ( $\circ$ ), temperature ( $\triangle$ ), pressure ( $\square$ ), wind direction ( $\nabla$ ), and wind speed ( $\diamond$ )).

Station RN17 exhibits negative cross-correlations with humidity at all scales (stronger at small scales) and positive cross-correlations with pressure (stronger at big scales). There are no cross-correlations with temperature. Wind direction and speed time series were not suitable for the analysis.

### 3.3.24 Nouakchott, Mauritania (RN43)

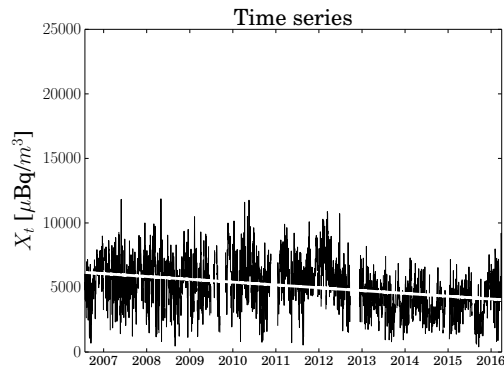


Figure 3.186: Time series with trend superimposed (solid white line).

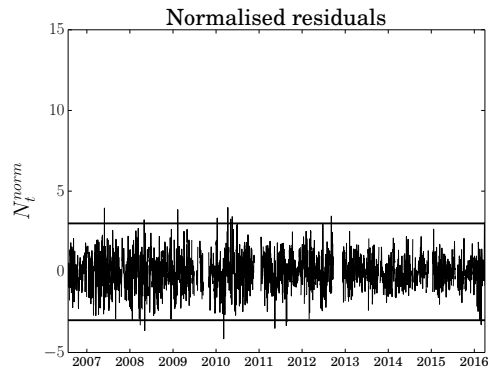


Figure 3.187: Normalised residual time series with the  $\pm 3\sigma$  thresholds (solid black lines).

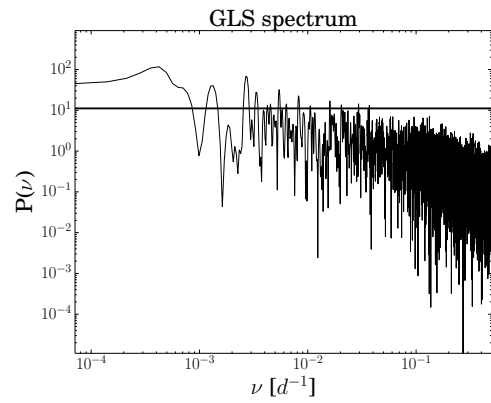


Figure 3.188: Log-log plot of the GLS spectrum with the associated threshold (solid black line).

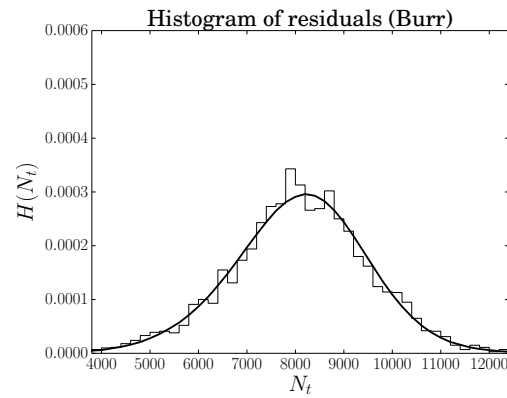


Figure 3.189: Histogram of residuals with the best-fitting distribution (no outliers).

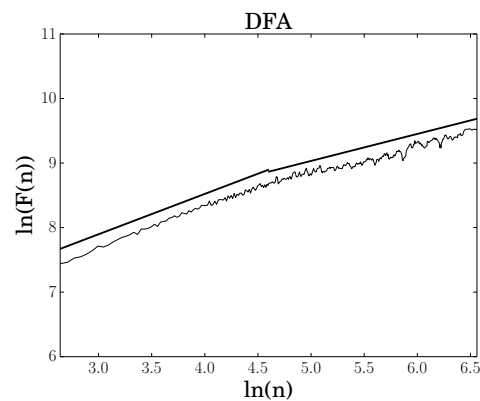


Figure 3.190: Detrended fluctuation analysis. The solid black lines are the best fit at different scales.

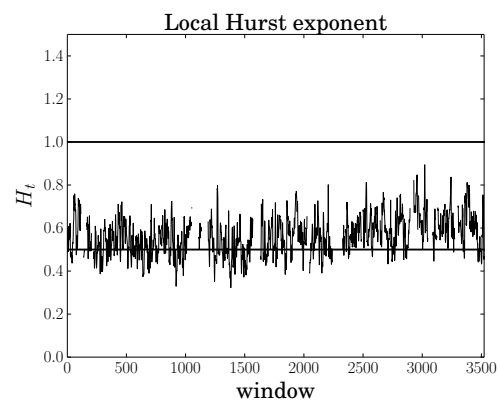


Figure 3.191: Local Hurst exponent  $H_t$  for a time window of two weeks. Solid lines represent the values of pink noise (top) and white noise (bottom).

Periodicity	Percentage	Value	Date
1 month	2.29	-4.150	2010/03/07
2 months	2.49		
3 months	0.80		
4 months	1.53		
6 months	3.03		
1 year	4.45		
2 years	2.11		
6.5 years	9.88		

Table 3.49: Outliers as values in the normalised residuals greater (less) than + (-)  $3\sigma$ . Only very high or very low outliers are listed.

Table 3.48: Periodicities as frequencies corresponding to peaks in the spectrum higher than the threshold.

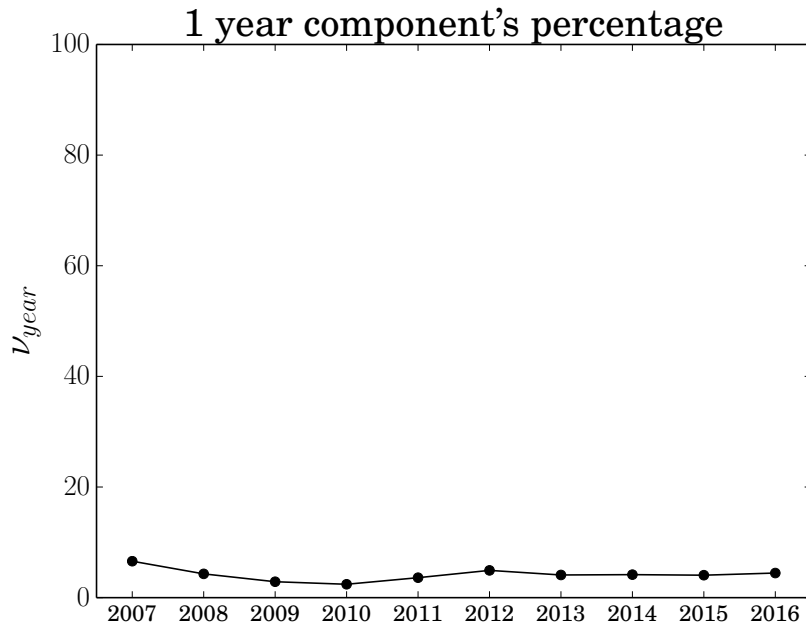


Figure 3.192: Dynamic analysis of the percentage of the one-year periodicity.

Station RN43 exhibits a predominant periodicity of 6.5 years, with a percentage weight of 9.88%, higher than the other periodicities. Time series shows a downward linear trend and data are approximately regular, except for periods in 2009, 2010 and 2012, respectively. High outliers do not occur in the residual time series, as confirmed by the absence of great variations in the time series. Residuals without outliers are best described by a Burr distribution. From DFA plot, two scaling regimes are found: The first, from 14 days to  $\sim 100$  days, has a Hurst exponent  $H = 0.6254 \pm 0.0056$ ; the second, from  $\sim 100$  days to the end of the series, has a Hurst exponent  $H = 0.4184 \pm 0.0056$ . The different regimes show a change in correlation properties of the residuals, from correlated to anti-correlated. This is

also an evidence of multifractality. The local Hurst exponent  $H_t$  is computed at a time window of two weeks and oscillates initially around a value compatible with white noise ( $\sim 0.5$ ), then around a value compatible with long-range correlations ( $\sim 0.6$ ). The one-year component's percentage remains approximately constant around a value of 5% when adding new years.

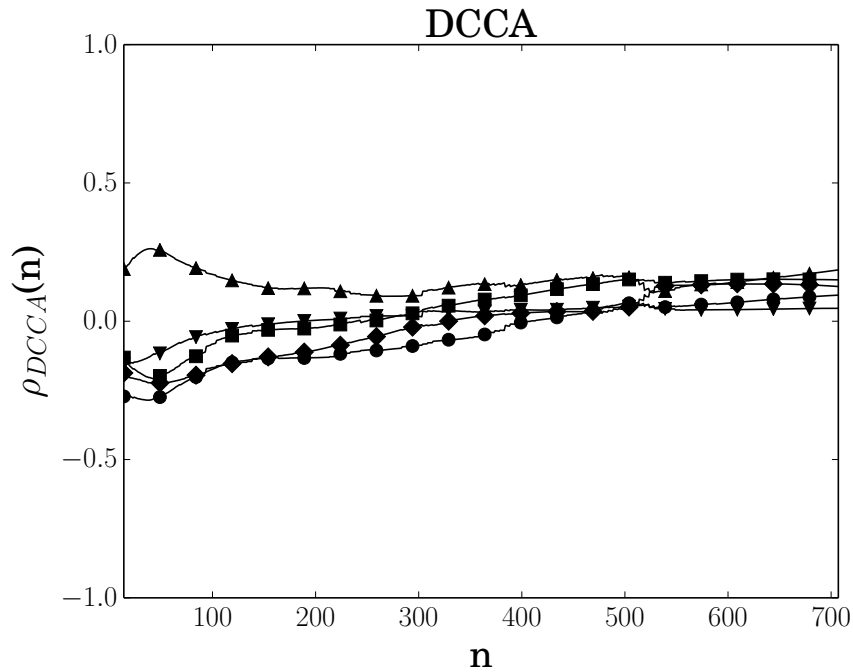


Figure 3.193: Detrended cross correlation between  ${}^7\text{Be}$  and available meteorological parameters (humidity (○), temperature (△), pressure (□), wind direction (▽), and wind speed (◇)).

Station RN43 exhibits slightly negative cross-correlations with humidity, pressure, and wind direction and speed at very small scales ( $< 100$  days) and slightly positive cross-correlations with temperature at very small scales ( $< 100$  days).

### 3.3.25 Okinawa, Japan (RN37)

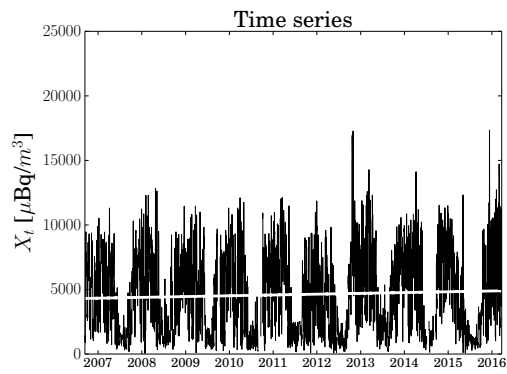


Figure 3.194: Time series with trend superimposed (solid white line).

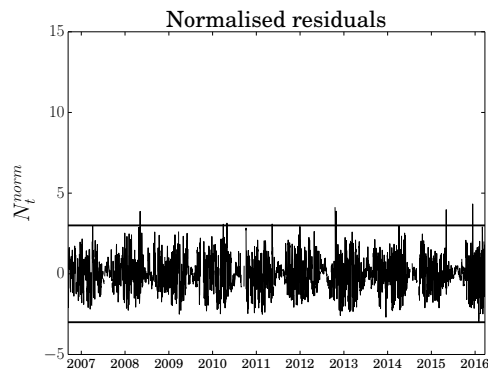


Figure 3.195: Normalised residual time series with the  $\pm 3\sigma$  thresholds (solid black lines).

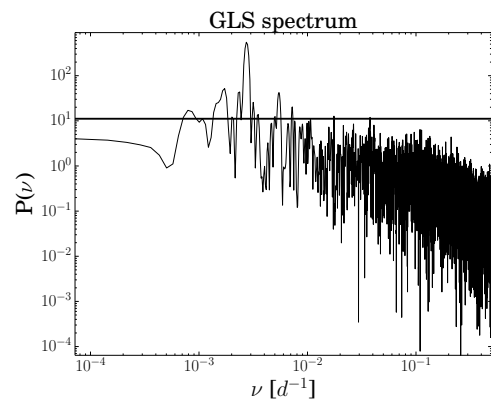


Figure 3.196: Log-log plot of the GLS spectrum with the associated threshold (solid black line).

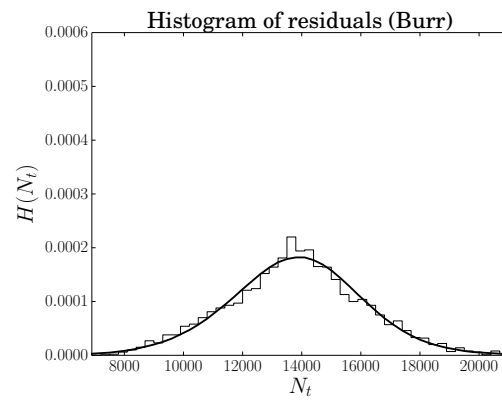


Figure 3.197: Histogram of residuals with the best-fitting distribution (no outliers).

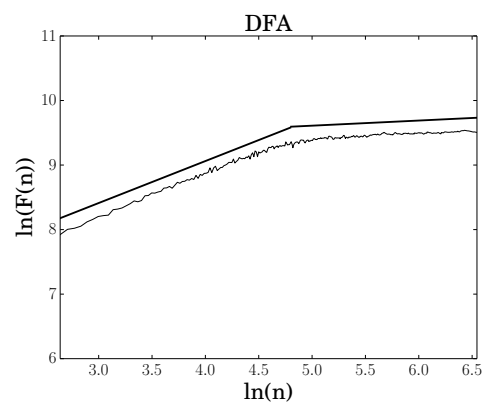


Figure 3.198: Detrended fluctuation analysis. The solid black lines are the best fit at different scales.

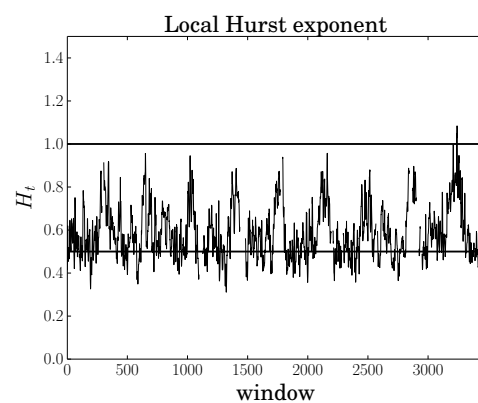


Figure 3.199: Local Hurst exponent  $H_t$  for a time window of two weeks. Solid lines represent the values of pink noise (top) and white noise (bottom).

Periodicity	Percentage	Value	Date
1 month	0.95	4.099	2012/10/19
2 months	0.64	4.330	2015/12/12
4 months	1.04		
6 months	3.61		
1 year	31.53		
1.5 years	3.76		
2.5 years	0.32		
3.5 years	1.04		

Table 3.51: Outliers as values in the normalised residuals greater (less) than + (-)  $3\sigma$ . Only very high or very low outliers are listed.

Table 3.50: Periodicities as frequencies corresponding to peaks in the spectrum higher than the threshold.

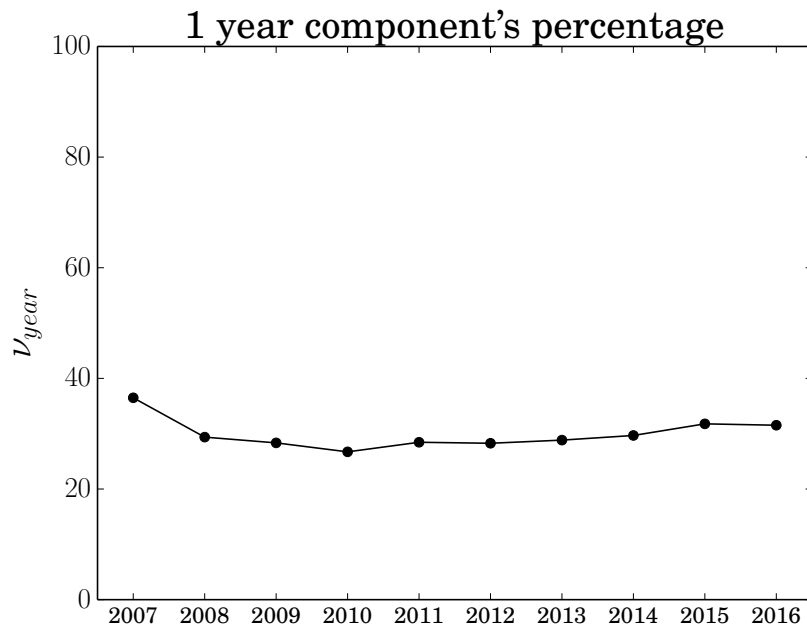


Figure 3.200: Dynamic analysis of the percentage of the one-year periodicity.

Station RN37 exhibits a predominant periodicity of one year, with a percentage weight of 31.53%, much higher than the other periodicities. Time series shows a slightly upward linear trend and data are approximately regular. High outliers do not occur in the residual time series, despite the presence of two great variations in the second half of the time series. Residuals without outliers are best described by a Burr distribution. From DFA plot, two scaling regimes are found: The first, from 14 days to  $\sim 120$  days, has a Hurst exponent  $H = 0.6504 \pm 0.0048$ ; the second, from  $\sim 120$  days to the end of the series, has a Hurst exponent  $H = 0.0794 \pm 0.0012$ . The different regimes show a change in correlation properties of the residuals, from correlated to anti-correlated, or more probably the second regime expresses the

limitations of the algorithm in accurately estimating the degree of correlations in the residual time series [94]. The local Hurst exponent  $H_t$  is computed at a time window of two weeks and oscillates (almost periodically) around a value compatible with long-range correlations ( $\sim 0.7$ ). The one-year component's percentage has initially a value of  $\sim 40\%$ , then remains approximately constant around a value of  $30\%$  when adding new years.

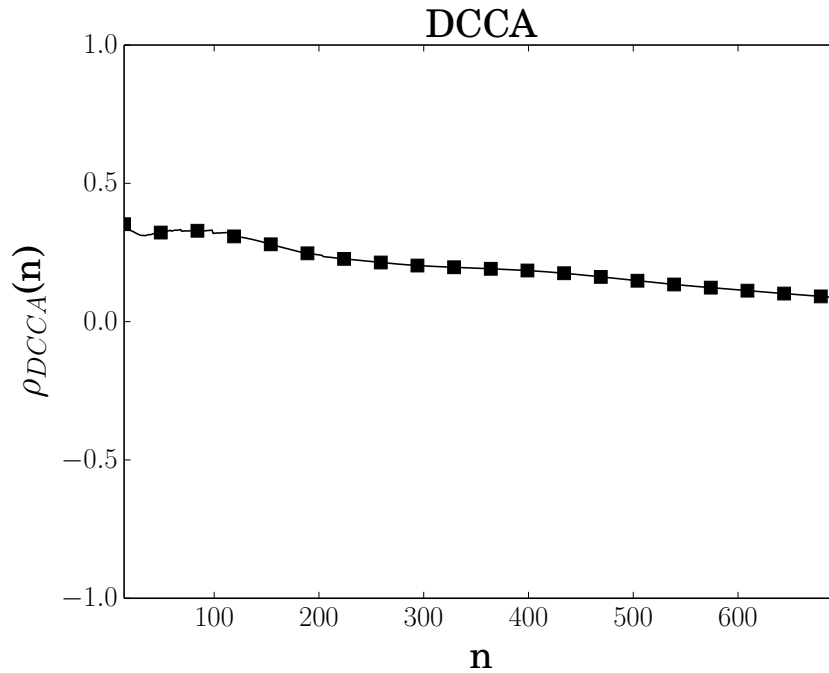


Figure 3.201: Detrended cross correlation between <sup>7</sup>Be and available meteorological parameters (humidity (○), temperature (△), pressure (□), wind direction (▽), and wind speed (◇)).

Station RN37 exhibits positive cross-correlations with pressure at scales less than 300 days. The other meteorological parameters time series were not suitable for the analysis.

### 3.3.26 Sand Point, Alaska, USA (RN71)

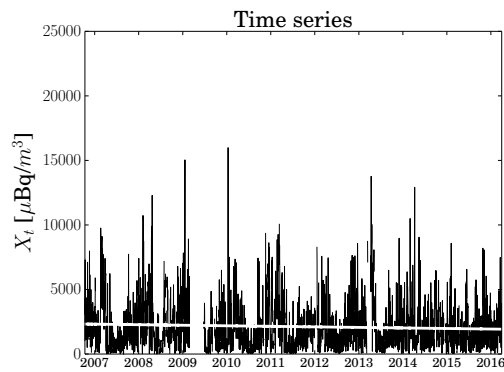


Figure 3.202: Time series with trend superimposed (solid white line).

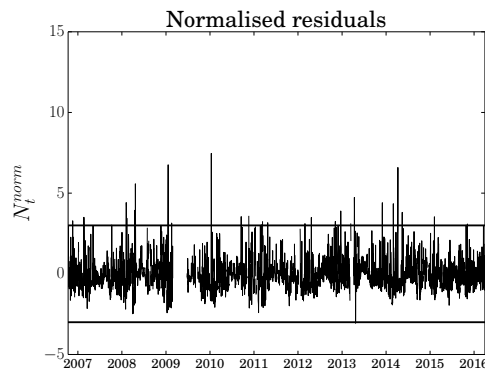


Figure 3.203: Normalised residual time series with the  $\pm 3\sigma$  thresholds (solid black lines).

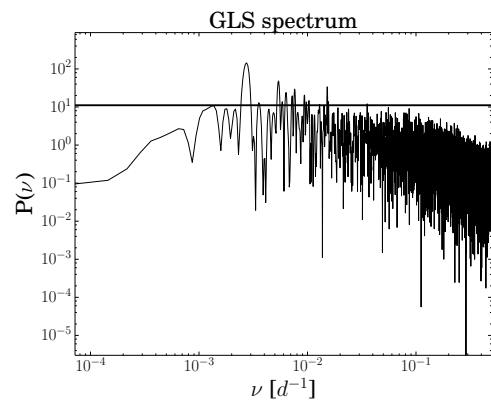


Figure 3.204: Log-log plot of the GLS spectrum with the associated threshold (solid black line).

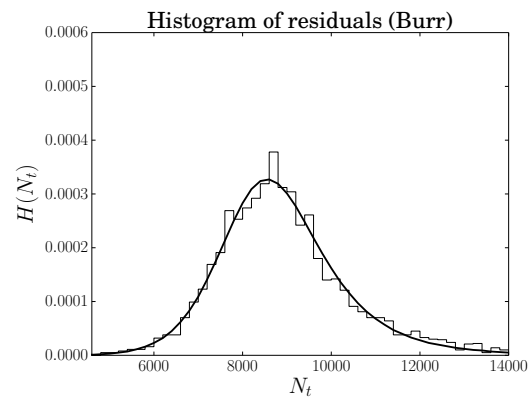


Figure 3.205: Histogram of residuals with the best-fitting distribution (no outliers).

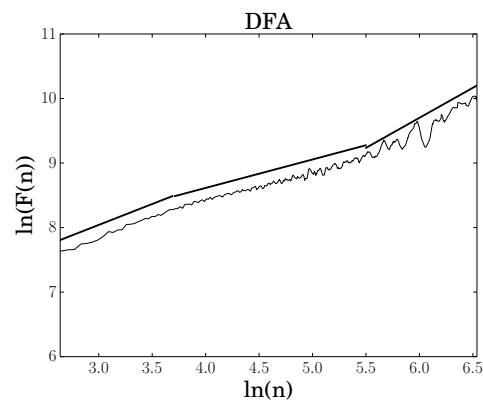


Figure 3.206: Detrended fluctuation analysis. The solid black lines are the best fit at different scales.

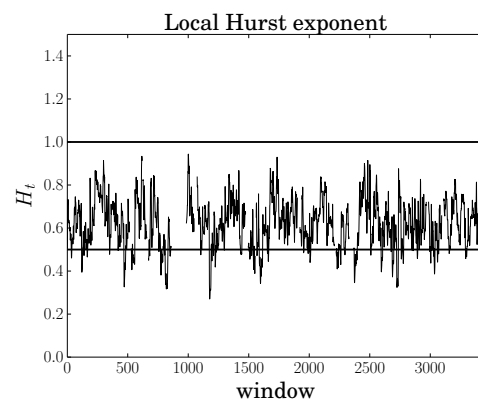


Figure 3.207: Local Hurst exponent  $H_t$  for a time window of two weeks. Solid lines represent the values of pink noise (top) and white noise (bottom).

Periodicity	Percentage	Value	Date
1 month	0.98	4.414	2008/02/06
2 months	2.89	4.128	2008/02/07
3 months	2.24	5.577	2008/04/22
4 months	3.24	5.283	2009/01/18
6 months	4.59	6.756	2009/01/19
1 year	10.63	6.422	2010/01/11
		7.463	2010/01/12
		4.589	2010/01/13
		4.731	2013/04/13
		4.405	2013/12/01
		4.343	2014/03/02
		4.104	2014/04/08
		6.590	2014/04/09

Table 3.52: Periodicities as frequencies corresponding to peaks in the spectrum higher than the threshold.

Table 3.53: Outliers as values in the normalised residuals greater (less) than + (-)  $3\sigma$ . Only very high or very low outliers are listed.

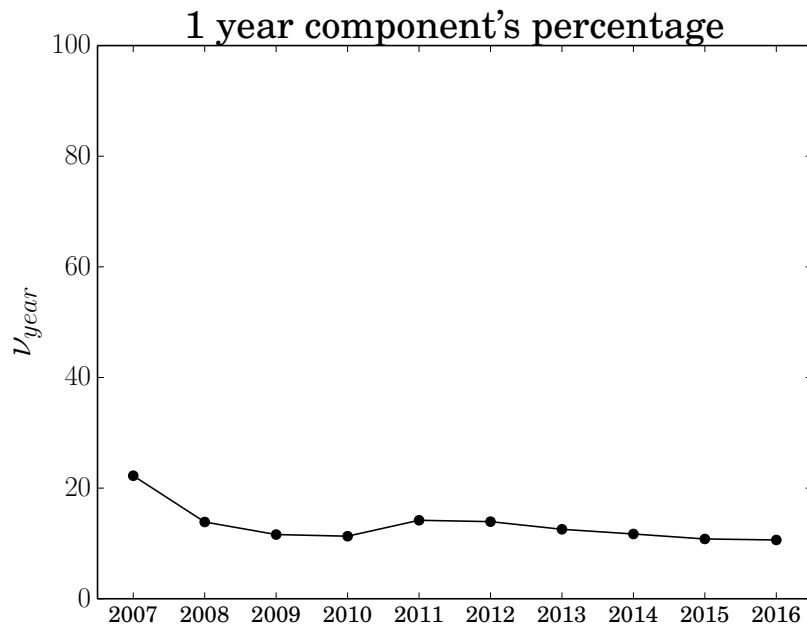


Figure 3.208: Dynamic analysis of the percentage of the one-year periodicity.

Station RN71 exhibits a predominant periodicity of one year, with a percentage weight of 10.63%, higher than the other periodicities. Time series shows a constant linear trend and data are approximately regular, except for a period at the beginning of 2009. High outliers occur in the residual time series at the beginning of 2009

and 2010, and in mid-2014 ( $6 - 7\sigma$ ). Residuals without outliers are best described by a Burr distribution. From DFA plot, three scaling regimes are found: The first, from 14 days to  $\sim 40$  days, has a Hurst exponent  $H = 0.6475 \pm 0.0123$ ; the second, from  $\sim 40$  days to  $\sim 245$  days, has a Hurst exponent  $H = 0.4411 \pm 0.0045$ ; the third, from  $\sim 245$  days to the end of the series, has a Hurst exponent  $H = 0.9309 \pm 0.0155$ . The first two regimes show a change in the series from a correlated behaviour to an anti-correlated one, while the third regime shows a highly correlated behaviour of the residuals at big time scales. The local Hurst exponent  $H_t$  is computed at a time window of two weeks and oscillates around a value compatible with long-range correlations ( $\sim 0.7$ ). The one-year component's percentage has initially a value of  $\sim 20\%$ , then decreases and approaches a value of 10% when adding new years.

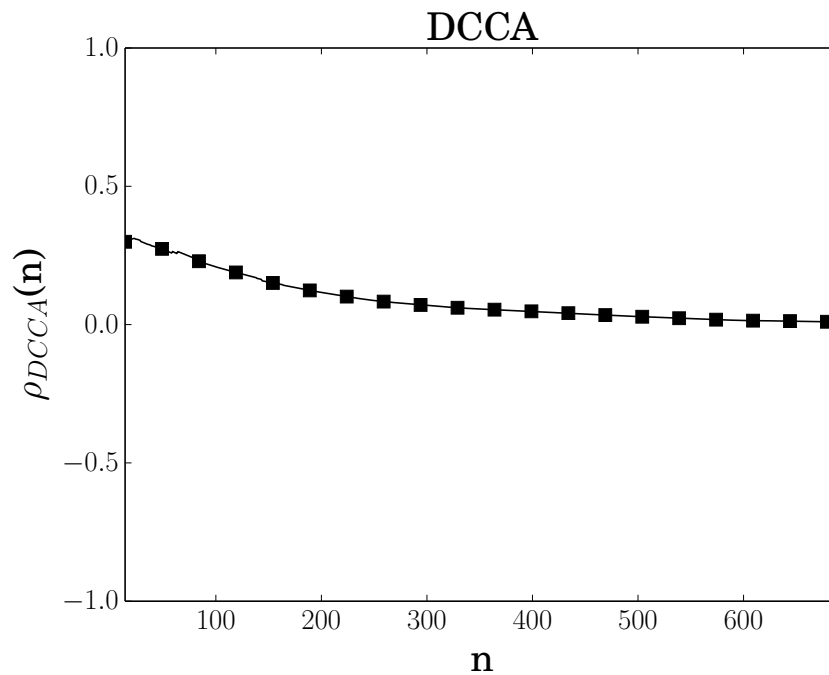


Figure 3.209: Detrended cross correlation between <sup>7</sup>Be and available meteorological parameters (humidity ( $\circ$ ), temperature ( $\triangle$ ), pressure ( $\square$ ), wind direction ( $\nabla$ ), and wind speed ( $\diamond$ )).

Station RN71 exhibits positive cross-correlations with pressure at scales less than 100 days. The other meteorological parameters time series were not suitable for the analysis.

### 3.3.27 Salchaket, Alaska, USA (RN76)

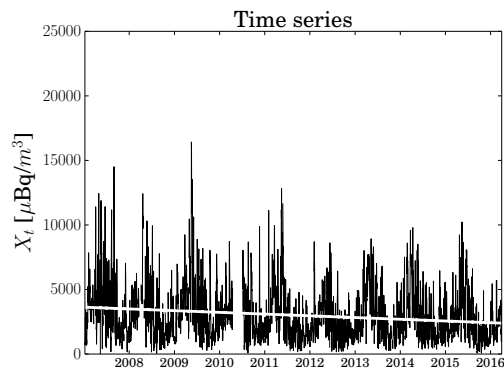


Figure 3.210: Time series with trend superimposed (solid white line).

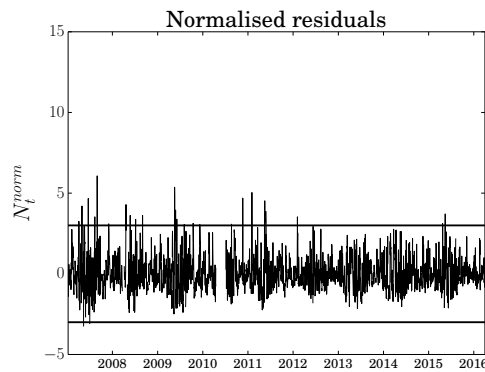


Figure 3.211: Normalised residual time series with the  $\pm 3\sigma$  thresholds (solid black lines).

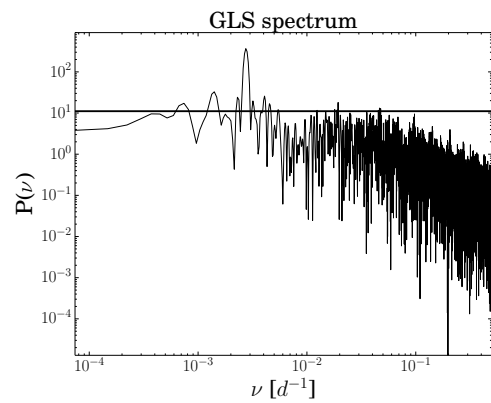


Figure 3.212: Log-log plot of the GLS spectrum with the associated threshold (solid black line).

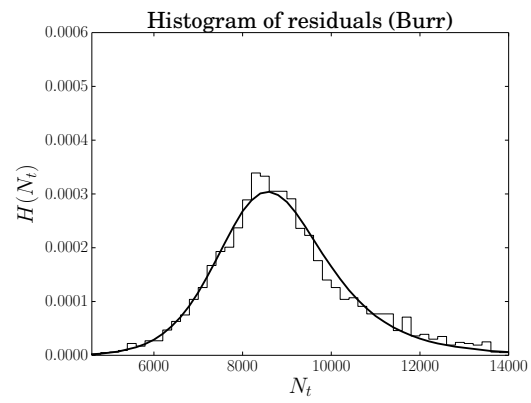


Figure 3.213: Histogram of residuals with the best-fitting distribution (no outliers).

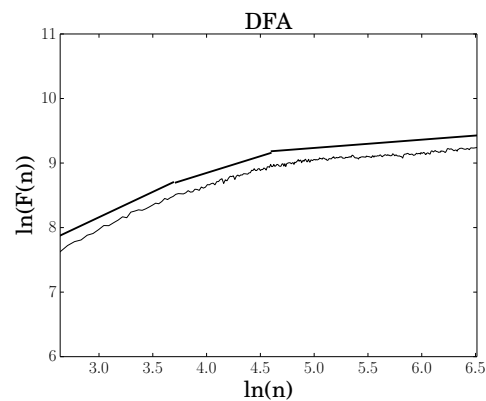


Figure 3.214: Detrended fluctuation analysis. The solid black lines are the best fit at different scales.

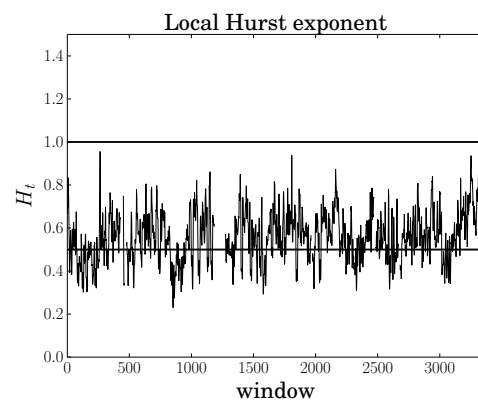


Figure 3.215: Local Hurst exponent  $H_t$  for a time window of two weeks. Solid lines represent the values of pink noise (top) and white noise (bottom).

Periodicity	Percentage	Value	Date
2 weeks	1.88	4.203	2007/04/30
1 month	0.69	4.669	2007/06/20
2 months	2.44	6.069	2007/08/31
3 months	0.61	4.291	2008/04/20
6 months	3.54	5.367	2009/05/18
1 year	21.32	4.803	2009/05/19
2 years	2.03	4.693	2010/11/20
3.5 years	0.99	5.040	2011/02/02
		4.524	2011/05/17

Table 3.54: Periodicities as frequencies corresponding to peaks in the spectrum higher than the threshold.

Table 3.55: Outliers as values in the normalised residuals greater (less) than + (-)  $3\sigma$ . Only very high or very low outliers are listed.

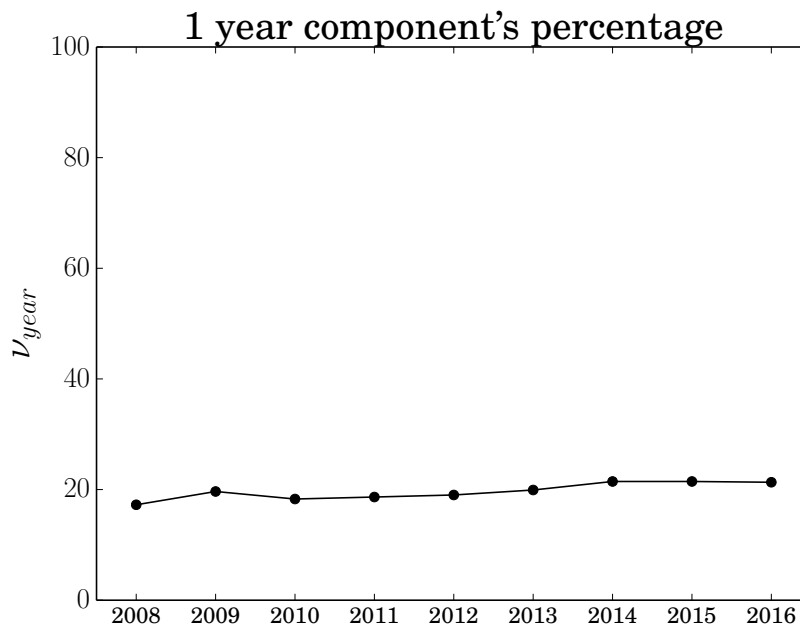


Figure 3.216: Dynamic analysis of the percentage of the one-year periodicity.

Station RN76 exhibits a predominant periodicity of one year, with a percentage weight of 21.32%, higher than the other periodicities. Time series shows a constant linear trend and data are approximately regular, except for a period in mid-2010. The highest outlier occurs in the residual time series in mid-2007, and not in mid-2009 where the maximum of the time series is reached. Residuals without outliers are best described by a Burr distribution. From DFA plot, three scaling regimes are found: The first, from 14 days to  $\sim 40$  days, has a Hurst exponent  $H = 0.7853 \pm 0.0143$ ; the second, from  $\sim 40$  days to  $\sim 100$  days, has a Hurst

exponent  $H = 0.5183 \pm 0.0099$ ; the third, from  $\sim 100$  days to the end of the series, has a Hurst exponent  $H = 0.1281 \pm 0.0014$ . The first two regimes show a change in the series from a correlated behaviour to an uncorrelated one, while the third regime shows a highly anti-correlated behaviour of the residuals at big time scales, or it probably expresses the limitations of the algorithm in accurately estimating the degree of correlations in the residual time series [94]. The local Hurst exponent  $H_t$  is computed at a time window of two weeks and oscillates around a value compatible with white noise ( $\sim 0.5$ ). The one-year component's percentage remains approximately constant around a value of 20% when adding new years.

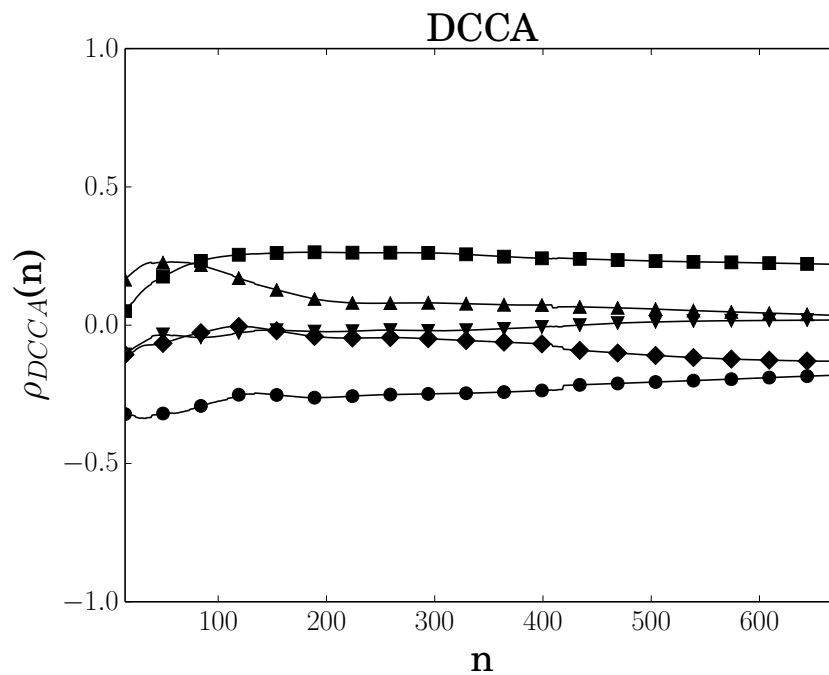


Figure 3.217: Detrended cross correlation between  ${}^7\text{Be}$  and available meteorological parameters (humidity ( $\circ$ ), temperature ( $\triangle$ ), pressure ( $\square$ ), wind direction ( $\nabla$ ), and wind speed ( $\diamond$ )).

Station RN76 exhibits negative cross-correlations with humidity at all scales and positive cross-correlations with pressure at scales greater than 100 days. There are no cross-correlations with temperature and wind direction and speed.

### 3.3.28 Dar Es Salaam, Tanzania (RN64)

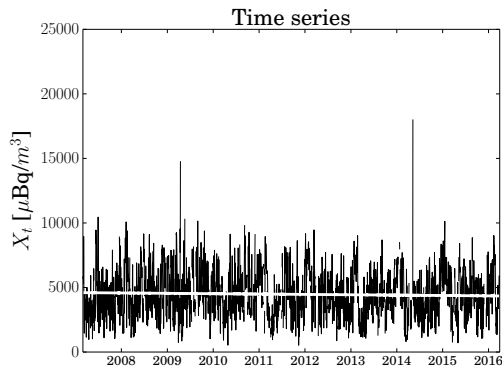


Figure 3.218: Time series with trend superimposed (solid white line).

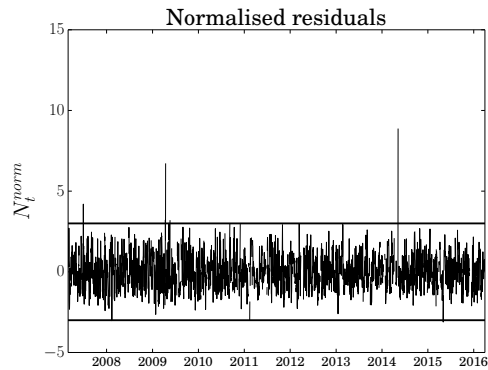


Figure 3.219: Normalised residual time series with the  $\pm 3\sigma$  thresholds (solid black lines).

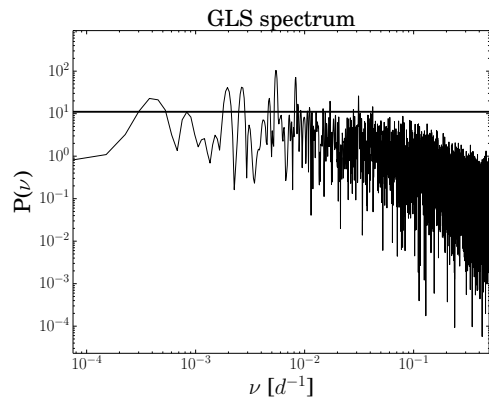


Figure 3.220: Log-log plot of the GLS spectrum with the associated threshold (solid black line).

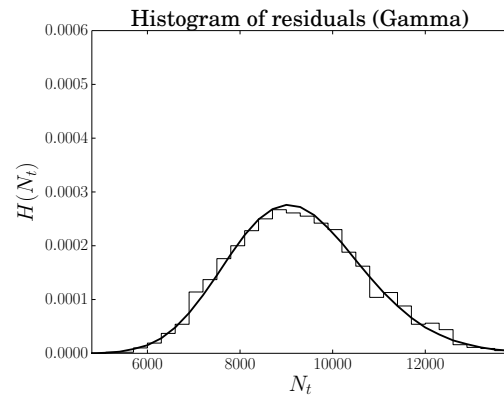


Figure 3.221: Histogram of residuals with the best-fitting distribution (no outliers).

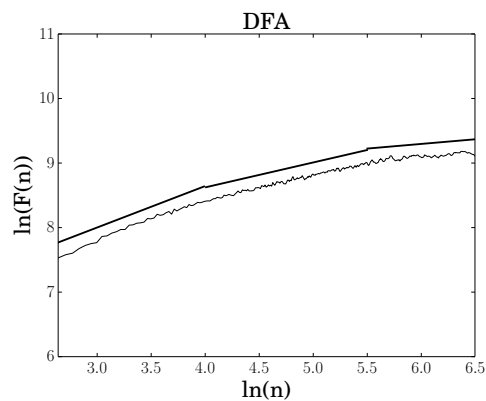


Figure 3.222: Detrended fluctuation analysis. The solid black lines are the best fit at different scales.

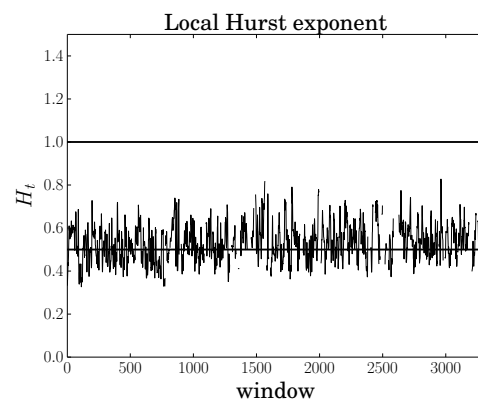


Figure 3.223: Local Hurst exponent  $H_t$  for a time window of two weeks. Solid lines represent the values of pink noise (top) and white noise (bottom).

Periodicity	Percentage	Value	Date
1 month	3.13	4.195	2007/06/30
2 months	1.64	6.690	2009/04/15
3 months	1.56	8.848	2014/05/09
4 months	5.21		
6 months	7.18		
1 year	2.33		
1.5 years	2.25		
7.5 years	1.16		

Table 3.57: Outliers as values in the normalised residuals greater (less) than  $+ (-) 3 \sigma$ . Only very high or very low outliers are listed.

Table 3.56: Periodicities as frequencies corresponding to peaks in the spectrum higher than the threshold.

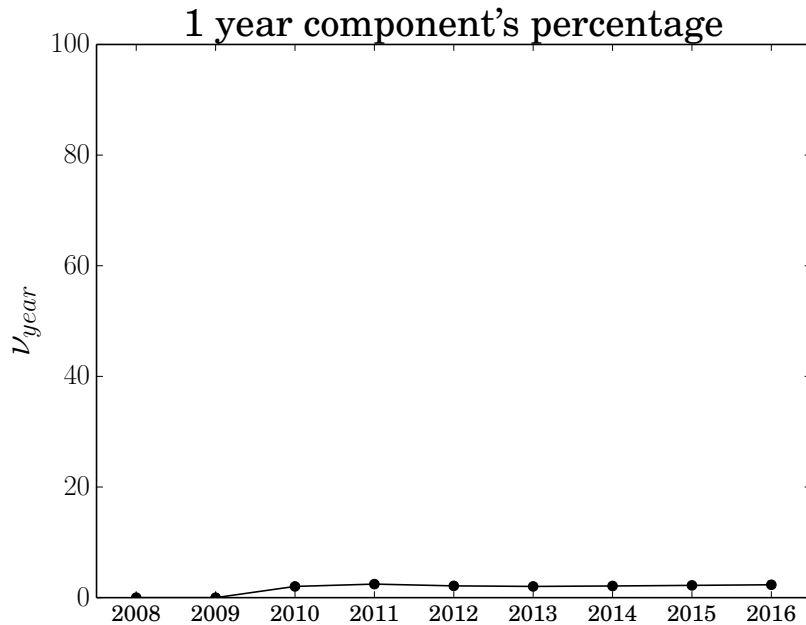


Figure 3.224: Dynamic analysis of the percentage of the one-year periodicity.

Station RN64 exhibits a predominant periodicity of six months, with a percentage weight of 7.18%, higher than the other periodicities. Time series shows a constant linear trend and data are approximately regular. The highest outliers occur in the residual time series in mid-2009 and in mid-2014, in correspondence of the two maxima of the time series. Residuals without outliers are best described by a Gamma distribution. From DFA plot, three scaling regimes are found: The first, from 14 days to  $\sim 55$  days, has a Hurst exponent  $H = 0.6425 \pm 0.0107$ ; the second, from  $\sim 55$  days to  $\sim 245$  days, has a Hurst exponent  $H = 0.3863 \pm 0.0028$ ; the third, from  $\sim 245$  days to the end of the series, has a Hurst exponent  $H = 0.1442 \pm 0.0038$ . The first two regimes show a change in the series from a correlated behaviour to an

anti-correlated one, while the third regime shows a highly anti-correlated behaviour of the residuals at big time scales, or it probably expresses the limitations of the algorithm in accurately estimating the degree of correlations in the residual time series [94]. The local Hurst exponent  $H_t$  is computed at a time window of two weeks and oscillates first around a value compatible with white noise ( $\sim 0.5$ ), then around a value compatible with long-range correlations ( $\sim 0.6$ ). The one-year component's percentage remains approximately constant around a value of 2% when adding new years.

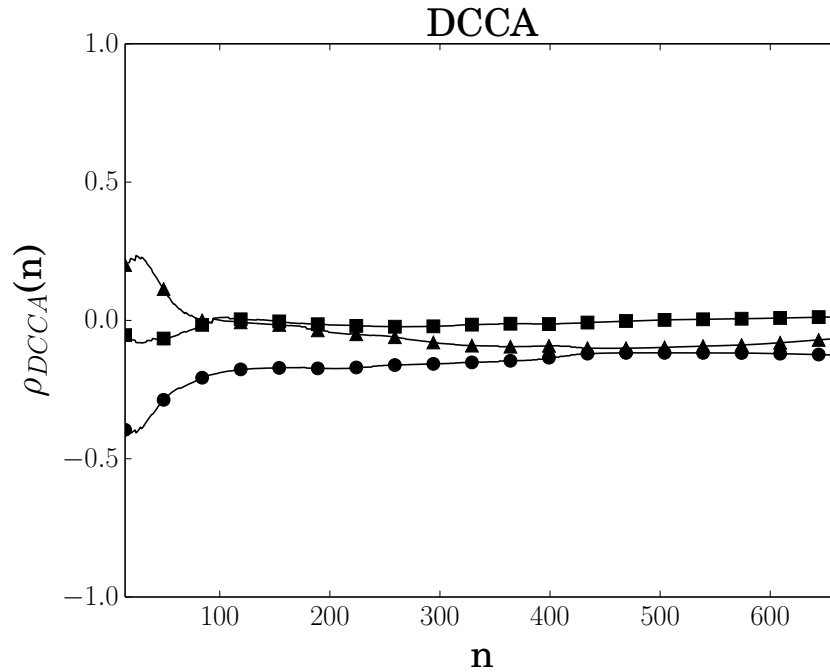


Figure 3.225: Detrended cross correlation between <sup>7</sup>Be and available meteorological parameters (humidity (○), temperature (△), pressure (□), wind direction (▽), and wind speed (◇)).

Station RN64 exhibits negative cross-correlations with humidity at small scales ( $< 100$  days) and positive cross-correlations with temperature at very small scales ( $< 50$  days). There are no cross-correlations with pressure. Wind direction and speed time series were not suitable for the analysis.

### 3.3.29 Petropavlovsk, Russian Federation (RN60)

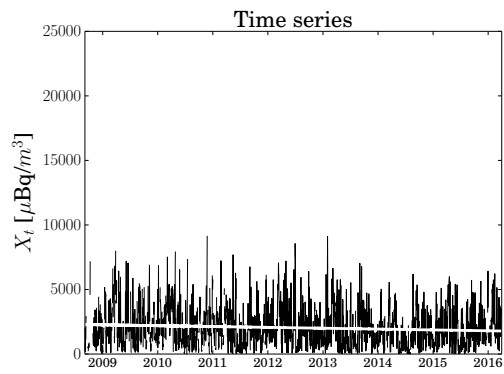


Figure 3.226: Time series with trend superimposed (solid white line).

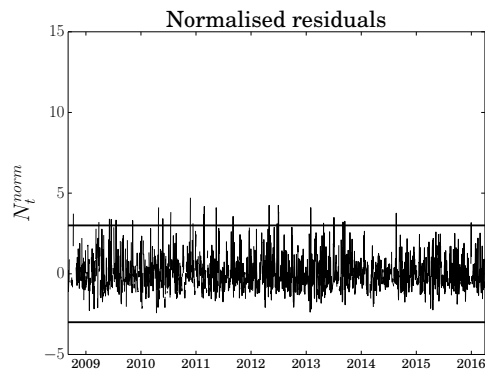


Figure 3.227: Normalised residual time series with the  $\pm 3\sigma$  thresholds (solid black lines).

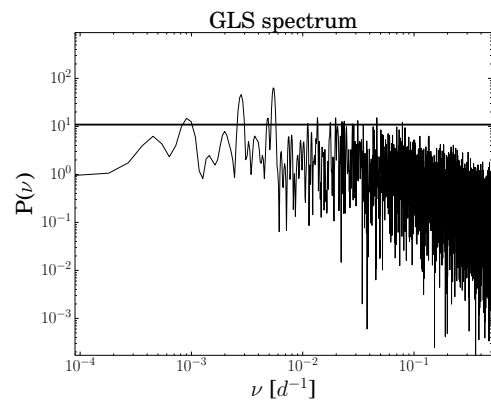


Figure 3.228: Log-log plot of the GLS spectrum with the associated threshold (solid black line).

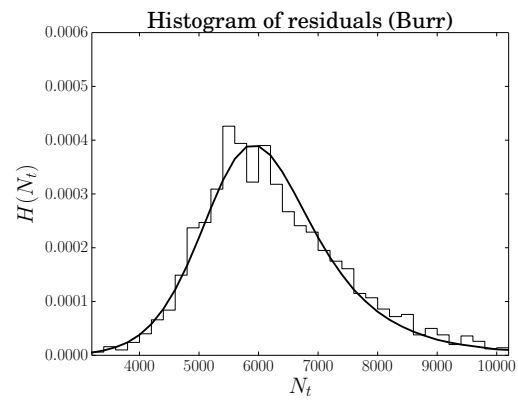


Figure 3.229: Histogram of residuals with the best-fitting distribution (no outliers).

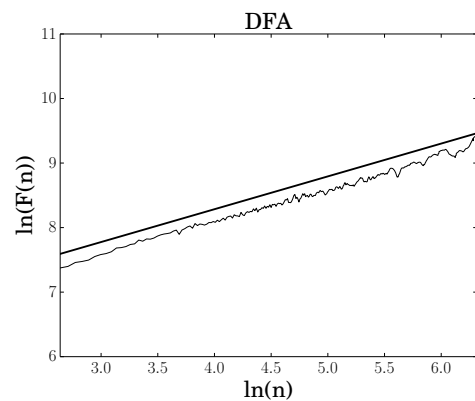


Figure 3.230: Detrended fluctuation analysis. The solid black lines are the best fit at different scales.

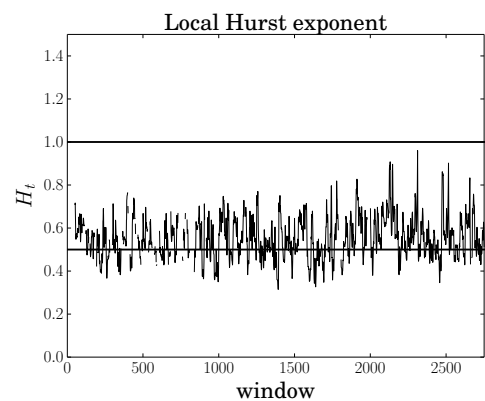


Figure 3.231: Local Hurst exponent  $H_t$  for a time window of two weeks. Solid lines represent the values of pink noise (top) and white noise (bottom).

Periodicity	Percentage	Value	Date
2 weeks	2.53	4.083	2010/04/28
1 month	5.12	4.682	2010/11/25
2 months	3.49	4.169	2011/02/25
3 months	0.79	4.094	2011/05/15
6 months	5.85	4.242	2012/04/30
1 year	2.92	4.244	2012/06/30
3 years	0.93	4.099	2013/01/31

Table 3.58: Periodicities as frequencies corresponding to peaks in the spectrum higher than the threshold.

Table 3.59: Outliers as values in the normalised residuals greater (less) than + (-)  $3\sigma$ . Only very high or very low outliers are listed.

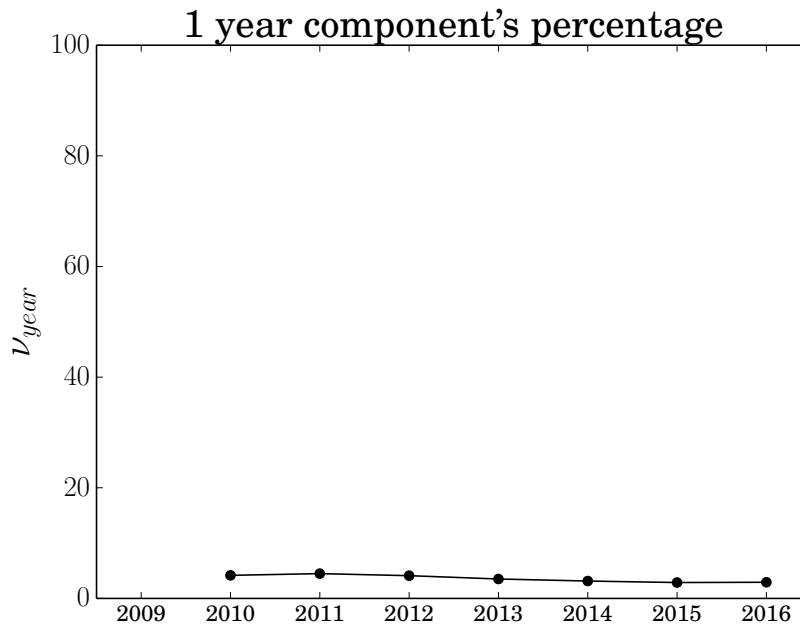


Figure 3.232: Dynamic analysis of the percentage of the one-year periodicity.

Station RN60 exhibits a predominant periodicity of six months, with a percentage weight of 5.85%, comparable with the other periodicities. Time series shows a constant linear trend and data are approximately regular. High outliers do not occur in the residual time series, as confirmed by the absence of great variations in the time series. Residuals without outliers are best described by a Burr distribution. From DFA plot, a single scaling regime is found, with a Hurst exponent  $H = 0.5086 \pm 0.0027$ . Residual time series are then uncorrelated (white noise). The local Hurst exponent  $H_t$  is computed at a time window of two weeks and oscillates first around a value compatible with white noise ( $\sim 0.5$ ), then around a value compatible with long-range correlations ( $\sim 0.6$ ), with great variations. The

one-year component's percentage remains approximately constant around a value of 3% when adding new years.

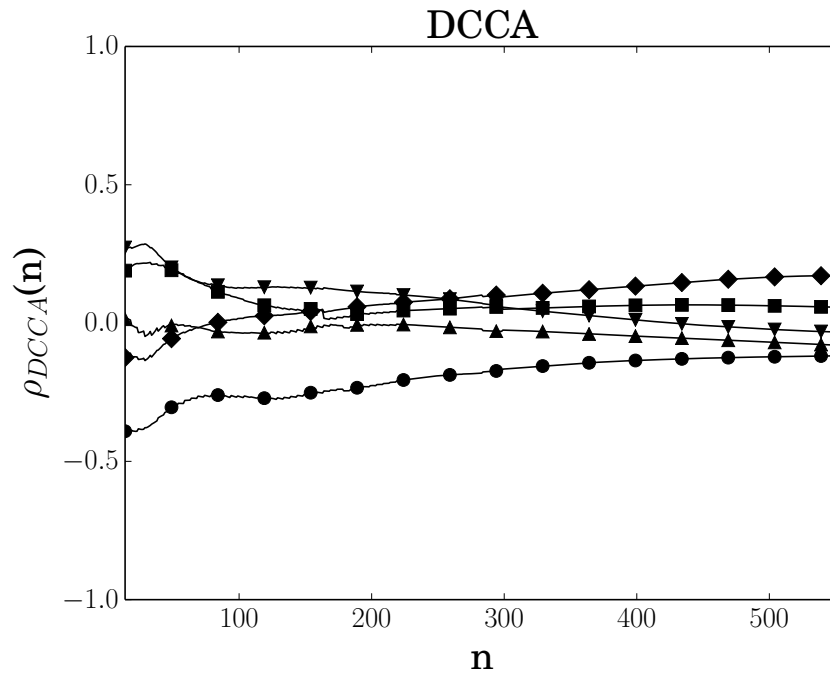


Figure 3.233: Detrended cross correlation between <sup>7</sup>Be and available meteorological parameters (humidity (○), temperature (△), pressure (□), wind direction (▽), and wind speed (◇)).

Station RN60 exhibits negative cross-correlations with humidity at small scales (< 200 days) and slightly positive cross-correlations with pressure and wind direction at very small scales (< 50 days). There are no cross-correlations with temperature and wind speed.

### 3.3.30 Dubna, Russian Federation (RN61)

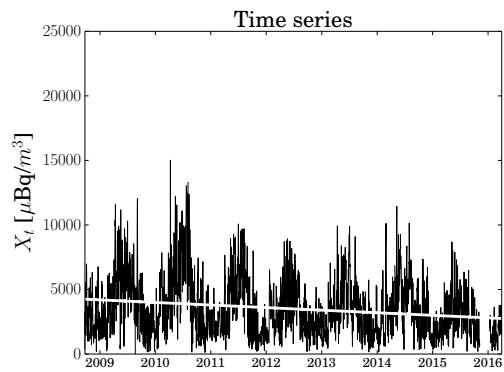


Figure 3.234: Time series with trend superimposed (solid white line).

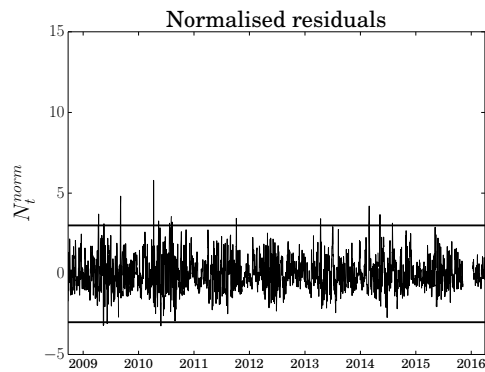


Figure 3.235: Normalised residual time series with the  $\pm 3\sigma$  thresholds (solid black lines).

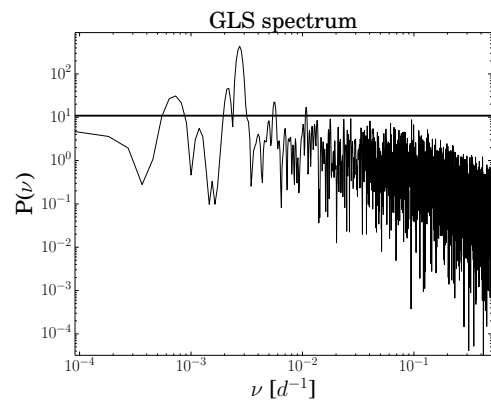


Figure 3.236: Log-log plot of the GLS spectrum with the associated threshold (solid black line).

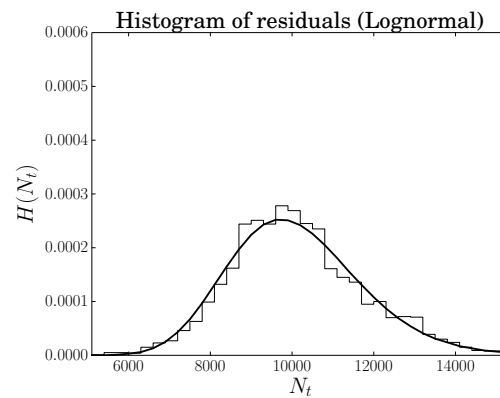


Figure 3.237: Histogram of residuals with the best-fitting distribution (no outliers).

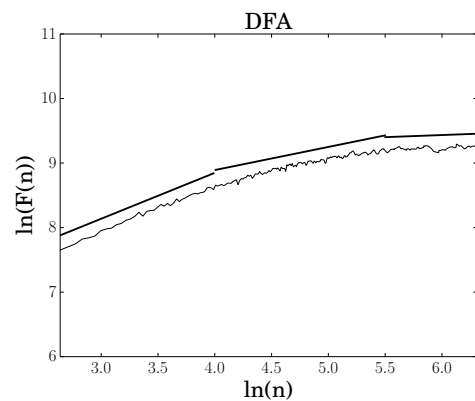


Figure 3.238: Detrended fluctuation analysis. The solid black lines are the best fit at different scales.

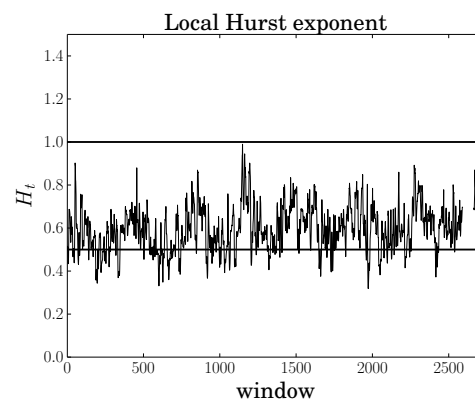


Figure 3.239: Local Hurst exponent  $H_t$  for a time window of two weeks. Solid lines represent the values of pink noise (top) and white noise (bottom).

Periodicity	Percentage	Value	Date
3 months	1.44	4.292	2009/09/04
6 months	1.91	4.811	2009/09/05
1 year	31.32	5.791	2010/04/10
1.5 years	2.72	4.199	2014/02/28
4 years	1.80		

Table 3.60: Periodicities as frequencies corresponding to peaks in the spectrum higher than the threshold.

Table 3.61: Outliers as values in the normalised residuals greater (less) than + (-)  $3\sigma$ . Only very high or very low outliers are listed.

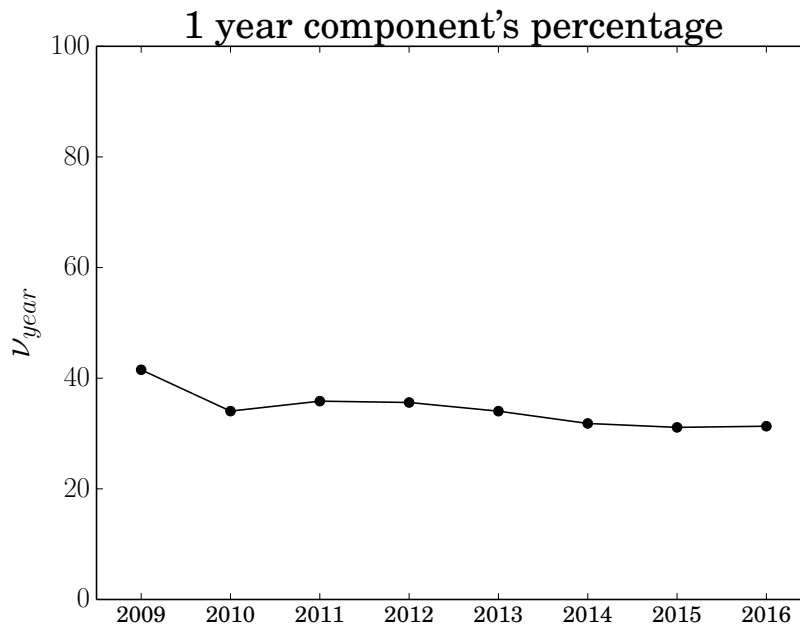


Figure 3.240: Dynamic analysis of the percentage of the one-year periodicity.

Station RN61 exhibits a predominant periodicity of one year, with a percentage weight of 31.32%, much higher than the other periodicities. Time series shows a downward linear trend and data are approximately regular, except for a period at the end of 2015. The highest outliers occur in the residual time series in mid-2010, in correspondence of the maximum of the time series. Residuals without outliers are best described by a Lognormal distribution. From DFA plot, three scaling regimes are found: The first, from 14 days to  $\sim 55$  days, has a Hurst exponent  $H = 0.7115 \pm 0.0099$ ; the second, from  $\sim 55$  days to  $\sim 245$  days, has a Hurst exponent  $H = 0.3584 \pm 0.0054$ ; the third, from  $\sim 245$  days to the end of the series, has a Hurst exponent  $H = 0.0653 \pm 0.0064$ . The first two regimes show a change in the series from a correlated behaviour to an anti-correlated one, while the third regime shows a highly anti-correlated behaviour of the residuals at big time scales, or it probably expresses the limitations of the algorithm in

accurately estimating the degree of correlations in the residual time series [94]. The local Hurst exponent  $H_t$  is computed at a time window of two weeks and oscillates first around a value compatible with long-range correlations ( $\sim 0.6$ ), then around another value compatible with long-range correlations ( $\sim 0.7$ ). The one-year component's percentage has an initial value that amounts to over 40% and then decreases up to a value of  $\sim 30\%$  when adding new years.

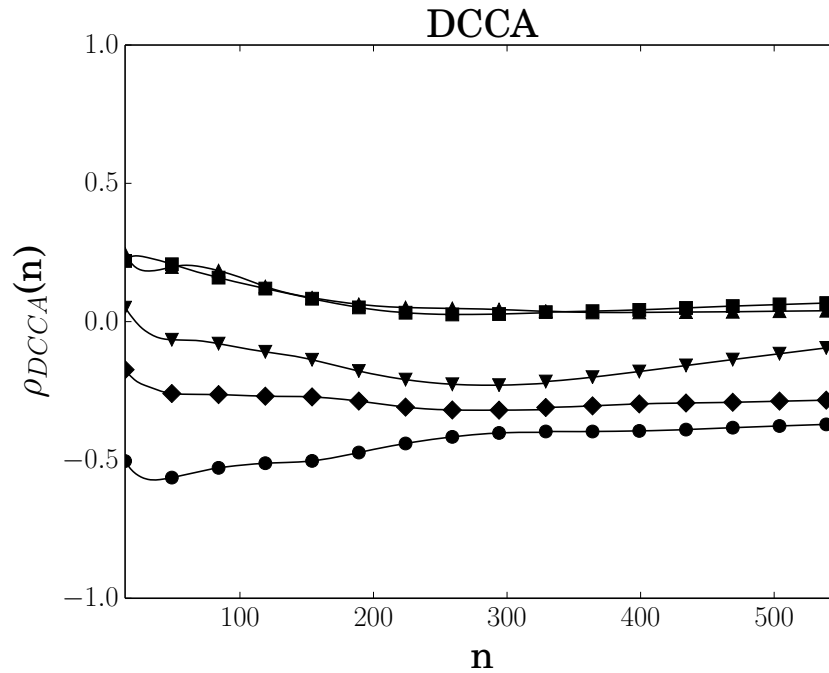


Figure 3.241: Detrended cross correlation between  $^7\text{Be}$  and available meteorological parameters (humidity (○), temperature (△), pressure (□), wind direction (▽), and wind speed (◇)).

Station RN61 exhibits negative cross-correlations with humidity and wind speed at all scales and slightly positive cross-correlations with pressure and temperature at small scales ( $< 100$  days). There are no cross-correlations with wind direction.

## CHAPTER 4

---

### Results and applications

---

In this Chapter, results of Chapter 3 are summarised in order to highlight similarities and differences among the stations. Some applications of the methodological approach described in Chapter 2 to other time series are presented in the appendices.

#### 4.1 Comparison of $^7\text{Be}$ stations

All the thirty stations described in Chapter 3 exhibit in their spectrum a periodicity of one year, even though it is not the predominant one for five stations: RN11, main periodicity of two weeks; RN17, main periodicity of one month; RN43, main periodicity of six years and a half; RN64, main periodicity of six months; RN60, main periodicity of six months. The effects of the one-year harmonic, due to atmospheric processes, are probably diminished by local properties of these five sites. The periodicity associated with the solar cycle ( $\sim 11$  years) is not detected in all those stations with a length suitable for detection. The effects of the solar cycle could also be masked by local properties of the site. Moreover, the 11-years periodicity is not always exactly eleven years and this is due to the fact that the solar cycle can last less or more than eleven years. Furthermore, the data cover the second part of the 23rd and the first part of the 24th solar cycles (Figure 4.1) and not a full solar cycle.

As far as the Southern hemisphere is concerned, all the stations in Australia show a periodicity associated with the solar cycle, along with a station in New Zealand (RN47), and the Argentinian and Brazilian stations (RN01 and RN11). In the Northern hemisphere, a possible solar cycle periodicity is found in some of the North American stations (RN75, RN16, RN74, RN72) and in the German one (RN33). From station RN26, time series are shorter than eleven years and the

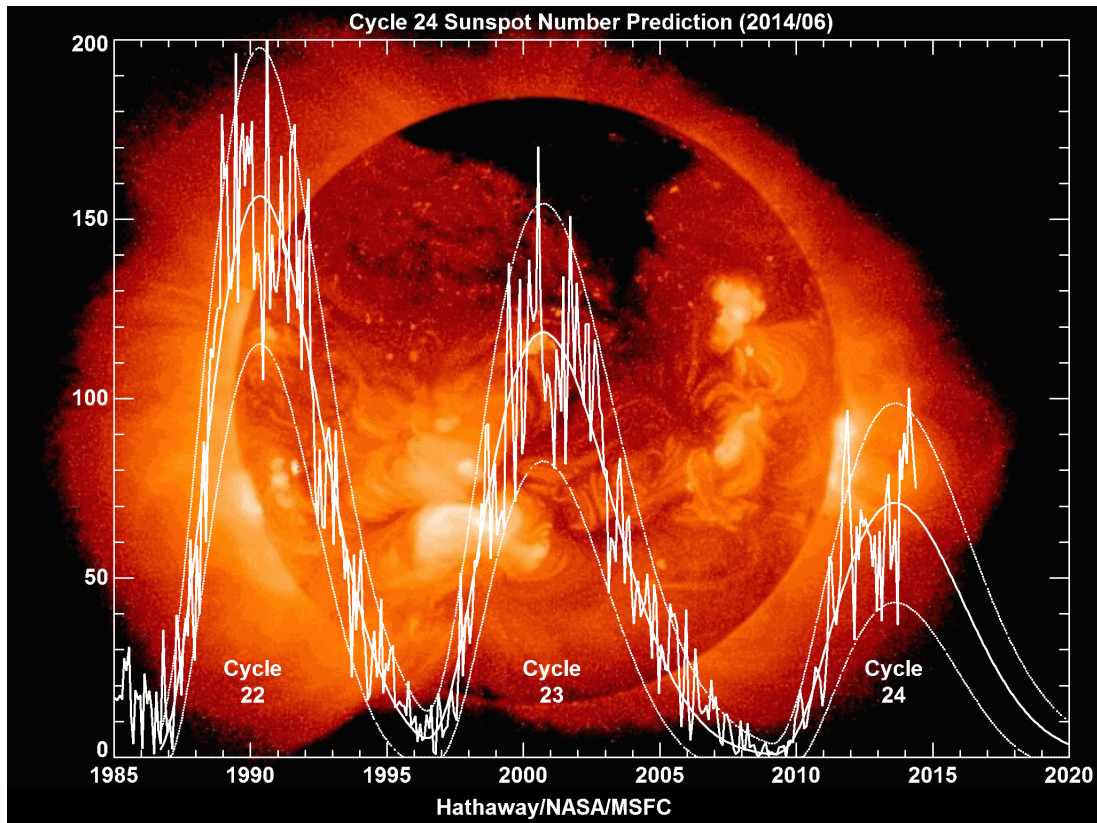


Figure 4.1: Sunspot number from 1985 to June 2014, with prediction up to 2020. (By David Hathaway - NASA, Public Domain)

solar cycle periodicity is not found.

The total percentage of the harmonics  $S_t$  is computed and the residuals percentage is obtained assuming the total time series has a percentage weight of 100%. Figure 4.2 shows the results of the spectral analysis for all the thirty  ${}^7\text{Be}$  stations. The percentage weight of the one-year harmonic (circles), the total percentage of the harmonic components  $S_t$ , without the one-year component (triangles) and the total percentage of the residuals  $N_t$  (squares) appear to be highly variable. In some regions there seem to be significant similarities among different stations (e.g. Oceania) while in other cases stations exhibit different behaviour (e.g. Europe or North America). This site characterisation approach should then be a preliminary step when studying atmospheric dynamics involving regional to global scales extrapolations, since interpolating data among IMS stations, which are globally distributed, inevitably results in information loss. The harmonic content of each station depends then on the specific location. It has to be noted anyway that the percentage weight of the one-year harmonic is below 30% for all but three stations (RN50, RN61, and RN37). The total percentage weight of the other harmonics is always below 30%.

The analysis of various years of sampling periods allows the evaluation of interannual variability. Percentage weight of the yearly component is shown in Fig-

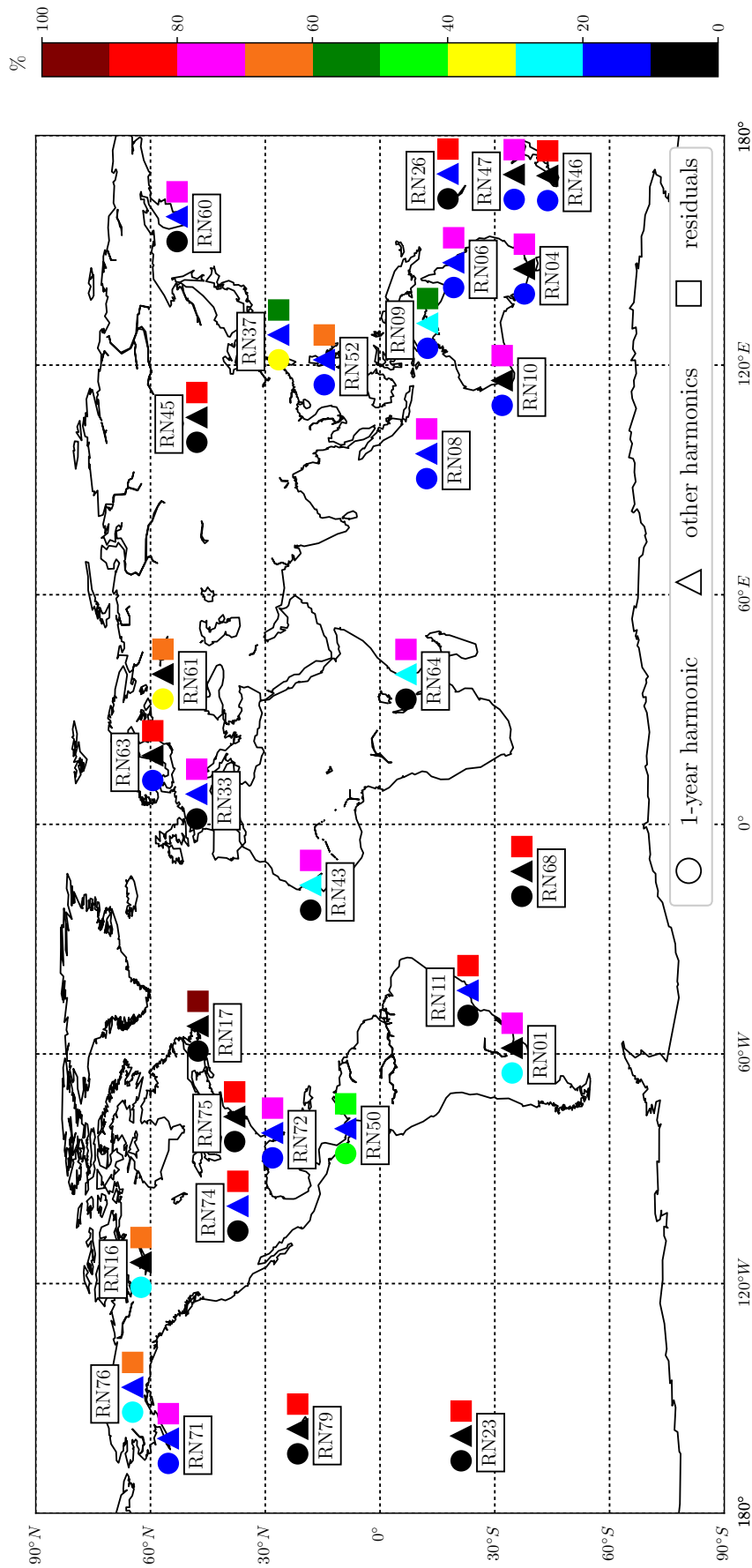


Figure 4.2: Map of percentages for  ${}^7\text{Be}$  for the thirty analysed stations. Each station is labelled with its ID, and the percentage of the 1-year harmonic ( $\circ$ ), the other harmonics ( $\triangle$ ), and the residuals ( $\square$ ) are shown.

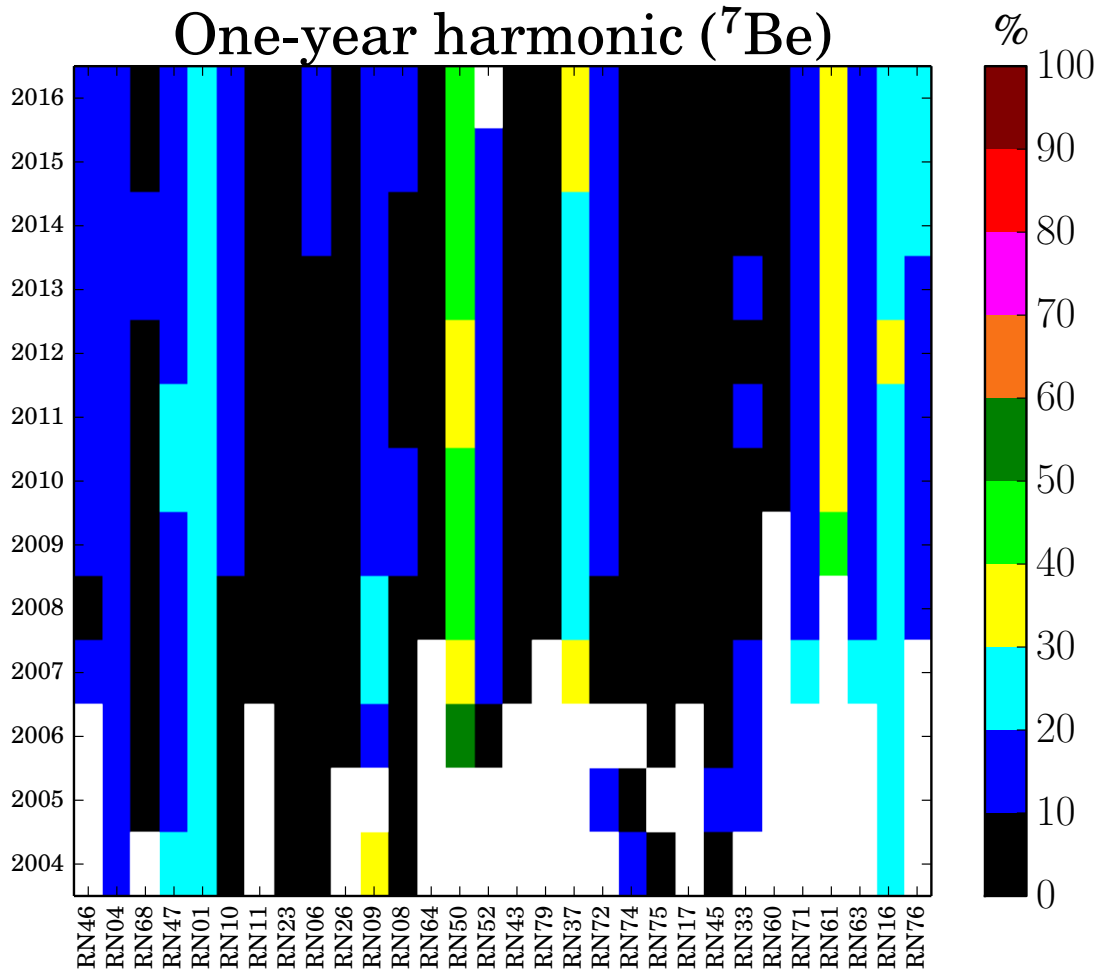


Figure 4.3: Variability of the one-year harmonic for the  $^7\text{Be}$  stations. Stations are organised in order of increasing latitude on the horizontal axis, while years are on the vertical axis. Different colours represent percentage weights of the annual harmonic in every year for every station.

Figure 4.3, with stations arranged in order of increasing latitude, and summarises the plots of the dynamic of the one-year harmonic shown in Chapter 3 for each station. Variability is present at every station. This means that the weight of the one-year component is modified when more data are included and added to the time series. The single periodic component is not stationary but varies within the time series. It is interesting to notice the very low percentage weight of the yearly component characterising some stations being clustered in correspondence of the black bands. As a geographical reference, RN64 and RN50 stations are respectively the last station in the Southern hemisphere and the first station in the Northern hemisphere. Thus, there is a total of 13 stations in the Southern hemisphere and 17 stations in the Northern hemisphere.

The scaling of the residuals shows instead similarities among the stations. Figure 4.4 shows the values of the Hurst exponent for the first two regimes found in the DFA plots of Chapter 3. At small time scales,  $^7\text{Be}$  residuals exhibit long-range

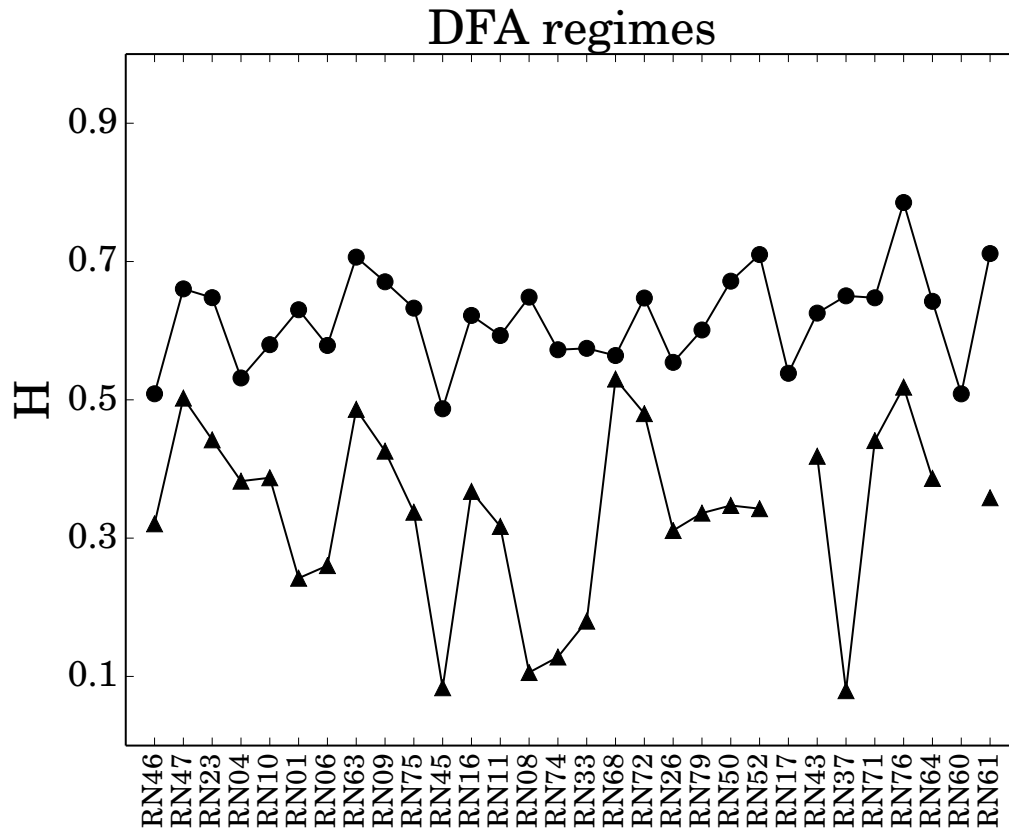


Figure 4.4: Values of the Hurst exponent for the first two regimes of DFA, i.e. small time scales (○) and big time scales (△).

correlations, and this is probably associated with the half-life of Beryllium 7, that is approximately 53 days and comparable to the small time scales of DFA. At longer time scales instead,  $^7\text{Be}$  residuals change their behaviour to uncorrelated or anti-correlated. This could also be associated with the short half-life, and also with precipitation that can remove Beryllium 7 from the air since it attaches to aerosols. However, the crossover, i.e. the change in the correlation properties, does not occur at the same scale for all the stations, some of them even exhibiting the crossover at a time scale of few months. This difference can be instead associated with the local properties of the site that can influence the transport of  $^7\text{Be}$ .

Where humidity time series is suitable for the analysis,  $^7\text{Be}$  exhibits negative cross-correlations with it, mostly at small time scales. This can be associated with the effects of precipitation on Beryllium 7 and the correlation is negative due to their inverse relationship. Cross-correlations with the other meteorological parameters vary instead from station to station and can be linked to local properties that can influence the transport of Beryllium 7, especially wind.

Four stations in different locations have been then chosen for a further detailed comparison between Northern hemisphere and Southern hemisphere [95]. Two stations are in the Southern hemisphere, RN01 (between  $60^\circ\text{S}$  and  $30^\circ\text{S}$ ) and RN06, (between  $30^\circ\text{S}$  and the equator), and the other two are in the Northern hemisphere,

RN72 (between the equator and 30°N), and RN63 (between 30°N and 60°N). Referring to Figure 4.3, a similar behaviour can be found in the variability of the one-year harmonic for the Northern hemisphere stations, while for the Southern hemisphere ones a different behaviour is clear, as RN01 is having a higher weight for the one-year component. Having removed all periodicities, it is possible to investigate the behaviour of the residuals. First, the local Hurst exponent is computed, as described in Chapter 2, to investigate how long-range correlations evolve during the time. Figure 4.5 shows the local Hurst exponent  $H_t$  for  $^7\text{Be}$  residuals. Northern (top) and Southern (bottom) hemisphere stations differ from each other, the former exhibiting larger fluctuations and also a higher mean value of  $H_t$ . If we

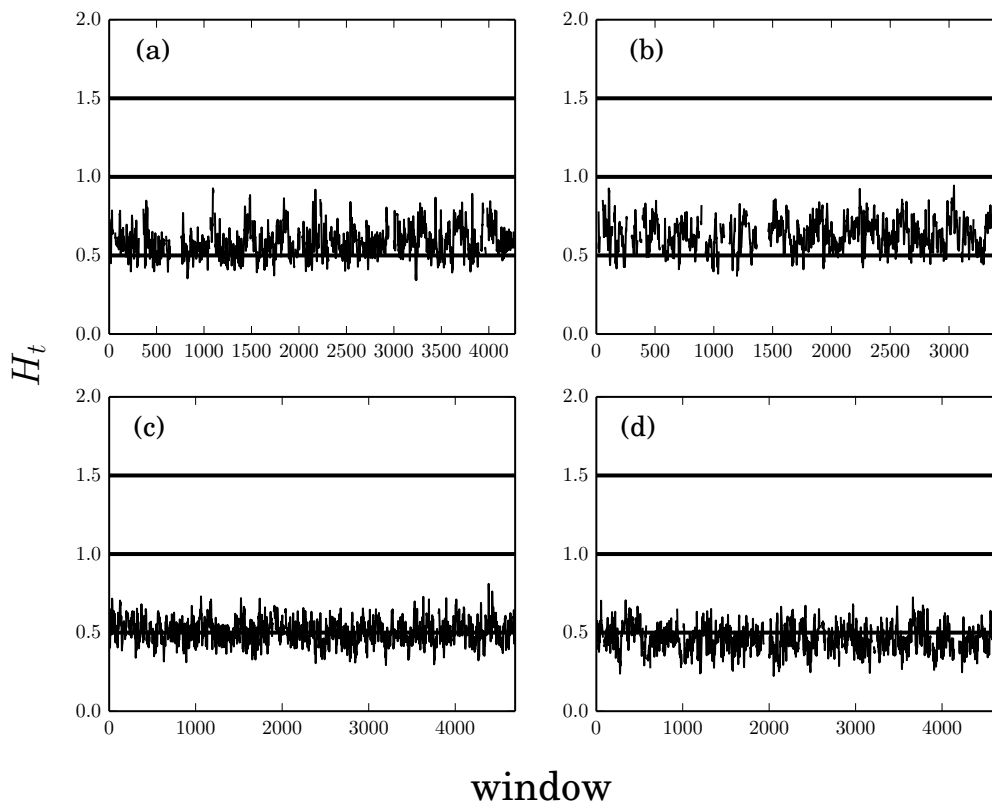


Figure 4.5: Values of the local Hurst exponent  $H_t$  for the four stations chosen for a detailed comparison. Two stations are in the Northern hemisphere (RN72 (a) and RN63 (b)) and the other two are in the Southern hemisphere (RN01 (c) and RN06 (d)).

compare the yearly mean of  $H_t$  with the total mean, the yearly-mean local Hurst exponent does not deviate substantially from the total mean and mean values for Southern hemisphere stations are comparable to white noise, while the Northern hemisphere stations exhibit long-range correlations. The normalised residuals are shown in Figure 4.6. The difference discussed for  $H_t$  affects the occurrence of outliers since Northern hemisphere stations exhibit a less compact structure and a higher number of significant outliers. To investigate how radionuclide time series are influenced by different meteorological parameters, detrended cross-correlation

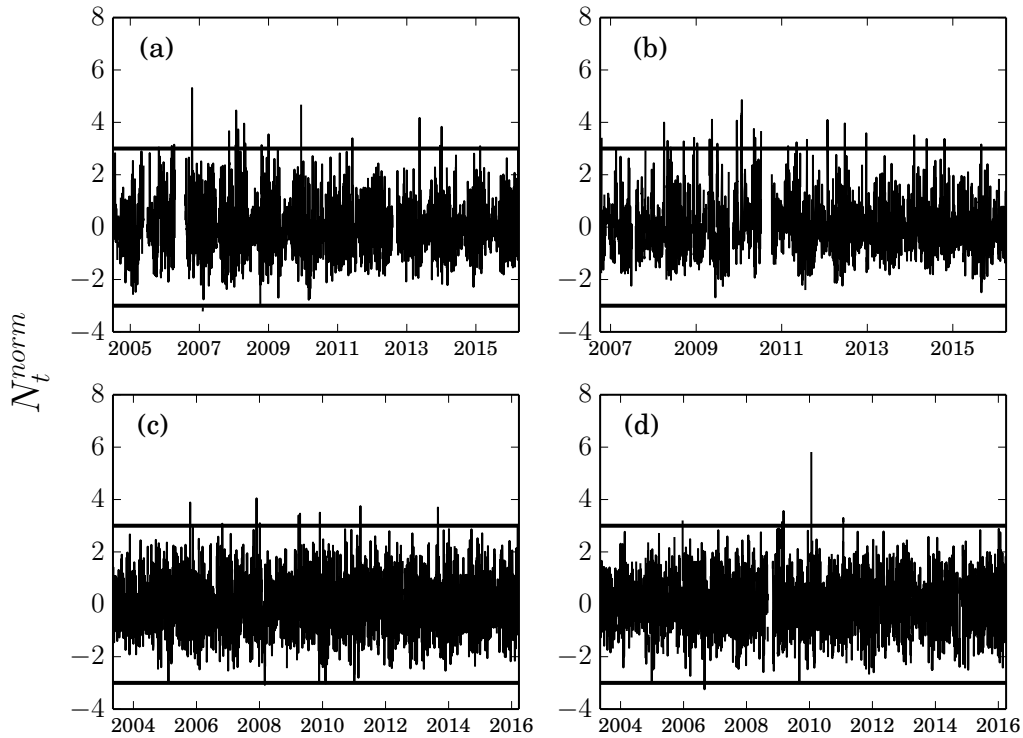


Figure 4.6: Normalised residuals for the four stations chosen for a detailed comparison. Two stations are in the Northern hemisphere (RN72 (a) and RN63 (b)) and the other two are in the Southern hemisphere (RN01 (c) and RN06 (d)).

analysis (DCCA) has been applied. Figure 4.7 shows cross-correlations at different scales between  $^7\text{Be}$  residuals and the other observables available for the particular site (among humidity, temperature, and pressure).  $^7\text{Be}$  at RN01 exhibits no correlation with pressure, while a correlation is found for the Australian (RN06) and American (RN72) stations, only at small scales, and for the Swedish station (RN63). Regarding the other observables, a correlation with temperature is found at small scales for the Swedish station (RN63). Relative humidity is anti-correlated with  $^7\text{Be}$  residuals at all scales for station RN06, while for the Swedish station (RN63) it is consistently less anti-correlated when going towards bigger scales.

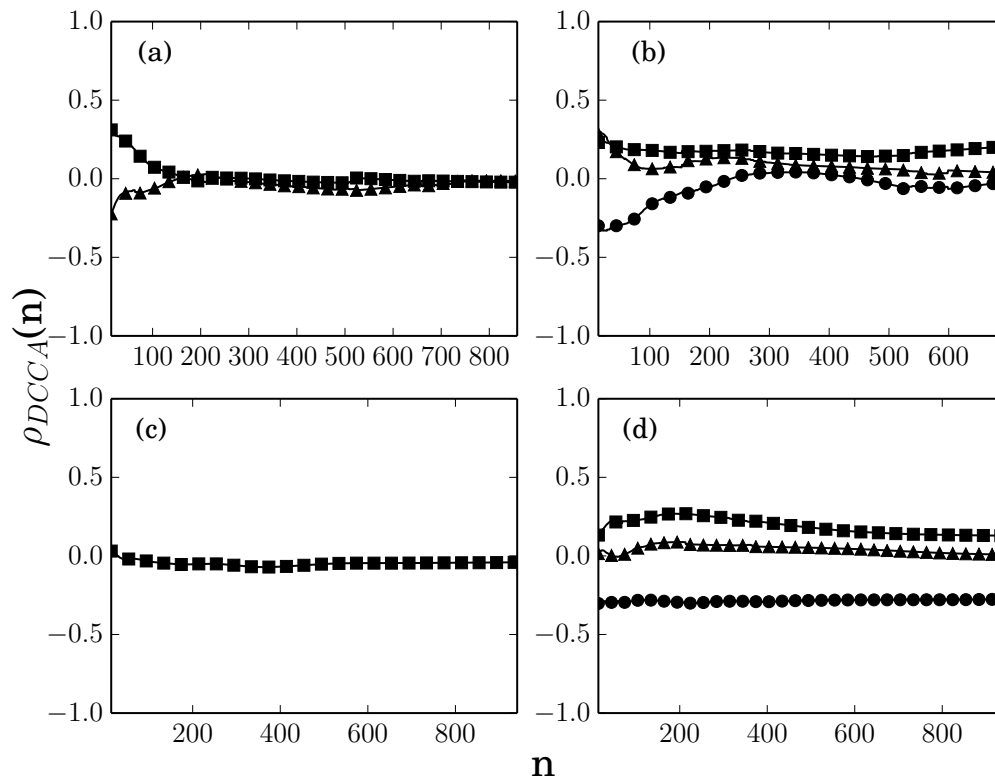


Figure 4.7: DCCA for the four stations chosen for a detailed comparison (only available meteorological parameters). Two stations are in the Northern hemisphere (RN72 (a) and RN63 (b)) and the other two are in the Southern hemisphere (RN01 (c) and RN06 (d)). Meteorological parameters are humidity ( $\circ$ ), temperature ( $\triangle$ ), and pressure ( $\square$ ).

---

## Conclusions

---

An approach based on time series analysis has been developed, in order to highlight differences and similarities in Beryllium 7 concentrations measured in various locations. The analysis is principally focused on the characterisation of three terms that compose the time series: The trend, i.e. a monotonic function that describes the overall growth of the data; the periodic term, from which the frequencies associated with the characteristic periodicities of the time series can be obtained; the residuals, i.e. the stochastic process underlying the trend and periodicities. Results have shown a great variability, in terms of both periodicities and residuals' persistence. In particular, the one-year harmonic has been found in every station and is the predominant one in the majority of them. A periodicity associated with the solar cycle has also been found in some of those stations with a time series length greater than 11 years. The total harmonic content's percentage is instead different in every station. The dynamic of the one-year component is also very different from station to station. As far as persistence is concerned, a similar behaviour can be found in the different sites. Residuals exhibit long-range correlations at relatively small scales, and this can be associated with the short half-life of Beryllium 7. At bigger scales instead, residuals became uncorrelated or anti-correlated. The crossover does not occur at the same scale for all the stations, and this can be due to differences in Beryllium 7 transport, depending on the particular site.

Finally, the procedure has been applied to other time series in order to show the validity of the method. Specifically, it has been applied to another cosmogenic radionuclide ( $^{22}\text{Na}$ ), a radionuclide of anthropogenic origin ( $^{133}\text{Xe}$ ),  $\text{CO}_2$  records, and uranium groundwater time series. The two radionuclides have been compared with Beryllium 7, while  $\text{CO}_2$  and uranium have been compared with other time series of the same observable. The analysis has thus been applied to problems concerning atmosphere, climate, and Earth's physics. It proved to be a valid procedure for characterising time series components and for a comparison among time series of the same observable.

## APPENDIX A

---

### ${}^7\text{Be}$ - ${}^{22}\text{Na}$

---

${}^{22}\text{Na}$  (sodium) data has been studied with the aim to look for possible differences with  ${}^7\text{Be}$  [95].  ${}^{22}\text{Na}$  has a half-life of 2.6 years, much longer than that of  ${}^7\text{Be}$ , is a cosmogenic radionuclide and is produced in reactions with argon. Since sodium time series from IMS lack a consistent amount of data, a comparison is only suitable for the American station RN72. Moreover, time series were rearranged in weekly samples to make the analysis possible, otherwise, there would be too missing data. Both radionuclides exhibit the same periodicities, 6 months and 1 year, the former having approximately the same weight and the latter having a higher percentage for the  ${}^7\text{Be}$  time series.  ${}^7\text{Be}$  and  ${}^{22}\text{Na}$  noises show a very different behaviour: While  ${}^7\text{Be}$  has a noise level that remains approximately constant around an average value of  $\mu \sim 0.5$ , with small fluctuations,  ${}^{22}\text{Na}$  is characterised by a higher local Hurst exponent, being subject to larger fluctuations around an average value  $\mu \sim 0.9$  (Figure A.1). Then, normalised residuals are shown in Figure A.2. It can be seen

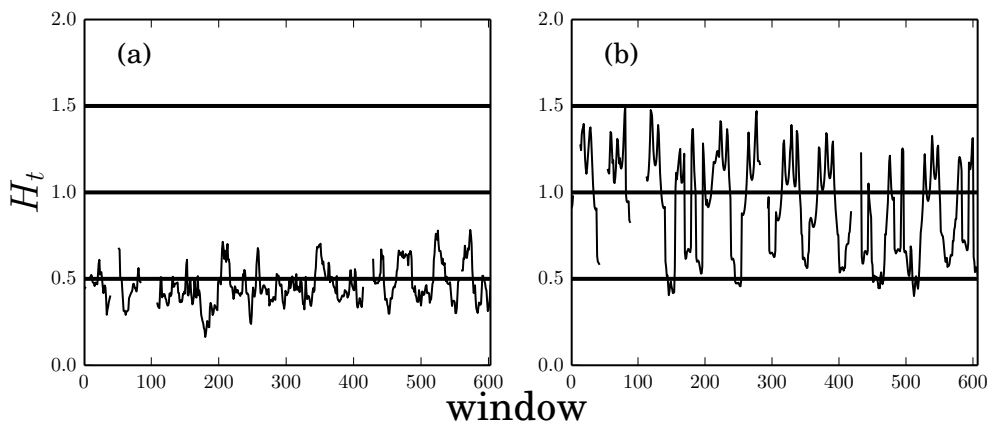


Figure A.1: Local Hurst exponent  $H_t$  for  ${}^7\text{Be}$  (a) and  ${}^{22}\text{Na}$  (b) comparison.

that higher and numerous outliers are observed for  ${}^{22}\text{Na}$ . Figure A.3 shows instead cross-correlations at different scales between  ${}^7\text{Be}$  ( ${}^{22}\text{Na}$ ) and the temperature and pressure for the American station RN72.  ${}^7\text{Be}$  has a slightly positive correlation with pressure and a slightly negative one with temperature, while  ${}^{22}\text{Na}$  shows no evident correlations with none of these meteorological parameters.

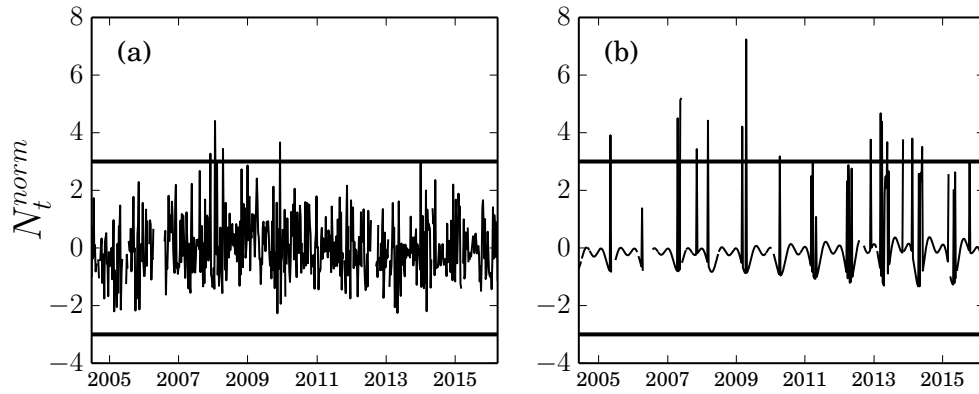


Figure A.2: Normalised residuals for  ${}^7\text{Be}$  (a) and  ${}^{22}\text{Na}$  (b) comparison.

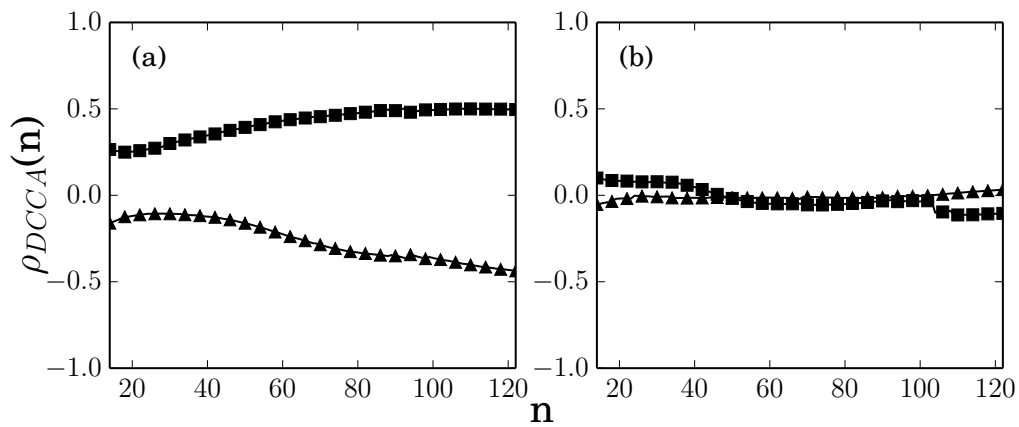


Figure A.3: DCCA for  ${}^7\text{Be}$  (a) and  ${}^{22}\text{Na}$  (b) comparison. Meteorological parameters are temperature ( $\triangle$ ) and pressure ( $\square$ ).

## APPENDIX B

---

### ${}^7\text{Be}$ - ${}^{133}\text{Xe}$

---

A comparison has been made between  ${}^{133}\text{Xe}$  and  ${}^7\text{Be}$  [96].  ${}^{133}\text{Xe}$  is a noble gas which has been produced during atmospheric and underground nuclear weapons tests, as well as by reprocessing nuclear facilities (RNF), nuclear power plants (NPP) and isotope production facilities (IPF) during their operational releases. Xenon is chemically inert and is not subject to dry or wet deposition like  ${}^7\text{Be}$ . Due to its suitable characteristics, it has been chosen as a possible signature of nuclear weapons tests. It is being monitored worldwide by the International Monitoring System (IMS). Due to radionuclide data availability, four stations of the IMS network's radionuclide component (RN) were chosen for data analysis, namely: RN75 (Charlottesville, USA) with data ranging from 7/06/2011 to 15/03/2015, RN33 (Schauinsland, Germany) from 30/06/2013 to 31/03/2016, RN63 (Stockholm, Sweden) from 1/09/2012 to 31/03/2016, and RN17 (St. John's, Canada) from 14/08/2014 to 31/03/2016. Having fully isolated the harmonic components, the residuals time series can be analysed. The local Hurst exponent obtained for  ${}^7\text{Be}$  and  ${}^{133}\text{Xe}$  residuals time series is shown in Figure B.1. The Hurst exponent  $H_t$  for Beryllium shows small fluctuations and is almost ever included between the lower and middle lines, that correspond to white and pink noise respectively. This indicates the presence of long-range correlations within the residuals time series. Gaps are due to missing data in the selected time window. Instead, xenon presents a very different behaviour. The Hurst exponent is on average in the pink-red noise band, and it has evident fluctuations. Notably, residuals time series for the Canadian station, which exhibits the highest average Hurst exponent for  ${}^{133}\text{Xe}$ , also presents the highest average value of  $H_t$  for  ${}^7\text{Be}$ . Differences come from the nature of the residuals time series, as can be seen in Figure B.2 where residuals, normalised to zero mean and unit variance, are shown. While beryllium is characterised by low values and a small occurrence of outliers, xenon residuals present an alternation of

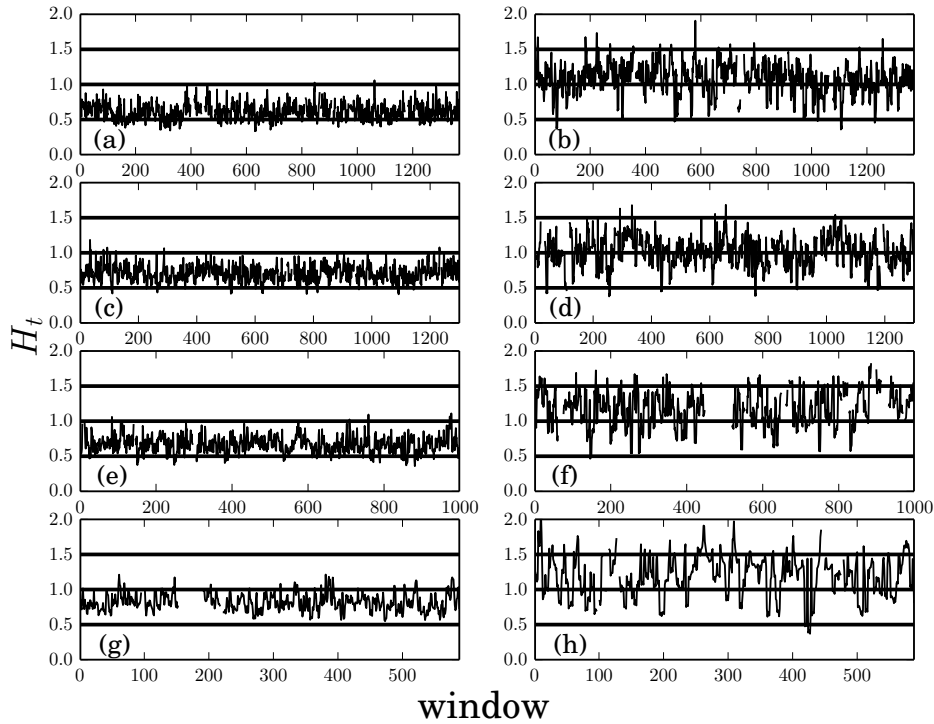


Figure B.1: Local Hurst exponent  $H_t$  for  ${}^7\text{Be}$  and  ${}^{133}\text{Xe}$  comparison. Stations are: RN75, (a) for  ${}^7\text{Be}$  and (b) for  ${}^{133}\text{Xe}$ ; RN63, (c) for  ${}^7\text{Be}$  and (d) for  ${}^{133}\text{Xe}$ ; RN33, (e) for  ${}^7\text{Be}$  and (f) for  ${}^{133}\text{Xe}$ ; RN17, (g) for  ${}^7\text{Be}$  and (h) for  ${}^{133}\text{Xe}$ .

low and high values, hence a higher number of outliers. The local Hurst exponent is in general high (small) when small (high) variations in the time series occur, and this reflects what Figures B.1 and B.2 show. Finally, residuals of beryllium and xenon have been cross-correlated with residuals of meteorological parameters, in order to highlight similarities in scaling behaviour. This has been done making use of the DCCA analysis, looking for a possible influence of meteorological parameters on radionuclide detections. Figure B.3 shows the results obtained for the four IMS stations, which exhibit distinctive cross-correlation patterns. For  ${}^7\text{Be}$ , stronger cross-correlations with meteorological parameters are found on average, compared to those found for xenon. Xenon residuals appear to be anti-correlated with pressure (American station) and wind direction (Canadian station). Interestingly, in the Canadian station both residual time series of xenon and beryllium appear to be anti-correlated with wind direction. This possibly indicates that this parameter influence detection of the two different radionuclides in a similar fashion. Moreover, while xenon at the American station is anti-correlated with residuals of atmospheric pressure for high values of  $n$ , beryllium is instead positively correlated with them. This could possibly indicate that activity concentrations measured at this station are more affected, with respect to the other stations, by low or high values of atmospheric pressure.

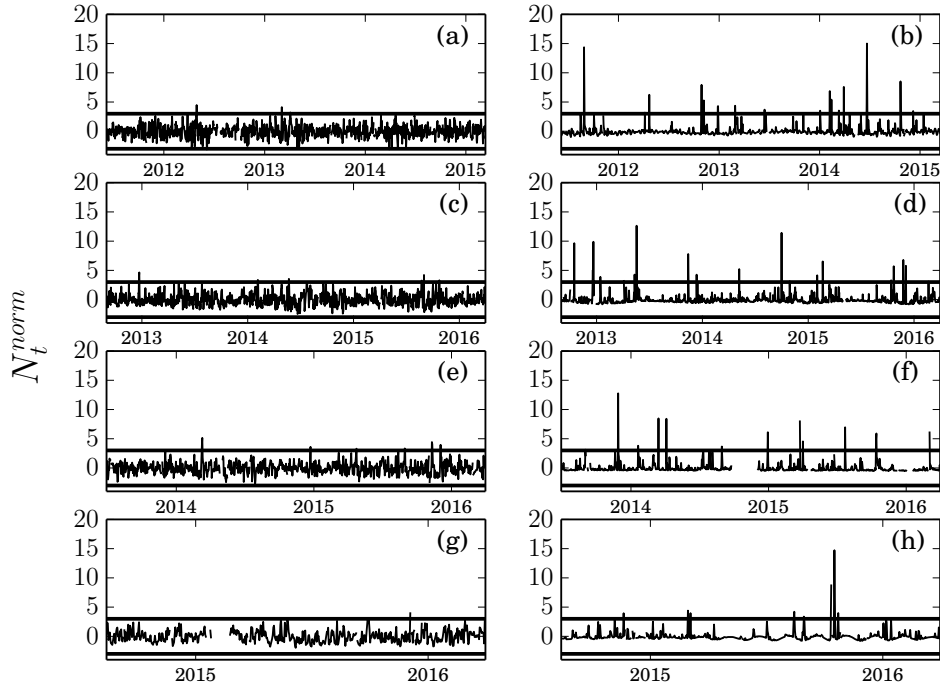


Figure B.2: Normalised residuals for  ${}^7\text{Be}$  and  ${}^{133}\text{Xe}$  comparison. Stations are: RN75, (a) for  ${}^7\text{Be}$  and (b) for  ${}^{133}\text{Xe}$ ; RN63, (c) for  ${}^7\text{Be}$  and (d) for  ${}^{133}\text{Xe}$ ; RN33, (e) for  ${}^7\text{Be}$  and (f) for  ${}^{133}\text{Xe}$ ; RN17, (g) for  ${}^7\text{Be}$  and (h) for  ${}^{133}\text{Xe}$ .

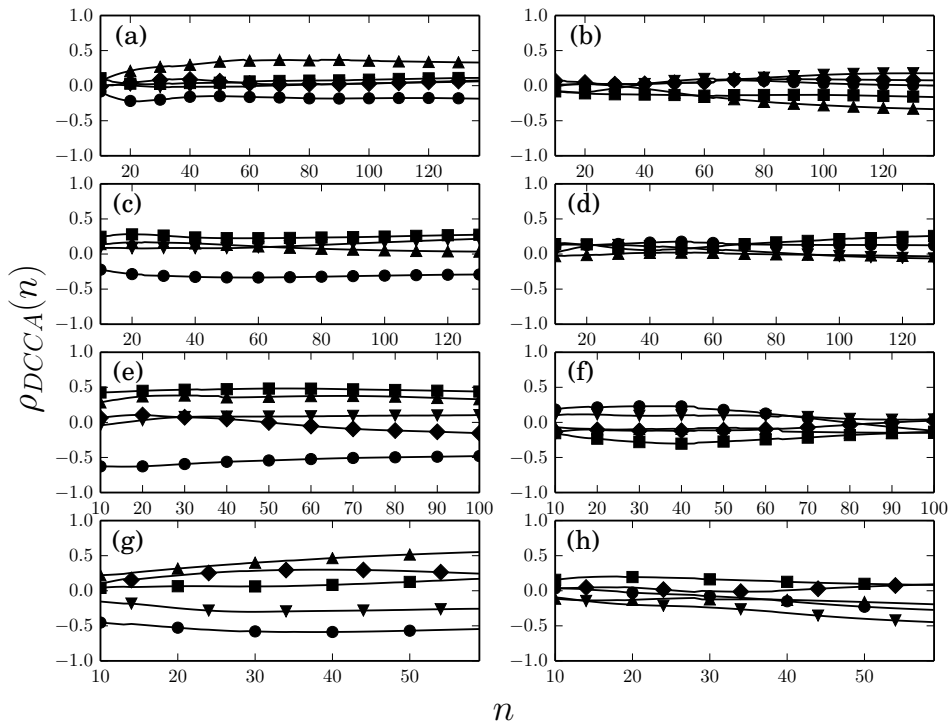


Figure B.3: DCCA for  ${}^7\text{Be}$  and  ${}^{133}\text{Xe}$  comparison. Stations are: RN75, (a) for  ${}^7\text{Be}$  and (b) for  ${}^{133}\text{Xe}$ ; RN63, (c) for  ${}^7\text{Be}$  and (d) for  ${}^{133}\text{Xe}$ ; RN33, (e) for  ${}^7\text{Be}$  and (f) for  ${}^{133}\text{Xe}$ ; RN17, (g) for  ${}^7\text{Be}$  and (h) for  ${}^{133}\text{Xe}$ .

## APPENDIX C

---

### CO<sub>2</sub>

---

The method described in Chapter 2 has been here applied to a climate related topic, i.e. the variability in  $CO_2$  records [97]. The observed increase of atmospheric  $CO_2$  is the result of various processes which include natural variability in emission and absorption, anthropic emissions, atmospheric transport and photochemical processes, and complex interactions among vegetation, the atmosphere, oceans, and, over very long time scales, geological structures. A relatively large number of sites has been setup starting from 1950's for the monitoring of atmospheric  $CO_2$  and the investigation of these complex processes and to quantify the human impact on climate. Several methods have been implemented to analyse these time series of  $CO_2$  surface observations [98, 99, 100, 101].

The analysis of the same variable in different locations is aimed at highlighting similarities, possibly linked to global processes, and differences related to regional and local phenomena. The first site is Lampedusa ( $35.52^\circ$  N,  $12.63^\circ$  E), a small island in the central Mediterranean sea. The measurement site is at an altitude of 45 m a.s.l., and is operative since 1992. The second station is Mauna Loa ( $19.54^\circ$  N,  $155.58^\circ$  W), where  $CO_2$  monitoring started in the 1950's at the remarkable height of 3397 m a.s.l. Its remote location, height, and minimal influences from vegetation and human activity are ideal for  $CO_2$  monitoring and analyses as far as climate change is concerned. The  $CO_2$  time series used in this study range from May 1992 to November 2014 for both Lampedusa and Mauna Loa. The dataset is constituted by weekly values. Ambient air is sampled in flasks at the two sites and subsequently analysed in the lab [102, 103]. Even though  $CO_2$  values range between 350 and 400 parts per million (*ppm*) for both the time series, the Lampedusa data appear to be more noisy, with higher variations than at Mauna Loa. This is reflected in the trend  $T_t$ , as shown in the upper part of Figure C.1. The trend for Lampedusa is less steady, due to years with a smaller amplitude. Once the trend

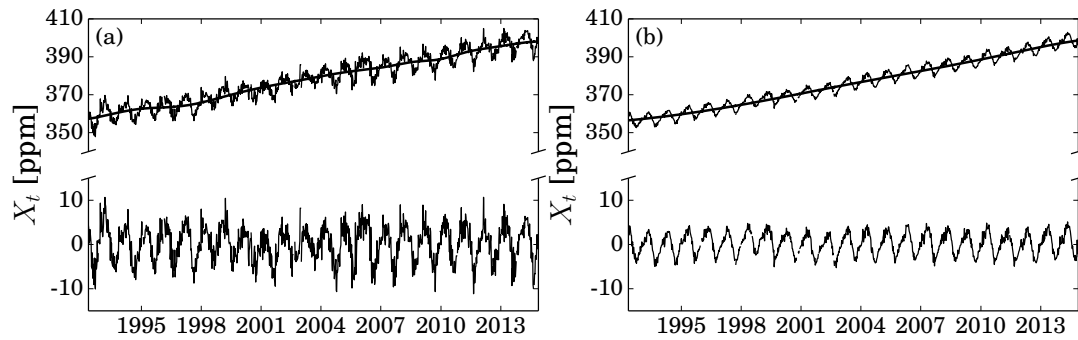


Figure C.1: Upper part: Trend estimation via empirical mode decomposition for CO<sub>2</sub> time series measured in Lampedusa (a) and Mauna Loa (b). The trend  $T_t$  is the solid line superimposed on the time series. Lower part: Detrended time series for Lampedusa (a) and Mauna Loa (b).

is removed, the difference in amplitude is more evident, as shown in the lower part of Figure C.1. Here the amplitude of the Lampedusa time series is about 20 ppm, while Mauna Loa time series only has half the amplitude.

An opposite result is found in the frequency domain, where the Mauna Loa time series gives higher contribution in terms of periodicities with respect to the Lampedusa time series. The GLS periodogram is shown in Figure C.2. Two peaks over the threshold are present in both spectra and correspond to the annual and semi-annual cycles. The annual peak is prominent in both periodograms and explains

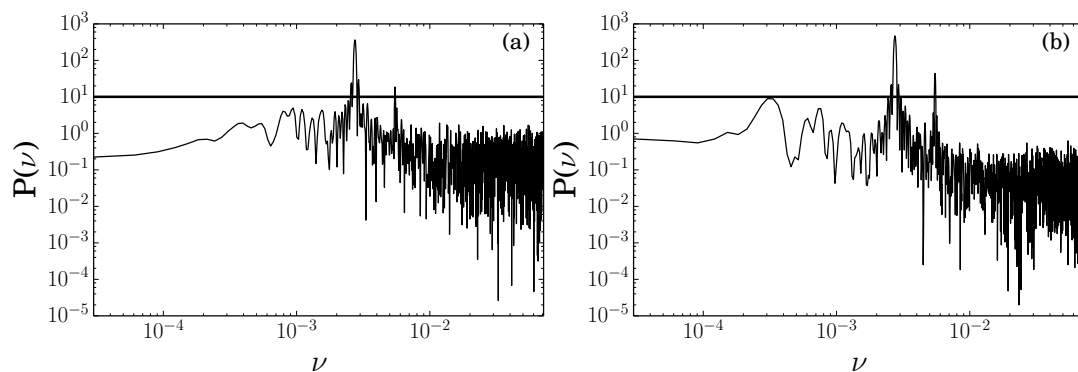


Figure C.2: GLS periodogram for Lampedusa (a) and Mauna Loa (b) time series. Peaks over the threshold (horizontal solid line) correspond to the annual and semi-annual cycles.

76.5% of the variability of the Mauna Loa time series, and 59.4% of the variability of the Lampedusa time series. Thus, even though the annual cycle of the Lampedusa time series has a bigger amplitude in the time domain, it contributes less in the frequency domain compared to the one of Mauna Loa. Similarly, the semi-annual cycle contributes by 6.6% to the periodogram of Mauna Loa, and by 2.5% to the periodogram of Lampedusa. If the annual and semi-annual cycles are removed, the GLS periodogram can be reapplied until no peaks above the threshold are found.

For Lampedusa, the other peaks correspond to periodicities of  $\sim 3.5$ ,  $\sim 3.0$ ,  $\sim 1.8$  years, all contributing by less than 1% to the periodogram. As emphasised by Chamard et al. [102] and Artuso et al. [98], a correlation exists between the  $CO_2$  growth rate at Lampedusa and global temperature and El Niño-Southern Oscillation, and these correlations involve similarities in the 3 and 3.5 year periodicities. For Mauna Loa instead, periodicities are  $\sim 8.2$ ,  $\sim 4.7$ ,  $\sim 3.8$ ,  $\sim 3.0$ ,  $\sim 2.4$  years, all contributing by less than 1% to the periodogram, except for the first one which has a percentage weight of 1.7%. Kane and de Paula [104] analysed Mauna Loa monthly  $CO_2$  observations over the period 1959-1992 and found highly significant periodicities of 14, 8, 5, and 3.4 years, as well as at 2.6 years, which appears to be connected with the Southern Oscillation. They also found a periodicity on the annual amplitude which seems to be related to the Quasi Biennial Oscillation. The frequency at about 3.4 years was found also in the global temperature time series. The similarities in some of the frequencies indicate that large scale/global processes, such as variations in the global temperature and the Southern Oscillation, are related to the  $CO_2$  evolution at least on the hemispheric scale. Some processes, like the quasi biennial oscillation, appear to specifically pertain the tropical regions and to have a negligible influence on  $CO_2$  at mid latitudes.

Peaks corresponding to the annual and semi-annual cycles are removed, and residual time series are normalised to zero mean and unit variance since both time series passed the test against a normal distribution. Normalised residual time series are shown in Figure C.3. As expected, the Mauna Loa residuals time series

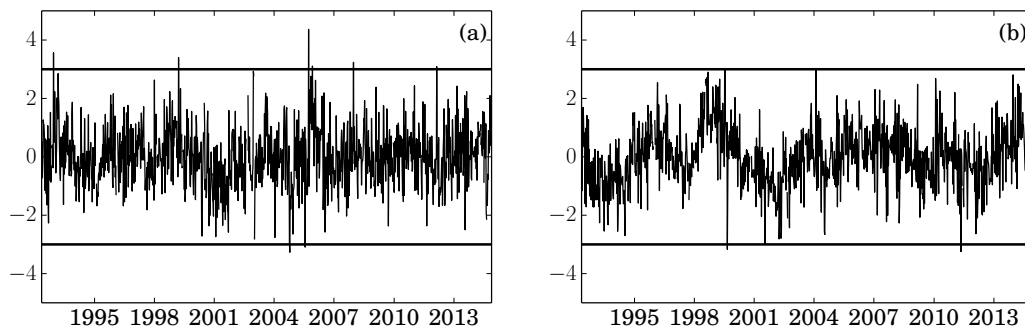


Figure C.3: Normalised residual for Lampedusa (a) and Mauna Loa (b) time series. The two horizontal lines represent the  $\pm 3\sigma$  thresholds.

is essentially devoid of outliers and is less noisy than at Lampedusa. The Lampedusa residual time series is instead noisier and an outlier above  $+4\sigma$  occurs on 16 September 2005. Correlative measurements and analyses with backward air-mass trajectories suggest that local gaseous sources have influenced the sampled air, which contains relatively high  $CH_4$ . The chemical composition of the aerosol sampled on the same day suggests that the dominant sources of particles are from the marine and the biogenic sector. Standard deviations used for normalisation are 2.23 ppm and 0.78 ppm for Lampedusa and Mauna Loa, respectively, confirming the larger fluctuations of  $CO_2$  records in the Italian station. This behaviour is

well explained by the influence from regions with contrasting characteristics with an uneven distribution of sources (mainly anthropic emissions, in particular from central and eastern Europe, fires in summer, ship traffic, and desert areas in the south) and sinks (mainly vegetation in Europe, and desert in Africa), the latitudinal  $CO_2$  gradient, and modulation by synoptic disturbances [98].

Finally, persistence is inspected via detrended fluctuation analysis (DFA), both globally and locally. A minimum window of about three months has been chosen for the analysis. Results of DFA are shown in Figure C.4, where once again fluctuations at Lampedusa are larger than those at Mauna Loa. The Hurst exponent is  $H = 0.994 \pm 0.014$  at Mauna Loa, i.e. residuals are in the pink noise regime, and  $H = 0.811 \pm 0.008$  at Lampedusa. Thus, even though both residual time series display long-range correlations, Mauna Loa exhibits stronger correlations than Lampedusa. The difference in the Hurst exponent, i.e. the difference in the scaling properties of the residual time series, is associated with the factors that can influence the  $CO_2$  concentrations in the two sites. Mauna Loa station is placed at a very high altitude and has minimal influences coming from vegetation and human activity. Similar results on the long-range correlation were found at Mauna Loa by Varotsos et al. [101]. Conversely, this long-range correlation might be masked by the higher shorter-term variability at Lampedusa.

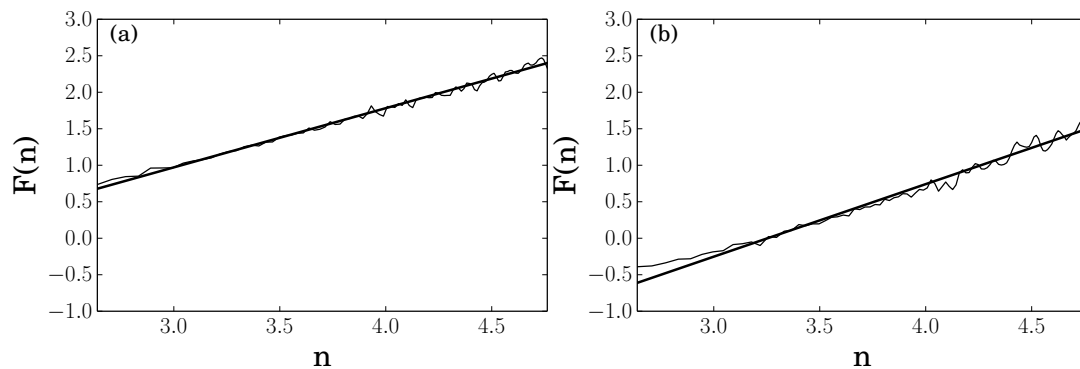


Figure C.4: DFA for Lampedusa (a) and Mauna Loa (b) time series. The best fit is represented by the solid straight line, whose slope is  $H = 0.811 \pm 0.008$  at Lampedusa and  $H = 0.994 \pm 0.014$  at Mauna Loa.

Then, the local Hurst exponent  $H_t$  is evaluated for the three months time window. Results are displayed in Figure C.5. The value of the local Hurst exponent fluctuates in time, with low values corresponding to periods with great  $CO_2$  variations, and high values corresponding to periods with small variations. The mean value of  $H_t$  is slightly smaller than the Hurst exponent  $H$ , as can be seen in Figure C.4, where for a time window of three months  $F(n)$  deviates from the straight line fit.

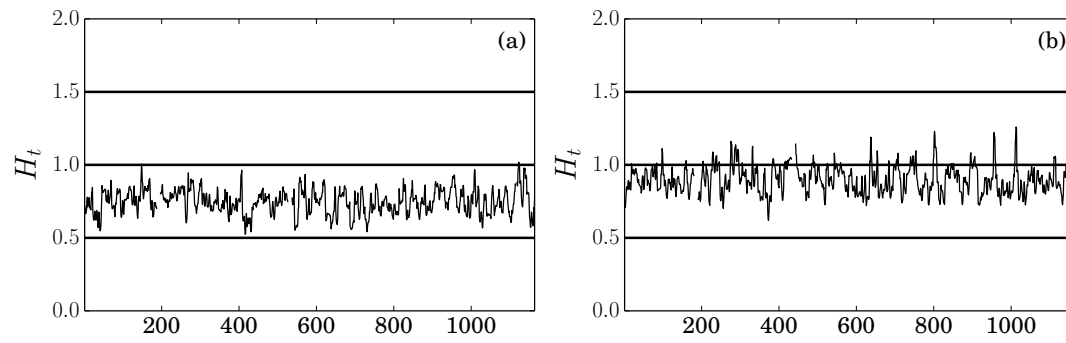


Figure C.5: Local Hurst exponent  $H_t$  for Lampedusa (a) and Mauna Loa (b) time series. The three horizontal lines represent the values for red noise (top), pink noise (middle), and white noise (bottom).

## APPENDIX D

---

### Uranium

---

The method described in Chapter 2 has been here applied to a different topic, i.e. variability in uranium groundwater concentrations [105]. Radon (Rn) has been investigated as a possible strain meter in geodynamical processes and its anomalies has been widely detected [106, 107, 108, 109, 110, 111, 112, 113, 114, 115, 116, 117], but there is no clear evidence that it is really a good earthquake's precursor. The physical processes associated with radon anomalies are based on changes in radon emanation rates due to strain signal near the earthquake's nucleation point. Particularly, it is unclear its behaviour before, during and after the main shock, considering the consolidated scheme for radon release due to stress-strain processes in the rock [118]. Therefore, uranium (U) has been investigated as a possible strain meter, particularly in those environments characterised by active normal faulting [118, 119, 120, 121, 122]. Since June 2008, in the Gran Sasso National Laboratory of the Italian National Institute of Nuclear Physics, uranium has been frequently analysed in groundwater, to study the possible pattern for radon sources in groundwater, its contribution to neutron flux background, and the hydrological patterns in the aquifer [123, 124]. The Gran Sasso area was marked by the relatively intense seismic activity, which could be mostly clustered between October 2008 and December 2010 and culminated in the event of April 6th, 2009 ( $M_w=6.3$ ), and by relatively quiet seismic periods preceding and following it. U anomalies in groundwater were detected until the beginning of March 2009 about one month before this earthquake. Those anomalies have been investigated by seismic analysis [118, 125] as well as by hydrological approach [124, 126]. Furthermore, U and Th decay chain disequilibria in different water environments have been widely used in investigating mixing problems among different reservoirs [127, 128, 129, 130]. All those analyses confirmed for the U groundwater anomalies observed before the seismic swarm and the main shock, a possible scenario characterised by a progres-

sive increase of deep  $CO_2$  fluxes at middle-lower crustal levels, directly associated with the geodynamics of the earthquake.

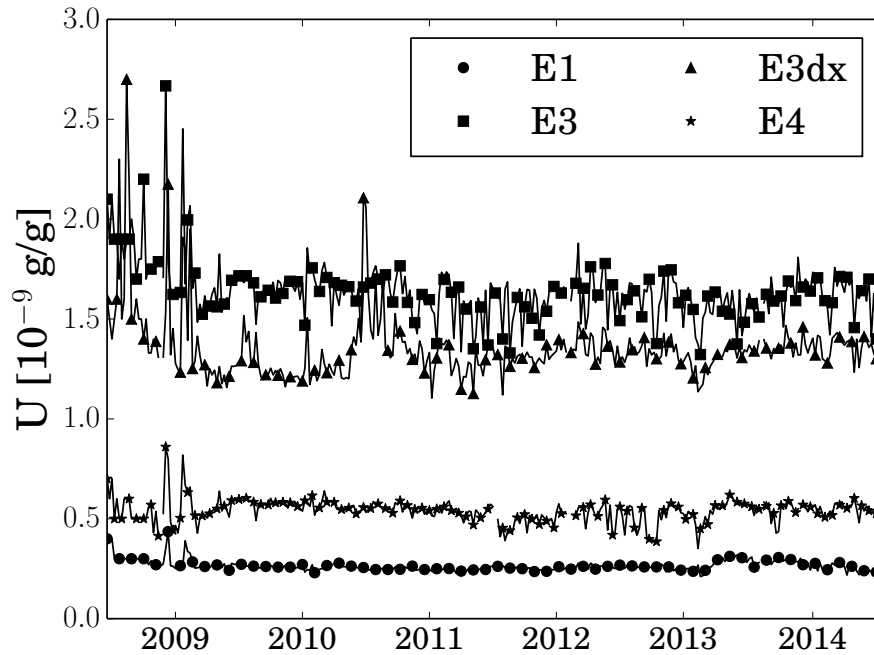


Figure D.1: Uranium time series.

From June 2008 to July 2014, U, electrical conductivity, pH, and the oxidation reduction potential (ORP) have been measured at the Gran Sasso National Laboratory of the National of the Italian Institute of Nuclear Physics [125]. The U concentration time series have been measured at four different sites (E1, E3, E3dx, and E4), and can be correlated with the other parameters in order to find possible correlations. The used approach differs from other methods employed for U time series analysis, and it is focused on outliers and noise structure. The four U time series are shown in Figure D.1. E1 and E4 exhibit small values of U concentrations, with respect to the other two sites, E3 being the one with the highest concentration. Significant peaks can be noticed around 2009, in correspondence of the L'Aquila earthquake occurred nearby the measuring sites. After the frequencies corresponding to periodicities in the periodogram have been filtered out, the residual time series is normalised to zero mean and unit variance in order to detect outliers. A threshold of  $\pm 3\sigma$  has been chosen for the analysis. Figure D.2 shows the normalised residual time series  $N_t^{norm}$ . Evident outliers are present in all the four time series in the period of the L'Aquila earthquake. Outliers are also found in 2008 for the E1 and E3dx sites. Remarkably, E3dx exhibit an outlier in mid-2010 [125]. In early 2013 an outlier (slightly less than  $-3\sigma$ ) is found in the E4 site. Figure D.3 shows the local Hurst exponent for the four sites, computed at a time window of one month.  $H_t$  shows a great variability, and oscillates around  $H_t = 1$  (pink noise) in E1 and E4, is between white and pink noise in E3, and goes from the white-pink noise regime to pink noise in E3dx. All the four residual time series

exhibit therefore long-range correlations. Since the Hurst exponent is characterised by small values in correspondence of great fluctuations,  $H_t$  is under 0.5 whenever a significantly high outlier occurs. The value of  $H_t > 2.0$  in E4 is due to a flat region in the time series and is not of physical relevance. Finally, cross-correlations between uranium and the other parameters are shown in Figure D.4. The sampling sites are located inside the Gran Sasso National Laboratory of the Italian National Institute of Nuclear Physics on both sides of the main overthrust fault: E3 being excavated in the dolomitic formation, while E4 and E1 in the limestone one. Particularly, at site E3 there are two sampling points: E3 which is parallel to the overthrust fault in the North direction, and E3dx which is orthogonal to the fault into the cataclastic rocks. None of the sites seem to be influenced by pH. Their different locations seem instead to determine the influence of the other two parameters on uranium. E1, E3, and E4 do not exhibit correlations with ORP but with electrical conductivity. Conversely E3dx, that is in a region of clay minerals with high specific surface areas and reactive surface groups for binding metals and radionuclides, does not exhibit correlations with electrical conductivity but with ORP, at scales greater than  $\sim 35$  weeks.

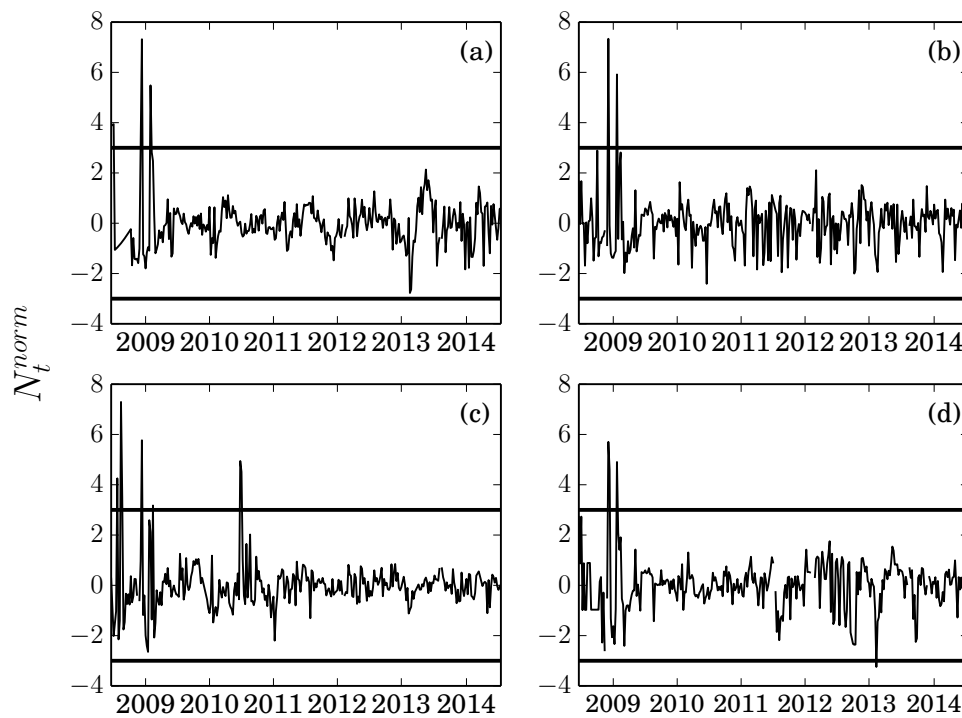


Figure D.2: Uranium residuals, for sites E1 (a), E3 (b), E3dx (c), and E4 (d).

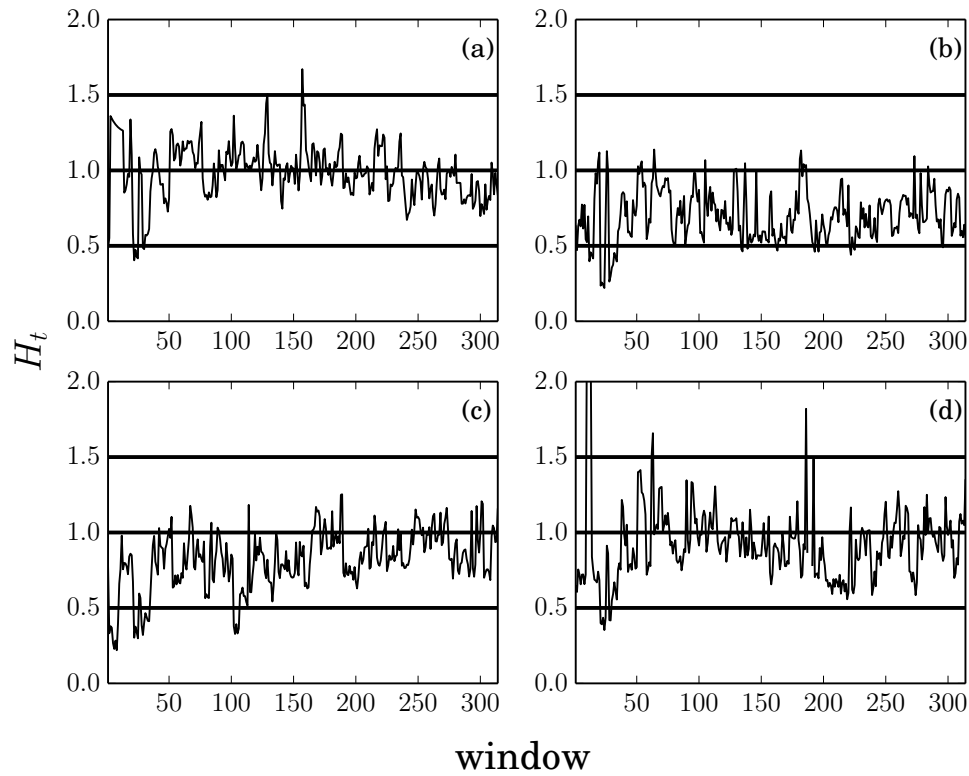


Figure D.3: Local Hurst exponent  $H_t$  of uranium residuals, for sites E1 (a), E3 (b), E3dx (c), and E4 (d).

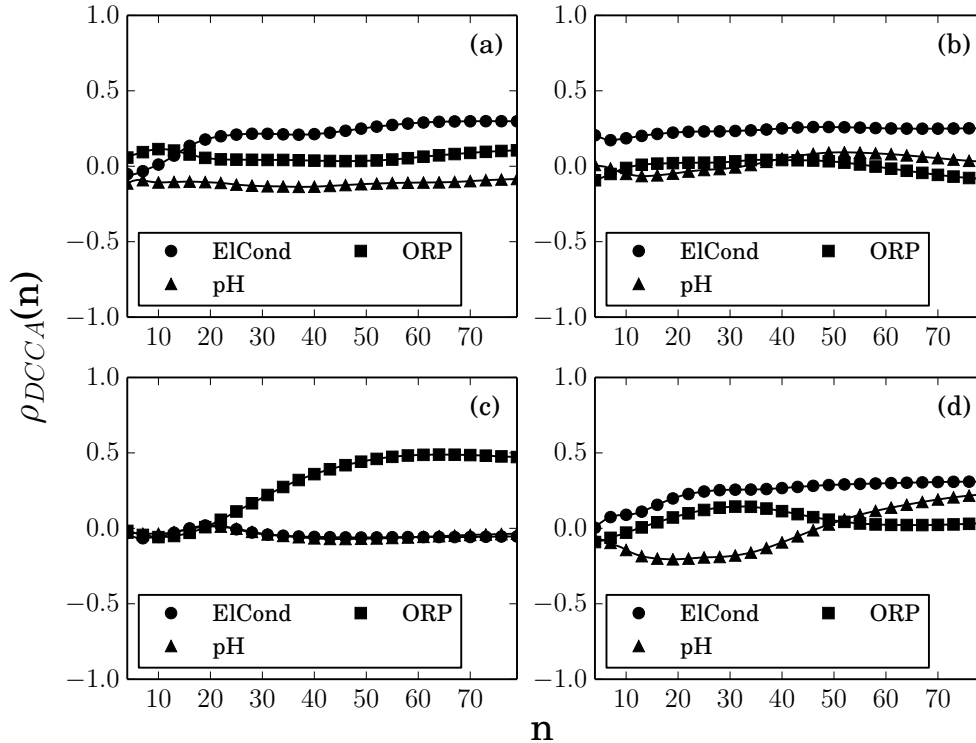


Figure D.4: DCCA between uranium residuals and the other parameters, for sites E1 (a), E3 (b), E3dx (c), and E4 (d).

---

## Bibliography

---

- [1] [www.ctbto.org](http://www.ctbto.org)
- [2] Lowrie, W., 2007. *Fundamentals of geophysics*. Cambridge university press.
- [3] Adushkin, V.V., An, V.A., 1993. *Teleseismic monitoring of underground nuclear explosions at the Nevada Test Site from Borovoye, Kazakhstan*. Science & Global Security, **3(3-4)**, 289-309.
- [4] *Certification of IMS particulate radionuclide stations (with guidelines for station installation)*. CTBT/PTS/INF.58/Rev.8.
- [5] Kaste, J.M., Norton, S.A., Hess, C.T., 2002. *Environmental chemistry of beryllium-7*. Reviews in mineralogy and geochemistry, **50(1)**, 271-289.
- [6] Feely, H.W., Larsen, R.J., Sanderson, C.G., 1989. *Factors that cause seasonal variations in beryllium-7 concentrations in surface air*. Journal of Environmental Radioactivity, **9(3)**, 223-249.
- [7] Jaeger, M., Wilmes, S., Kölle, V., Staudt, G., Mohr, P., 1996. *Precision measurement of the half-life of  $^7\text{Be}$* . Physical Review C, **54(1)**, 423.
- [8] Lal, D., Peters, B., 1967. *Cosmic ray produced radioactivity on the earth*. Kosmische Strahlung II / Cosmic Rays II, 551-612. Springer Berlin Heidelberg.
- [9] Holton, J.R., Haynes, P.H., McIntyre, M.E., Douglass, A.R., Rood, R.B., Pfister, L., 1995. *Stratosphere-troposphere exchange*. Reviews of geophysics, **33(4)**, 403-439.
- [10] Gerasopoulos, E., Zerefos, C., Papastefanou, C., Zanis, P., O'Brien, K., 2003. *Low-frequency variability of beryllium-7 surface concentrations over the eastern Mediterranean*. Atmos. Environ., **37(13)**, 1745-1756.

- [11] Cannizzaro, F., Greco, G., Raneli, M., Spitale, M., Tomarchio, E., 2004. *Concentration measurements of  $^7\text{Be}$  at ground level air at Palermo, Italy - comparison with solar activity over a period of 21 years*. J. Environ. Radioact., **72(3)**, 259-271.
- [12] Pham, M.K., Betti, M., Nies, H., Povinec, P.P., 2011. *Temporal changes of  $^7\text{Be}$ ,  $^{137}\text{Cs}$  and  $^{210}\text{Pb}$  activity concentrations in surface air at Monaco and their correlation with meteorological parameters*. J. Environ. Radioact., **102(11)**, 1045-1054.
- [13] Gerasopoulos, E., Zanis, P., Stohl, A., Zerefos, C., Papastefanou, C., Ringer, W., Tobler, L., Hübener, S., Gäggeler, H., Kanter, H., Tositti, L., Sandrini, S., 2001. *A climatology of  $^7\text{Be}$  at four high-altitude stations at the Alps and the northern Apennines*. Atmos. Environ., **35(36)**, 6347-6360.
- [14] Ioannidou, A., Vasileiadis, A., Melas, D., 2014. *Time lag between the tropopause height and  $^7\text{Be}$  activity concentrations on surface air*. J. Environ. Radioact., **129**, 80-85.
- [15] Raisbeck, G.M., Yiou, F., Fruneau, M., Loiseaux, J.M., Lieuvain, M., Ravel, J.C., 1981. *Cosmogenic  $^{10}\text{Be}$  /  $^7\text{Be}$  as a probe of atmospheric transport processes*. Geophysical Research Letters, **8(9)**, 1015-1018.
- [16] Dibb, J.E., Meeker, L.D., Finkel, R.C., Southon, J.R., Caffee, M.W., Barrie, L.A., 1994. *Estimation of stratospheric input to the Arctic troposphere:  $^7\text{Be}$  and  $^{10}\text{Be}$  in aerosols at Alert, Canada*. Journal of Geophysical Research: Atmospheres, **99(D6)**, 12855-12864.
- [17] Rehfeld, S., Heimann, M., 1995. *Three dimensional atmospheric transport simulation of the radioactive tracers  $^{210}\text{Pb}$ ,  $^7\text{Be}$ ,  $^{10}\text{Be}$ , and  $^{90}\text{Sr}$* . Journal of Geophysical Research: Atmospheres, **100(D12)**, 26141-26161.
- [18] Koch, D., Rind, D., 1998. *Beryllium 10 / beryllium 7 as a tracer of stratospheric transport*. Journal of Geophysical Research: Atmospheres, **103(D4)**, 3907-3917.
- [19] Kollar, D., Leya, I., Masarik, J., Michel, R., 2000. *Calculation of cosmogenic nuclide production rates in the Earth's atmosphere and in terrestrial surface rocks using improved neutron cross sections*. Meteoritics and Planetary Science Supplement, **35**, A90.
- [20] Zanis, P., Gerasopoulos, E., Priller, A., Schnabel, C., Stohl, A., Zerefos, C., Gäggeler, H., Tobler, L., Kubik, P., Kanter, H., Scheel, H., Luterbacher, J., Berger, M., 2003. *An estimate of the impact of stratosphere-to-troposphere transport (STT) on the lower free tropospheric ozone over the Alps using  $^{10}\text{Be}$  and  $^7\text{Be}$  measurements*. J. Geophys. Res., **108(D12)**, 8520.

- [21] Dibb, J.E., Talbot, R.W., Gregory, G.L., 1992. *Beryllium 7 and Lead 210 in the western hemisphere Arctic atmosphere: Observations from three recent aircraft-based sampling programs*. Journal of Geophysical Research: Atmospheres, **97(D15)**, 16709-16715.
- [22] Baskaran, M., Coleman, C.H., Santschi, P.H., 1993. *Atmospheric depositional fluxes of  $^7\text{Be}$  and  $^{210}\text{Pb}$  at Galveston and College Station, Texas*. Journal of Geophysical Research: Atmospheres, **98(D11)**, 20555-20571.
- [23] Koch, D.M., Jacob, D.J., Graustein, W.C., 1996. *Vertical transport of tropospheric aerosols as indicated by  $^7\text{Be}$  and  $^{210}\text{Pb}$  in a chemical tracer model*. Journal of Geophysical Research: Atmospheres, **101(D13)**, 18651-18666.
- [24] Graustein, W.C., Turekian, K.K., 1996.  *$^7\text{Be}$  and  $^{210}\text{Pb}$  indicate an upper troposphere source for elevated ozone in the summertime subtropical free troposphere of the eastern North Atlantic*. Geophysical Research Letters, **23(5)**, 539-542.
- [25] Benitez-Nelson, C.R., Buesseler, K.O., 1999. *Phosphorus 32, phosphorus 37, beryllium 7, and lead 210: Atmospheric fluxes and utility in tracing stratosphere / troposphere exchange*. Journal of Geophysical Research: Atmospheres, **104(D9)**, 11745-11754.
- [26] Chao, J.H., Chiu, Y.J., Lee, H.P., Lee, M.C., 2012. *Deposition of beryllium-7 in Hsinchu, Taiwan*. Applied Radiation and Isotopes, **70(2)**, 415-422.
- [27] García, F.P., García, M.F., Azahra, M., 2012.  *$^7\text{Be}$  behaviour in the atmosphere of the city of Granada January 2005 to December 2009*. Atmospheric environment, **47**, 84-91.
- [28] Papastefanou, C., Ioannidou, A., 1991. *Depositional fluxes and other physical characteristics of atmospheric beryllium-7 in the temperate zones (40 N) with a dry (precipitation-free) climate*. Atmospheric Environment. Part A. General Topics, **25(10)**, 2335-2343.
- [29] Todorovic, D., Popovic, D., Djuric, G., 1999. *Concentration measurements of  $^7\text{Be}$  and  $^{137}\text{Cs}$  in ground level air in the Belgrade city area*. Environment International, **25(1)**, 59-66.
- [30] Todorovic, D., Popovic, D., Nikolic, J., Ajtic, J., 2010. *Radioactivity monitoring in ground level air in Belgrade urban area*. Radiation protection dosimetry, **142(2-4)**, 308-313.
- [31] Ajtic, J., Todorovic, D., Filipovic, A., Nikolic, J., 2008. *Ground level air beryllium-7 and ozone in Belgrade*. Nuclear Technology and Radiation Protection, **23(2)**, 65-71.

- [32] Ajtic, J., Todorovic, D., Filipovic, A., Nikolic, J., 2008. *Ground level air beryllium-7 and ozone in Belgrade*. Nuclear Technology and Radiation Protection, **23(2)**, 65-71.
- [33] Papandreou, S., Savva, M.I., Karfopoulos, K.L., Karangelos, D.J., Anagnostakis, M.J., Simopoulos, S.E., 2011. *Monitoring of  $^7\text{Be}$  atmospheric activity concentration using short term measurements*. Nuclear Technology and Radiation Protection, **26(2)**, 101-109.
- [34] Carvalho, A.C., Reis, M., Silva, L., Madruga, M.J., 2013. *A decade of  $^7\text{Be}$  and  $^{210}\text{Pb}$  activity in surface aerosols measured over the Western Iberian Peninsula*. Atmospheric environment, **67**, 193-202.
- [35] Lozano, R.L., Hernandez-Ceballos, M.A., Rodrigo, J.F., San Miguel, E.G., Casas-Ruiz, M., Garcia-Tenorio, R., Bolivar, J.P., 2013. *Mesoscale behavior of  $^7\text{Be}$  and  $^{210}\text{Pb}$  in superficial air along the Gulf of Cadiz (south of Iberian Peninsula)*. Atmospheric environment, **80**, 75-84.
- [36] Tositti, L., Brattich, E., Cinelli, G., Baldacci, D., 2014. *12 years of  $^7\text{Be}$  and  $^{210}\text{Pb}$  in Mt. Cimone, and their correlation with meteorological parameters*. Atmospheric environment, **87**, 108-122.
- [37] Chatfield, C., 2013. *The analysis of time series: an introduction*. CRC Press.
- [38] Huang, N.E., Shen, Z., Long, S.R., Wu, M.C., & al., 1998. *The empirical mode decomposition and the Hilbert spectrum for nonlinear and non-stationary time series analysis*. Proceedings of the Royal Society of London A: mathematical, physical and engineering sciences. **454**, 903-995.
- [39] Huang, N.E., Wu, M.C., Long, S.R., Shen, S.S., Qu, W., Gloersen, P., Fan, K.L., 2003. *A confidence limit for the empirical mode decomposition and Hilbert spectral analysis*. Proceedings of the royal society of London A: mathematical, physical and engineering sciences. **459**, 2317-2345.
- [40] Wu, Z., Huang, N.E., Long, S.R., Peng, C.K., 2007. *On the trend, detrending, and variability of nonlinear and nonstationary time series*. Proceedings of the National Academy of Sciences. **104(38)**, 14889-14894.
- [41] Huang, T.L., Ren, W.X., Lou, M.L., 2008. *The orthogonal Hilbert-Huang transform and its application in earthquake motion recordings analysis*. 14th World Conference on Earthquake Engineering, Beijing. 12-17.
- [42] Stoica, P., Moses, R.L., 2005. *Spectral analysis of signals*. Upper Saddle River, NJ: Pearson Prentice Hall.
- [43] Lomb, N.R., 1976. *Least-squares frequency analysis of unequally spaced data*. Astrophysics and space science, **39(2)**, 447-462.

- [44] Scargle, J.D., 1982. *Studies in astronomical time series analysis. II-Statistical aspects of spectral analysis of unevenly spaced data*. The Astrophysical Journal, **263**, 835-853.
- [45] Zeichmeister, M., Kürster, M. 2009. *The generalised Lomb-Scargle periodogram: A new formalism for the floating-mean and Keplerian periodograms*. Astronomy & Astrophysics, **496(2)**, 577-584.
- [46] Press, W.H., Rybicki, G.B., 1989. *Fast algorithm for spectral analysis of unevenly sampled data*. The Astrophysical Journal, **338**, 277-280.
- [47] Dilmaghani, S., Henry, I.C., Soonthornnonda, P., Christensen, E.R., Henry, R.C., 2007. *Harmonic analysis of environmental time series with missing data or irregular sample spacing*. Environmental science & technology, **41(20)**, 7030-7038.
- [48] Kolmogorov, A., 1933. *Sulla determinazione empirica di una legge di distribuzione*. G. Ist. Ital. Attuari, **4**, 83-91.
- [49] Anderson, T.W., Darling, D.A., 1952. *Asymptotic theory of certain "goodness of fit" criteria based on stochastic processes*. The annals of mathematical statistics, 193-212.
- [50] Peng, C.K., Buldyrev, S.V., Goldberger, A.L., Havlin, S., Simons, M., Stanley, H.E., 1993. *Finite-size effects on long-range correlations: Implications for analyzing DNA sequences*. Physical Review E, **47(5)**, 3730.
- [51] Robinson, P.A., 2003. *Interpretation of scaling properties of electroencephalographic fluctuations via spectral analysis and underlying physiology*. Physical Review E, **67(3)**, 032902.
- [52] Ivanova, K., Ackerman, T.P., Clothiaux, E.E., Ivanov, P.C., Stanley, H.E., Ausloos, M., 2003. *Time correlations and 1/f behavior in backscattering radar reflectivity measurements from cirrus cloud ice fluctuations*. Journal of Geophysical Research: Atmospheres, **108(D9)**, 4268.
- [53] Siwy, Z., Ausloos, M., Ivanova, K., 2002. *Correlation studies of open and closed state fluctuations in an ion channel: Analysis of ion current through a large-conductance locust potassium channel*. Physical Review E, **65(3)**, 031907.
- [54] Varotsos, P.A., Sarlis, N.V., Skordas, E.S., 2003. *Long-range correlations in the electric signals that precede rupture: Further investigations*. Physical Review E, **67(2)**, 021109.
- [55] Varotsos, P.A., Sarlis, N.V., Skordas, E.S., 2003. *Attempt to distinguish electric signals of a dichotomous nature*. Physical Review E, **68(3)**, 031106.

- [56] Varotsos, C., Assimakopoulos, M.N., Efstathiou, M., 2007. *Long-term memory effect in the atmospheric CO<sub>2</sub> concentration at Mauna Loa*. Atmospheric Chemistry and Physics, **7(3)**, 629-634.
- [57] Koscielny-Bunde, E., Bunde, A., Havlin, S., Roman, H.E., Goldreich, Y., Schellnhuber, H.J., 1998. *Indication of a universal persistence law governing atmospheric variability*. Physical Review Letters, **81(3)**, 729.
- [58] Talkner, P., Weber, R.O., 2000. *Power spectrum and detrended fluctuation analysis: Application to daily temperatures*. Physical Review E, **62(1)**, 150.
- [59] Eichner, J.F., Koscielny-Bunde, E., Bunde, A., Havlin, S., Schellnhuber, H.J., 2003. *Power-law persistence and trends in the atmosphere: A detailed study of long temperature records*. Physical Review E, **68(4)**, 046133.
- [60] Fraedrich, K., Blender, R., 2003. *Scaling of atmosphere and ocean temperature correlations in observations and climate models*. Physical Review Letters, **90(10)**, 108501.
- [61] Pattantyùs-Abrahàm, M., Kiràly, A., Jànosi, I.M., 2004. *Nonuniversal atmospheric persistence: Different scaling of daily minimum and maximum temperatures*. Physical Review E, **69(2)**, 021110.
- [62] Matsoukas, C., Islam, S., Rodriguez-Iturbe, I., 2000. *Detrended fluctuation analysis of rainfall and streamflow time series*. Journal of Geophysical Research: Atmospheres, **105(D23)**, 29165-29172.
- [63] Moret, M.A., Zebende, G.F., Nogueira Jr, E., Pereira, M.G., 2003. *Fluctuation analysis of stellar x-ray binary systems*. Physical Review E, **68(4)**, 041104.
- [64] Kavasseri, R.G., Nagarajan, R., 2004. *Evidence of crossover phenomena in wind-speed data*. IEEE Transactions on Circuits and Systems I: Regular Papers, **51(11)**, 2255-2262.
- [65] Zebende, G.F., Da Silva, M.V.S., Rosa, A.C.P., Alves, A.S., De Jesus, J.C.O., Moret, M.A., 2004. *Studying long-range correlations in a liquid-vapor-phase transition*. Physica A: Statistical Mechanics and its Applications, **342(1)**, 322-328.
- [66] Ausloos, M., Ivanova, K., 2001. *Power-law correlations in the southern-oscillation-index fluctuations characterizing El Niño*. Physical Review E, **63(4)**, 047201.
- [67] Vandewalle, N., Ausloos, M., 1998. *Crossing of two mobile averages: A method for measuring the roughness exponent*. Physical Review E, **58(5)**, 6832.
- [68] Liu, Y., Gopikrishnan, P., Stanley, H.E., 1999. *Statistical properties of the volatility of price fluctuations*. Physical review E, **60(2)**, 1390.

- [69] Jànosi, I.M., Janecsò, B., Kondor, I., 1999. *Statistical analysis of 5 s index data of the Budapest Stock Exchange*. Physica A: Statistical Mechanics and its Applications, **269(1)**, 111-124.
- [70] Ausloos, M., Vandewalle, N., Boveroux, P., Minguet, A., Ivanova, K., 1999. *Applications of statistical physics to economic and financial topics*. Physica A: Statistical Mechanics and its Applications, **274(1)**, 229-240.
- [71] Raberto, M., Scalas, E., Cuniberti, G., Riani, M., 1999. *Volatility in the Italian stock market: an empirical study*. Physica A: Statistical Mechanics and its Applications, **269(1)**, 148-155.
- [72] Grau-Carles, P., 2000. *Empirical evidence of long-range correlations in stock returns*. Physica A: Statistical Mechanics and its Applications, **287(3)**, 396-404.
- [73] Ivanov, P.C., Yuen, A., Podobnik, B., Lee, Y., 2004. *Common scaling patterns in intertrade times of US stocks*. Physical Review E, **69(5)**, 056107.
- [74] Serinaldi, F., 2010. *Use and misuse of some Hurst parameter estimators applied to stationary and non-stationary financial time series*. Physica A: Statistical Mechanics and its Applications, **389(14)**, 2770-2781.
- [75] Kantelhardt, J.W., Zschiegner, S.A., Koscielny-Bunde, E., Bunde, A., Havlin, S., Stanley, H.E., 2002. *Multifractal detrended fluctuation analysis of nonstationary time series*. Physica A: Statistical Mechanics and its Applications, **316(1)**, 87-114.
- [76] Peng, C.K., Havlin, S., Stanley, H.E., Goldberger, A.L., 1995. *Quantification of scaling exponents and crossover phenomena in nonstationary heartbeat time series*. Chaos: An Interdisciplinary Journal of Nonlinear Science, **5.1**, 82-87.
- [77] Hu, K., Ivanov, P.C., Chen, Z., Carpena, P., Stanley, H.E., 2001. *Effect of trends on detrended fluctuation analysis*. Physical Review E, **64(1)**, 011114.
- [78] Kantz, H., Schreiber, T., 2004. *Nonlinear time series analysis*. Cambridge university press.
- [79] Feder, J., 2013. *Fractals*. Springer Science & Business Media.
- [80] Cencini, M., Cecconi, F., Vulpiani, A., 2010. *Chaos: from simple models to complex systems*. World Scientific.
- [81] Paladin, G., Vulpiani, A., 1987. *Anomalous scaling laws in multifractal objects*. Physics Reports, **156(4)**, 147-225.
- [82] Ihlen, E.A., 2012. *Introduction to multifractal detrended fluctuation analysis in Matlab*. Fractal analysis, **3**, 97.

- [83] Buldyrev, S.V., Goldberger, A.L., Havlin, S., Mantegna, R.N., Malsa, M.E., Peng, C.K., Stanley, H.E., 1995. *Long-range correlation properties of coding and noncoding DNA sequences: GenBank analysis*. Physical Review E, **51(5)**, 5084.
- [84] Podobnik, B, Stanley, H.E., 2008. *Detrended cross-correlation analysis: a new method for analyzing two nonstationary time series*. Physical review letters, **100.8**, 084102.
- [85] Horvatic, D., Stanley, H.E., Podobnik, B., 2011. *Detrended cross-correlation analysis for non-stationary time series with periodic trends*. Europhysics Letters, **94(1)**, 18007.
- [86] Zebende, G.F., Machado Filho, A., 2009. *Cross-correlation between time series of vehicles and passengers*. Physica A: Statistical Mechanics and its Applications, **388(23)**, 4863-4866.
- [87] Zebende, G.F., 2011. *DCCA cross-correlation coefficient: quantifying level of cross-correlation*. Physica A: Statistical Mechanics and its Applications, **390.4**, 614-618.
- [88] Vassoler, R.T., Zebende, G.F., 2012. *DCCA cross-correlation coefficient apply in time series of air temperature and air relative humidity*. Physica A: Statistical Mechanics and its Applications, **391(7)**, 2438-2443.
- [89] Marinho, E.B.S., Sousa, A.M.Y.R., Andrade, R.F.S., 2013. *Using detrended cross-correlation analysis in geophysical data*. Physica A: Statistical Mechanics and its Applications, **392(9)**, 2195-2201.
- [90] Zebende, G.F., Da Silva, M.F., Machado Filho, A., 2013. *DCCA cross-correlation coefficient differentiation: Theoretical and practical approaches*. Physica A: Statistical Mechanics and its Applications, **392(8)**, 1756-1761.
- [91] Du Kang, D., Lee, D.I., Kwon, B.H., Kim, K., Park, J.K., 2013. *Features of the detrended cross-correlation analysis in the time series between absorbable particulate matter and meteorological factors*. Journal of the Korean Physical Society, **63(1)**, 10-17.
- [92] Kristoufek, L., 2014. *Measuring correlations between non-stationary series with DCCA coefficient*. Physica A: Statistical Mechanics and its Applications, **402**, 291-298.
- [93] Seibert, P., Jank, C., Philipp A. *Quality Assessment of Meteorological Data from CTBTO/IMS Radionuclide Stations*. Poster at the CTBT: Science and Technology Conference, 26-30 June 2017.

- [94] Xu, L., Ivanov, P.C., Hu, K., Chen, Z., Carbone, A., Stanley, H.E., 2005. *Quantifying signals with power-law correlations: A comparative study of detrended fluctuation analysis and detrended moving average techniques*. Physical Review E, **71**(5), 051101.
- [95] Bianchi, S., Longo, A., Plastino, W., 2017. *A new methodological approach for worldwide beryllium-7 time series analysis*. Physica A, submitted.
- [96] Bianchi, S., Longo, A., Plastino, W., Povinec, P., 2018. *Evaluation of  $^7\text{Be}$  and  $^{133}\text{Xe}$  atmospheric radioactivity time series measured at four CTBTO radionuclide stations*. Applied Radiation and Isotopes, **132**, 24-28.
- [97] Bianchi, S., Plastino, W., di Sarra, A., Piacentino, S., Sferlazzo, D., 2018. *Carbon dioxide time series analysis: A new methodological approach for event screening categorisation*. In Mathematical Approach to Climate Change Impacts, Springer, in press.
- [98] Artuso, F., Chamard, P., Piacentino, S., Sferlazzo, D.M., De Silvestri, L., di Sarra, A., Meloni, D., Monteleone, F., 2009. *Influence of transport and trends in atmospheric  $\text{CO}_2$  at Lampedusa*. Atmos. Environ., **43**, 3044-3051.
- [99] Nakazawa, T., Ishizawa, M., Higuchi, K., Trivett, N.B.A., 1997. *Two curve fitting methods applied to  $\text{CO}_2$  flask data*. Environmetrics, **8**, 197-218.
- [100] Thoning, K.W., Tans, P.P., Komhyr, W.D., 1989. *Atmospheric carbon dioxide at Mauna Loa Observatory, 2. Analysis of the NOAA/GMCC data, 1974-1985*. J. Geophys. Res., **94**, 8549-8565.
- [101] Varotsos, C., Assimakopoulos, M.N., Efstathiou, M., 2007. *Technical Note: Long-term memory effect in the atmospheric  $\text{CO}_2$  concentration at Mauna Loa*. Atmos. Chem. Phys., **7**, 629-634.
- [102] Chamard, P., Thiery, F., di Sarra, A., Ciattaglia, L., De Silvestri, L., Grigioni, P., Monteleone, F., Piacentino, S., 2003. *Interannual variability of atmospheric  $\text{CO}_2$  in the Mediterranean: Measurements at the island of Lampedusa*. Tellus, **55B**, 83-93.
- [103] Komhyr, W.D., Gammon, R.H., Harris, T.B., Waterman, L.S., Conway, T.J., Taylor, W.R., Thoning, K. W., 1985. *Global atmospheric  $\text{CO}_2$  distribution and variations from 1968-1982 NOAA/GMCC  $\text{CO}_2$  flask sample data*. J. Geophys. Res., **90**, 5567-5596.
- [104] Kane, R.P., de Paula, E.R., 1996. *Atmospheric  $\text{CO}_2$  changes at Mauna Loa, Hawaii*. J. Atmos. Terr. Phys., **58**, 1673-1681.
- [105] Bianchi, S., Plastino, W., 2018. *Uranium time series analysis: a new methodological approach for event screening categorisation*. Journal of Environmental Radioactivity, **183**, 37-40.

- [106] Ulomov, V.I., Mavashev, B.Z., 1967. *A precursor of a strong tectonic earthquake*. Doklady Akademii Sciences SSSR, Earth Sciences Sections, **176**, 9-11.
- [107] Scholz, C.H., Sykes, L.R., Aggarwal, Y.P., 1973. *Earthquake prediction: a physical basis*. Science, **181**, 803-810.
- [108] Wakita, H., Igarashi, G., Nakamura, Y., Sano, Y., Notsu, K., 1989. *Coseismic radon changes in groundwater*. Geophysical Research Letters, **16**, 417-420.
- [109] Hauksson, E., 1981. *Radon content of groundwater as an earthquake precursor: evaluation of world-wide data and physical basis*. Journal of Geophysical Research, **86**, 9397-9410.
- [110] Monnin, M.M., Seidel, J.L., 1992. *Radon in soil and in groundwater related to major geophysical events: a survey*. Nuclear Instruments and Methods in Physics Research A, **314**, 316-330.
- [111] Virk, H.S., Singh, B., 1994. *Radon recording of Uttarkashi earthquake*. Geophysical Research Letters, **21**, 737-740.
- [112] Igarashi, G., Saeki, S., Takahata, N., Sumikawa, K., Tasaka, S., Sasaki, Y., Takahashi, M., Sano, Y., 1995. *Ground-water radon anomaly before the Kobe earthquake in Japan*. Science, **269**, 60-61.
- [113] King, C.Y., Koizumi, N., Kitagawa, Y., 1995. *Hydrogeochemical anomalies and the 1995 Kobe earthquake*. Science, **269**, 38-39.
- [114] Plastino, W., Bella, F., 2001. *Radon groundwater monitoring at underground laboratories of Gran Sasso (Italy)*. Geophysical Research Letters, **28(14)**, 2675-2677.
- [115] Plastino, W., 2006. *Monitoring of geochemical and geophysical parameters in the Gran Sasso aquifer*. Radionuclides in the Environment, Elsevier, 335-342.
- [116] Richon, P., Sabroux, J.C., Halbwachs, M., Vandemeulebrouck, J., Poussielgue, N., Tabbagh, J., Punongbayan, R., 2003. *Radon anomaly in the soil of Taal volcano, the Philippines: a likely precursor of the M 7.1 Mindoro earthquake (1994)*. Geophysical Research Letters, **30**.
- [117] Kawada, Y., Nagahama, H., Omori, Y., Yasuoka, Y., Ishikawa, T., Tokonami, S., Shinogi, M., 2007. *Time-scale invariant changes in atmospheric radon concentration and crustal strain prior to a large earthquake*. Nonlinear Processes in Geophysics, **14**, 123-130.
- [118] Plastino, W., Povinec, P.P., De Luca, G., Doglioni, C., Nisi, S., Ioannucci, L., Balata, M., Laubenstein, M., Bella, F., Coccia, E., 2010. *Uranium groundwater anomalies and L'Aquila earthquake, 6th April 2009 (Italy)*. Journal of Environmental Radioactivity, **101**, 45-50.

- [119] Gorbushina, L.V., Tyminskiz, V.G., Spiridinov, A.I., 1973. *Significance of radio-hydrogeological anomalies in a seismically active area for predicting earthquakes*. International Geology Review, **15**, 380-384.
- [120] Kuleff, I., Petrov, P., Kostadinov, K., 1980. *Uranium content variations in thermal waters from the west Rhodope crystalline massif during earthquakes in the Chepino valley (south Bulgaria)*. Journal of Radioanalytical Chemistry, **58**, 267-274.
- [121] Finkel, R.C., 1981. *Uranium concentrations and  $^{234}\text{U}/^{238}\text{U}$  activity ratios in fault associated groundwater as possible earthquake precursors*. Geophysical Research Letters, **8**, 453-456.
- [122] Plastino, W., Panza, G.F., Doglioni, C., Frezzotti, M.L., Peccerillo, A., De Felice, P., Bella, F., Povinec, P.P., Nisi, S., Ioannucci, L., Aprili, P., Balata, M., Cozzella, M.L., Laubenstein, M., 2011. *Uranium groundwater anomalies and active normal faulting*. J. Radioanal. Nucl. Chem., **288**, 101-107.
- [123] Plastino, W., Nisi, S., De Luca, G., Balata, M., Laubenstein, M., Bella, F., 2009. *Environmental radioactivity in the ground water at the Gran Sasso National Laboratory (Italy): a possible contribution to the variation of the neutron flux background*. J. Radioanal. Nucl. Chem., **282**, 809-813.
- [124] Plastino, W., Laubenstein, M., Nisi, S., Peresan, A., Povinec, P.P., Balata, M., Bella, F., Cardarelli, A., Ciarletti, M., Copia, L., De Deo, M., Gallese, B., Ioannucci, L., 2013. *Uranium, radium and tritium groundwater monitoring at INFN-Gran Sasso National Laboratory, Italy*. J. Radioanal. Nucl. Chem., **295**, 585-592.
- [125] Ciarletti, M., Plastino, W., Peresan, A., Nisi, S., Copia, L., Panza, G.F., Povinec, P.P., 2016. *Uranium Groundwater Monitoring and Seismic Analysis: A Case Study of the Gran Sasso Hydrogeological Basin, Italy*. Pure Appl. Geophys., **173(4)**, 1079-1095.
- [126] Plastino, W., Chereji, I., Cuna, S., Kaihola, L., De Felice, P., Lupsa, N., Balas, G., Mirel, V., Berdea, P., Baciu, C., 2007. *Tritium in water electrolytic enrichment and liquid scintillation counting*. Radiation Measurements, **42**, 68-73.
- [127] Bourdon, B., Henderson, G.M., Lundstrom, C.C., Turner, S.P., 2003. *Uranium-series geochemistry*. Reviews in Mineralogy & Geochemistry, **52**, Mineralogical Society of America.
- [128] Smith, C., Swarzenski, P., Dimova, N., Zhang, J., 2012. *Natural radium and radon tracers to quantify water exchange and movement in reservoirs*. Handbook of environmental isotope geochemistry. Springer, 345-365.

- 
- [129] Copia, L., Nisi, S., Plastino, W., Ciarletti, M., Povinec, P.P., 2015. *Low-level  $^{226}\text{Ra}$  determination in groundwater by SF-ICP-MS: optimization of separation and pre-concentration methods*. Journal of Analytical Science and Technology, **6**, 1-7.
- [130] Copia, L., Plastino, W., Nisi, S., Ciarletti, M., Povinec, P.P., 2017.  *$^{226}\text{Ra}$  and uranium isotopic ratios characterization into the Gran Sasso aquifer, Italy*. J. Radioanal. Nucl. Chem., **311**, 385-393.